



Noor Aziz, Muhamad Hifzhudin Bin (2021) *Analysis and applications of models of single-cell cardiac electrical excitation*. PhD thesis.

<http://theses.gla.ac.uk/81912/>

Copyright and moral rights for this work are retained by the author

A copy can be downloaded for personal non-commercial research or study, without prior permission or charge

This work cannot be reproduced or quoted extensively from without first obtaining permission in writing from the author

The content must not be changed in any way or sold commercially in any format or medium without the formal permission of the author

When referring to this work, full bibliographic details including the author, title, awarding institution and date of the thesis must be given

Enlighten: Theses

<https://theses.gla.ac.uk/>
research-enlighten@glasgow.ac.uk

Analysis and applications of models of single-cell cardiac electrical excitation

Muhamad Hifzhudin Bin Noor Aziz

Submitted in fulfilment of the requirements for the
Degree of Doctor of Philosophy

School of Mathematics and Statistics
College of Science and Engineering
University of Glasgow



University
of Glasgow

Winter 2020

Abstract

For over a century, cardiac electrophysiology modelling has been widely used for studying various problems of normal or abnormal heart rhythm, which is essential for understanding the disease mechanisms, provide accurate diagnoses and develop a new treatment. This thesis focuses on several analysis and applications of models in single-cell cardiac electrical excitation. In particular, I aim to study some typical challenges present in cardiac electrophysiology modelling, which is, variability in action potentials (AP) and their effects on cardiac anti-arrhythmic drugs, mechanisms of cardiac alternans and efficient numerical solver. To address the problems, I use various action potential models initially a range of biophysically detailed models, then focusing on a single simplified model.

This thesis consists of two main parts, excluding the part for background and introductory materials. The first and most important part, in terms of effort and time spent, is devoted to the investigation of action potential variability in a population of rabbit ventricular myocytes and their effects on cardiac anti-arrhythmic drugs. To determine the distributions of ion channel conductance values that capture the electrophysiological heterogeneity measured in large populations of cells, I apply the experimentally-calibrated population of models introduced by [Britton et al. \(2013\)](#), constructing from randomly varied ion conductances combinations. The model population is further used to quantitatively predict the range of response to the application of hERG and L-type calcium channel blocks. I implement the methodologies on three different AP models to study the capability of the cell models in predicting the drug effects. The models are a rabbit AP model by [Shannon et al. \(2004\)](#) and two human AP models by [Ten Tusscher et al. \(2004\)](#) and [O'Hara et al. \(2011\)](#). The AP responses following channel blocks are compared and analysed.

The second part of the thesis covers the analysis and application of a simplified ionic cardiac model. The model used is a modified version of caricature Noble model by [Biktashev et al. \(2008\)](#). Our first task is to propose the model as a generic model of cardiac electrophysiology by using a parameter estimation method. The model's parameters are adjusted so that it can reproduce AP morphologies of various cell types. In particular, the model is fitted to three different AP models which are Purkinje model by [Noble \(1962\)](#), ventricular model by [Luo and Rudy \(1991\)](#) and atrial model by [Courtemanche et al. \(1998\)](#). The action potential duration restitution curve of targeted models are also reproduced. The similar model template now can be used for various regions

of the heart by changing the parameter values. Furthermore, the modified caricature Noble model is fitted to experimental measurements of healthy and failing myocytes by [McIntosh et al. \(2000\)](#). I analyse the difference between parameter values from fitting works intending to find the physiological meaning for AP differences shown in experimental recordings. Parameter fitting of modified caricature Noble model demonstrates that it can replace other more complicated models, and it can also be used as a prototype to look for cardiac alternans and to construct an efficient numerical method.

The modified caricature Noble model is further used to develop an efficient numerical method for simulation of cardiac action potential model by taking into account the asymptotic solutions of the system. In order to achieve this, I implement the heterogenous multiscale method proposed by [Weinan and Engquist \(2003\)](#). The proposed method exhibits better stability and efficiency compared to other numerical solvers. The drawbacks of the method are also explained. Finally, the application of the model is extended by utilising it to study the mechanisms of cardiac alternans. The objective is to determine parameters and variables in the model that are responsible for generating action potential duration alternans. Using the slow-slow-time system of the model, an explicit discrete restitution map is derived and their equilibrium branches and bifurcations are studied. The bifurcations of equilibria of these maps are studied to identify regions in the parameter space of the model where normal response and alternans exhibit. Also, using the full system of the model, a framework formulated in terms of a boundary value problem is developed, which can be used to construct various branches of the action potential duration restitution map. At the end of the work, I perform some numerical simulations by fitting the caricature Noble model to models of normal response and alternans. The differences in parameter values are analysed and used to understand the onset of alternans. Importantly, the result shows that the magnitude of time-dependent potassium current can induce or suppress alternans.

Publications and Talks

Here we list out the publications and talks resulting from the work described in this thesis.

Publications

- Q. Lachaud, **M.H.N. Aziz**, F.L. Burton, R.C. Myles, R.D. Simitev, G.L. Smith: Electrophysiological heterogeneity in large populations of rabbit ventricular cardiomyocytes. *In preparation*.
- A. Asgari-Targhi, **M.H.N. Aziz**, A. Workman, R.D. Simitev: Analysis of action potential alternans in an archetypal model of cardiac cell excitation. *In preparation*.
- **M.H.N. Aziz**, R.D. Simitev: Estimation of parameters in models of single-cell cardiac action potential. *In preparation*.
- P. Mortensen, **M.H.N. Aziz**, H. Gao, R.D. Simitev: Modelling and simulation of electrical propagation in transmural slabs of scarred left ventricle tissue, 6th European Conference on Computational Mechanics (ECCM 6) 7th European Conference on Computational Fluid Dynamics (ECFD 7) 11–15 June 2018, Glasgow, UK.

Presentation/Talks

- (Poster presentation) A hybrid asymptotic-numerical method for excitable system. British Applied Mathematics Colloquium (BAMC). 10–12 April 2017. University of Surrey.
- (Poster presentation) An insight to mathematical modelling of cardiac electrophysiology. Malaysian Students Conference and Research Showcase (MySECON 2017). 13 May 2017. University of Edinburgh.
- (Oral presentation) Slow-fast analysis for excitable systems. Postgraduate seminar. 26 May 2017. University of Glasgow.
- (Poster presentation) A hybrid asymptotic-numerical method for excitable system. 3rd International Workshop on Soft Tissue Mechanics. 7–9 June 2017. University of Glasgow.
- (Poster presentation) Multiscale methods for cardiac electrophysiology model. SoftMech Industry Dialogue. 24 November 2017. University of Glasgow.

- (Oral presentation) Heterogeneous multiscale method. Postgraduate seminar. 8 December 2017. University of Glasgow.
- (Oral presentation) A generic model of single cell cardiac electrophysiology. British Applied Mathematics Colloquium (BAMC). 26–29 March 2018. University of St Andrews.
- (Poster presentation) Estimation of parameters in model of single cell cardiac electrophysiology. Multi-scale hard and soft tissue modelling workshop. 18–20 June 2018. University of Sheffield.
- (Oral presentation) Inter-subject variability in rabbit ventricular myocytes and their responses to IKr block. British Applied Mathematics Colloquium (BAMC). 24–26 April 2019. University of Bath.
- (Poster presentation) A computational study of inter-subject variability in rabbit ventricular myocytes and their responses to IKr block. Workshop on uncertainty quantification for cardiac models. 5–6 June 2019. University of Cambridge.
- (Oral presentation) Electrophysiological heterogeneity in large populations of rabbit ventricular cardiomyocytes and their effects to cardiac anti-arrhythmic drugs. ISM Virtual Research Seminar. 21–24 September 2020. University of Malaya, Malaysia.

Contents

Abstract	i
Publications and Talks	iii
Acknowledgements	xiv
Declaration	xv
I Background and thesis goals	1
1 Introduction	2
1.1 Context and motivation	2
1.2 Goals of thesis	6
1.3 Structure of thesis	12
2 Mathematical models and experimental methods for cardiac electrophysiology	14
2.1 The heart	14
2.2 The cardiac action potential	16
2.3 Calcium cycling and signalling	18
2.4 Mathematical models of cellular bioelectrical activity	19
2.4.1 Electrical circuit model of the cellular membrane	20
2.4.2 Models for the current/ionic flux	20
2.4.3 Ion channel gating	22
2.5 Overview of cardiac electrophysiology models	22
2.5.1 Purkinje fibre models	23
2.5.2 Atrial models	24
2.5.3 Ventricular models	25
2.5.4 Reduced ionic models	26
2.6 Some applications of cardiac electrophysiology models	27
2.6.1 Drug safety evaluation	27
2.6.2 Alternans	29

2.7	Experimental techniques	30
2.7.1	Micro-electrode recording method	30
2.7.2	Voltage and patch-clamp methods	30
2.7.3	Optical mapping technique	32
2.8	How close are animal and human hearts?	33
2.9	Action potential variability in cardiac cells	34
2.10	Anti-arrhythmic drugs	37
II	Applications of detailed models of the cardiac action potential	39
3	Experimental database of rabbit ventricular myocytes	41
3.1	Dataset features and method	41
3.2	Data analysis	43
3.2.1	Statistical tools	43
3.2.2	APD variation in left ventricle myocytes	43
3.2.3	Calculation of calibration ranges	45
3.2.4	Response to hERG block	46
3.2.5	Response to L-type calcium block	48
3.3	Conclusion	49
4	Action potential variability and drug pharmacodynamics	51
4.1	Motivation	51
4.2	Objectives of the chapter	52
4.3	Materials and methods	53
4.3.1	Baseline models and software	53
4.3.2	Parameter sensitivity analysis	57
4.3.3	Sampling method	59
4.3.4	Partial correlation coefficient	59
4.4	Experimentally-calibrated population of models	60
4.4.1	Constructing the control population	60
4.4.2	Constructing the drug population	62
4.5	Results and discussion	63
4.5.1	Development of the populations of models in control conditions	63
4.5.2	Parameter distributions in the control population of each model	67
4.5.3	Partial correlation coefficient for model biomarkers	70
4.5.4	Response to hERG block by dofetilide	71
4.5.4.1	Normal response	72
4.5.4.2	Hyper-response	74

4.5.4.3	Early after-depolarizations (EADs)	75
4.5.4.4	Parameter distributions for each AP response	75
4.5.4.5	Correlation between ion conductances of sub-populations	77
4.5.4.6	The ionic mechanisms of hyper-responders and EADs	79
4.5.4.7	IKr and ICaL conductances are the main determinant of APD prolongation	81
4.5.5	Response to L-type calcium block by nifedipine	84
4.5.5.1	Larger calcium transient leads to larger drug effect	85
4.5.6	Adding noise to simulation data	87
4.6	Conclusion	89
III Analysis of a simplified model of the cardiac action potential		91
5	The caricature Noble model	93
5.1	Introduction	93
5.2	Model formulation	94
5.3	Exact solutions	95
5.3.1	Solution of the initial value problem	95
5.3.2	Solution of the boundary value problem	98
5.4	Asymptotic solutions	100
5.4.1	Superfast-time system	100
5.4.2	Slow-time system	101
5.4.2.1	Fast-slow-time subsystem	101
5.4.2.2	Slow-slow-time subsystem	102
5.5	Phase plane analysis	102
5.5.1	Phase plane of modified caricature Noble model	103
5.6	Conclusion	104
6	Estimation of parameters in models of single-cell cardiac action potential	106
6.1	Introduction	106
6.2	Methods	107
6.2.1	Parameter selection and sensitivity analysis	107
6.2.2	Method of parameter estimation	110
6.2.3	Fitting protocols	111
6.2.3.1	Data used	111
6.2.3.2	Fitness function	112
6.2.3.3	Restitution curves	112
6.2.3.4	Simulation workflow	112

6.3	Fitting to action potential models	113
6.3.1	Fitting to a single action potential	113
6.3.2	Fitting to a restitution curve	114
6.3.3	Insights into models and the influence of parameters	114
6.3.4	Model performance	117
6.4	Fitting to experimental data	117
6.4.1	Fitting to a single action potential	119
6.4.2	Fitting to a restitution curve	119
6.5	Conclusion	119
7	Efficient numerical method for the solution of the modified caricature Noble model	121
7.1	Introduction	121
7.2	Heterogeneous multiscale method	123
7.3	Implementation of heterogeneous multiscale method on modified caricature Noble model	124
7.4	The efficiency of the method	128
7.5	Error analysis for heterogeneous multiscale method	131
7.6	Drawbacks of the heterogeneous multiscale method	134
7.7	Conclusion	134
8	Mechanisms of cardiac alternans	136
8.1	Introduction	136
8.2	APD restitution map from the slow-slow-time system	137
8.3	Constructing the APD restitution curves	144
8.3.1	1:1 restitution curves	145
8.3.2	Alternans (2:2) restitution curves	146
8.4	Numerical simulation: Fitting to a ventricular model	147
8.4.1	Action potential waveform	147
8.4.2	APD restitution curve	150
8.5	Conclusion	150
IV	Conclusion and supporting materials	151
9	Conclusion	152
9.1	Summary and discussion	152
9.2	Future directions	156
A	Codes and supplementary materials	158
A.1	Variability in action potential	158

A.1.1	Parameter range	159
A.1.2	Contour plot of APD90	160
A.1.3	AP morphologies in models and experiment	161
A.1.4	Archetypal models	162
A.1.5	Tissue sample with cell heterogeneity	163
A.1.5.1	Cell synchronisation	163
A.2	Caricature Noble model	167
A.2.1	Exact analytical solutions	167
A.2.1.1	Solution of the initial value problem	167
A.2.1.2	Solution of the boundary value problem	168
A.2.2	Asymptotic decomposition	169
A.2.2.1	Superfast-time system	169
A.2.2.2	Slow-time system	170
A.2.2.3	Slow-slow-time system	170
A.3	MATLAB codes for parameter fitting	170
A.3.1	Code 1	171
A.3.2	Code 2	171
A.3.3	Code 3	173

List of Tables

- 3.1 Calibration ranges for constructing models population 46
- 4.1 Ionic currents in the Shannon, TenTusscher and Ohara model. 54
- 4.2 Size of sub-populations in the drug population of cell models and experiment . 72
- 4.3 Parameter values for each archetypal model 80
- 4.4 Effects of L-type calcium block on AP and CaT biomarkers in the model popula-
tion of Shannon 84
- 5.1 Parameter values in the modified caricature Noble model 96
- 6.1 Influence of parameters on AP features of modified caricature Noble model . . 110
- 6.2 List of parameter values in modified caricature Noble model after fitting 116
- 6.3 The mean relative error of AP morphology between the modified caricature Noble
model and targeted models 116
- 6.4 The parameters values of modified caricature Noble model after fitting to the
experimental data of healthy and failing myocytes at 0.3 Hz pacing rate. 118
- 7.1 Maximum time step in each numerical solver 128
- 8.1 Parameter values of caricature Noble model after fitting to CVM 148

List of Figures

1.1	Action potential phenotypes and electrical system of the heart	3
1.2	Action potential variation in mouse ventricular cells	7
2.1	Anatomical structure of the heart	15
2.2	Action potential phases	17
2.3	Cellular membrane and electrical circuit	19
2.4	Patch clamp technique	31
2.5	AP morphology and profile of ionic currents of various animals	36
3.1	Action potential biomarkers	42
3.2	Distribution of APD90 in epicardium and endocardium cells	44
3.3	Inter-animal variation	44
3.4	DMSO and dofetilide effects on action potential duration	46
3.5	Scatter plot net drug effect on APD90 of individual cells in epicardial basal	47
3.6	Traces of normal AP responder and hyper-responder	47
3.7	DMSO and nifedipine effects on action potential duration	48
4.1	Action potential and calcium transient morphologies in the Shannon, TenTusscher and Ohara models	55
4.2	Profile of ionic currents in the Shannon, TenTusscher and Ohara models	56
4.3	Parameter sensitivity analysis in Shannon model	58
4.4	Diagrammatic representation of model calibration	61
4.5	Trace of action potentials in the accepted models of control population and range variation of APD90	63
4.6	Distributions of AP biomarkers in control population	65
4.7	Partial correlation coefficient and parameter distributions in $P_{\text{calibrated}}$ and P_{control}	67
4.8	Box-whisker plot of parameter distributions in the Shannon, TenTusscher and Ohara model population	68
4.9	Bar graph of the Q_{net} in the archetypal model of Shannon, TenTusscher and Ohara model	69

4.10	Partial correlation coefficient for model AP biomarkers in the Shannon, TenTusscher and Ohara model	70
4.11	Traces of action potential responses to 30% IKr block	72
4.12	Scatter plot of net effect of IKr block on APD90 against baseline APD90 by individual cell models	73
4.13	Distribution of 8 ionic conductances in normal responder, hyper-responder and EADs	76
4.14	2D density plot of ion conductances in each AP response	78
4.15	PCC in each AP response	79
4.16	Archetypal model of hyper-response	80
4.17	Archetypal model of EADs	81
4.18	Parameter distributions in models with small Δ APD90 and large Δ APD90	82
4.19	Parameter distributions in models with small APD90 and large APD90	83
4.20	Distributions of calcium transient amplitude in normal responders and hyper-responders	84
4.21	Traces of action potential and calcium transient responses to 60% ICaL block	85
4.22	Scatter plot of net effect of 60% ICaL block on APD90 against baseline APD90 by individual cell models	86
4.23	Distribution of calcium transient amplitude and baseline APD90 across model population	87
4.24	Scatter net effect of IKr and ICaL blocks on APD in model population of Shannon (with noise)	88
5.1	Exact analytical solutions of modified caricature Noble model	96
5.2	Exact analytical solutions of modified caricature Noble model solved using boundary value problem	99
5.3	Phase portrait of modified caricature Noble model	103
6.1	Sensitivity analysis test for parameters in the modified caricature Noble model	108
6.2	Action potential morphologies of the respective models after fitting process	113
6.3	Restitution curves of modified caricature Noble model in comparison to the target AP models	115
6.4	Action potential waveforms of modified caricature Noble model and experimental data	118
6.5	Parameters values of modified caricature Noble model after fitting to the experimental data	118
7.1	General framework of HMM model	123
7.2	Representation of the macroscopic and microscopic time scales in HMM	125
7.3	Solution of E solved using heterogenous multiscale method	126

7.4	CPU time and global mean error for various numerical methods used to solve the modified caricature Noble model	129
7.5	Efficiency of HMM compared to other numerical method	130
8.1	Bifurcation set in the Estim-r-B parameter space	141
8.2	Cross-sections of the bifurcation set in Figure 8.1 at particular parameter values	142
8.3	Examples of AP trace for different parameter sets	143
8.4	1:1 and 2:2 restitution curves using analytical and numerical BVP	144
8.5	1:1 and 2:2 restitution curves in the case of (unstable) alternans	145
8.6	Action potential morphology of caricature Noble model after the fitting process	147
8.7	Profile of potassium currents in the models of alternans and no alternans.	148
8.8	APD restitution curves of caricature Noble model and canine ventricular model	149
A.1	Scatter plot of drug effect on APD for $\pm 30\%$ and $\pm 50\%$ parameter variations .	159
A.2	Contour plot of APD90 as a function of parameter space	160
A.3	Action potential morphologies in the Shannon, TenTusscher and Ohara models	161
A.4	Archetypal model of hyper-response	162
A.5	Illustration of cells arrangement in tissue sample	163
A.6	Simulated temporal variability in 30 Shannon cell models before and after the cell coupling	165
A.7	Effect of gap-junction strength and number of cell interaction on cell coupling .	165

Acknowledgements

First of all, I would like to express my sincere gratitude to Ministry of Higher Education Malaysia and University of Malaya for giving me the opportunity via a SLAB scholarship to pursue my PhD.

I would like to express my sincere gratitude to my supervisor Dr. Radostin Simitev for his consistent support and guidance of my PhD study, for his patience, motivation and immense knowledge. His guidance helped me in all the time of research and writing of this thesis.

Besides my supervisor, I would like to thank the rest of my thesis committee: Prof. Blanca Rodriguez (University of Oxford) and Dr. Hao Gao (University of Glasgow) for their encouragement, insightful comments, and hard questions.

My sincere thanks also goes to my research collaborators at Institute of Cardiovascular and Medical Sciences: Prof. Godfrey Smith, Dr. Francis Burton, Dr. Quentin Lachaud and Dr. Rachel Myles, for their collaborative effort during data collection and analysis. Massive thanks to Prof. Godfrey Smith and Dr. Francis Burton for their effort to read and review this thesis.

Also, special thanks to my research group members in SoftMech for their continuous support and comments of my research works.

I am very much thankful to my lovely wife, Siti Hafizha for her love, understanding, prayers and continuing support to complete this study. I am also extremely grateful to my parents for their love, prayers, caring and sacrifices for educating and preparing me for my future. Finally, I express my thanks to my other friends and relatives for their support and valuable prayers.

Declaration

I declare that this thesis has been composed solely by myself and that it has not been submitted, in whole or in part, in any previous application for a degree. Except where stated otherwise by reference or acknowledgement, the work presented is entirely my own.

The data presented in Chapter 3 was obtained in an experiment carried out by our collaborators (Prof. Godfrey Smith, Dr Francis Burton and Dr Quentin Lachaud) in Institute of Cardiovascular and Medical Sciences, University of Glasgow. Any contributions from colleagues in the collaboration, such as diagrams, are explicitly referenced in the text.

Also, part of the work presented in Chapter 8 was previously published in a PhD thesis by Dr Amene Asgari-Targhi. I have revised and made additional contributions to the prior work, and they are clearly stated in the chapter.

Part I

Background and thesis goals

Chapter 1

Introduction

1.1 Context and motivation

The heart is a muscular organ and serves as a pump to circulate the blood through the blood vessels of the circulatory system. Like other muscles, the heart can mechanically contract and relax to serve its purposes. The mechanical contraction is triggered by the electrical excitation of cardiac cells, the so-called ‘action potential (AP)’. Figure 1.1 exhibits AP phenotypes at a different region of the heart. Due to its important role, it cannot truly rest or lose its rhythm as this would lead to loss of cardiac output, affecting the body’s organ systems including the heart itself. The heart has been a focus of intensive study, probably because heart failure, either mechanical or electrical, has caused millions of deaths globally. For instance, in the United Kingdom (UK) alone, cardiovascular disease was the main caused of death in 2012 and resulted in more than 50,000 deaths (Townsend et al. 2014). Hence, knowledge concerning the electrophysiology of the heart is important for the understanding of many aspects of the physiological and pathophysiological cardiac behaviour, and the problem has been actively investigated by many researchers.

For over a century, cardiac electrophysiology modelling has become a vital tool for studying normal and abnormal cardiac functions. Investigations at various levels of the membrane, cellular, tissue and organ have contributed to the development of a large number of biophysically detailed cardiac action potential models for various types of cardiac cells and species. Overall long term goal of the research community is to make a fully-integrated electro-mechanical model of the human heart that is fast-enough and fine-tuned enough to enable general clinical use, to provide accurate diagnoses and to study disease mechanism at the molecular, cell, tissue and organ level simultaneously. Nevertheless, at each scale and each model pose significant mathematical and technical problems that are of interest on their own. The models also will demand continuous alteration of new elements, such as model redesign and evaluation, improvements in the computational time of biophysically detailed models, implementation of standard protocols for comparison with experimental measurements, and investing in efforts to make sure the modelling results are repeatable and consistent.

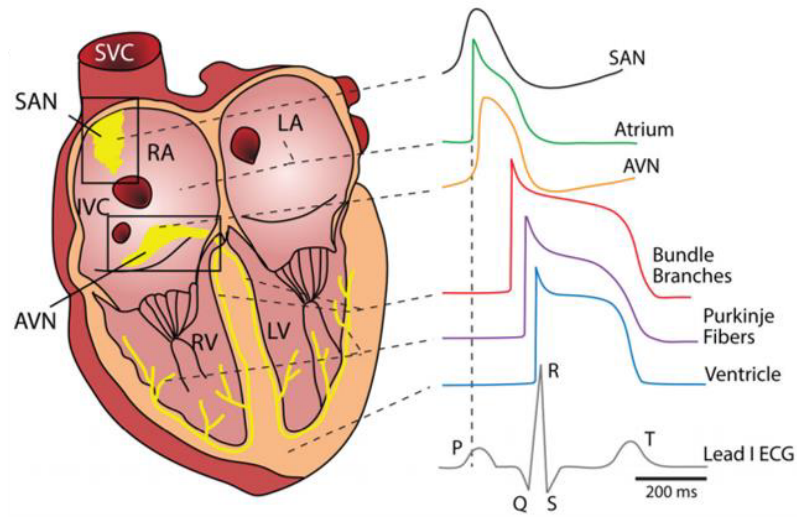


Figure 1.1: Electrical system and action potential phenotypes in different cell types of human heart. Figure was taken from [Bartos et al. \(2015\)](#).

More specifically, the topics covered in the thesis focus on the analysis of single-cell models of the AP and their applications in cardiac electrophysiology. The creation of a cardiac action potential model starts typically with the development of a representation of the underlying transmembrane currents. The mathematical structure of such a model is formulated as an ordinary differential equation (ODE),

$$\frac{dV}{dt} = -\frac{I_{\text{ion}}}{C_m}, \quad (1.1)$$

where I_{ion} is the sum of all transmembrane currents and C_m is the membrane capacitance. The negative sign is important since, by convention, the inward currents are negative, and the outward currents are positive, such that the inward depolarizing current is negative but also increases the membrane potential. The number and type of ionic currents incorporated in each AP model are varied, depending on the experimental data available at the time of constructing the model. More detailed models also may include descriptions of intracellular ion concentrations and processes. An overview of modelling these different components will be discussed in details in Chapter 2.

The ground-breaking action potential model by [Hodgkin and Huxley \(1952\)](#) took the quantitative and computational interpretation of physiological function to a whole new level. Precise measurements of sodium and potassium ion channel kinetics were used to formulate differential equations that were then solved to provide precise predictions of the nerve impulse voltage waveform and its conduction velocity. This work paved the way for the development of more accurate and complete ionic models with the introduction of important new mechanisms and involved major reformulations. In parallel, with the extension of the voltage clamp technique to the heart, various ion channels could be measured, including multiple delayed rectification channels ([Noble and Tsien 1968; 1969a,b](#)), calcium channels ([Reuter 1967](#)), and the incorporation of the sodium-potassium ([Gadsby 1980](#)) and sodium-calcium ([Reuter and Seitz 1968](#)) exchangers.

To date, hundreds of cardiac action potential models have been developed (Noble et al. 2012) to characterise the dynamic response of membrane potential under healthy and arrhythmias conditions.

There are now various ionic representations of SAN pacemaker cells (Demir et al. 1994, Lovell et al. 2004), atrial myocytes (Aslanidi et al. 2009a, Courtemanche et al. 1998), ventricular myocytes (Mahajan et al. 2008, Shannon et al. 2004) and Purkinje fibres (Noble 1962, Noble and Tsien 1969a;b). Different applications will lay stress on the accuracy of the different aspects of cell models. That is one of the reasons why so many models are now available. Each of them has its own strengths and weaknesses.

In reality, however, detailed AP models of cardiac excitation are extremely complicated, in the sense that complex models may not be suitable for simulations of cardiac tissue electrophysiology in clinical applications which require a faster outcome for the clinicians to make an instant decision. Parameters in the model also need to be re-estimated to fit the available clinical data, in which the process is not straightforward due to large parameters and variables included in the model. These complex models are also not amenable for theoretical works because of the nonlinearity of the kinetic terms that describe the process, suggesting a need for reduced complexity of the cardiac AP. Many attempts have been made to develop simplified mathematical models of cardiac action potential that do not aim to model sub-cellular processes, but rather to produce an action potential at a minimal cost. To mention a few of them, see reduced membrane models by FitzHugh (1961), Mitchell and Schaeffer (2003), Barkley (1991), Aliev and Panfilov (1996), Rogers and McCulloch (1994) and Fenton and Karma (1998). Unlike detailed ionic cardiac models which were initially developed following Hodgkin-Huxley formulation, simplified cardiac models are often based on the elegant Fitzhugh-Nagumo two-variable reduction of the Hodgkin-Huxley model. A common approach is either to make an appropriate functional generalisation of the FitzHugh-Nagumo system (Franzone et al. 2014), or directly truncate a detailed ionic model.

An attractive feature of these models is that, along with a reasonable description of excitability, threshold, plateau, and refractoriness, they focus on generic formulations that can often be treated analytically. Further examples of such impressive theoretical works using a simplified model can be obtained in Biktashev et al. (2008), Simitev and Biktashev (2011; 2006), Mitchell and Schaeffer (2003) and Tolkacheva et al. (2002). In addition, a simplified model may improve the computational tractability of large-scale tissue simulations (Clayton et al. 2011) and could also be used for whole heart simulation with various cell types (Balakrishnan et al. 2015, Sovilj et al. 2013). The common disadvantage of these models, however, is their lack of an explicit correspondence between model components and constituent parts of the biological system, e.g., ion channels, transporter proteins and ion concentrations. This hampers our ability to understand the physiology behind particular AP behaviour when the information is needed. A good simplified model must have the ability to reproduce important properties of action potential, including AP

duration and conduction velocity (CV) restitution curves, but computationally more efficient than other detailed models (Bueno-Orovio et al. 2008).

To date, mathematical models of cardiac electrophysiology already play a variety of roles, including the performing of ‘test series’ for verification of suitability of experimental designs, identification of targets for more detailed research, interpretation of experimental data, and description of causal relationships in complex biological responses (Thompson et al. 2000). Specifically, many types of research involving mathematical models of action potential have been conducted to understand the complex interaction between abnormal structure and function that underlies the development of cardiac arrhythmias (Clayton 2001). Cardiac alternans, for example, is an important precursor to arrhythmia and has also been linked to the incidence of ventricular fibrillation and sudden cardiac death (Bayer et al. 2016, Ten Tusscher et al. 2007, Trayanova and Boyle 2014, Trayanova and Chang 2016). Alternans is typically linked to oscillation of action potential duration and calcium cycling, particularly in the sarcoplasmic reticulum. To date, while APD restitution properties is widely used to observe the onset, the mechanism of the behaviour is not yet fully understood. Advances in experimental techniques have allowed us to get more data and visualise the electrical behaviour of the heart in more detail, hence, making the observation and understanding of lethal arrhythmia, including cardiac alternans more plausible.

The term ‘heterogeneity’ quite often signifies various features in cardiac physiology, including both electrical and mechanical properties of the cells. Distinctions in the intracellular expression of various ion channel ensure a pattern of cellular electrical heterogeneity. In particular, cardiac cells may have different expressions of the voltage-dependent sodium channels, potassium channels and L-type channels which can alter the balance of the ionic currents. In consequence, this may result in significant differences in the morphology and duration of the action potential (Muszkiewicz et al. 2016, Ni et al. 2018). Cell-to-cell variation present in the cardiac electrophysiology may influence the cell responses to cardiac drugs which could potentially lead to pro-arrhythmic effects. Due to recent advances in experimental and computational techniques, many studies have taken into account physiological variability and started to move beyond the traditional cardiac model-building scheme. The methodology is important and can be applied to study the mechanisms of cardiac arrhythmias, with a special emphasis on atrial fibrillation, and improve the assessment of pro-arrhythmic risk and drug response.

In conclusion, computational models of action potential are potentially robust tools for studying normal and pathological processes of cardiac functions. Most of the tools for constructing accurate models are well established and are being used increasingly in tandem with experimental and clinical studies. Despite this positive progress in cardiac modelling, the underlying problem, in most cases, remained constant, and the problem should be placed under further investigation.

1.2 Goals of thesis

In the thesis, we aim to solve several unresolved issues in cardiac electrophysiology using either detailed biophysically or simplified models of action potential, depending on the state of the respective problems. The problems may be grouped into several topics as following;

Variability in action potential and drug pharmacodynamics

In this topic, our goals are;

- to determine the distributions of ion channel conductance values that capture the electrophysiological heterogeneity measured in large populations of rabbit ventricular cardiomyocytes
- to investigate the effects of action potential heterogeneity on the application of drug blocking of hERG and L-type calcium channels
- to study the capability of cell models in predicting the drug effects.

The action potential of excitable cells, for example, cardiac cells and neurons, reflects the orchestrated activity of various ion channels and electrogenic transporters. In many studies, including both experimental and computational modelling, have shown that there is significant inter-individual variability in the combinations of molecular-input parameters that can generate very similar integrated outputs (Britton et al. 2013; 2017b, Romero et al. 2009, Sobie 2009). The traditional way to construct a cardiac cell model is by using the mean behaviour of available experimental data, technically from the species and cell type being modelled. The model is then represented the typical or average response of an isolated cardiac cell, creating a ‘cell-specific model’ with a unique parameter set. Unfortunately, this model cannot reproduce output for different experimental data taken from other laboratories due to difference in experimental protocols and conditions such as temperature and solution concentration, which can influence the dynamics of ionic currents. This has led to a paradigm shift in computational modelling of cardiac electrophysiology that relies not on generating idealised output based on mean data but rather development of populations of models that account for the observed variability in molecular inputs.

As shown in Figure 1.2, the action potential recordings from a population of mouse ventricular cells are significantly different, even being stimulated at similar external stimuli and conditions. Cell variability in cardiac electrophysiology occurs due to many factors. A likely source of this behavioural variability is differences in the levels of ion channels, pumps, and transporters, which arise as the cellular expression system interacts with stochastic effects (Zaniboni et al. 2000), pathological processes (Rahm et al. 2018), local environmental effects (Muszkiewicz et al. 2016), and extrinsic effects such circadian rhythm (Jeyaraj et al. 2012). Variability in action potentials

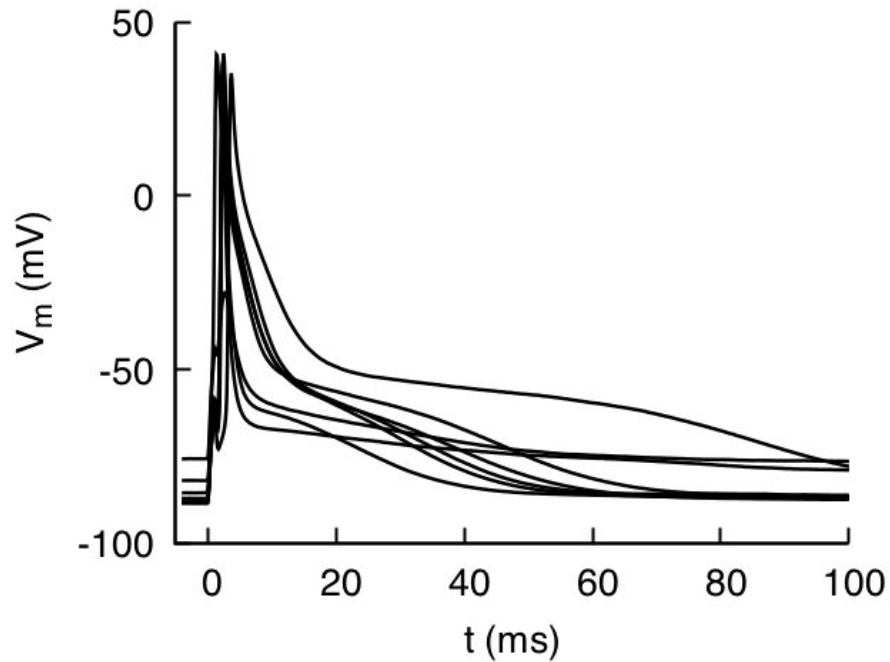


Figure 1.2: Traces of action potentials of isolated mouse ventricular cells paced at 4 Hz under current clamp. The recordings illustrate the typical degree of cell-to-cell variability of AP waveform observed in a population of cells. Figure originally from [Rees et al. \(2018\)](#).

is a vital phenomenon as it usually happens in nature but yet poorly understood. Besides, the limited ability of experimental techniques to probe complex interactions between components has hindered our understanding of the factors that cause a range of behaviours within cell populations.

Previous studies to modelling variability have incorporated variation in the strength of ionic currents in a cardiac cell but did not fully link the modelled variability to variability observed in experimental measurements ([Romero et al. 2009](#), [Sarkar and Sobie 2010; 2011](#), [Sobie 2009](#)). Hence, following the work, [Britton et al. \(2013\)](#) introduced a new experimentally-calibrated population-based approach and developed a population of models in order to exhibit the variability in rabbit Purkinje cells. The model population was further used to study the effect of AP variability to potassium block. Their results, however, were limited to small sample size (12 different Purkinje fibres), which could possibly mask the level of variation seen in the experiments, suggesting large sample size is needed to improve estimates of variation.

Our collaborators (lead by Prof. Godfrey Smith) based in Institute of Cardiovascular and Medical Sciences, University of Glasgow have developed a medium/high throughput assay using optical fluorescence techniques which can be used to measure the electrical and mechanical response within large of populations of cardio-myocytes ranging from 100 to 500 cells per heart ([Lachaud 2019](#)). These large datasets show very pronounced heterogeneity in the electrophysiological signatures of individual ventricular myocytes, including heterogeneity in response to drug blocking of hERG and L-type calcium channels. Using these experimental measurements and several biophysically detailed action potential models, we construct a population of rabbit ven-

tricular models and then use them to study the impact of variability in cellular electrophysiology on hERG and L-type calcium blocks. Also, quantitative comparison of effects of these channel blocks between three different ventricular models are investigated.

Estimation of parameters in models of single-cell cardiac action potential

In this topic, the goals are,

- to demonstrate parameter estimation method and fitting protocols with multiple objective functions.
- to introduce the caricature Noble model as a generic action potential model by fitting the model to various detailed action potential models and experimental measurements of healthy and failing myocytes.
- to compare the AP morphologies and restitution curves with the respective models and experimental data.
- to provide the parameter interpretation of the fitting results and essential differences between models.

Often, action potential models compose of a large number of parameters and variables using a set of ordinary differential equations (ODEs) to describe the interacting ion currents and calcium handling mechanisms. This, however, makes the process of understanding the relationship between model outputs and model parameters more complicated, suggesting a need for simple, reduced-complexity cardiac AP models. Simplified AP model is a representation of more biophysically complex models and contains a small number of equations with less parameter and variable. Despite its simplicity, it still preserves the important fundamental characteristics of cardiac electrophysiology. Some even allow for analytical works (Biktashev et al. 2008, Mitchell and Schaeffer 2003, Simitev and Biktashev 2011). Another obvious advantage of the simplified model is that the small number of parameters in the model makes parameter fitting less complicated, as many parameters govern/contribute to only a single property. The model usually is not limited to fitting to experimental data only, but the model parameters can be adjusted to fit data from more detailed models of various cell types and species (Bueno-Orovio et al. 2008, Groenendaal et al. 2015, Guo et al. 2013). Owing to the several number of free parameters in action potential models, these parameters, in practice, can be modified, so that the model can be used to reproduce different AP morphologies (Clayton et al. 2011).

An example of a generic model like the Fitzhugh-Nagumo type system lacks important cardiac properties, including a realistic APD restitution curve (Clayton 2001, Kogan et al. 1991), and fails to reproduce some qualitative features of cardiac action potential (Biktashev et al. 2008). Hence, using the modified version of caricature Noble model by Biktashev et al. (2008), we

aim to reproduce action potential morphologies and restitution curves from even more complex electrophysiological models of various cell types, like Purkinje fibre, ventricular and atrial cell. In addition to fitting to more biophysically detailed models, the model can also be used to fit data from the experimental data of healthy and failing myocytes, since this model only focuses on reproducing the dynamical properties of AP rather than detailed ion currents. The results can be used further to investigate the cause of AP behaviours.

In this study, we show that the modified caricature Noble model is flexible enough to accurately capture the electrical properties of cardiac myocytes by adjusting the parameter values. The model also has the advantage of being less computational demanding than other biophysically detailed action potential models. Fitting qualitatively different models to a common mathematical structure offers a number of advantages for their use and interpretation as well essential differences in their AP waveform can be identified. The model also is amenable for further mathematical analysis, for instance, to develop an efficient numerical method and study the mechanisms of cardiac alternans.

Efficient numerical method for the solution of the modified caricature Noble model

In this topic, the goals are,

- to develop an efficient numerical method for simulation of cardiac action potential model using its asymptotic structures.
- to compare the stability and efficiency of such method with other numerical methods.

The wide variety of existing cardiac cell models encompasses many different properties, including the complexity of the model and the degree of stiffness (Spiteri and Dean 2010). Accordingly, no single numerical method can be expected to be the most efficient for every model. One such challenge is that the ionic model is usually a stiff, non-linear set of ODEs that must be solved for each node in the simulation. This causes the simulation to be computationally expensive and time-consuming. Large scale 3D virtual heart model, for instance, may involve millions of grid points, and the solution has to be evolved over tens of thousands of time steps. Such enormous computational demands can only be solved with the aid of advanced numerical techniques and parallel computing approaches. However, even with current supercomputing facilities, execution times are still slow, lagging real-time by roughly a factor of 10^4 to 10^5 (Plank et al. 2009). Berenfeld and Jalife (1998) also demonstrated that simulation for Purkinje-muscle reentry in a 3-dimensional Fitzhugh-Nagumo model required about 1.5 hours to run 10 ms of cardiac activity. Generally speaking, simulations involving tissue samples and observation of longer period are expensive, and further significant performance improvements are needed. Other than using a simplified model, constructing a robust numerical algorithm is considered to be the most effective way to speed up the simulation time.

To date, various numerical schemes have been implemented to solve action potential models (Ji and Fenton 2016, Roy et al. 2017, Victorri et al. 1985). A typical method like explicit Euler method is one of the conventional method used to solve the system due to its easy implementation, but its stability is stringent in the sense that user needs to use a relatively small size of time-step, leading to longer computational times. Another advanced method, for example, fully implicit solvers are faster than explicit method but require the solution of a nonlinear system of equations. Hence, developing the most robust numerical method with easy implementation has remained a popular endeavour among researchers. In the thesis, we aim to develop a robust numerical method for an efficient simulation taking advantage of the fast and slow manifolds of a cardiac model. The method is the implementation of a conventional method by Weinan and Engquist (2003), the so-called ‘heterogeneous multiscale method’. It is a method for solving a mathematical model with multiple time scales. We will apply the method on the modified caricature Noble model and then compare the result with other available numerical schemes. To our knowledge, no research in cardiac electrophysiology has applied this approach on an action potential model and hence, motivating us to explore the feasibility of the method.

Mechanisms of cardiac alternans

In this topic, the goals are,

- to identify the parameters and variables in the model that are responsible for generating action potential duration alternans.
- to derive an analytical formula to construct the restitution curve in both normal and alternans conditions.
- to develop a framework formulated in terms of boundary value problems for studying cardiac restitution.
- to validate the theoretical work derived in this chapter by fitting the caricature Noble model to models of alternans and no alternans.

Cardiac electrophysiology models have made significant contributions to our understanding of how the electrophysiological heterogeneities predispose to various types of cardiac arrhythmias. This includes the mechanisms that govern the beginning, maintenance and elimination of arrhythmia, which are still not fully understood. As a consequence, treatment of cardiac arrhythmia remains disappointingly ineffective compared to other pharmacological therapies, emerging a significant potential for improvement (Trayanova 2014). There are many types of arrhythmias, and this thesis only focuses on cardiac alternans. This is because repolarisation alternans, or alternans that manifests during ventricular repolarisation has been linked with an increased vulnerability to ventricular arrhythmias and sudden cardiac death under a wide range

of pathophysiologic conditions, for example, myocardial ischemia (Armoundas et al. 2002). At the cellular level, cardiac alternans is defined by cyclic, beat-to-beat alternations in contraction amplitude (mechanical alternans), action potential duration (APD; electrical or APD alternans), and calcium transient amplitude (calcium alternans) at constant stimulation frequency (Edwards and Blatter 2014). However, in this study, we will only consider the APD alternans because the model does not include the calcium current and variable for cell contractility.

For the time being, the most efficient way to study cardiac alternans is by using the restitution properties of cardiac cells. A restitution curve describes a functional relationship between the duration of a cardiac action potential and the length of its previous diastolic interval. However, the experimental protocols for measuring restitution encounter a number of difficulties, including that of distinguishing the ultimate periodic regime from transient behaviour. This is because of the presence of cardiac memory (Gilmour et al. 1997, Tolkacheva et al. 2003). Common experimental protocols like dynamic restitution pacing method require the cell to be periodically stimulated at a fixed interval of basic cycle length until it settles into a stable periodic response. Several periodic responses have been recorded in experiments (Hall et al. 1999, Visweswaran et al. 2013). For instance, every successful stimulus may excite an action potential with identical shape (1:1 response). However, under certain conditions, only every second stimulus may excite an action potential and create a 2:1 response. Under different conditions, the action potential duration may alternate between long and short (alternans 2:2 response). It is commonly assumed that the 1:1 response represents the healthy function of the cardiac cell; meanwhile, the other two responses are viewed as ‘instabilities’ of the normal response which may potentially lead to cardiac arrhythmias (Cherry et al. 2012, Karma 1994). Hence, the action potential duration (APD) restitution maps can be used to study such instabilities.

With this motivation, we aim to derive an explicit discrete restitution map for caricature Noble model and study their equilibrium branches and bifurcations. This approach has been done earlier by Tolkacheva et al. (2002) and Mitchell and Schaeffer (2003) on a simplified version of Fenton and Karma (1998) model. Nevertheless, the model does not represent the real physiology of a cardiac cell, unlike the caricature Noble model, which is more realistic and preserve the fundamental structures of an ionic model (Biktashev et al. 2008). We then explore the regions in the parameter space of caricature model where normal 1:1 response and alternans 2:2 occur. The parameter space is validated with numerical simulations. We also develop a framework formulated in terms of boundary value problems for studying cardiac restitution. This framework can be used to derive analytically or compute numerically different branches of the action potential duration restitution map from the full excitable models. Finally, our method is validated by comparing the asymptotic restitution map with the boundary value problem formulated restitution curves.

1.3 Structure of thesis

The thesis is composed of four main parts. They are outlined as follows,

Part I (Background and thesis goals) The first part is divided into two chapters. Both chapters mostly contain the introductory materials which are needed for this thesis. Chapter 1 provides a brief introduction to cardiac electrophysiology and the motivation behind the works. Importantly, the objectives and attempted research questions of each project are outlined. In the second chapter, the background of cardiac electrophysiology is discussed in more detail. The development of action potential models since the pioneer model by [Hodgkin and Huxley \(1952\)](#) is discussed. The underlying mathematical equations of cardiac cellular electrophysiology model and the contribution of particular ionic currents in the AP generation are explained. Moreover, several experimental techniques used to measure the transmembrane potential in an isolated cardiac cell is discussed. The chapter is ended by providing some essential information on cardiac anti-arrhythmic drugs.

Part II (Applications of a detailed models of the cardiac action potential) The second part consists of two chapters (Chapter 3 and 4) and is the most significant part, in terms of effort and time spent. In this second part, the focus mostly on the investigation of action potential variability in a population of rabbit ventricular myocytes and their effects on cardiac anti-arrhythmic drugs. The second part of this thesis is begun by explaining the experimental data and the experimental methods used to measure the recordings of APs under control and drug conditions (Chapter 3). Using the information gathered from the experimental data, the underlying mechanisms in the variability of action potentials in a population of rabbit cardio-myocytes is studied. In order to achieve this, an experimentally calibrated population of models is constructed and the population is used to investigate how the cell-to-cell variability may influence the action of drugs. Several detailed biophysically ionic models are used, and quantitative comparison of effects of hERG and L-type calcium blocks between the three models and experimental measurements are carried out.

Part III (Applications of a simplified model of the cardiac action potential) Biophysically detailed model of action potential is very complex due to a large number of equations and parameters exist in the model in order to describe the complex process of electrical excitation in a cardiac cell. Due to this complexity, it is almost impossible to use the model for analytical works. Hence, such a model can be replaced with a more simple model that has less parameters and variables but still accurately preserve the essential properties of an action potential. From this point onwards, I shift from studying the complex model of action potential to studying simpler model. A modified version of caricature Noble model by [Biktashev et al. \(2008\)](#) is used.

This part consists of three main chapters (Chapter 5–8). In Chapter 5, the governing equations of modified caricature Noble model is described and its exact analytical and asymptotic solutions

are derived. The analytical solutions are derived using both initial and boundary value problems. The phase portrait of the system is illustrated and the excitation conditions of an AP is also explained. The main work begins in Chapter 6, where a simple parameter estimation method in single-cell modelling is demonstrated. The modified caricature Noble model is fitted to even more complex biophysically action potential models of various cell types and experimental measurements of healthy and failing rabbit ventricular myocytes. Specifically, the focus is to fit the AP morphology and APD restitution curves of targeted data. Parameter fitting of the modified caricature Noble model demonstrates that it can be used as substitution to other more complicated models when other ionic properties are not needed. Moreover, in this thesis, we show that this model can be used as a prototype to look for cardiac alternans and to develop an efficient numerical method.

The asymptotic structures of modified caricature Noble model derived in Chapter 5 is exploited by implementing a conventional numerical method, the so-called ‘heterogeneous multiscale method’ on this model (Chapter 7). The stability and drawbacks of such method are analysed. Also, the asymptotic-numerical method is compared with other available numerical methods. Finally, in Chapter 8, the caricature Noble model is used to study the mechanisms of action potential duration alternans. In particular, an explicit discrete restitution map for the model is derived and the parameter region where alternans occurs is identified. Following the fitting methodologies in Chapter 6, the caricature Noble model is fitted to a canine ventricular model and the results are used to verify the parameter space where alternans occurs.

Part IV (Conclusion and supporting materials) The final part provides a summary of the research works and outlines of some future directions. MATLAB codes and some additional materials are provided in the end of this chapter.

Chapter 2

Mathematical models and experimental methods for cardiac electrophysiology

In this chapter we provide essential biological and mathematical background to the topics discussed in the upcoming chapters. We begin this chapter by explaining the anatomy of the heart and its function as a muscular pump. We also describe the mechanisms behind the cardiac electrical excitation and propagation of action potentials. We then explain the general mathematical description of an action potential model in describing cardiac electrical behaviour at the cellular level. A brief overview of cardiac cellular electrophysiology model development since the ground-breaking model by [Hodgkin and Huxley \(1952\)](#) is reviewed. These models are useful in many ways, for instance, they can serve as a powerful tool for investigating abnormal heart conditions, from individual cells to the whole heart. Later in this chapter, we outline some applications of cardiac action potential models to study cardiac diseases and treatment. Following the overview of cardiac electrophysiology, we end this chapter by discussing some of the experimental techniques used to measure transmembrane potential and ionic currents of cardiomyocyte.

2.1 The heart

The heart is a muscular organ consisting of four chambers that are located just to the left of the midline of the thoracic cavity. The upper two chambers are known as atria, and the bottom two chambers are called ventricles, as shown in [Figure 2.1](#). The right atrium and ventricle are separated by the tricuspid valve, whereas, the left atrium and ventricle are separated by the mitral valve. These valves function to prevent the backward flow of blood. Our heart is a muscular organ, where its main function is to maintain adequate cardiac output. Cardiac output is the amount of blood our heart is able to pump in one minute. In particular, the heart function to deliver ample supply of blood to our body part at adequate pressure to encounter tissue demands for oxygen and nutrients. The pumped blood also carries metabolic waste such as carbon dioxide

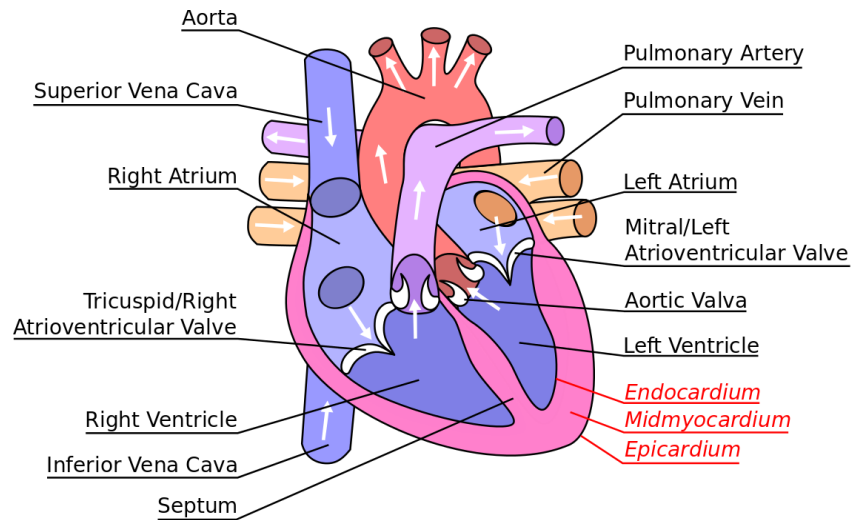


Figure 2.1: Anatomical structure of the heart. The white arrows indicate the blood flow in the heart. Reproduced from [Gemmell \(2014\)](#).

to the lungs.

Our heart is auto-rhythmical and the rate is determined by body's needs via autonomic nerves (through the vagus nerve and sympathetic trunk that connect to the brain). Particularly, these nerves act to influence, but not control, the heart rate. The brain signals our heart to beat faster by sending messages to our heart's electrical system, which regulates the timing of the heartbeat. If the cardiac output is low, the adrenal glands will release more hormone adrenaline, which travels in the bloodstream and stimulates our heart to beat faster. Although this mechanism is important to maintain cardiac output, but a faster heart rate can be counterproductive as it causes less time for the ventricle to fill with blood after each heartbeat.

The mechanism of the pumping action of the heart easily understandable. The blood circulation consists of the systemic (left) and pulmonary (right) circulation. Pulmonary circulation transports blood between the heart to the lungs, whereas systemic circulation moves blood between the heart and the other part of body. The right heart deoxygenated blood is collected from two large veins, superior and inferior vena cavae (Figure 2.1) and the blood is then pumped from right atrium into the right ventricle through tricuspid valve. As right ventricle begins to contract, the tricuspid valve closes and the blood is pumped into the pulmonary artery and then to the lungs. The carbon dioxide in the blood is exchanged for oxygen. In the left heart, oxygen-rich blood is returned to the left atrium through the pulmonary veins. It is then pumped into the left ventricle via mitral valve. Finally, the oxygenated blood is delivered to the rest of body through a large artery, aorta.

The muscular tissue surrounding the chambers of the heart is known as myocardium, and it is responsible for contraction of the heart by providing sufficient pumping force to squeeze blood from the ventricles. The septum is the middle region of the cardiac wall that separates the left and right chambers, and its primary function is to prevent the mixing of oxygenated

and deoxygenated blood. The myocardium is composed mainly of contracting cells, called as cardiomyocyte. In tissue, they are connected together as a sheet of cells by gap junctions. The gap junctions permit various molecules and ions to directly travel between individual cells, hence allow electrical impulses to propagate through cardiac tissue.

The mechanical contraction of the heart is triggered by the electrical excitation of cardiac cells, the so-called 'action potential' (AP) across their membranes. The cardiac AP is a rapid change in voltage across the cell membrane caused by the movement of charged ions between the inside and outside of the cell. The electrical signal is generated by the sino-atrial (SA) node (also known as a pacemaker) which is located at the top of the right atrium (Figure 2.1). The signal then travels from the SA node to both right and left atria and trigger the atria to contract. As the atria contracts, the blood is pumped to respective ventricles. After the contraction of atria, the electrical signal reaches the bottom of the right atrium, called the atrioventricular (AV) node. At this point, the signal slows down a bit to provide sufficient time for the ventricles to receive the blood from the atria. The electrical signal then leaves the AV node and moves down to the bundle of His. The signal is separated into two branches; one branch goes to the left ventricle, and another goes to the right ventricle, causing the contraction of the right and left ventricles. This cycle of an electrical signal followed by a contraction represents one heartbeat. In an average human lifetime, this cycle normally occurs roughly about two billion times, without fail, as any chronic and/or severe interruptions in normal rhythm may potentially lead to sudden cardiac arrest.

2.2 The cardiac action potential

There are estimated 2-3 billion cardiac muscle cells in a normal human heart (Tirziu et al. 2010), and these excitable cells are responsible for the AP generation. All living cells including cardiac cells have a boundary that separates the intracellular fluid and intracellular organelles from the outside fluid. The semi-permeable boundary is known as cell membrane, and they are made up of two layers of phospholipid molecules with embedded protein channels (also called ionic channels). These pores allow the flow of particular ions such as, Na^+ , K^+ , Cl^- and Ca^{2+} which can only travel through its specific ion channel, each channel type typically displaying high selectivity to a particular ion and being relatively impermeable to others. The membrane acts as a barrier to the free flow of ions and preserves concentration differences of these ions. The gradients of electric charge create a potential difference across the membrane, the transmembrane potential, which provides the driving force for the ionic currents.

When the cell is not stimulated and in an equilibrium state, most of these ion channels are closed, prohibiting the ions from moving in and out across the membrane easily. However, in the presence of the external stimulus, which in the case of cardiac myocytes is membrane depolarisation from adjacent, connected cells, or experimentally via electrodes, the membrane

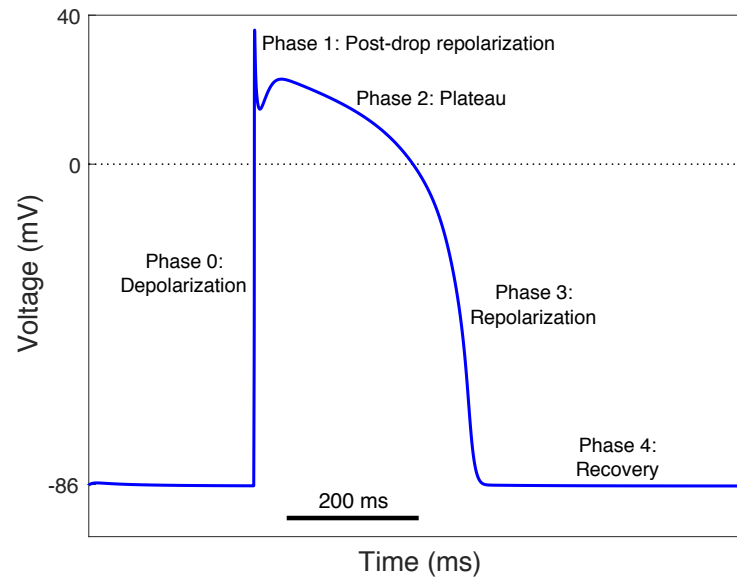


Figure 2.2: Sketch of the five typical phases of an action potential.

potential changes and leads the alterations in membrane permeability of different ions. This activates the opening of some of the ion channels and allows ions to travel across the cell membrane. In consequence, it triggers the onset of an action potential. In most of the electrically excitable cells like a neurons, the action potential occurs for a short duration (at most a few milliseconds), but in the myocytes, the action potential lasts much longer, typically for a hundred milliseconds or more, depending on the cell type and species. The longer duration here prevents the cell from firing another action potential and results in a refractory period for the heart to beat and then recover.

The action potential morphology is different at the different type of cardiac cells (refer Figure 1.1) and a typical action potential can be divided into five different phases (Santana et al. 2010) which are depolarisation, post drop, plateau, repolarisation and recovery, as seen in Figure 2.2. We briefly outline the five phases of an action potential with the dominant current in every phase.

- Phase 0 (Depolarisation): This is the leading edge of the AP and usually is very steep. It corresponds to the period of rapid depolarisation from the diastolic membrane potential. The voltage reaches a threshold value due to the rapid activation of sodium ion channels when the external stimulus is present.
- Phase 1 (Post-drop repolarisation): The transient repolarisation period in phase 1 is produced by inactivation and closing of sodium channels due to inactivation and the concomitant activation of the transient outward potassium, (I_{to}) and $\text{Na}^+/\text{Ca}^{2+}$ exchanger (I_{NaCa}) currents. The direction of I_{NaCa} transiently reverses where it brings in calcium Ca^{2+} and removes sodium ions. Depending on the strength of these currents, the transient repolarisation may cause a ‘notch’ in the AP where the voltage repolarises slightly below

the later plateau potential. However, such AP characteristic is species-dependent and differs between cardiac cells (Di Diego et al. 1996).

- Phase 2 (Plateau): Phase 2 is the long (hundreds of milliseconds) plateau phase of the action potential during which the membrane potential remains depolarised and changes more slowly. The plateau region is produced by a balance between inward movement of calcium ions, the I_{Ca} current through L-type calcium channels and outward movement of potassium ions, I_{Ks} current through the slow delayed rectifier potassium channels. The sodium-calcium exchanger current, I_{NaCa} and the sodium-potassium pump current, I_{NaK} also play secondary roles during this phase.
- Phase 3 (Repolarisation): In phase 3, the transmembrane potential begins to drop rapidly. Ca^{2+} is reduced due to the inactivation of L-type Ca^{2+} current channels and continuous activation of I_{Ks} channels have increased the K^+ efflux. This ensures a net outward current, corresponding to a negative change in membrane potential, hence allowing more types of potassium channels to open. The channels are the rapidly inactivating delayed rectifier potassium channels (I_{Kr} current) and the inwardly rectifying potassium current, I_{K1} . All these positive current contribute to the repolarisation of the myocyte to the resting potential. When the voltage value reaches approximately -80 to -85 mV, the delayed rectifier potassium channels close, whereas I_{K1} remains activated throughout phase 4, contributing to set the resting membrane potential (Dhamoon and Jalife 2005).
- Phase 4 (Recovery): Phase 4 is the diastolic membrane potential of an action potential. I_{NaCa} is reactivated during this stage in order to restore the calcium concentration in the cell. The voltage value stays roughly between -80 to 90 mV until the cell is being stimulated again by an external electrical stimulus.

2.3 Calcium cycling and signalling

For the time being, our knowledge of calcium as a versatile signalling molecule that is responsible for electrical-contraction coupling in the heart has grown tremendously. In this section, we briefly discuss the mechanism of calcium cycling and signalling in cardiac myocytes. Although calcium involves in regulating diverse functions such as fertilisation, secretion, gene transcription and cell death, our focus in this section mainly on cell contraction. The details on the calcium signalling mechanisms can also be found in Bers (2008), Fearnley et al. (2011) and Kaestner (2013).

Regular heart contraction requires electrical stimulation to be converted into mechanical force and the process demands a coordinated flow of Ca^{2+} ions at the cardiomyocyte level. Generation of an action potential is triggered by a rapid influx of sodium ions via voltage-gated sodium channel, thereby creating the I_{Na} current. In consequence, this induces Ca^{2+} influx through voltage-activated L-type calcium channels, generating the I_{CaL} current. Flow of calcium

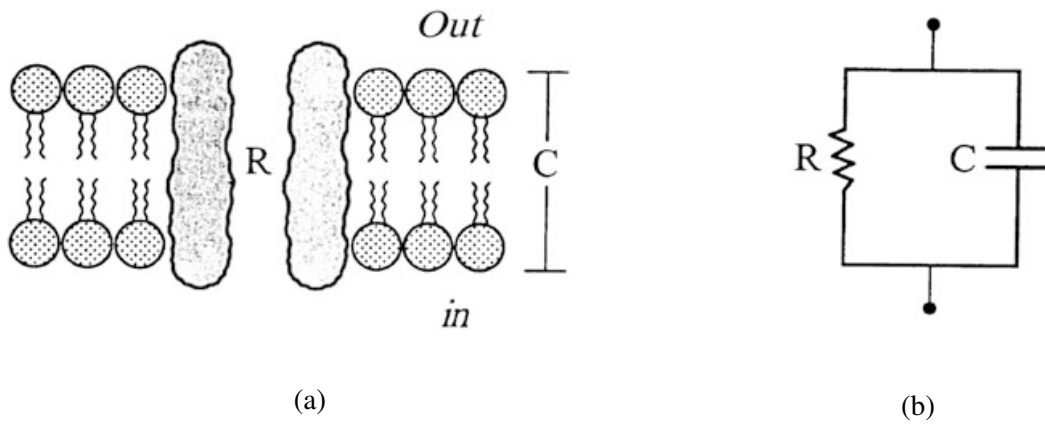


Figure 2.3: Diagram of (a) a cellular membrane and (b) a simple electrical circuit. Reproduced from [Franzone et al. \(2014\)](#).

ions into the cell triggers a much larger calcium release from the sarcoplasmic reticulum (an organelle that stores the intracellular calcium). Calcium ions are released from SR through specialised Ca^{2+} -release channels, expressed as ryanodine receptor type-2 (RyR2), and the process is known as calcium-induced calcium release (CICR). The free cytosolic calcium ions then bind to cardiac troponin C (TnC), a calcium-sensing protein of the contractile apparatus and instigate myofilament contraction. Calcium ions are removed from the myocyte by sequestration into the SR by SR calcium-ATPase type-2a (SERCA2a). Also, sodium-calcium exchanger (NCX) is responsible for exporting a calcium ion out into the extracellular space, by exchanging with three sodium ions. The whole process of calcium release and re-uptake forms a calcium wave that flows through the cardiac cells and is recognised as the calcium transient. The amount of calcium released from the SR also determines the calcium-transient amplitude, which then influences the strength of systolic contraction.

2.4 Mathematical models of cellular bioelectrical activity

Cardiac cell models can provide insights into the processes underlying the electrical dynamics of the cardiac. Such a model begins with a mathematical description that describes the cardiac electrical behaviour at the cellular level. This model incorporates some formulations of trans-membrane ionic currents, voltage and ion channels dynamics. In this section, we briefly review some of the main mathematical compartments used in cellular electrophysiology and we refer to [Franzone et al. \(2014\)](#), [Keener and Sneyd \(1991\)](#), [Sundnes et al. \(2006\)](#) for a more complete discussion and additional topics.

2.4.1 Electrical circuit model of the cellular membrane

In Figure 2.3, we show a schematic representation of the cell membrane as a simple electrical circuit. The cell membrane serves to separate the intra- and extracellular ion substances and is thus regarded as a capacitor with capacitance C_m . The capacitance is defined as the ratio between the charge Q across the capacitor and the voltage potential drop V necessary to hold the charge

$$C_m = \frac{Q}{V}. \quad (2.1)$$

The current across a capacitance is defined as

$$I_{\text{cap}} = \frac{dQ}{dt} \quad (2.2)$$

and if C_m is constant, we have the following relation,

$$I_{\text{cap}} = \frac{dQ}{dt} = C_m \frac{dV}{dt}. \quad (2.3)$$

The cell membrane can be modelled as a capacitor in parallel with some resistors to represent the ionic currents. Hence, by the current conservation law, the sum of the current across the capacitor and resistors must be equal to the applied current (external stimulus) I_{app} , yielding,

$$C_m \frac{dV}{dt} + \sum I_{\text{ion}} = I_{\text{app}} \quad (2.4)$$

where V denotes the internal minus the external potential. The basic structure of action potential models is normally formulated as above. The number of ionic currents incorporated in the model depends on the available experimental data at the time the model is developed. In essence, for a given transmembrane potential drop, ionic current flows through a population of ionic channels is specified in a unit area of a membrane surface. A significant challenge is to determine the form of I_{ion} . This topic is discussed further shortly.

2.4.2 Models for the current/ionic flux

In general, model for ionic flux can be modelled either using Ohmic or Goldman-Hodgkin-Katz (GHK) formulation. There is no one ‘correct’ expression for the ionic current as different cells have different types of ion channels, each of which may have different current-voltage relations. The choice of which formulation to use for a specific current is depends on which model best fits the experimental data. The first formulation was given by [Hodgkin and Huxley \(1952\)](#) in their classic work on squid giant axons and the formulation is described as follows,

$$I_X = g(V, t)\phi(V), \quad (2.5)$$

where $g(V, t)$ is the proportion of open channels in a unit area of the membrane surface and $\phi(V)$ is the current-voltage (I-V) relation of a single open channel. Typically, it can be modelled as a product $\phi(V) = g_c(V - E_X)$ such that g_c is the channel conductance and E_X is the equilibrium potential difference across the membrane (also called as Nernst potential). The equation of Nernst potential is

$$E_X = \frac{RT}{z_X F} \ln \left(\frac{[X]_e}{[X]_i} \right), \quad (2.6)$$

where R is the gas constant, T is the absolute temperature, z_X is the charge on the ion X , F is the Faraday constant, and $[X]_e$ and $[X]_i$ are the extra- and intracellular concentrations of ion X , respectively. The Nernst equation does not depend on how the ions travel through the membrane but depends only on the ratio of concentrations (Keener and Sneyd 1991). The proportion of open channels in a unit area of the membrane surface can be described as

$$g(V, t) = \frac{N}{S} = \frac{N_{tot}}{S} \frac{N}{N_{tot}}, \quad (2.7)$$

where N is the number of open channels on the membrane surface, N_{tot} is the total number of membrane channels and S is the membrane surface area. Hence, ionic current can be formulated as following,

$$I_X = \bar{G}_c w (V - E_X), \quad (2.8)$$

such that $\bar{G}_c = N_{tot} g_c / S$ is the maximal channel conductance per unit area of the membrane surface and $w = N / N_{tot}$ is the probability of open channels (also known as gating variable). We will explain how to model the gating variable in the next subsection.

A central assumption of Hodgkin-Huxley analysis is that ionic current, I_X is linearly proportional to the driving force $(V - E_X)$. This, however, is not always true as numerous studies (Binstock and Goldman 1971, Clay 1991, Frankenhaeuser 1962, Tagliatela and Stefani 1993) have shown that ionic current could have a non-linear dependence on $(V - E_X)$ for physiological conditions which is well described by the Goldman-Hodgkin-Katz equation (Goldman 1943, Hodgkin and Katz 1949). The GHK current equation for an ion species X is defined as below,

$$I_X = P_X z_X F \frac{z_X F V}{RT} \left(\frac{[X]_i - [X]_e \exp(-z_X F V / RT)}{1 - \exp(-z_X F V / RT)} \right). \quad (2.9)$$

where P_X is the permeability of the membrane for ion X and the other constants are as defined earlier. A study by Clay (2009) has shown both formulation for ionic current may significantly influence the AP excitation. The revised model of Hodgkin-Huxley (using GHK formulation) fired only once which showed better agreement with experimental results. In contrast the original model using Ohmic formulation (2.5) fired an unending train of action potentials in response to a sustained depolarising current pulse. The analysis given in the paper has demonstrated the importance of choosing an accurate description of ion channel activation curve, which should be

kept in mind when constructing models of action potential.

2.4.3 Ion channel gating

Principally speaking, there are many ways to model the gating variable. For the purpose of this thesis, we only discuss the simplest case which is the single-unit two-state channel. See [Franzone et al. \(2014\)](#) or [Keener and Sneyd \(1991\)](#) for an extensive discussion.

The simplest approach to model the gating channel is by assuming that the channel can present in either an open state, S_o or a closed state, S_c . The transition rate from one state to another can be represented by some constants, α and β , although in general, the rate is dependent on the transmembrane potential, V . Thus, we have,



If $S_o(t)$ and $S_c(t)$ are the average numbers of channels that at time t are in the open and closed state, respectively, then by law of mass action, we have,

$$\frac{dS_o(t)}{dt} = \alpha S_c(t) - \beta S_o(t), \quad (2.11)$$

where $S_o(t) + S_c(t) = S$. We set $s_o = S_o(t)/S$ and $s_c = S_c(t)/S$, the probability of open and close channels per unit area of the surface membrane, we then get,

$$\frac{ds_o(t)}{dt} = \alpha s_c(t) - \beta s_o(t), \quad (2.12)$$

such that $s_o(t) + s_c(t) = 1$. We denote $w = s_o$ and substitute $s_c = 1 - s_o$ into above equation to yield,

$$\frac{dw}{dt} = \alpha(1 - w) - \beta w. \quad (2.13)$$

The equation can also be written as

$$\frac{dw}{dt} = \frac{w_\infty - w}{\tau_w}, \quad (2.14)$$

where $w_\infty = \alpha/(\alpha + \beta)$ and $\tau_w = 1/(\alpha + \beta)$ are the equilibrium state and the time constant, respectively.

2.5 Overview of cardiac electrophysiology models

This section is dedicated to state of the art in the development of cardiac cellular electrophysiology model. Since the last 60 years, the development of cardiac AP models had evolved rapidly, and

the effort to develop a complete cardiac cellular electrophysiology is still ongoing with the support of advanced experimental technique. The pioneer model of action potential was introduced by [Hodgkin and Huxley \(1952\)](#). This model of the electric properties of squid nerve was the first to describe the physiology of cell excitability by comparing to an electrical circuit. The model has raised computational modelling of physiological function to a new level. The model itself had established an unrealistic expectation for the rapid implementation of a similar approach to other cardiac cells. The model was successfully model the AP neuron by incorporating only three ionic currents: a Na^+ current, a K^+ current and a leak current to describe the remaining unknown current. However, the model was unsuitable to be used for the human cardiac cell as the AP could only last for a short duration (1-5 ms), as the average human ventricular AP may last for 400 ms.

The Hodgkin-Huxley model was a major ground-breaking development in the computational modelling of electrophysiology had paved the way for model development. Following their success, there was substantial work done to apply their modelling approach to various different cell types, including cardiac cells. To date, there are hundreds of cardiac electrophysiology model for various species. Among the many other cardiac ionic models, we mention several cardiac action potential models of Purkinje fibre, atrial and ventricular cells that we believe to have a significant impact on the later model. For further, more detailed review of the development of cardiac electrophysiology model, the reader is advised to refer to the original paper and to these published review articles: [Kohl et al. \(2001\)](#), [Niederer et al. \(2009\)](#), [Noble \(2011\)](#), [Wilhelms et al. \(2013\)](#) and [Noble et al. \(2012\)](#).

2.5.1 Purkinje fibre models

In 1962, [Noble](#) proposed the first model of cardiac action potential for Purkinje fibre cells. The model framework was adapted from Hodgkin-Huxley type, expressed in terms of ionic currents and conductances. The model used three ionic currents, known as an inward sodium current, an outward potassium current and a chloride leak current. The potassium current was further refined so that the model could produce more prolonged AP of cardiac cell. Also, the Noble model ([Noble 1962](#)) incorporated two different types of potassium conductances, identified as I_K and I_{K1} . While the Noble model succeeds in reproducing the Purkinje fibre action potential with a Hodgkin-Huxley style model, the underlying physiology is inaccurate, mainly because the model was developed before data on the ionic currents were available. Particularly, the inward sodium current was given the dual role of generating the upstroke and maintaining the plateau. The calcium current was also not included in the model as it was not discovered until 1967 ([Reuter 1967](#)).

Following the finding of calcium current and recent experimental evidence, [McAllister et al. \(1975\)](#) introduced an improved model for the action potential of Purkinje fibres. The description of the kinetics of the currents was still based on the Hodgkin-Huxley formulation, but with more detailed individual ionic fluxes (the previous three ionic currents of the Noble model were

now replaced with nine). In the model, there are two inward currents (I_{Na} and I_{si}), three time-dependent outward potassium currents (I_{K2} , I_{x1} and I_{x2}), a time-dependent outward current I_{Cl} carried by chloride ions and several background (leak) currents. Nevertheless, the I_{K2} mechanism in the model could not correctly describe the process of ion accumulation and depletion in the extracellular space. In consequence, [Di Francesco and Noble \(1985\)](#) introduced a better model of Purkinje fibre by taking into account the intracellular and extracellular ion concentration changes and the influence of ionic pumps. Recent studies of ion channels, based on experiments using assembled ion channels in highly regulated expression systems, have allowed the development of more sophisticated models of the kinetics of ion channels that are expressed in Purkinje fibre cells. These ionic models are ideally suited for studying ion channel disruptions and membrane currents in disease and treatment, e.g. changes caused by drug block ([Sampson et al. 2010](#)).

The most recent Purkinje model was developed by [Trovato et al. \(2020\)](#). This model incorporates detailed Purkinje-specific ionic currents and calcium handling, and was developed, calibrated and validated using human experimental data acquired at multiple frequencies, both in control conditions and following drug application. Multiscale investigations were performed in a Purkinje cell, in fibre and using an experimentally-calibrated population of Purkinje cells to evaluate biological variability.

2.5.2 Atrial models

One of the earliest models of action potential behaviour for atrial cells is due to [Courtemanche et al. \(1998\)](#) and [Nygren et al. \(1998\)](#). Both models are based largely on similar experimental human data. In the absence of human data, both models rely in part on data from other mammals and have slightly different formulations of ionic currents, pumps, exchangers, ion concentrations, resulting in divergent responses (AP morphology and APD restitution curve), as reviewed before by [Nygren et al. \(1998\)](#). The Courtemanche model exhibits a spike-and-dome morphology, whereas that of Nygren et al. shows a more triangular shape. Although these two models have been extensively used in consecutive studies of atrial fibrillation ([Tsujiama et al. 2008](#), [Zhang et al. 2005](#)), very little has been made to improve the physiological accuracy of the models, until recently.

In 2008, a re-implementation of the Nygren model was published by [Maleckar et al. \(2008\)](#), to provide a more accurate reconstruction of the repolarisation of the atrial action potential at a number of different steady-state frequencies of stimulation. [Koivumaki et al. \(2011\)](#) further extended the Nygren and Maleckar models by developing a human atrial model that incorporated the heterogeneity of intracellular calcium dynamics emerging from a structurally detailed sarcoplasmic reticulum (SR). Additionally, [Grandi et al. \(2011\)](#) have proposed a novel model using recent experimental evidence to explain intracellular calcium handling and incorporated cellular function β -adrenergic and cholinergic regulation into the human atrial model system. Using the atrial model by [Grandi et al. \(2011\)](#) as the general framework, an extensive model was

then created by [Voigt et al. \(2014\)](#) to study arrhythmogenic mechanisms in paroxysmal atrial fibrillation. The model includes $I_{K,ACh}$ current and modifications to I_{K1} and its dependence on the external potassium concentration.

2.5.3 Ventricular models

While the development of AP Purkinje fibre and atrial model was still being explored, a new focus had shifted to the modelling of AP ventricular myocytes. [Beeler and Reuter \(1977\)](#) proposed the first widely used AP model for mammalian ventricular myocyte. The model equations were based on the formulation Hodgkin-Huxley model and the model assumed that sodium and potassium intracellular concentrations ($[Na^+]_i$, $[K^+]_i$) remain constant during the generation of the action potential. Though, in cardiac myocytes entry of Ca^{2+} through the L-type calcium channel, I_{CaL} creates a significant change in the intracellular calcium concentration ($[Ca^{2+}]_i$), largely by triggering Ca^{2+} release from the sarcoplasmic reticulum (SR) via the calcium-induced calcium-release (CICR) process. Four distinct ionic currents were included in the model where the main emphasis was on the role of the calcium current. The current was shown to play a significant part in the creation of the AP plateau.

Also, variations in $[Na^+]_i$ and $[K^+]_i$ may also affect the action potential waveform when cells are paced at a fast rate. The first model including detailed information regarding $[Na^+]_i$ and $[K^+]_i$ dynamic concentration changes was the [Di Francesco and Noble \(1985\)](#) model of the Purkinje fibres. In cardiac ventricular model, the first attempt to take into account the dynamic changes in intracellular ion concentrations (Na^+ , K^+ , Ca^{2+}) was introduced in the Luo-Rudy model ([Luo and Rudy 1994a;b](#)). These models were founding members in a new class of second-generation models that account for dynamic ion concentration changes. The key components in the Luo-Rudy model were further adapted into other AP models of various cell types and species (see, e.g. [Courtemanche et al. \(1998\)](#), [Fox et al. \(2002\)](#), [Mahajan et al. \(2008\)](#), [Priebe and Beuckelmann \(1998\)](#), [Shannon et al. \(2004\)](#)). It is so inspiring to see that the models were kept updated and expanded in order to incorporate any new findings in cardiac electrophysiology, such as newly discovered ion currents and modifications of ion current responses as well as more intricate intracellular calcium handling.

Recently, [Tomek et al. \(2019\)](#) proposed the human ventricular ToR-OTd model of cellular electrophysiology and excitation-contraction coupling. This model was constructed based on the overall structure of the human ventricular model by [O'Hara et al. \(2011\)](#), but with some reformulations in the L-type calcium, hERG and chloride currents to improve the agreement with experimental data in terms of action potential waveform and response to channel block. The development of the ToR-ORd model also involved the use of independent experimental datasets for calibration and validation. The intracellular chloride in the model was then further refined by [Tomek et al. \(2020\)](#) to increase the stability properties of the model over very long simulations.

2.5.4 Reduced ionic models

On the other hand, the second type of action potential model is a simplification of the biophysically detailed ionic model; the objective is not to reproduce the experimental data but to understand the role of action potentials in cardiac circuits qualitatively at a minimal computational cost. Typically, these models are often based on the elegant Fitzhugh-Nagumo two-variable reduction of the Hodgkin-Huxley system or truncated from a detailed model. There are now many simplified models, for examples, [FitzHugh \(1961\)](#), [Mitchell and Schaeffer \(2003\)](#), [Barkley \(1991\)](#), [Aliev and Panfilov \(1996\)](#), [Rogers and McCulloch \(1994\)](#) and [Fenton and Karma \(1998\)](#). The unknowns of these models are a normalised transmembrane potential v and a gating variable u , following the general kinetics,

$$\begin{aligned}\frac{dv}{dt} &= f(v, u). \\ \frac{du}{dt} &= g(v, u).\end{aligned}\tag{2.15}$$

The kinetic terms in some models are defined as follows,

- Fitzhugh-Nagumo model:

$$f(v, u) = -kv(v - a)(v - 1) - u, \quad g(v, u) = \varepsilon(v - \gamma u);\tag{2.16}$$

- Roger-McCulloch model:

$$f(v, u) = -kv(v - a)(v - 1) - uv, \quad g(v, u) = \varepsilon(v - \gamma u);\tag{2.17}$$

- Aliev-Panfilov model:

$$f(v, u) = -kv(v - a)(v - 1) - u, \quad g(v, u) = \varepsilon(\gamma v(v - 1 - a) + u);\tag{2.18}$$

- Mitchell-Schaeffer model:

$$f(v, u) = -\frac{u}{\tau_{in}}v^2(v - 1) - \frac{v}{\tau_{out}}, \quad g(v, u) = \begin{cases} \frac{1-u}{\tau_{open}} & v \leq v_{gate} \\ \frac{-u}{\tau_{close}} & v > v_{gate}. \end{cases}\tag{2.19}$$

Here $a, k, \varepsilon, \gamma, \tau_{in}, \tau_{out}, \tau_{open}, \tau_{close}, v_{gate}$ are given constants. These models, however, do not preserve the important characteristics of an action potential ([Biktashev et al. 2008](#)). [Bueno-Orovio et al. \(2008\)](#) then introduced a minimal ventricular human model that is designated to reproduce important tissue-level characteristics of epicardial, endocardial and midmyocardial cells, including AP amplitudes and morphologies, upstroke velocities, steady-state action potential duration and conduction velocity restitution curves.

In general, the advantages of using the simplified models is that they 1) are computationally cheap and tractable (Clayton et al. 2011); 2) allow for further analytical works such as deriving explicit formula of APD restitution curve and asymptotic expressions for the conduction velocity restitution in cardiac tissues (Mitchell and Schaeffer 2003, Simitev and Biktashev 2011, Tolkacheva et al. 2002); 3) reproduce experimental measurement (Guo et al. 2013) 4) can be used for patient-specific simulation (Corrado and Niederer 2016); 5) can be used for 2-dimensional (2D) wave propagation (Bueno-Orovio et al. 2008, Fenton and Karma 1998, Kogan et al. 1991) and even intensive 3-dimensional (3D) computations of the whole heart (Aliev and Panfilov 1996). Ideally, models should be as simple as needed to describe the phenomena of interest - but no simpler.

In this thesis, the characteristics and behaviour of both detailed and simplified action potential models are examined. Particularly, these models are used to investigate the underlying effects of AP variability on cardiac drugs, to study mechanisms of cardiac alternans and to develop efficient numerical method for solving such models.

2.6 Some applications of cardiac electrophysiology models

Modern cardiac research has become increasingly aware that suitable models and simulation can help interpret a wide range of experimental data and dissect crucial hypothesis (Clayton et al. 2011). The hypothesis can be translated into predictions of observable events. To date, cardiac electrophysiology models are undeniably important for many clinical applications, including functional imaging and mapping, drug safety evaluation, disease diagnosis, patient-specific clinical predictions, and therapy optimisation (Pathmanathan and Gray 2018). Indeed, overall long term goal of the research community is to make a fully-integrated electro-mechanical model of the human heart that is fast-enough and fine-tuned enough to enable general clinical use at the molecular, cell, tissue and organ level simultaneously.

In this section, we outline some applications of cardiac AP models as a quantitative tool to look into various cardiac-related problems. A complete account of these is outside the scope of this thesis; only some examples will be discussed here. Some reviews can be found in Wei (2005), Potse (2012) and Trayanova and Chang (2016).

2.6.1 Drug safety evaluation

Cardiac drug safety is of utmost importance in the growth of drug development due to the possibly destructive nature of unforeseen ‘off-target’ drug-related cardiovascular complications. Reports have shown that the potential of several drugs to cause cardiac toxicity, such as inducing Torsades de Pointes (TdP) in the context of existing long QT syndrome (LQTS) or the development of ‘acquired’ (drug-induced) LQTS. In consequence, it resulted in the removal of several drugs from

the market, for example, terodiline in 1993 (Shah 2007), terfenadine in 1997 (Anonymous 1997) and cisapride in 2000 (Henney 2000). Hence, a thorough evaluation of drug safety is vital in order to understand the responses and toxicity of any drugs before they are released for public use.

Traditionally, drugs are commonly tested on animals to detect any possible risks and side effects before commencing trials on humans. It is undeniable that animal testing has been the most precise and reliable way of examining new drugs. However, this method costs an enormous amount of money, time-consuming protocols and indeed highly controversial for some as countless animals need to be killed (Festing and Wilkinson 2007, Knight 2013). Hence, various approaches have been suggested to minimise the use of animals in drug and chemical testing (Doke and Dhawale 2015), for instance, in vitro cell cultures and mathematical models.

In modelling, mathematical techniques are used to represent a real-world situation by taking into account key variables and constraints so as to determine an optimal solution that is feasible and achieves certain objectives. Simulation, on the other hand, evaluates multiple different scenarios in an attempt to understand how a real-life system would work. In cardiac electrophysiology, computer simulation via a mathematical model of action potential is used to gain insight into how the electrical excitation in the heart performs under different scenarios. This method is cheap, less time-consuming and require less human resources. Passini et al. (2017) demonstrated that computational models are likely to produce higher accuracy than animal models in predicting the cardiac drug effect like arrhythmias. It indicates that a mathematical model can potentially be a robust tool and advantageous way for improving the drug safety evaluation, hence reducing the use of animal experiments in the early stage of drug testing.

One of the most significant challenges encountered by the pharmaceutical industry is to develop a new drug that works on everyone without contributing to serious side effects. Furthermore, no two individuals are identical, and they may respond to the same drug differently. Due to this variability at the physiological level, it is neither practical nor desirable to examine a new drug on the entire population to ensure it is safe and effective. With the support of computational models and new population-based approach, we can now study the effect of drug application on a population of subject both faster and at lower cost. For example, Britton et al. (2013) have used a model of Purkinje fibre to investigate how the differences in the underlying ionic properties of rabbit Purkinje cells from different individual rabbits could affect their action potential response to potassium channel blocker dofetilide. Other studies have used an ionic mathematical model to study the effect of sodium channel blockade (Class I anti-arrhythmic drug) in terminating fibrillation in cardiac tissue (Kneller et al. 2005, Moreno et al. 2011, Qu and Weiss 2005). In a nutshell, we believe that in-silico modelling could soon become a mainstream and robust method for drug testing development.

2.6.2 Alternans

Cardiac alternans refers to a condition in which there is a periodic beat-to-beat oscillation in electrical activity and the strength of cardiac muscle contraction at a constant heart rate. In this context, electrical alternans might be interpreted as a marker that the system of cardiac electrical activation is approaching its chaotic pattern, characterised by the induction of reentrant rhythm disturbances such as ventricular tachycardia and fibrillation. The initiation of alternans usually happen due to instabilities involving the transmembrane voltage, but it can also be driven by intracellular calcium cycling dynamics where the amplitude alternates small and large magnitude (Edwards and Blatter 2014). Hence, knowing the factors that lead to the onset of alternans are critically important, so that, it helps us to build up targeted strategies to control and prevent alternans.

Numerous simulation and experimental studies have made outstanding contributions to understand the mechanism of alternans and even the dynamics of ventricular fibrillation (Bayer et al. 2016, Fox et al. 2002, Karma 1994, Ten Tusscher et al. 2007). To date, the primary method for exploring alternans behaviour is by studying responses of action potentials to periodic stimulation and constructing a restitution curve of cardiac cells. Restitution curve describes the dynamics of an action potential when the cell is stimulating at a various basic cycle length (BCL). The mathematical equation can be written as,

$$APD_{n+1} = f(DI_n) \quad (2.20)$$

where DI_n is the diastolic interval of the current action potential and APD_{n+1} is the subsequent APD where BCL is kept constant, such that $BCL = APD_n + DI_n$. Therefore, the restitution curve is always assumed that the APD is a function of its previous DI. The membrane recovers its resting properties during the diastolic interval until the next excitation. Typically, a DI that is sufficiently long for the membrane to have fully recovered will be followed by a long APD that is independent of the DI. In contrast, a short DI that only allows partial recovery will be followed by a short APD. There is a minimum DI for which the ionic currents are activated (and hence refractory) to the extent that it is not possible to elicit another action potential. Furthermore, APD restitution slope is an important indicator of wave stability and a linear stability study by Guevara et al. (1984) has shown that the steady-state solution of this function could become unstable when the slope of f is larger than one in magnitude, hence resulting in a period-doubling bifurcation. A steep gradient (greater than unity) of the restitution curve has been observed as one of the major cause to the onset of alternans and later leading to the transition of ventricular fibrillation (Karma 1994). Following the hypothesis, Garfinkel et al. (2000) showed that flattening the restitution curve may prevent the alternans from occurring and thus inhibit fibrillation. Moreover, it can convert existing fibrillation either to a periodic state or to quiescent healthy tissue. However, other experimental and simulation studies have shown the slope of the restitution curve might

not be a sufficiently good indicator to the onset of APD alternans, as the behaviour can still be seen even at gradient value less than unity (Banville et al. 2004, Goldhaber et al. 2005). The finding provides a clue that there might be some other properties inherent in the restitution curve that determine the onset of alternans, for instance, the spatial heterogeneity of restitution slopes (Keldermann et al. 2008, Nash et al. 2006). In general, the onset of alternans is not due to a single cause but many factors, for example, cardiac memory (Gilmour et al. 1997, Tolkacheva et al. 2003), intracellular calcium dynamics (Goldhaber et al. 2005), and mechano-electric feedback (Kohl et al. 2006).

2.7 Experimental techniques

The ability to record the electrical activity of cardiac cells and tissues brought about an immense increase in understanding of the basis for normal and abnormal cardiac behaviours. In this section, we now discuss several experimental techniques that have been applied widely in cardiac cellular electrophysiology studies and that are also been used to develop cardiac cell model. The advantages and limitations of each method are discussed.

2.7.1 Micro-electrode recording method

Micro-electrode method is the gold-standard method for measuring the transmembrane potential of cardiac cells. The technique requires tiny (sharp) electrodes to be inserted into an isolated cardiac cell. Typically, one electrode will be placed into the cell in order to send sufficient (constant) stimulus current that will onset the action potential, while the other electrode is used to measure the cell's membrane potential and thus record the trace of the action potential. This method authorises the experimentalists to control the magnitude of the stimulus current as well as pacing rate, which then allow steady pacing at various rates. As a consequence, the cell's responses to different pacing rate (restitution curve) can be studied.

The first transmembrane action potential in cardiac tissue recorded using the micro-electrode method was done by Draper and Weidmann (1951). These experiments managed to reveal the accurate voltage-time course of an action potential. In addition, the exact magnitude of the resting potential and upstroke of an action potential were also discovered. Since then, the micro-electrode method was further developed and improved, and it was used to investigate many types of cardiac tissues to understand the electrophysiological basis of the particular cell (West 1955) or arrhythmic condition (Hoffman and Cranefield 1964).

2.7.2 Voltage and patch-clamp methods

A significant advance made possible by the use of the micro-electrode was the development of voltage and patch-clamp techniques. Unlike the previous method which can only measure the

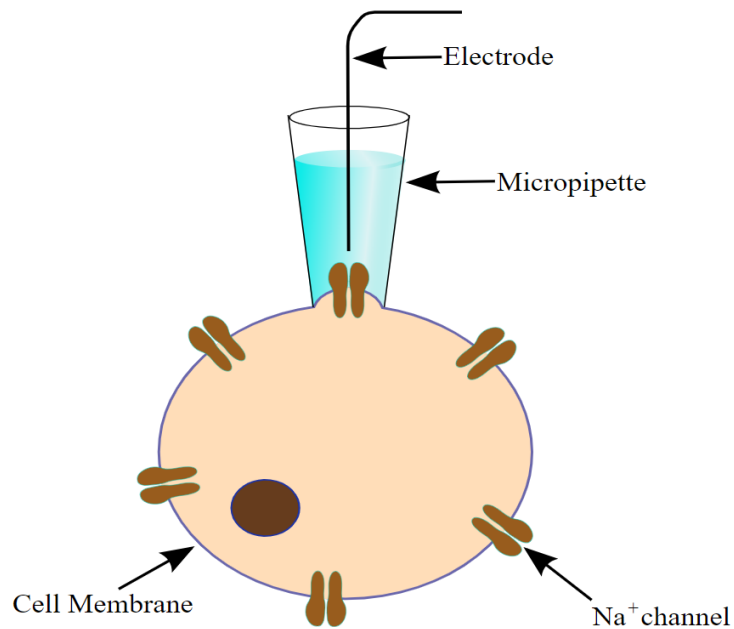


Figure 2.4: Sketch of patch clamp set up in experiment. A glass micropipette is attached to the cell membrane to allow recording of current across a single ion channel. Figure is adapted from Wikipedia (<https://en.wikipedia.org/wiki/Electrophysiology>).

transmembrane potential, these methods are widely used to record the current flows through ion channels. In voltage-clamp technique, the cell potential is ‘clamped’ at the desired (‘command’) value, and the ionic current that crosses a cell’s membrane at the given voltage is measured. The step is essential as many ion channels in the membrane are voltage-gated ion channels, in the sense that the ion channel will only open when the membrane voltage reaches a particular value. In 1952, Hodgkin and Huxley applied this method to describe how ionic currents give rise to the action potential in squid giant axon, which then eventually lead to the development of the first action potential model.

The patch-clamp technique was introduced by [Neher and Sakmann \(1976\)](#) to refine the voltage clamp method by permitting the measurement of current through individual ion channels. The method uses a glass micropipette, and it is brought into contact with the membrane of the isolated cell. Gentle suction is applied with the glass tip to create a high resistance ‘seal’ with the cell membrane, as seen in Figure 2.4. Nevertheless, forming and maintaining a perfect seal between the cell membrane and the tip of micropipette can be quite challenging as the micropipette has to stay still during the entire recording process. A slight movement may cause leakage or rupture the entire cell. Several configurations of patch-clamp have been introduced since then, for instance, whole-cell recording, inside-out patch and outside-out patch, but the goal remains similar, which is to measure the individual ionic currents (see [Sakmann and Neher \(1984\)](#) for a detailed review).

However, due to the complex and time-consuming protocols, the above methods are restricted to measuring a small number of cells (~ 5-10 cells) per individual heart. This reduces the

experimental yield and hampers the study of cellular variability within large populations of cardiomyocytes. Moreover, the use of sharp micro-electrodes in clamp methods may also damage the cell membrane and lead to cell death (Fendyur and Spira 2012). Alternatively, many laboratories begin to use voltage- or calcium-sensitive dyes in order to track the changes in membrane voltage and calcium transient of contracting muscle cells (Herron et al. 2012).

2.7.3 Optical mapping technique

The problems of achieving multiple micro-electrode impalements in whole tissue for measurement of action potential can be overcome by the technique of optical mapping with voltage-sensitive dyes. The first optical recording of the membrane potential of nerve fibre was first conducted in 1968 by Cohen et al. (1968), with a poor signal-to-noise ratio (SNR). Since then, more than 1,000 fluorescent dyes have been screened as possible membrane potential probes in search of better signals (Cohen and Salzberg 1978). The method was first applied to the cardiac application by Kamino et al. (1981), where they successfully measured the pacemaker activity in embryonic heart preparations. Although optical mapping of the heart was initially restricted to a few laboratories, this procedure became more common in the 1990s.

The optical mapping system aims to produce high SNR and high temporal and spatial resolution optical signals while reducing the possibility of side effects, such as photobleaching. Most cardiac optical mapping studies involve heart staining with voltage-sensitive and/or calcium dye, and then use imaging devices to monitor heart surface electrical activity and calcium transients. Voltage-sensitive dyes carry molecules that bind to cell membranes when supplied through coronary perfusion to the whole heart, cardiac tissue, or myocytes. In experimental studies of cardiac electrophysiology, styryl dyes, for example, di-4-ANEPPS, are commonly used due to their characteristics; produce large SNR, short excitation wavelengths and the ability to exclude the scattered and reflected light and the filtering away of the background autofluorescence (Wuskell et al. 2006). However, an important limitation of the optical mapping technique is signal distortion due to scattering of fluorescent photons from excited tissue. Such distortion could compromise experimental data analysis and interpretation as well as the use of optical recordings to validate computer simulations of electrical activity (Bishop et al. 2007).

The recording of membrane voltage in isolated cardiac cells presented in the thesis (Chapter 3) was measured using voltage-sensitive dye FluoVolt (Thermo Fisher Scientific). The method uses optical fluorescence techniques and automated image and electric signal analysis to characterise the electrical and mechanical response within large populations of cardio-myocytes ranging between 100 to 500 cells per individual hearts (Lachaud 2019). The recording is then monitored using the CelloPTIQ program designed by our collaborator Dr Francis Burton. The software is used to collect fluorescent measurements from isolated cardiomyocytes loaded with fluorescent dyes. With such a technique, it is now possible to quantitatively measure the cellular and regional heterogeneity across the population cells, including under the effect of an intervention like drug

application. Compared to other fluorescence-based technique, this method yields better signal output and resolution, allow for larger sampling and coincidentally reduce animal usage.

In general, optical mapping techniques offer a unique opportunity for investigating ventricular arrhythmias in the whole heart. Rapid technological developments will allow the study of ventricular fibrillation in complex settings in normal and diseased human heart. A complete review of this method can be found in [Attin and Clusin \(2009\)](#).

2.8 How close are animal and human hearts?

Animal experimentations have contributed to a number of important cardiac medical breakthroughs. Developments such as the cardiac pacemaker, the cardioverter defibrillator, the heart-and-lung machine, and numerous drug and gene therapies were made possible because of the knowledge gained from animal research ([Sigg 2010](#)). Hence, alongside with the advanced experimental techniques to record the APs, the appropriate animal model must be chosen so that the results produce the most transferable information to humans.

The most common small animal models for cardiac investigations are the rat, guinea pig and mouse ([Kaese et al. 2013](#)). These animals are affordable, highly available, and serve as efficient models for understanding electrophysiological mechanisms of cardiac arrhythmias seen in humans ([Janse et al. 1998](#), [Kaese et al. 2013](#)). Nevertheless, murine and rodent cardiac electrophysiology investigations are mostly limited to changes in ECG patterns and incidences of electrophysiological changes ([Janse et al. 1998](#)) because of their order of magnitude faster heart rate (HR), significantly different AP morphologies and substantially smaller heart sizes. In addition, guinea pig, rat and mouse hearts are lacking of particular potassium channels, which are important in humans for regulating cardiac excitability ([Nerbonne and Kass 2005](#)). Large animal models such as the pig, sheep, goat and canine have hearts that are more anatomically and physiologically same to that of the human, making them a better option for studying atrial and ventricular arrhythmia in comparison to those smaller species ([Kaese et al. 2013](#)).

Indeed, larger mammals also exhibit HRs, cardiac ion channel expressions, and ECG and AP waveforms identical to humans ([Kaese et al. 2013](#)). Due to these factors, such models are more relevant for translational pre-clinical validation studies that examine the safety and efficacy of putative cardiovascular therapies. Unfortunately, usage of larger animal models in testing laboratories is costly, possess complex procedures and highly controversial, which then limit their widespread use in important basic and translational research endeavours ([Towbin and Bowles 2001](#)). Moreover, not all large mammalian hearts have similar physiology with the human heart. For instance, the pig heart tends to have a highly penetrating transmural Purkinje fibre network, an inconsistent size of the aortic valve cusps and a higher ratio of wall thicknesses between the left and right ventricle than the human heart which limits its clinical use for some disease models ([Lelovas et al. 2014](#)).

Interestingly, among the many options for animal models, the rabbit shows the optimal selection for investigating cardiac electrophysiology, specifically those involving myocardial repolarisation. The rabbit cardiac electrophysiology properties exhibits many similarities with the human heart (Bers 2002, Kang et al. 2016, Odening et al. 2020) and is the most used model for human heart physiology and pathophysiology (Lou et al. 2011). This is because the rabbit has significantly lower cost compared to other large mammals, similar AP morphology to human, and possess both rapid and slow activating delayed rectifying potassium channels (Kaese et al. 2013). Furthermore, compared to pigs and dogs, the effective size of the rabbit heart is closest to the effective size of the human heart, making the rabbit heart the superior experimental model in the studying of human arrhythmias (Panfilov 2006).

2.9 Action potential variability in cardiac cells

The motivation for this study is that variation between individuals modulates cardiac electrophysiological activity, requiring the incorporation of experimental data and computational modelling to resolve the nature of a biological system that varies from individual to individual. In this section, we provide evidence for variability in cellular cardiac electrophysiology between individuals of the same species.

In cardiac electrophysiology, there are significant differences in the electrical activity of cardiac tissues from a similar region of the heart (Gemmell et al. 2016, Muszkiewicz et al. 2016, Ni et al. 2018, Walmsley et al. 2015, Zhu et al. 2016). The electrophysiological variability is even more pronounced in isolated cardiac cells, leading to differences in the morphology and duration of the action potential (see Chapter 3). A likely source of this behavioural variability is differences in the levels of ion channels, pumps, and transporters, which arise as the cellular expression system interacts with stochastic effects, genetic factors and environmental effects (e.g. drugs and circadian rhythm). The physiology of the cell can therefore be thought as a complicated input-output function, where the behavioural outputs (features of action potential and calcium waveform) result from the cardiomyocyte system's integration of the activity levels of functional expression of ion channels, pumps and transporters.

Evidence for variation in the properties of ionic currents in the cell membrane of cardiac cells arises from various reasons and mechanisms. We focus on factors that include stochastic effects; pathological processes; circadian rhythm effects; spatial location of the cell within the heart; and inter-species effects.

Several studies have found that stochastic behaviour of any of the ion channels could be involved in APD variability (Heijman et al. 2013, Pueyo et al. 2008, Walmsley et al. 2015, Zaniboni et al. 2000). Zaniboni et al. (2000) demonstrated that variations in late sodium current could account for beat-to-beat variations in APD observed in guinea pig ventricular cells. Also, calcium ions release by the SR is a stochastic process (Lopez-Lopez et al. 1994) and these

ions modulate several sarcolemmal currents, including L-type calcium and sodium-exchanger currents. Hence, beat-to-beat variations in subsarcolemmal calcium ions might be expected to influence sarcolemmal channels and electrogenic transporters, hence promoting beat-to-beat APD. Nevertheless, beat-to-beat variability of repolarisation induced by stochasticity in ion channel gating is dramatically reduced when cells are electronically coupled in tissue.

Numerous types of heart disease and rhythm disruptions may result to ion channel and transporter changes. Heart failure (HF) itself leads to various remodelling processes including changes in ion channel composition and function. To date, numerous investigations have highlighted the influence of potassium current (I_{Ks} , I_{K1} and I_{to}) downregulation in HF myocytes (Akar and Rosenbaum 2003, Beuckelmann et al. 1993, Tsuji et al. 2000). The changes in these channels have resulted in the prolongation of the action potential repolarisation which is a common feature of ventricular myocardium from patients/animals with severe HF (Hegyi et al. 2018, McIntosh et al. 2000). Furthermore, channelopathies (inherited genetic disorders with mutations) may also alter ion channel genes. Depending on the respective ion channel mutation, function and/or expression level of the respective ionic current will change with effect on the cardiac action potential. Unlike natural variability, ion channel remodelling processes in HF and in channelopathies are often pathological in general. Although individuals who possess these mutations are not considered to be part of the healthy normal population in terms of their heart function, and these mutations are uncommon and only happen in a small fraction of the population.

Circadian rhythm is also another source of variation in channel protein expression. A circadian rhythm is a natural, internal process that governs the period of sleep-wake, and repeats approximately every 24 hours. In a study on mice, Yamashita et al. (2003) demonstrated that the expression of cardiac ion channels indeed fluctuated during the course of a day. Their main finding showed that among 14 cardiac potassium channel genes, the expression of Kv1.5 and Kv4.2 exhibited significant circadian variations that were the reverse of each other, whereas that of the other 12 potassium channels was maintained stable. As a consequence, this could contribute to the fluctuating alterations of cardiac electrophysiological characteristics and subsequent arrhythmogenesis. In another study on mice, Jeyaraj et al. (2012) demonstrated that circadian clock may regulate rhythmic variation in repolarisation and alter susceptibility to arrhythmias through *Klf15* expression. Gene expression microarrays in hearts of mice revealed that *Klf15* altered expression of the *KChIP2* gene, the regulatory β -subunit for the repolarising transient outward potassium current (I_{to}) is responsible for electrophysiology variation in the heart.

The configuration of cardiomyocyte AP arising from different layers of the ventricular wall in mammalian myocardium is well known to exhibit variations (Antzelevitch and Fish 2001, Antzelevitch et al. 1991, Kimura et al. 1986, Weissenburger et al. 2000). In general, these variations are due to the asymmetric distribution of different potassium currents such as I_{to} , I_{Kr} , I_{Ks} and I_{K1} (Liu et al. 1993). The transmural heterogeneity in AP morphology is probably most prominent in ventricular myocytes of canine, where endocardial APs show a prominent plateau,

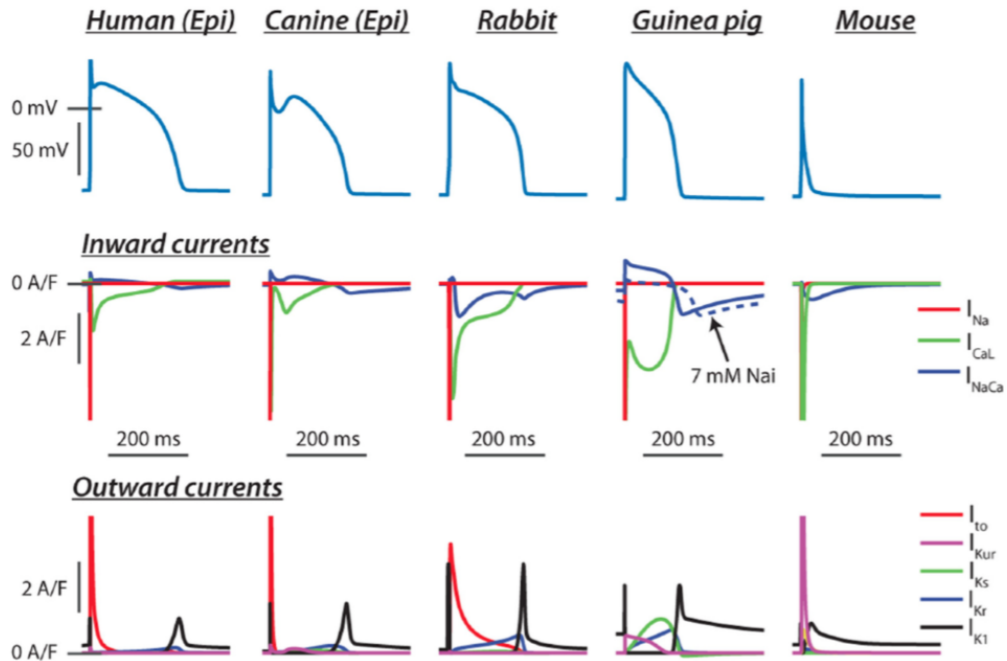


Figure 2.5: AP morphology and profile of ionic currents of ventricular model from various animals. Reproduced from [Edwards and Louch \(2017\)](#).

while epicardial APs exhibit a spike-and-dome appearance. A probable reason is due to the difference in the magnitude of I_{to} current, in which, large I_{to} measured in epicardial cells is responsible for the prominent spike-and-dome configuration and small AP duration ([Litovsky and Antzelevitch 1988](#)). Also, it is now well established that the transmural differences in the profile of I_{CaL} could contribute to differences in AP configuration of endo- and epi- canine ventricular myocytes, where epicardial cells exhibited a higher net charge of I_{CaL} ([Banyasz et al. 2003](#)).

Source of variability in cardiac electrophysiology encompass multiple spatial and temporal scales, including inter-species. The molecular constituents of ionic currents are thought to be relatively consistent across species. Nevertheless, many studies have shown that these ion current expressions are species dependent, which in turn, influencing the AP variability (see [Figure 2.5](#)). For example, sodium-calcium exchanger current varies significantly in rat, guinea-pig, hamster and human, which the density of the current was highest in hamster and lowest in rat myocytes ([Sham et al. 1995](#)). In addition, peak I_{CaL} is slightly reduced in rats compared with larger mammals ([Su et al. 2003](#)) and in part, this is because of lower channel expression, specifically compared with guinea-pig ([Bers 1993](#)). The ensemble of potassium currents contributing to repolarisation is relatively large, and varying expression of the different potassium currents is the primary explanation for major species differences in cardiac electrophysiology ([Edwards and Louch 2017](#)). Like humans, rabbits rely more heavily on I_{Kr} in modulating the AP repolarisation.

In the context of brief APs of mouse and rat myocytes, repolarisation occurs so rapidly due to high expression of both I_{to} and I_{Kur} which then dominates other inward currents in these cells (Figure 2.5).

From the above discussion, we can see that many factors may lead to action potential variability that could be present simultaneously in a cardiac cell. Such variation should not be ignored as it can have a significant impact on cardiomyocyte behaviour and on the chances of promoting arrhythmias in the heart.

2.10 Anti-arrhythmic drugs

Other than studying variability in action potential, our objective is also to investigate the effects of cardiac anti-arrhythmic drugs on cardiac cellular electrophysiology. As part of the introductory material, we discuss several types of cardiac drugs used in pharmaceutical nowadays.

Anti-arrhythmic drugs have been used widely to reduce and eliminate various lethal arrhythmias, such as atrial fibrillation, atrial flutter, ventricular tachycardia, and ventricular fibrillation. In particular, these drugs are used to decrease the conduction velocity of cardiac action potential, alter the excitability of cardiac cells by changing the effective refractory period (ERP) and suppress abnormal rhythms. All anti-arrhythmic drugs directly alter membrane ion conductances, which lead to changes in the physical characteristics of the action potential. In general, these drugs are classified into five main classes according to the Vaughan-Williams classification system. The system categorises the medications based on the primary mechanism of action (although some of the drugs retain properties from several classes). The five main classes are,

- Class I : fast sodium channel blockers
- Class II : beta blockers
- Class III : potassium channel blockers
- Class IV : calcium channel blockers
- Class V : other or unknown mechanisms

Each of these agents has different mechanisms, and they are used for a particular type of arrhythmia. However, all these cardiac drugs have important efficacy and safety limitations which require further development in parallel with a better understanding of complex mechanisms involved in the arrhythmia. For the purpose of this thesis, we will only discuss on Class III and IV agents, and we suggest the readers read the review article by [Dan et al. \(2018\)](#) and [Tamargo et al. \(2004\)](#) for further discussion.

The class III drugs are the potassium channel blockers. In the human heart, potassium channels, including voltage-gated channels, for example, I_{Kr} , I_{Ks} , I_{K1} , I_{Kur} and I_{to} , are responsible

for modulating the shape and duration of the cardiac action potential and the frequency of pacemaker cells. Blocking the expression of these potassium channels can cause a marked prolongation of the action potential duration (increase the effective refractory period), without affecting intracardiac conduction velocity. Examples of class III agents are amiodarone, sotalol, ibutilide and dofetilide. These agents are very effective in the treatment of atrial fibrillation (Anderson and Prystowsky 1999, Jaiswal and Goldbarg 2014), except for amiodarone which has been approved by FDA for the treatment of ventricular tachycardia. Nevertheless, in certain conditions, these drugs may be proarrhythmic. It has been shown in many experimental (Guo et al. 2011, Lu et al. 2001, Nalos et al. 2012) and computational (Cooper et al. 2016, Costabal et al. 2018, O'Hara and Rudy 2012) studies that blocking potassium channels may also lead to arrhythmic effects such as long QT syndrome and arrhythmogenic early afterdepolarisations (EADs).

The class IV agent is the calcium channel blockers. In particular, these drugs block the L-type calcium channels. This channel is a voltage-dependent calcium channel, which is important for the excitation-contraction coupling of cardiac muscles. L-type calcium current, I_{CaL} is responsible for maintaining the plateau region of an action potential, by opposing the repolarising outward potassium currents. Inhibition of this current may result in action potential shortening as I_{CaL} is no longer providing resistance to I_{Kr} and I_{Ks} currents, which then leads the membrane potential to restore to its resting membrane quickly. Examples of I_{CaL} blocker are nifedipine, verapamil and diltiazem. Nifedipine is usually used to treat hypertension and chest pain but sometimes, may also cause tachycardia (fast heart rate) for some people (Castaneda et al. 2005). Hence, understanding the drug mechanisms and effects are extremely important, and the study is our main focus in the next part (Chapter 3 and 4).

Part II

Applications of detailed models of the cardiac action potential

We have experimental data via collaborators (lead by Prof. Godfrey Smith) in the Institute of Cardiovascular and Medical Sciences, University of Glasgow, that shows significant variability in AP biomarkers between single cells and between cells from various regions in the heart. In this part, we perform complementary mathematical modelling and analysis in order to understand the origins of this variability and quantify it. Data presented in the next chapter can be found in [Lachaud \(2019\)](#).

As discussed in the previous chapter, transmembrane potential morphology and time course can vary considerably between different regions of the heart muscle. In the past, technical limitations prevented experimentalists to obtain high enough throughput (>30) within one heart. For instance, a low-throughput method like patch-clamp recording is limited to small numbers of cells due to its time-consuming protocols. This hampers our ability to study the action potential variability present in the cell population, as well as variability within individual hearts. To overcome the problem, a medium/high throughput method was implemented in order to study electrophysiological variation and excitation-contraction (E-C) coupling in large cell populations. Furthermore, quantification of heterogeneity between cell populations sampled from discrete regions of the myocardium could therefore also provide valuable information about the underlying electrical phenotypes within the myocardium.

Chapter 3

Experimental database of rabbit ventricular myocytes

This chapter describes the general features of the experimental data and how the experiments were performed by our collaborators (Dr Quentin Lachaud and Dr Francis Burton). Using this dataset, action potential biomarker values for each of the available control conditions experiments were measured and the distributions of these biomarkers were then quantified in order to understand the variability in AP behaviour present in these measurements. Also, the calibration ranges of each AP biomarker were extracted, which will be used to construct experimentally calibrated population of models in the next chapter. Lastly, the effects of two different cardiac anti-arrhythmic drugs on the electrophysiological heterogeneity of rabbit ventricular cells were examined. We will use what we learn in this chapter from the experiments with drug to application to design a study using the population on investigating how inter-subject variability affects the susceptibility of cardiomyocytes to developing drug-induced repolarisation abnormalities.

3.1 Dataset features and method

In this section, a database of experimentally measured biomarker values characterising the features of the transmembrane action potentials of cardiac myocytes are analysed. All the experiments were conducted by our collaborator Dr Quentin Lachaud. The complete dataset contains recordings of the action potential under control conditions and under a wide array of different drug applications. The experimental dataset contains data from 6 adult rabbits. The measurements that have been analysed were obtained from the sub-epicardial (base and apex regions) and sub-endocardial layers of the left ventricle (LV) of healthy rabbit hearts.

The cells from the specified region were isolated, loaded with the fluorescent, voltage-sensitive dye FluoVolt (1:6000), and plated on to 35 mm glass-bottomed plates (Krebs solution at 37C; 1.8 mM CaCl₂). Cells were then continually paced at a cycle length of 500 ms (2Hz) using field stimulation (2x20 mm graphite electrodes; 40V, 2 ms pulse width). The pacing was maintained

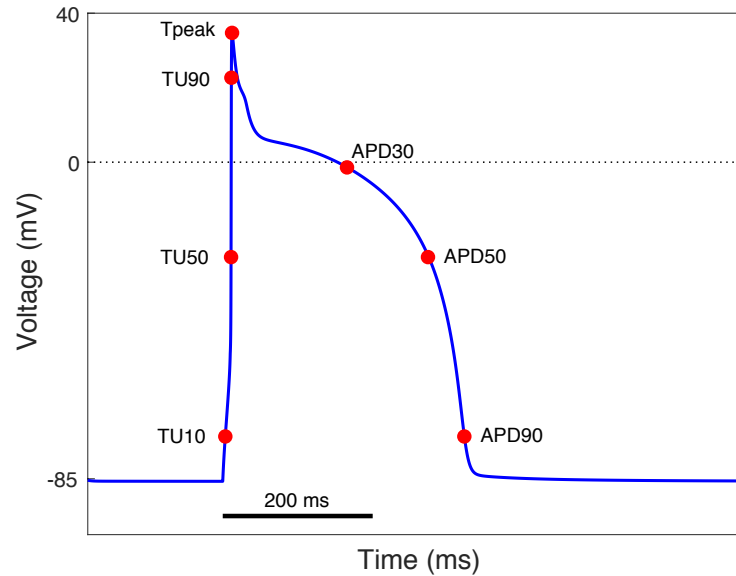


Figure 3.1: **Action potential recorded biomarkers.** APD_x values are the time intervals between the beginning of an AP and *x*% repolarisation from maximum voltage (*V*_{peak}). *T*_{peak} is the time at *V*_{peak}. *TU*_{*x*} refers to the time relative to the start of the AP and *x*% of *V*_{peak}. Trise is measured from 10% depolarised to 90% depolarisation of *V*_{peak} i.e. $Trise = TU_{90} - TU_{10}$. Triangulation index is calculated using $TRI = (APD_{90} - APD_{30})/APD_{90}$. All measured biomarkers are in milliseconds (ms).

for 5 minutes, and a train of action potentials of 2.5s was recorded for each cell. Measurements were only performed on cells with normal electrical behaviour while excluding cells with EADs or alternans properties. The voltage signal is then passed through an analogue-to-digital converter and shown on the monitor using the CelloPTIQ program (proprietary software from Clyde Biosciences Ltd.) which was designed by our collaborator Dr. Francis Burton. CelloPTIQ was also used to analyse fluorescent traces acquired for each cell, by averaging the last 5 action potential trains. Several AP biomarkers such as APD₉₀, APD₅₀, APD₃₀, Triangulation index and Trise were measured for further analysis. Figure 3.1 depicts the action potential recorded biomarkers.

After recording all the measurements of cells in the control condition, the drug was applied to the medium. The effect of cardiac anti-arrhythmic drugs of Class III and IV that blocking hERG and L-type calcium channels, respectively, was investigated. In this study, the drugs chosen to represent these classes were: dofetilide (hERG block) and nifedipine (L-type calcium block). All drugs applied were prepared in 100% dimethyl sulfoxide (DMSO); DMSO was used to dissolve the drugs as they sometimes were insoluble or partially soluble in the saline solution that the cells were kept in. The final concentration of DMSO was 0.05% when dofetilide and nifedipine were applied. At low concentration, DMSO do not give any significant effect to the electrophysiology of the cells (Ogura et al. 1995). This can also be seen in Figure 3.4 and 3.7 where the mean

effect of DMSO on individual cells was negligible (Mean \pm S.D.: approximately 0 \pm 20.5 ms). A concentration of 30nM of dofetilide and 1 μ M of nifedipine were used throughout. The pacing was restored for 10–15 mins and action potential trains were again recorded from the same cells. Finally, the AP biomarkers (Figure 3.1) of each cell under the drug condition were measured.

3.2 Data analysis

3.2.1 Statistical tools

In most cases, the data is presented as mean \pm standard deviation, unless otherwise mentioned. Statistical analyses were computed using MATLAB R2017b. Standard paired sample t-test (using MATLAB function ‘ttest’) was used to compare the means of two distributions. It is often used in hypothesis testing to determine whether a process or treatment actually has an effect on the population of interest, or whether two groups are different from one another. All tests with p -value lower than 0.05 are considered as statistically significant.

3.2.2 APD variation in left ventricle myocytes

Cardiac action potentials differ significantly in different regions of the heart. Indeed, isolated myocytes with different action potential waveforms have been seen in the epicardial and endocardial regions (transmural heterogeneity) due to differences in ion-channel expression. Numerous studies in isolated cardiac cells in several animal species have found differences in APD across the ventricular wall, highlighting a transmural dispersion with shorter APD exhibited in epicardial cells compared to endocardial cells (Antzelevitch and Fish 2001, Kimura et al. 1986, Weissenburger et al. 2000). Their results are consistent with this finding, as shown in Figure 3.2a. Cells in epicardium of rabbit ventricular exhibited shorter APD₉₀ than the endocardial cells (Epi: 245.4 \pm 25.6 vs Endo: 265.0 \pm 23.3 ms), and APD₉₀ difference is 19.6 ms. The distributions of APD₉₀ from these two regions have an identical range with an IQR of approximately 30 ms. A major advantage of the experimental technique used by our collaborators is that it allows measurements of a large number of single-cells recordings from the same heart, which cannot be achieved using low-throughput method. This allows us to assess accurately the variation present within each heart. From Figure 3.3a, mean APD₉₀ of endocardial cells in 4 out of 5 hearts was generally greater than epicardial cells by on average Δ 21.9 ms. The value is comparable to APD₉₀ difference in intra-heart (19.6 ms).

Figure 3.2b shows the distribution of action potential duration in a population of cells in epicardial basal and apical regions from LV of a single heart. The two subregions exhibited extensive overlap between the two cell populations, with a comparable level of heterogeneity (IQR of both regions was approximately 54 ms). The mean APD₉₀ for cells in the base of epicardium was slightly less (241.8 \pm 52.1 ms) than the apex of the epicardium (270.7 \pm 51.0

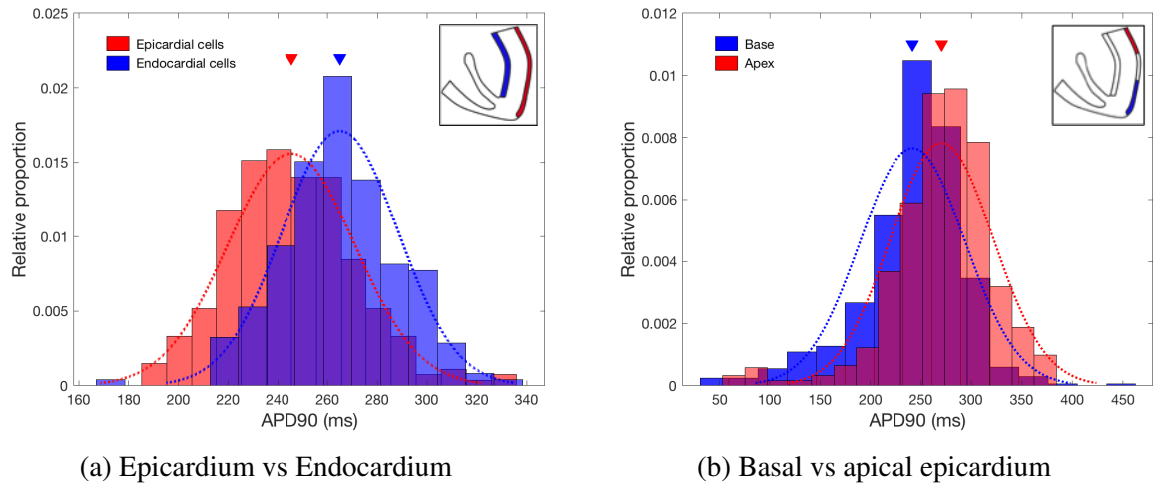


Figure 3.2: Cell-to-cell variability in action potential duration in the left ventricle of rabbit heart. (a) Measurements of APD90 in the epicardial ($n = 273$) and endocardial ($n = 216$) cells from LV of a single heart. (b) Measurements of APD90 in the region of apical ($n = 561$) and basal ($n = 576$) of epicardium from LV of a single heart. The inverted triangle (∇) indicates the mean value of the respective distributions. Dotted line is the respective Gaussian fit generated using mean and standard deviation of each cell population. Overlay panels were taken from [Lachaud \(2019\)](#) and they show the position of (a) epicardial and endocardial regions and (b) epicardial basal region and apical region in the LV.

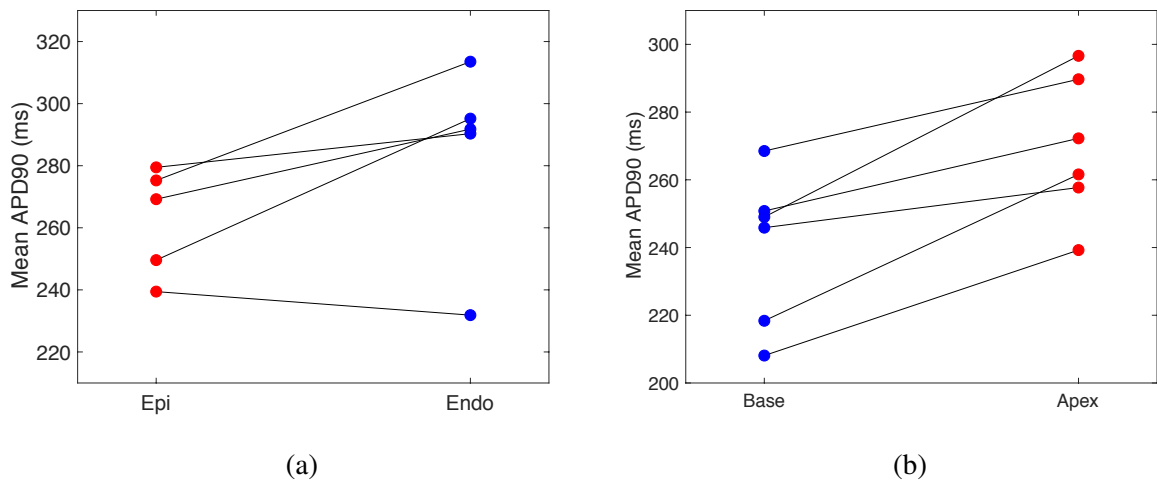


Figure 3.3: Inter-animal variation. (a) Comparison of mean endocardial and epicardial APD90 in 5 animals. (b) Comparison of mean APD90 values from cells isolated from basal and apical epicardium in 6 animals.

ms). The mean APD90 difference between the two regions was 28.9 ms. Also, cells isolated from the apical epicardial region had a larger mean APD90 than cells from the basal epicardial region in all of 6 animals, as shown in [Figure 3.3b](#). The average APD90 difference was approximately 29.4 ms and this is comparable to result in intra-heart. [Franzone et al. \(2014\)](#) reported that the difference was probably due to IKr and IKs currents being smaller in apical than in basal

myocytes, with IKr the largest in apical cells and IKs the largest in basal cells. The shorter basal APD causes ventricular repolarisation to proceed from the basal toward the apical region. Overall, the relatively large range of cell-to-cell differences compared to difference in mean APD90 values between regions means that most of the cells isolated from different parts of the LV free wall have overlapping electrophysiological properties. Also, this study is the first to demonstrate cell-to-cell variation in APD90 may be at least as large as that seen in a population of hearts, highlighting that there exist significant variations in the expression level of ion channels and pump exchangers in between cells that are genetically similar.

It is important to emphasise that the apparent variation in APD discussed above are most readily shown in isolated myocytes, and are least evident in the intact heart. The mostly likely explanation for this phenomenon is that the intrinsic differences in APD in cells from different regions (epi- vs endocardial region and base vs apex region) are reduced in the intact heart due to electronic interactions between cells, mediated by gap-junctions (Burton and Cobbe 2001). The electrotonic coupling acts to attenuate and spatially average the differences between individual cells. In a study by Zaniboni et al. (2000), they showed that cell-to-cell coupling could suppress the variability and induce an asymmetric response in which APD90 shortening of intrinsically long action potentials was more pronounced than APD90 prolongation of short action potentials. The suppression is very important, which not only to attenuate the variability between cells but may essentially protect the heart from sub-populations of myocytes that would provoke arrhythmias in healthy hearts.

3.2.3 Calculation of calibration ranges

Our next goal is to use the recording of AP biomarkers in the cell population to generate the biomarker ranges that could be used to construct a population of models in Chapter 4. The calibration criteria usually differ from study to study, depending on the experimental data available. In the majority of cardiomyocyte studies, only AP characteristics were used to develop the population of models (Britton et al. 2017a; 2013; 2014, Romero et al. 2009, Sarkar and Sobie 2011), while a few used additional information from the calcium transient (Passini et al. 2016). Since the experimental data was limited to recordings of APs, a single calibration criterion based on the range of AP biomarkers will be used. Technically, there are several ways to determine the calibration range. Perhaps the simplest way is by calculating the minimum and maximum values (while excluding all the extreme outliers) obtained from experimental measurements (Gemell et al. 2014). Others used limits of 2 standard deviations from the mean of AP biomarker distributions (Prinz et al. 2004). We used the first of these alternatives in this work.

In order to determine the calibration ranges from the experimental data, we treat the independent measurement of 6 rabbit hearts as a collective measurement and only use the dataset of epicardial basal region, since the difference with epicardial apex was negligible. Several AP biomarkers under the control conditions were selected. The biomarkers were APD90, APD50,

Biomarker (Dofetilide)	APD90	APD50	APD30	TRise
Min range (ms)	90.9	75.5	46.1	1.0
Max range (ms)	376.5	323.2	263.5	5.5
Biomarker (Nifedipine)	APD90	APD50	APD30	TRise
Min range (ms)	30.6	20.3	14.1	1.3
Max range (ms)	333.2	273.3	229.9	5.5

Table 3.1: Experimental ranges of selected biomarkers used in the calibration of two sets of model populations, for the drugs dofetilide and nifedipine.

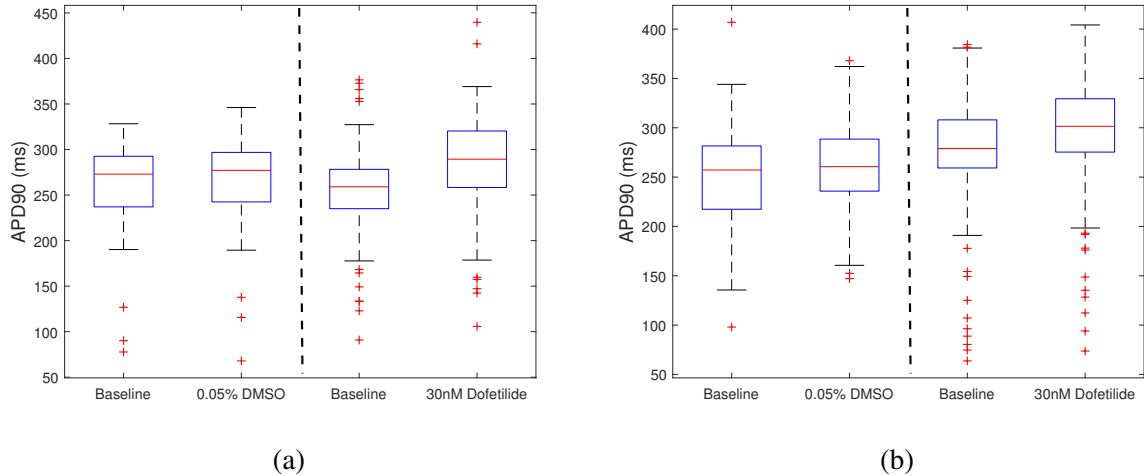


Figure 3.4: Effect of DMSO and 30 nM dofetilide on electrophysiology of the cells in (a) epicardial basal and (b) epicardial apical region.

APD30 and Trise, and their calibration ranges are shown in Table 3.1. Two set of model populations will be constructed as the two drugs were applied to two different cell populations.

3.2.4 Response to hERG block

hERG block was introduced by administration of a dose of 30 nM of the drug dofetilide. Many clinical (Guo et al. 2011, Lu et al. 2001, Nalos et al. 2012) and modelling (Cooper et al. 2016, Costabal et al. 2018, O’Hara and Rudy 2012) studies have shown that blocking the rapid delayed rectifier potassium current, IKr (Class III agent) prolongs the duration of action potential and increase the effective refractory period of the cell. Their results regarding the APD prolongation are completely consistent with this experimental dataset, as depicted in Figure 3.4. Both regions of epicardial cells exhibited a significant increase in the mean APD90 after the application of dofetilide. The mean values of APD90 difference (APD90 after drug treatment - baseline APD90) for epicardial basal and apical cells are 30.9 ± 39.4 ms and 21.4 ± 29.0 ms, respectively. These values show that hERG block has comparable effects on the cells across the epicardium of the heart in response to hERG block.

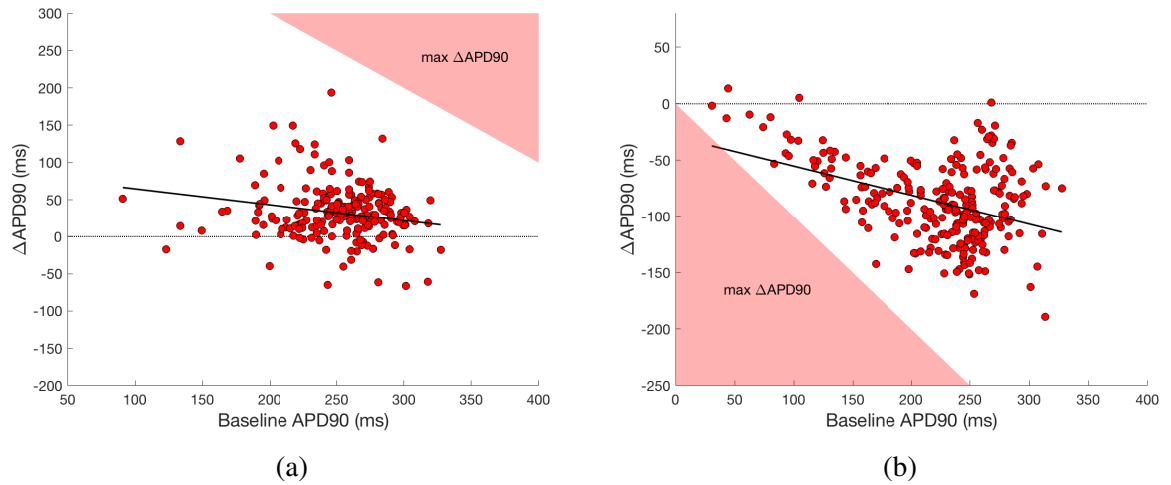


Figure 3.5: Scatter plot net drug effect on APD90 of individual cells in epicardial basal of 5 animals. (a) Effect of dofetilide and (b) effect of nifedipine. The red region indicates the maximum measurable Δ when the cells were paced at 500 ms. A linear regression was fitted to each cell population to determine the relationship between baseline APD and observed drug effect (black line).

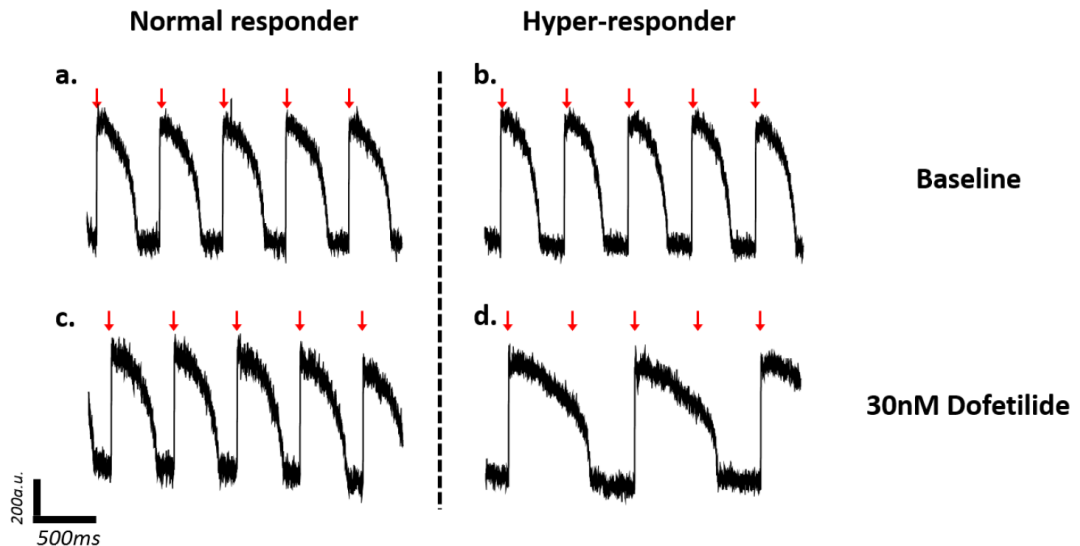


Figure 3.6: Examples of normal AP responder and hyper-responder. The upper row shows the action potential traces before the drug treatment and the bottom row shows the AP responses. (d) During hyper-response, the APD exhibits extreme prolongation beyond its stimulus cycle length (500 ms). The red arrow indicates the applied of external stimuli. Figure is adapted from [Lachaud \(2019\)](#).

A majority of the cells in basal epicardium ($> 85\%$ out of cell population) experienced APD prolongation in response to hERG block. However, there was no reliable evidence to conclude the correlation between baseline and recorded effect on APD, as shown in Figure 3.5a. The APD-prolonging effect of dofetilide seems to be uniform across the cell population, as indicated by the R^2 value ($R^2 = 0.04$, $P = 0.005$; paired t-test). The negative Δ APD seen in some of the AP

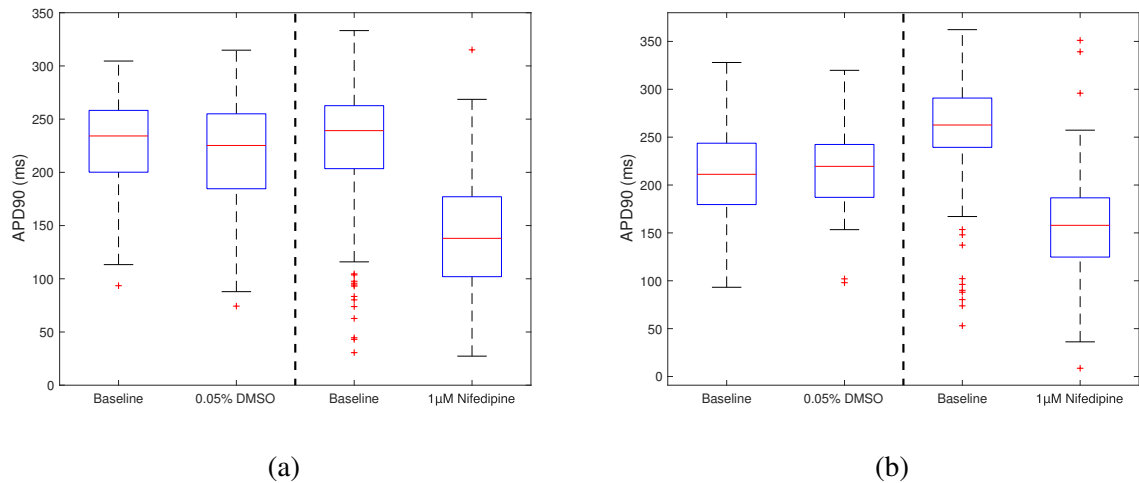


Figure 3.7: Effect of DMSO and nifedipine on epicardial cells in (a) base and (b) apex region.

measurements in Figure 3.5a (14.1% out of cell population) was resulted due to effect of DMSO. The DMSO is the chemical (commonly referred to as ‘vehicle’) that the drug had to be dissolved into, so that the drug could dissolve into the cells. Hence, the effect that our collaborators have seen in the measurements is due to the effect of the drug and DMSO. Nevertheless, DMSO has a negligible effect on APD (Ogura et al. 1995) with mean Δ APD is close to 0ms, as depicted in Figure 3.4 and 3.7.

Interestingly, a small proportion of cells (about 12% in basal cells and 20% in apical cells) showed extreme APD prolongation, which was characterised as ‘hyper-response’. An example of hyper-responder is depicted in Figure 3.6. The hyper-response occurs when the cells do not have sufficient time to recover to its resting potential before the arrival of the next stimulus. Such extreme prolongation would then cause the next AP to decay. The mean of baseline APD90 in these group of cells showed no significant difference from normal responders. (Base: 277 ± 9 vs 282 ± 4 ms; Apex: 299 ± 5 vs 290 ± 4 ms).

3.2.5 Response to L-type calcium block

In contrast to the effect of dofetilide, L-type calcium block by nifedipine resulted in APD shortening, as depicted in Figure 3.7. The mean value of APD90 has reduced from 228.4 ± 56.5 ms to 141.1 ± 54.6 ms for epicardial basal cells. Similarly, to apical cells which decrease from 259.0 ± 46.5 ms to 155.3 ± 48.2 ms. In Figure 3.5b, one can observe that vast majority of the cells in basal epicardium (> 90% out of cell population) experienced APD shortening following L-type calcium block. The net APD90 effect of $1\mu\text{M}$ nifedipine showed a negative correlation between baseline APD90 and drug effect. The correlation coefficient value is -0.41 ($P < 0.00001$; paired t-test). Figure 3.5b also shows that in general cells with relatively short baseline APD90 values exhibit minimal responses to nifedipine. Meanwhile, cells with longer APD90 values show a wide range of responses to the same nifedipine concentration. A probable reason is that

in cells with large APD have a larger calcium current which then contributed to a large Δ APD. This requires further study to support the hypothesis, which will be addressed in the next chapter.

3.3 Conclusion

In this chapter, a database of medium/high throughput recordings from rabbit ventricular myocytes, in control and under drug blocks was analysed. The experimental procedures to measure the AP of a population of cells were also explained. Comparing to the lower-throughput method, the experimental technique presented in this chapter has allowed large measurements of single-cell recording from the same heart, hence, enabling us to have an accurate assessment of understanding the variation present within each heart. Furthermore, the method has significantly reduced the use of animals as large samples (100-500 cells) could be collected from a single heart.

Under the control condition, the cells exhibited a large amount of variability within a single region of the myocardium (epicardium vs endocardium and epicardial basal vs epicardial apical). The coefficients of variation, CV ((std. dev/mean)*100) in epicardium and endocardium regions are approximately 10% and 9%, respectively. Similarly, CV in epicardial basal and apical regions are roughly 22% and 19%, respectively. The results showed that both regions have extensive overlap between the two cell populations. Interestingly, this study is the first to demonstrate cell-to-cell variation in APD₉₀ may be at least as large as that seen in a population of hearts. The mean APD₉₀ difference between epicardial basal and apical regions is approximately 28.9 ms and this is comparable to result in intra-heart (29.4 ms). The finding highlights that there exist significant variations in the expression level of ion channels and pump exchangers in between cells that are genetically similar.

The vast heterogeneity present in isolated cells is always ignored as the variation is naturally reduced in electrically coupled tissue (Walmsley et al. 2015, Zaniboni et al. 2000). Nevertheless, the results showed that the heterogeneity of the cellular population has a significant impact on the intervention of drug application. In the hERG block by dofetilide, the cells experienced a various degree of APD prolonging effect, as depicted in Figure 3.5a. No correlation was observed between the baseline APD of the cells and the drug net effect following hERG block. Also, a group of cells exhibited extreme APD prolongation (hyper-response). In the most recent study by Britton et al. (2017a), they reported that AP recordings from stimulated ex vivo human ventricular trabeculae showed APD prolongation beyond the cycle length (2 Hz) when 0.1 μ M dofetilide was applied to the cells. However, the ionic mechanism is not known. We will discuss the AP behaviour further in the next chapter. In contrast, ICaL reduction by nifedipine which shortens the APD showed a negative linear correlation between baseline APD and the APD of post-drug treatment (Figure 3.5b). However, the root cause of such responses is not fully understood as the experimental data was only comprised of AP measurements. A likely hypothesis is that in cells with a more significant degree of Δ APD have higher calcium transient amplitude, which directly

translates to increased fractional shortening.

On top of that, it is important to know that the variability in cardiac electrophysiology cannot be studied using experimental measurements alone due to limitation in experiment protocols to gather information. Even-though the experimental procedures used the study have allowed us to quantify the transmembrane action potential for a large population of cells; this method is still limited in the sense that it cannot measure the individual ionic currents, ion concentrations and other components in the cells. The AP alone does not carry sufficient information to pinpoint all ionic current properties of each cell, which could hamper our ability to understand the physiology behind AP responses toward drug blocks. Hence, with the aid of computational modelling which is designed to encapsulate physiological understanding and to provide quantitative predictions of such knowledge, we are capable of gathering more insightful information and use them to determine the distributions of ion channel conductance values that capture the electrophysiological heterogeneity measured in the cells. Based on the data we have analysed and the calibration ranges we have generated in this chapter, we will construct a population of rabbit ventricular cell models. We allow this population to cover a wide range of different possible cell models by letting parameter values to vary widely. The model population are then used to investigate the drug blocking hERG and L-type calcium channels. We also want to investigate which ionic current are responsible for determining susceptibility to drug-induced repolarization abnormalities like hyper-response and EADs.

Chapter 4

Action potential variability and drug pharmacodynamics

4.1 Motivation

The action potential (AP) of cardiac cells has many features important to excitation-contraction coupling, the time-course and magnitude of the 4 phases of the AP reflects the orchestrated activity of various ion channels and electrogenic transporters. In many studies, including both experimental and computational modelling, have shown that there is significant inter-individual variability in the combinations of molecular-input parameters that can generate very similar integrated outputs (Britton et al. 2013; 2017b, Romero et al. 2009, Sobie 2009). The electrophysiological variability is very pronounced in isolated cardiac cells, leading to differences in the morphology and duration of the action potential (see Chapter 3). The implications of AP variability are important, for example in drug cardio-toxicity screening or heart disease treatment, but it has traditionally been ignored in experimental and theoretical studies that have sought to understand generic drug pharmacodynamics. Such investigations normally focus on a typical response within a particular population rather than quantitatively examining variability.

In a traditional cardiac cell modelling approach, the AP models are constructed to represent the mean response of a cardiac cell of the studied tissue type or species. However, the model would lose its ability to explain the underlying variability and cannot be used for studies of inter-subject variability. Modellers have considered two main approaches to include the variability effects into an existing modelling framework. The methodologies are sensitivity analysis based methods and use of a model populations. In sensitivity analysis based method, one or more parameters in the model are perturbed within its baseline values for a certain amount. The model's output in correspondence to such perturbation is then measured and the difference is analysed. In most of the variability studies, this approach has been widely used.

In a study by Romero et al. (2009), a single parameter sensitivity analysis was implemented on a human ventricular cell model to investigate the impact of ionic current variability on action

potential properties, calcium and sodium dynamics, and their rate dependence. They varied several sets of ionic conductances and time constants in the model, one at a time for $\pm 15\%$ and $\pm 30\%$. Their studies were able to provide quantitative insights into the sensitivity of preclinical biomarkers of arrhythmic risk to variations in ionic current properties in humans. Another series of studies was performed by [Sarkar and Sobie \(2010; 2011\)](#), [Sobie \(2009\)](#). Instead of using a single-cell model, they used a population of models based approach generated from log-normal distribution to study the impact of variability, but without calibrating the population to experimental data. In the absence of experimental calibration, this approach can be thought of as an extension of the sensitivity analysis framework, which then allowed the parameters to be varied simultaneously ([Muszkiewicz et al. 2016](#)).

Recently, [Britton et al. \(2013; 2014\)](#) have proposed a new methodology to study AP variability, by calibrating the population of models to a set of experimental measurements. Several models parameters, mostly ion conductances, were randomly varied using a sampling technique to generate a large number of parameter sets. The models outputs were then measured and calibrated to experimental ranges of Purkinje fibres. The model population was further used to investigate the effects of variability to four concentration of potassium blocks. Their results showed a good agreement with experimental data. Nevertheless, their results are limited to small sample size (12 different Purkinje fibres) which could mask the level of variation seen in the experiments. Hence, using large sample sizes from several animals could potentially improve estimates of variation.

4.2 Objectives of the chapter

The current generation of cardiac electrophysiology models usually incorporates parameters that describe numerous interacting ion current and calcium handling processes, the diversity of which depends on the experimental data available to their authors at the time of constructing the model. The data is also measured from different laboratories under different conditions. In consequence, this may lead to inconsistency in model output and predictions when the model is used to data other than the data on which their parameter values have been fitted, even between models which we assume to represent similar cell types or region ([Gemmell et al. 2014](#), [Ten Tusscher et al. 2006](#), [Wilhelms et al. 2013](#)). It explains why it has become difficult for us to rely on model output alone without recourse to experimental data. The dissimilarities between model responses also highlight the importance of careful model selection and appropriate use for computational studies, which will be the focus of our studies.

In this chapter, the objectives are,

- to determine the distributions of ion channel conductance values that capture the electrophysiological heterogeneity measured in large populations of rabbit ventricular cardiomyocytes

- to investigate the effects of action potential heterogeneity on the application of drug blocking of hERG and L-type calcium channels.
- to understand the ionic mechanisms of hyper-responders observed in the experimental measurement (Chapter 3).
- to understand the ionic mechanisms of any drug-induced repolarisation abnormalities.
- to study the capability of cell models in predicting the drug effects.

In this chapter, we tightly combine experimental measurements and computational modelling to construct and calibrate a population of action potential cell models based on experimental ranges in the previous chapter. Three different action potential models of cardiac ventricular are used for this study, which will allow us to make quantitative comparisons between each model outputs. For model calibration, we follow the established methodology by [Britton et al. \(2013\)](#). The model population is constructed by matching the model output to both experimental ranges and distribution. These cell models are used to represent the variability exhibited in particular experimental measurements of rabbit ventricular cardiomyocytes. We then demonstrate the capacity of the model population to predict variability in response to drug blocking of hERG and L-type calcium channels. Quantitative comparison of effects of hERG and L-type calcium blocks between the three models and experimental measurements are carried out.

We begin the chapter with a brief discussion on the action potential model used in our work. We then provide the essential mathematical/statistical tools that are needed to create a population of models and analyse the simulation results. In the following section, the calibration methodology and simulation of drug action are explained. Finally, we show and discuss the effect of hERG and L-type calcium blocks on three model populations.

4.3 Materials and methods

4.3.1 Baseline models and software

Three different ventricular AP models are selected and used as the baseline model in our computational studies. The models are; 1) a rabbit ventricular model by [Shannon et al. \(2004\)](#); 2) a human ventricular model by [Ten Tusscher et al. \(2004\)](#) and 3) a human ventricular model by [O’Hara et al. \(2011\)](#). Next, we will briefly discuss the background of each model.

Shannon model (2004) The model is a detailed model for rabbit ventricular myocytes and it incorporates 15 different ionic currents as listed in Table 4.1. The model was modified from [Puglisi and Bers \(2001\)](#) model with some updates on calcium mechanisms. Specifically, the model was reformulated to include; 1) a subsarcolemmal compartment; 2) use of realistic cytosolic Ca

Shannon	Tentusscher	Ohara	Description
IKr	IKr	IKr	rapid delayed rectifier potassium current
IKs	IKs	IKs	slow delayed rectifier potassium current
ICaL	ICaL	ICaL	L-type calcium current
IK1	IK1	IK1	inward rectifying potassium
INaK	INaK	INaK	sodium-potassium pump current
INaCa	INaCa	INaCa	sodium-calcium exchanger current
Ito Itof	Ito	Ito	slow transient outward potassium current fast transient outward potassium current
IClb	-	-	background chloride current
ICap	ICap	ICap	sarcolemmal calcium pump current
INa	INa	INa	fast sodium current
INab	INab	INab	background sodium current
ICiCa	-	-	chloride-calcium pump current
ICab	ICab	ICab	background calcium current
IKp	IKp	-	plateau potassium current
-	-	INaL	late sodium current
-	-	ICaK	calcium-potassium pump current
-	-	IKb	background potassium current

Table 4.1: List of ionic currents and pumps in the Shannon, TenTusscher and Ohara model. Ionic currents/pumps in red colour were varied to construct populations of models.

buffering; 3) a reversible sarcoplasmic reticulum (SR) Ca pump; 4) a scheme for Na-Ca exchange transport that is $[Na]_i$ dependent and allosterically controlled by $[Ca]_i$ and; 5) a practical model of SR Ca release including both inactivation/adaptation and SR Ca load dependence.

A drawback of this model is that it fails to exhibit calcium transient alternans during rapid stimulation rates. The deficiency was then resolved in the latter model by [Mahajan et al. \(2008\)](#). However, since we do not particularly look into alternans behaviour in this work, the Shannon model should be sufficient. Furthermore, L-type calcium current expression in the Mahajan model was developed using Markov formulation. A known drawback of the Markov formulation is the increasing complexity of the model and eventually increases the computational cost of the model. From our analysis, we find that the Shannon model runs more quickly than the Mahajan model. For instance, to run a simulation of 500 action potentials pacing at 2Hz in the Mahajan model required about 60 mins. In contrast, in the Shannon model, the simulation could be completed in approximately 2 mins. The models were both executed using MATLAB v2017b with 64-bit Intel processor. To avoid such a long simulation time when constructing the model population, we chose the Shannon model as our baseline model. Extensive model comparison between these two models can be obtained in [Gemmell et al. \(2014\)](#).

TenTusscher model (2004) The TenTusscher model is a model for human ventricular myocytes, and it includes 12 ionic currents (Table 4.1). The model can reproduce three different regions of

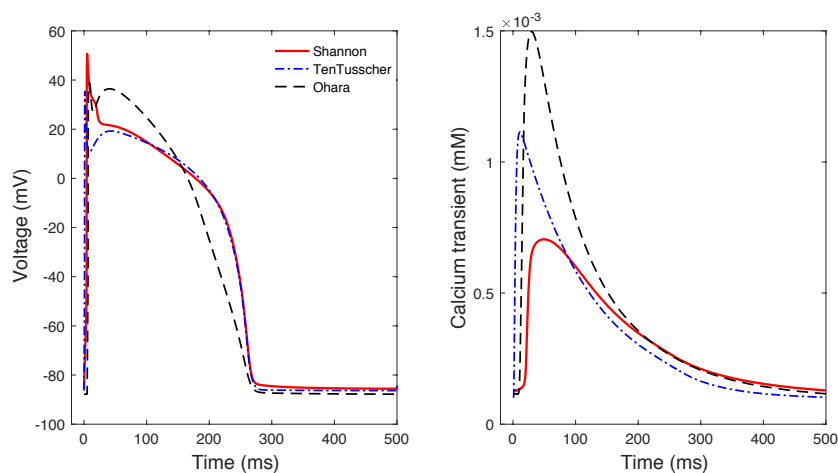


Figure 4.1: Action potential and calcium transient morphologies in the Shannon (solid line), TenTusscher (dash dotted line) and Ohara models (dashed line).

cardiac ventricular (epi-, endo- and mid-myocardial) with different characteristic action potential morphologies. In contrast to the experimental data which was recorded from rabbit ventricular cells, the model was constructed using data from human ventricular myocytes.

Ohara model (2011) Experimental data for the human heart is very difficult to obtain, and some of the ionic currents in the model (for example [Priebe and Beuckelmann \(1998\)](#) model) were constructed based on animal data (rodent or other mammalian). Even the TenTusscher model used guinea-pig data to compare the conduction velocity restitution (CVR) curve because no experimental data on human CVR were available at that time. The Ohara model, however, was developed based on recent human data, which is critically important for the correct formulation of mathematical models of simulation for human electrophysiology. The model can also reproduce important arrhythmogenic behaviours such as early after-depolarizations and alternans, which is crucial for studying the mechanisms of cardiac arrhythmias in human and simulate clinical interventions like drugs.

Both the Shannon and TenTusscher models were downloaded from CellML model repository (<https://models.physiomeproject.org/cellml>) and were executed using MATLAB v2017b with a 64-bit Intel processor. The model equations were solved using the MATLAB function `ode15s` with relative and absolute tolerances at 10^{-6} , respectively. MATLAB function `ode15s` is used for solving stiff differential equations using variable order method. On the other hand, the Ohara model was downloaded from Rudy laboratory model repository (<http://rudylab.wustl.edu/research/cell/code/AllCodes.html>). The simulation was executed in MATLAB v2017b using a similar setting as the other two models.

Ionic currents and action potentials in rabbit and human models In this work, the numerical simulations were undertaken using both rabbit and human AP ventricular models. In contrast

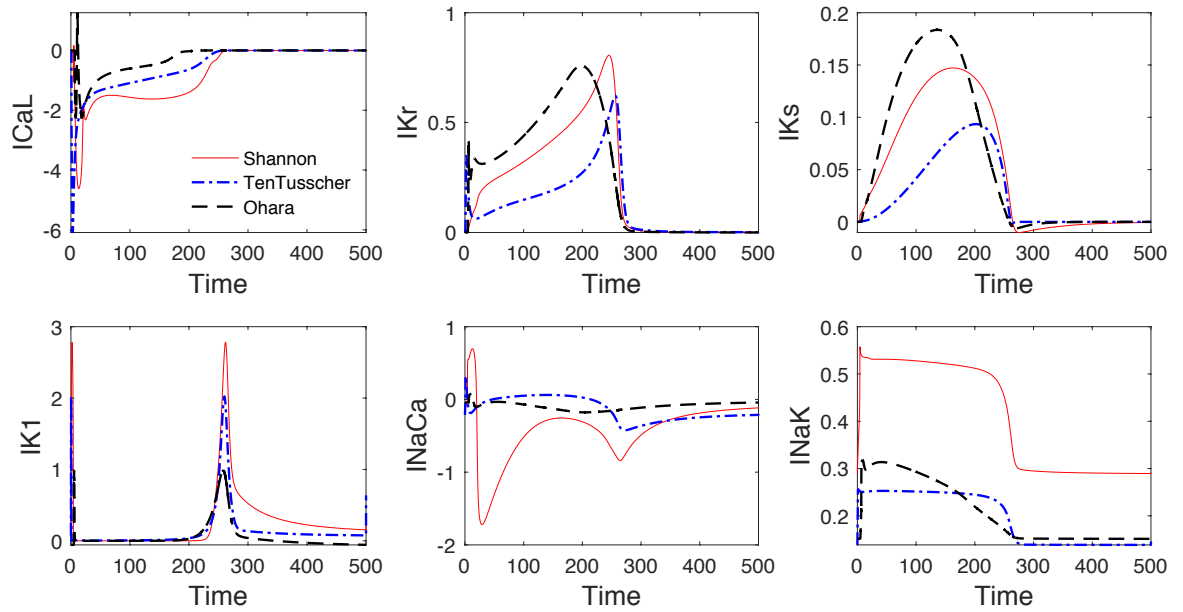


Figure 4.2: Comparison of profile of several common ionic currents found in the Shannon model (solid line), TenTusscher model (dash dotted line) and Ohara model (dashed line).

to rodents, the cardiac electrophysiology properties present in rabbit heart are very similar to those in human heart (Bers 2002, Kang et al. 2016, Odening et al. 2020, Panfilov 2006). Key electrical features show pronounced similarities in the two species, such as the shape of action potential and the biophysical properties of the underlying cardiac ion channels/currents. These rabbit models have been instrumental in increasing our understanding of mechanisms initiating and sustaining ventricular arrhythmias as seen in humans (Brunner et al. 2008, Lang et al. 2016).

Hence, both human AP models mentioned earlier are still appropriate for this work (refer Section 2.8 for an extensive discussion). In the Shannon and TenTusscher models, the ionic currents are generally reconstructed using mathematical formulation as in Luo and Rudy (1994a;b) with variations in and additions to individual equations and parameters. Hence, it is expected that the ionic currents shape in these two models are identical (Figure 4.2). On the other hand, the Ohara model uses their novel mathematical formulation to describe the ionic currents in the model, which then validated to various experimental data obtained from their experiment and literature. However, the general waveform of the ionic currents are almost similar to the other two models.

Distinct differences exist in action potentials and ionic currents between rabbit and human models, as shown in Figure 4.1 and 4.2. From Figure 4.1, we can see that the Shannon model generates action potential with significantly larger amplitude (Phase 0 peak) and more prominent Phase 1 compared to other two models. Action potential in the Ohara model resembles the AP from the TenTusscher model exhibiting deep notch at the onset of the plateau. AP rabbit model, however, does not produce the notch. Unlike Shannon and TenTusscher models, the Ohara model

lacks a well defined plateau phase during repolarisation and produces faster repolarisation phase. Overall, both Shannon and TenTusscher models exhibit a good overlap between each other, with minimal discrepancy at the Phase 1 of the action potential. The differences in AP waveform between cell models are likely because the data used to generate the model were from different laboratories with different experimental setting and conditions. The type of ionic currents/pump exchanger included in each model is also different, as listed in Table 4.1, which might influence the generation of AP waveform. For example, chloride current can only be found in the Shannon model, whereas sodium late current is included in the Ohara model only.

From Figure 4.2, we can also observe that each model produces different magnitude and morphology of ionic currents. It is well known that AP repolarisation is largely controlled by the inward calcium current and the various outward potassium currents. Despite of these differences, all models produce a comparable APD₉₀ as plotted in Figure 4.1. This is because the AP repolarisation difference mostly depends on the counterbalance of ionic currents between each other. Furthermore, larger AP amplitude shown in the Shannon model is probably caused by the large I_{K1} current in this model.

4.3.2 Parameter sensitivity analysis

Sensitivity analysis is typically used to evaluate the uncertainty in the output of the mathematical model or system to various changes of the input parameter. Modellers may implement sensitivity analyses for many purposes, for instance, to determine

- which parameters need further research for strengthening the knowledge base, hence minimising output uncertainty
- which parameters are less important and can be removed from the final system
- which parameter inputs are the most sensitive and contribute the most to model output uncertainty
- which parameters have larger correlation with the output and increase the understanding of the relationship between input and output variables.

In general, there are many different methods of conducting parameter sensitivity analysis such as differential sensitivity analysis, the sensitivity index, the relative deviation method and others (see Hamby (1994) for a complete review on parameter sensitivity analysis). For this thesis, we focus on a local sensitivity test known as ‘one-at-a-time sensitivity measures’ described in Snowden et al. (2017). Conceptually, this is one of the simplest methods of parameter sensitivity analysis by repeatedly varying one parameter with respect to small perturbation at a time while keeping the other parameters fixed and then quantify the change in model output. The sensitivity

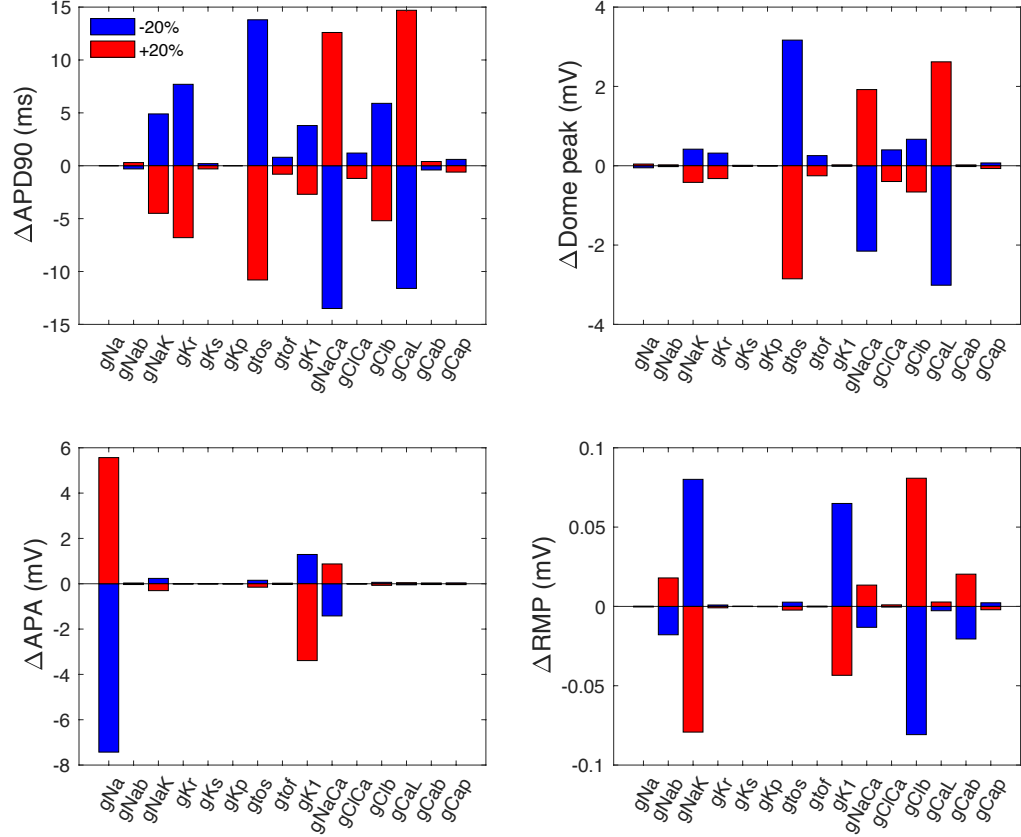


Figure 4.3: Sensitivity of transmembrane voltage potential to variation of ionic conductances in Shannon model. Several biomarkers extracted from functions $\partial V/\partial p_j$ are plotted. Each parameter was perturbed by $\pm 20\%$ and the changes on AP biomarkers were recorded.

function is expressed as following,

$$z_{ij}(t) = \frac{\partial x_i(t, \mathbf{p})}{\partial p_j} \approx \frac{x_i(p_j + \Delta p_j, t) - x_i(p_j, t)}{\Delta p_j} \quad (4.1)$$

where x_i is the i -th component of the vector of state variables in the model. \mathbf{p} is a parameter vector in the model and Δp_j is the amount of perturbation of j -th parameter. These partial derivatives approximate the relative point-wise difference between the original and perturbed outputs when parameter j -th is changed, while the other parameters are held constant.

We carried out a parameter sensitivity test on some parameters in Shannon model (as listed in Table 4.1). Each parameter was perturbed by $\pm 20\%$, while the other parameters were held constant. Figure 4.3 shows the result of the test on all the ionic conductances in the model. From the figure, we can observe that each parameter has different level of sensitivity. Some are very sensitive to small perturbation and some do not alter the AP waveform. More importantly, each parameter has particular effects on the AP morphology, highlighting its role in modulating the specific phase of an AP. For instance, the amplitude of action potential is governed by g_{Na} and

gK1; meanwhile, the action potential duration is influenced by gCaL, gNaCa, gtoS, gKr and several others. The results of this test were used to select the parameters needed for constructing the population of models. In particular, we only chose the parameters that have most significant influence on the action potential duration. The parameters were gNaK, gKr, gKs, gK1, gtoS, gNaCa, gCaL, gClb.

4.3.3 Sampling method

Building a model population needs the generation of a large parameter sets with various combinations, sampled from a high-dimensional parameter space. There are various sampling methods which can be used to vary the parameters randomly, for instance, parameter sweeping (Peachey et al. 2008), Monte Carlo sampling and Latin hypercube sampling (LHS).

Monte-Carlo methods include any techniques that draw samples from a probability distribution function in order to produce various parameter combinations. This includes the use of log-normal distribution centred around the baseline parameter values and within specific standard deviation that controls the limit to which parameters varied. Using this distribution also ensured that the non-physiological conditions due to negative conductance are never included in the parameter sets. Such approach has been used in several studies to construct the model population (Ballouz et al. 2019, Lawson et al. 2018, Sobie 2009, Varshneya et al. 2018). In this method, parameters are chosen randomly from the probability distribution to generate as many parameters as needed.

Another sampling method is Latin hypercube sampling. LHS was first introduced by McKay et al. (1979). This sampling method is very efficient in creating a random sample of parameter values from a multidimensional distribution without bias. The LHS method begins by specifying an upper and lower bound on the range of values of every parameter with the aim to spread the sample points more evenly across all possible values. For M parameter sets, the method divides each interval into M intervals of equal probability. One sample is randomly chosen from every interval but with the condition that each parameter set can only contain parameter values from intervals that have not been used in any other parameter set. This allows us to generate large parameter sets with various and unbiased combinations. This makes the method suitable for sampling high-dimensional parameter spaces where the relative significance of every parameter in determining model output is not yet understood. In our work, we use the LHS to create the parameter samples for the initial model population. The method is implemented using the MATLAB built-up function ‘lhsdesign’.

4.3.4 Partial correlation coefficient

We use the partial correlation coefficient for characterising the properties of subsets of the population further below in Section 4.5.1, 4.5.3 and 4.5.4.5, i.e. to look for correlations between conductances in the control population and subset of drug population. PCC measures the strength

and relationship between two random variables while considering the changes of one or more other additional variables. However, before choosing any particular partial correlation, it is important that we know the type of distribution of our data. We use Spearman's partial correlation coefficient since most of our variables have non-normal distribution. To find the PCC between variables x and y , given a set of m controlling variables $p = \{p_1, p_2, \dots, p_m\}$, we first measure the linear regression of x with p_i y with p_i :

$$\hat{x} = c_0 + \sum_{i=1}^m c_i p_i, \quad \text{and} \quad \hat{y} = b_0 + \sum_{i=1}^m b_i p_i. \quad (4.2)$$

PCC between x and y can be found by calculating the correlation coefficient between the residuals $e_x = x - \hat{x}$ and $e_y = y - \hat{y}$ and it is defined as following,

$$\text{PCC}(x, y, p_i) = \frac{\text{cov}(e_x, e_y)}{\text{var}(e_x)\text{var}(e_y)}. \quad (4.3)$$

PCC takes on a value in the range between $[-1, 1]$ where 1 indicates a strong positive correlation and -1 indicates a strong negative correlation. In MATLAB routine, PCC is defined in a built-up function called '*partialcorr*'.

4.4 Experimentally-calibrated population of models

In this section, we describe the calibration methodologies used to construct the model population in the control condition, as well as the model population under the action of drugs.

4.4.1 Constructing the control population

To create the control population, we generated an initial population between 10,000 - 30,000 rabbit/human ventricular action potential models by independently varying the value of ion channel conductances in each model. These chosen parameters were based on the parameter sensitivity analysis, as discussed earlier, by looking at the parameters that largely influenced the action potential repolarisation. Technically, the parameters control the level of ionic current magnitudes. The list of selected ionic currents are as shown in Table 4.1 and the expression for each ionic currents in the model was replaced by,

$$I_x = \alpha_x g_x \mathcal{F}(V, \mathbf{y}, \mathbf{w}, \mathbf{p}, \dots), \quad (4.4)$$

where α_x is the multiplicative factor that relatively determines the maximal amplitude of the respective current. g_x and $\mathcal{F}(V, \mathbf{y}, \mathbf{w}, \mathbf{p}, \dots)$ are the ionic conductance of the different currents and the function that describe the ionic current, respectively.

Initial model population

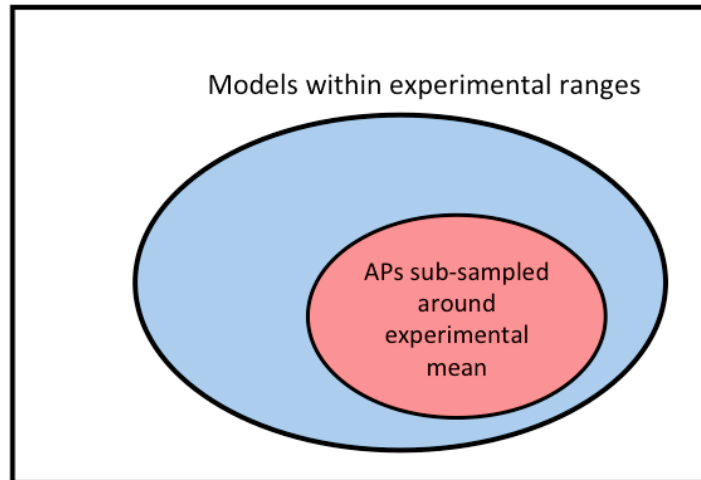


Figure 4.4: Diagrammatic representation of model calibration.

Selecting ranges for parameter variation. The multiplicative factors were varied between the range of 0.1 and 2 times the baseline value in the original model. The range allows substantial level of channel expressions, so that the output distributions could cover the entire experimental ranges.

APs quality control. Beat-to-beat repolarisation variability could be a major source to AP variation in isolated cells due to stochastic behaviour of ion channels (Zaniboni et al. 2000) and period of stimulation. In order to minimise the effect of beat-to-beat variability and ensure that each model in the population reached its steady state, the model was numerically solved by stimulation a train of 1000 action potentials at pacing rate 2Hz (500 ms). The last two APs of the simulation were saved for further analysis. Then, the model AP biomarkers (APD90, APD50, APD30, Trise) were computed for each model. As part of our quality control, a model variant was eliminated from the initial sample populations if it failed to depolarise above 0 mV or had a resting membrane potential larger than -65 mV. We also removed the model if it showed APD90 differences between the final two action potentials larger than 5 ms and this is similar to quality control used experimentally. These filters were implemented to ensure that the accepted models had viable APs.

Calibration criteria. A two step protocol was used to calibrate the model population to experimental measurements, an approach similar to that of Lawson et al. (2018). Illustration of our calibration steps can be seen in Figure 4.4. We first calibrated the initial model population (constructed using the LHS) with the experimental ranges in Table 3.1. In most of the previous works, calibration of a population of models has been achieved almost exclusively by eliminating all the models that produced AP biomarkers falling outside the experimental ranges (Britton et al.

2013, Gemmell et al. 2016, Sanchez et al. 2014). This is overdetermined as the accepted models may not necessarily produce a good correspondence with the biomarker distribution shown in the experimental data. One of the reason is that the baseline model was not constructed using similar experimental measurements and the outputs produced by the model may not accurately capture the response seen in the experimental data due to differences in experimental technique and setting.

Therefore, to improve the model response relative to the experiment, the biomarker distributions were also fitted by randomly sub-sampled a model population around experimental mean. This model subpopulation was randomly picked from the model population that fall within the calibration ranges, as illustrated in Figure 4.4. In order to do that, we chose APD90 as the main biomarker, considered that APD90 is the most affected biomarker when studying Class III and IV channel blocks. Our goal was to fit the APD90 distribution alone and we expected the other biomarker distribution would follow. To demonstrate our method, the range of APD90 values was split into 11 equal sized bins and random model variants were removed from each bin until the relative histograms of the model population and the experimental data were identical. Both calibration criteria are critically important in order to ensure that the inferences from *in-silico* modelling more physiologically relevant. The entire processes were repeated for all three cell models, and the results were analysed.

4.4.2 Constructing the drug population

We simulated the administration of 30nM of dofetilide and 1 μ M of nifedipine, by modelling the action of the drug as a single-pore IKr and ICaL block, respectively (Brennan et al. 2009). A dose of 30 nM of dofetilide is known to induce 30% inhibition of IKr channel. On the other hand, a dose of 1 μ M of nifedipine is known to induce 60% inhibition of ICaL channel. Each IKr/ICaL in the model of the control population was reduced by this amount, and each model was paced again to a new steady-state (1000 action potentials) at 2Hz pacing rate. The last two APs were kept for further analysis.

The most common approach that has been used by others (Britton et al. 2017a; 2013; 2014) to determine the degree of channel block is by using the Hill equation (Hill 1910) as formulated below,

$$\text{Fraction of blocked site, } Y = K^n / (IC50 + K^n), \quad (4.5)$$

where n is the Hill coefficient and K is the drug concentration. IC50 is the drug concentration that blocks 50% of the respective current. Nevertheless, there is no standardisation of IC50 measurement at present, which favours the existence of a high variability of the IC50 values reported in the literature and databases (Crumb et al. 2016). There is experimental evidence of the IC50 dependency on the experimental conditions, such as voltage protocol and temperature (Kirsch et al. 2004, Yao et al. 2005). This makes the process of determining the accurate degree

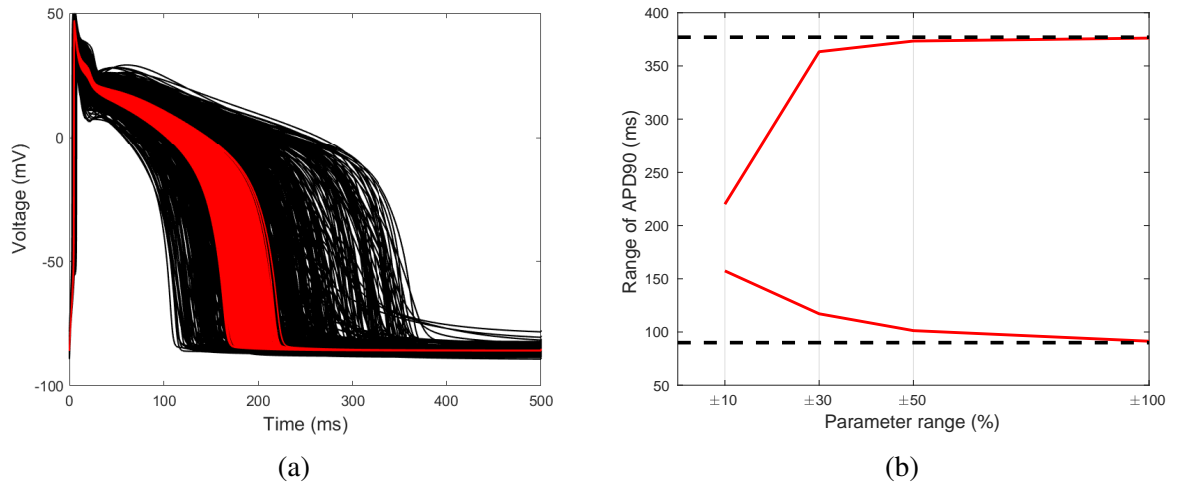


Figure 4.5: (a) Selected action potentials for cell models accepted in the control population (black lines) when the conductances scaling factor were randomly varied in the range 0.1–2. The red lines show the trace of action potentials when conductances scaling factor was varied across a range of 0.9–1.1. (b) Variation of range of APD90 as a function of the parameter range. Dashed lines indicate the experimental range used to calibrate the population of models.

of channel block a little bit difficult and challenging.

Hence, we used a pragmatic approach in our work to determine the degree of ion channel block. For the given concentration of dofetilide, the range of inhibition of IKr channel is approximately between 25–35%. We varied the amount of IKr block and ended up with 30% such that the AP responses could match the experimental observation (Table 4.2 and Figure 4.12b). Similar procedure was used for the second drug.

4.5 Results and discussion

In this section, we present and discuss the results obtained from our computational studies using three different AP ventricular models. Results obtained with the Shannon model are presented in the greatest detail because the model produced the most significant results compared to the experimental measurements.

4.5.1 Development of the populations of models in control conditions

Parameter variation. Figure 4.5a shows the corresponding relationship between model action potential to the level of parameter variation. We initially considered smaller parameter ranges ($\pm 10\%$, $\pm 30\%$ and $\pm 50\%$), attaining results that implied such variation levels were insufficient to explain the experimental data. As we can see from Figure 4.5b, for a smaller range of parameter variation, the range of model output (in this case the APD90) is small and not sufficient to capture the variation level showed in the experimental data, suggesting further variation in these

cell model properties was needed. Although at $\pm 50\%$ parameter variation the model output is relatively close to experimental range, the population of models is not able to capture the effects of drug block, as shown in the supplementary Figure A.1. Addition of ion channel blocking drugs (dofetilide) exhibited a small range of effects within models, which is far from the experimental observation. The results presented here demonstrate the importance of choosing the appropriate level of ion channel expressions when constructing a population of models.

Biomarker distributions in each model population. Figure 4.6 shows distributions of selected AP biomarkers in populations of models in comparison to experimental dataset. When experimental ranges were the only calibration criteria used to construct the experimentally-calibrated model population, we can see that both Shannon and Ohara model produce a right-skewed distribution (green distribution in Figure 4.6(a) and 4.6(c)) compared to the experimental measurements (blue distribution). An obvious reason is that the data used to construct the model was from different laboratories with different experimental conditions. In consequence, randomly varying the parameters from the baseline value would only produce a distribution within the baseline value of the model. Only the TenTusscher model (Figure 4.6(b)) managed to give nearly identical distribution to the experimental data and this is, of course, because the baseline model is close enough to the mean value of the experimental recordings.

Hence, to improve the outcome of the biomarker distributions, we fitted the distribution of the models to the experimental data, as discussed earlier in Section 4.4.1. Using this approach, 3425 Shannon models (11.4%), 7036 TenTusscher models (35.2%) and 2337 Ohara models (23.4%) were accepted into the control population. We realised that the method presented here was simplistic but sufficient enough to meet our objective, i.e., to fit the distribution. Lawson et al. (2018) has demonstrated a more efficient approach (using a combination of Monte Carlo sampling and simulated annealing-type algorithm) to address the problem, but yet the method still failed to fit all the biomarker distributions simultaneously. A probable reason is because the parameters that explicitly controlled the AP shape were not modelled, hence inhibiting a good correspondence with the biomarker's distribution in the experimental data (Britton et al. 2017a).

Figure 4.6 shows the biomarker distributions (red distribution) for each model after fitting to the experimental data. After the optimisation, we can observe that the AP biomarkers show a good overlap with the experimental biomarker distribution. In Shannon model population, both APD90 and APD50 produce a good correspondence with the experimental dataset. APD30 has similar variability between models and experiments, but the distribution mean is shifted ~ -50 ms in the model distribution relative to experiments. This happens because Shannon model has higher amplitude compared to the experimental signal (see Figure A.3(a)). Compared to APD90 and APD50, APD30 is a very sensitive biomarker which can be influenced by the value of AP amplitude as it determines the 'cut-off' value for each APD. Overall, the TenTusscher model population produces a remarkable correspondence with experimental distributions (refer

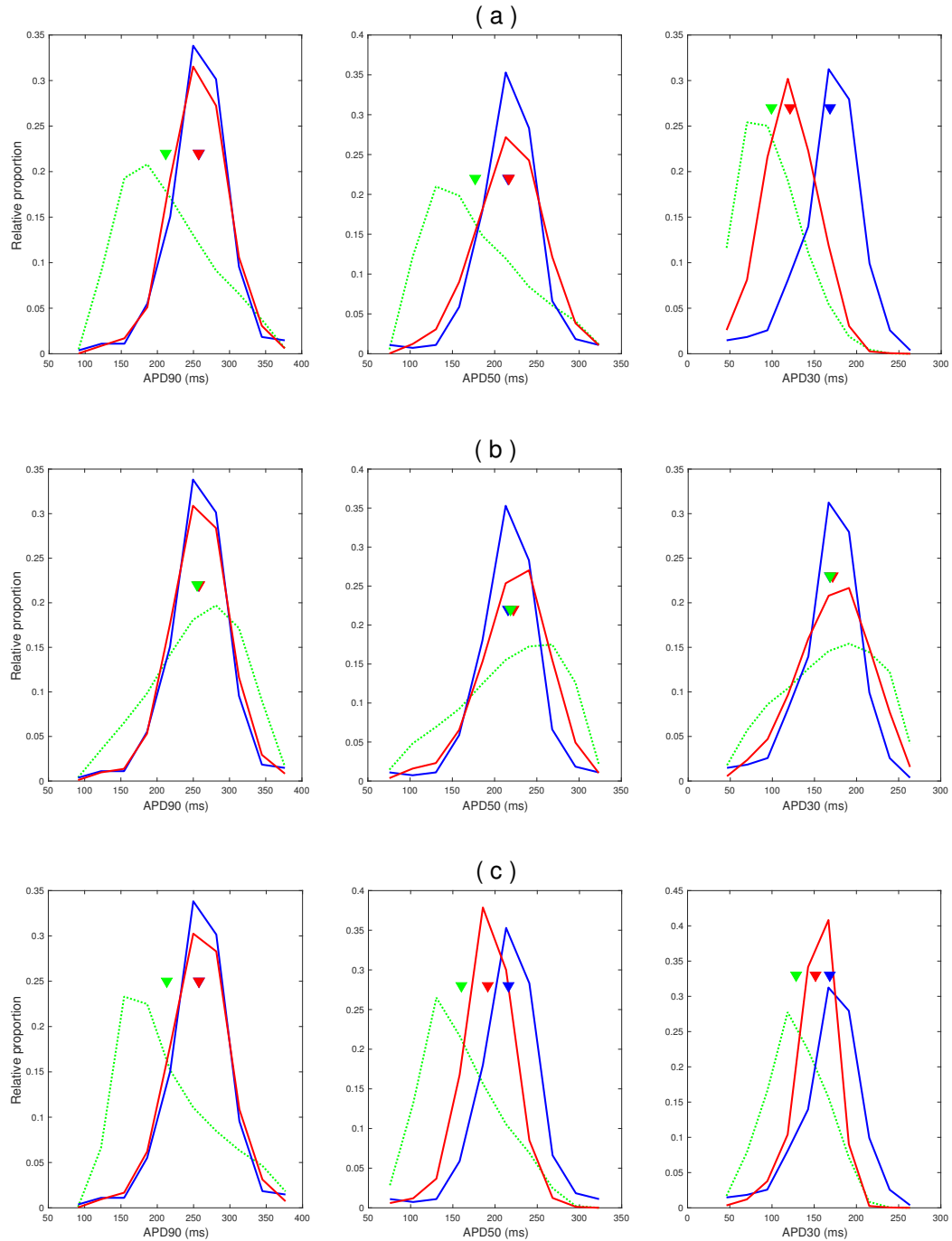


Figure 4.6: Distributions of AP biomarkers in populations of models in comparison to experimental data. (a) **Top row** is for the Shannon model, (b) **Middle row** is for the Ten Tusscher model and (c) **Bottom row** is for the Ohara model. The green line represents the distribution of biomarkers in the baseline model that fall within the experimental ranges, the red line represents the distribution of biomarkers after fitting to experimental distributions and the blue line is the distribution of biomarkers in experimental data. The inverted (\blacktriangledown) indicates the mean value of the respective distributions.

to Figure 4.6(b)). All biomarkers show a perfect agreement with identical mean values. Also, the Ohara model gives a similar level of variability for every biomarker distribution, but the mean has shifted for approximately -20 ms (APD50 and APD30). Importantly, the %IQR coefficient ($IQR \cdot 100 / \text{mean}$) of the APD90 at 2 Hz for each model population was 24%, close to the average reported experimentally (19% – 25%).

The set of model populations reproduce the spread of AP waveform features in terms of the gross timings of the AP event. Absolute levels of diastolic, peak and plateau voltages are not available from the optical measurements and would normally be additional important biomarkers available from sharp micro-electrode measurements. However, the refinement of the models based on the AP waveform shape alone resulted in a narrow range of diastolic and peak potentials from the AP models. In Shannon model population, the mean of diastolic potential and AP amplitude are -85.5 ± 1.1 mV and 134 ± 3.9 mV, respectively. Similarly, mean of diastolic potential and AP amplitude in the TenTusscher (diastolic = -85.7 ± 1.9 mV, AP amplitude = 119.3 ± 8.6 mV) and the Ohara (diastolic = -87.8 ± 0.7 mV, AP amplitude = 126.6 ± 3.5 mV) model populations have a good overlap with literature reports from isolated rabbit ventricular myocytes. The difference in AP amplitude in each model population is probably due to difference in the strength of stimulus current or sodium current which was not altered when constructing the model population.

In general, our findings show that each model exhibits a different level of heterogeneities and distinct model outputs. In comparison to the experimental dataset, the TenTusscher model produces the most significant agreement, followed by the Ohara and then Shannon models. This, however, does not guarantee that the TenTusscher model would produce a better outcome for drug blocks compared to the other two models as the underlying ionic properties in the respective model may influence the responses. In the next section, we investigate the capability of each model population to predict the AP responses following drug blocks of hERG and L-type calcium channels.

Correlations between ion channel expressions. One question that arises from this result is whether the accepted models in the control population has similar ionic properties with the rejected models. To answer this, we measured and compared the partial coefficient correlation (as defined in section 4.3.4) for a pair of ionic currents in the model population of Shannon. Particularly, the correlation between a pair of ionic currents while including the effect of other ionic currents were measured. Figure 4.7 depicts the PCC values between the initial model population (calibrated models within experimental ranges) and the accepted models in the control population (randomly subsampled around experimental mean). For simplicity, we refer to the first model population as $P_{\text{calibrated}}$ and the latter as P_{control} .

We can see that for the selected pair of ionic currents in P_{control} have more pronounced and stronger correlation than $P_{\text{calibrated}}$. Importantly, four pairs (gCaL-gNaK, gCaL-gKr, gCaL-gNaCa and gCaL-gClb) of ionic current show significant correlation with PCC greater than 0.5. The

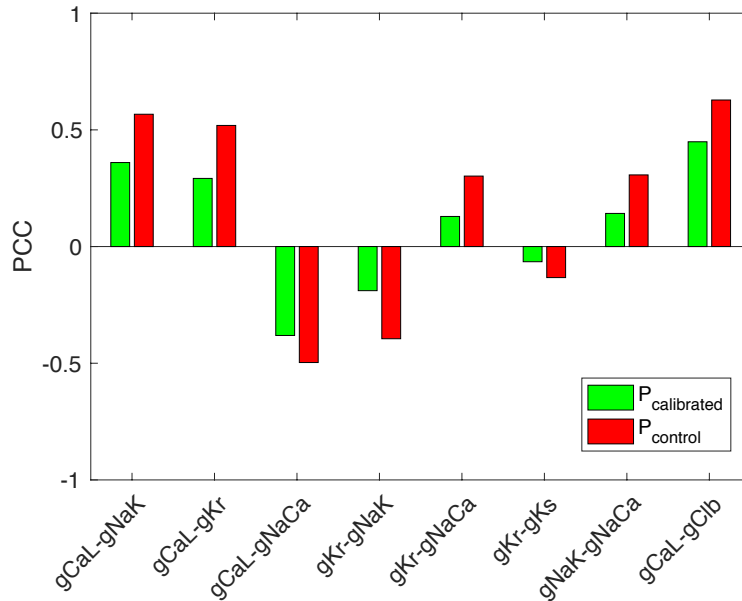


Figure 4.7: Partial correlation coefficient (PCC) for selected pairs of ionic currents in the models within the experimental ranges, $P_{\text{calibrated}}$ and the models that have been accepted in the control population, P_{control} . All results have p-values < 0.001 (paired t-test). Data presented here is for Shannon model population only.

strong positive correlation showed between ICaL and IKr indicates that viable APs required a balanced expression of these two ion channels. Also, in a recent study by Ballouz et al. (2019), they observed that the most notable correlation in mRNA extracted from human induced pluripotent stem cell-derived cardiomyocyte was between IKr and ICaL currents ($r^2 = 0.89$). This result is consistent with our own where the IKr and ICaL in the model population exhibits a strong positive correlation (PCC = 0.52). Also, the negative correlation of ICaL and INaCa has not been previously reported, the mechanistic basis for this is uncertain, but may be linked to the maintenance of the plateau phase to which both ICaL and INaCa contribute.

Interestingly, there is a strong positive correlation shown between gCaL and the baseline chloride conductance, IC1b (PCC = 0.63). The role of chloride channels in the generation of cardiac action potential is well known. Cardiac chloride channels have the unique ability to generate both inward and outward currents and cause both depolarisation and repolarisation during the action potential (Duan 2009). This feature may be the basis for the positive correlation with gCaL.

4.5.2 Parameter distributions in the control population of each model

We observe and compare the differences in parameter distributions of the accepted model population of each AP model. This is plotted in Figure 4.8. In the figure, most of the conductances span the full sampled range (0.1–2 times the baseline value for that conductance), highlighting the

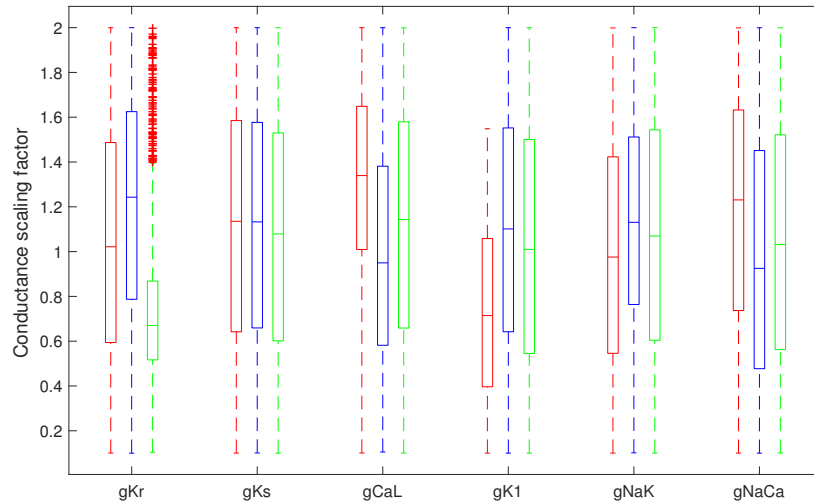


Figure 4.8: Box-whisker plot of selected parameter distributions in the Shannon (red), TenTusscher (blue) and Ohara (green) model population. Lower and upper box boundaries is the 25th and 75th percentiles, respectively. Median is denoted by a line inside box, outliers are marked with a plus sign (+).

robustness of the rabbit AP against conductances variations. In the Shannon model population, the median of most of the parameters is close to baseline value, with the two exceptions being gCaL and gK1. The baseline Shannon model has APD90 approximately 188 ms and this value is shorter than the mean APD90 of the experimental distribution (approximately 257 ms). A high gCaL and small gK1 were needed to compensate the APD difference between the model and experimental distributions. Similarly, the APD90 of baseline Ohara model is about 50 ms shorter than the mean APD90 of the experimental data. A small gKr value (as shown in Figure 4.8) would prolong the APD and compensated the difference.

Furthermore, in the Ohara model, gKr confined the smallest range and median value, in comparison to the other two models. 95% of the models in the control population of Ohara model have gKr values clustered between 0.1 and 1.4. The TenTusscher model shows the most significant median value of gKr (x1.2). gCaL values are equally spanned between 0.1 and 2 in all the three models, with different in median values. 76% of the models in the Shannon population have gCaL larger than 1, followed by the Ohara model (59%) and lastly by the TenTusscher model (47%). This highlights the importance of gCaL to adjust the APD in the respective model so that the APD mean in the model population could match the experimental mean. Also, the Shannon model shows a restricted value of gK1, which only span between 0.1 and 1.5. gK1 in the other two model population is uniformly distributed within the sampled range. For larger gK1, stronger stimulus amplitude is needed to depolarise the action potential. In essence, it is impossible to directly compare the parameter distribution between the model populations as the excitation of AP depends on the counterbalance of ionic currents between each other. In other words, the

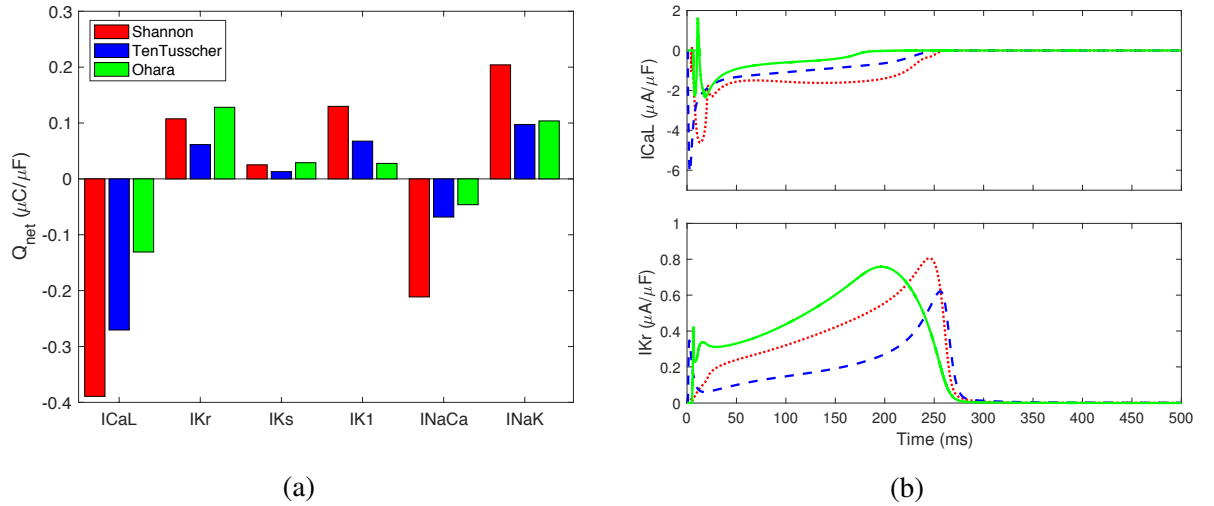


Figure 4.9: (a) Bar graph of the Q_{net} in the archetypal model of Shannon, TenTusscher and Ohara model. (b) Profiles of I_{CaL} and I_{Kr} in the respective models.

same AP can be generated as long as the inward and outward currents are equivalent (Banyasz et al. 2011) and there are many ways to achieve that. Hence, it is not surprising that each model population exhibited different ion conductance distributions, although all the model populations were calibrated to a similar experimental distribution. Overall, our results demonstrate that a viable AP can be generated by a wide variety of different balances of ionic currents, although these balances may have different responses to drug blocks.

In addition, it is crucial to realise that the baseline current magnitude differed between each model and hence the conductance scaling factor plotted in Figure 4.8 did not provide a fair basis for comparison between the Shannon, TenTusscher and Ohara models. To make the comparison, we generated the ionic currents (I_{CaL}, I_{Kr}, I_{Ks}, I_{NaCa} and I_{K1}) in each model and then measured the net charge transported by individual currents over the duration of one action potential Q_{net} ,

$$Q_{\text{net}} = \int_{t_0}^{t_1} I_j(t) dt, \quad (4.6)$$

where t_0 and t_1 are the start and end of the simulated beat, respectively. I_j is the current in the respective model. The Q_{net} of each ionic current was computed using the trapezoidal integration method. Instead of using the entire accepted model population, we constructed an archetypal model for each of them by taking the median values of the conductances scaling factor (Figure 4.8). Figure 4.9a shows the Q_{net} of common ionic currents in each archetypal models. We can see that most of the ionic currents in the Shannon model dominate the ionic currents in the other two models. The Q_{net} of I_{CaL}, I_{NaCa}, I_{NaK} and I_{K1} is the largest in the Shannon model. Ohara has the smallest Q_{net} of I_{CaL} but possesses the largest I_{Kr}. In the next section, we will show how these differences in the Q_{net} may significantly affect the model's responses to channel blocks.

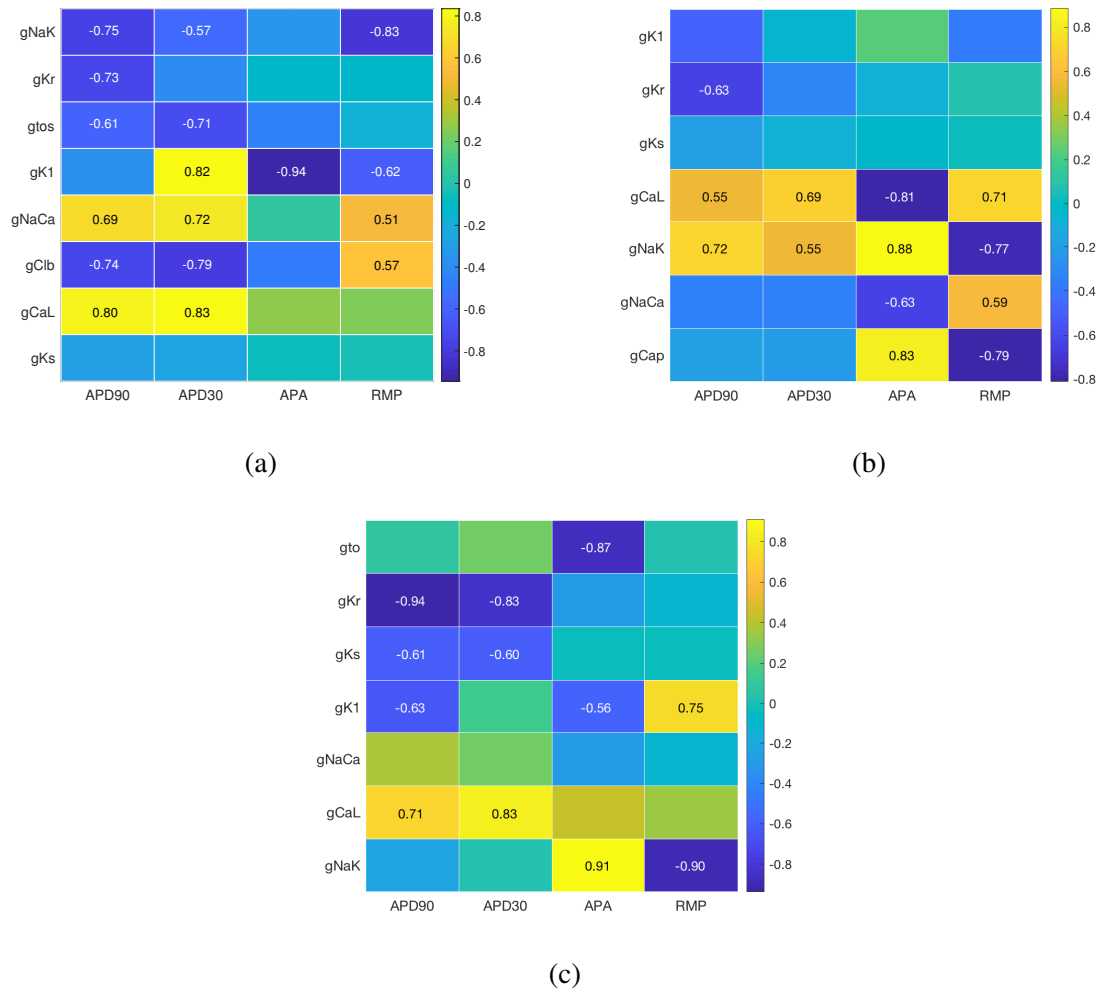


Figure 4.10: PCC values between selected biomarkers and parameters varied in the control population of (a) Shannon model, (b) TenTusscher model and (c) Ohara model. PCC values are displayed for coefficient values larger (or smaller) than 0.5 (-0.5). Positive value indicates strong positive correlation and vice versa. Colour map is shown using a bar to the right in each panel. All indicated PCCs have $P < 0.001$ (paired t-test).

4.5.3 Partial correlation coefficient for model biomarkers

Ionic currents are well known to act together in a different region of the action potential, and some are very sensitive to perturbation, which could alter the AP shape. We investigated whether there were correlations between parameter values in the models of the control population and the AP biomarkers. The parameters were initially varied randomly, and they were uncorrelated, hence any correlations found are due to the calibration process. To measure the correlations, we used the PCC which identifies correlations between variables while controlling for the effects of the remaining parameters. PCC for selected AP biomarkers in each cell model is depicted in Figure 4.10.

In the Shannon model, we can see that all model parameters have a strong correlation with APD90, except for gK1 and gKs. gCaL has the strongest positive correlation with the APD90,

followed by gNaCa. The results are as expected since the selected parameters to construct the model population were based on their effect on AP repolarization, and this finding is consistent with our parameter sensitivity test earlier (see Figure 4.3). A similar outcome can be observed in the Ohara model, where almost all model parameters correlate strongly with APD90. Only gto, gNaCa and gNaK have a small influence on APD90. Compared to the other two models, many conductances in the TenTusscher model show a more insignificant effect on AP repolarization. Only gKr, gCaL, gNaK exhibit strong correlation with APD90. For consistency, the same parameters as those in the Shannon model were varied in the TenTusscher and Ohara models. However, all selected conductances in all models influence APD, but not always strongly.

It is known that the inwardly rectifying potassium current (IK1) is responsible for forming the initial depolarization, final repolarization, and resting phases of the action potential (Dhamoon and Jalife 2005). In the Shannon and Ohara model, the conductance of this current has strong correlations with the amplitude and resting membrane potential (RMP) of the action potential. However, the correlation is weaker in the TenTusscher model. Also, gNaCa in the Shannon and TenTusscher models has a strong positive correlation with RMP due to reactivation of INaCa during this stage in order to restore the calcium concentration in the cell. Other than these two ionic currents, INaK is also responsible for the generation of the resting membrane potential of the action potential by transporting sodium ions out and potassium ions into the cell (Bueno-Orovio et al. 2014). This is consistent with our result where gNaK in all cell models shows a strong negative correlation with the RMP.

4.5.4 Response to hERG block by dofetilide

Following the calibration of the model population, we used the population of rabbit/human ventricular myocytes to predict electrophysiological response to dofetilide. From our computational modelling, we observed various AP responses when IKr was blocked as follows,

- (Normal response) AP with normal APD prolongation.
- (Hyper-response) AP with extreme APD prolongation, i.e, the AP slowly repolarizes, but fails to reach the resting potential (> -65 mV) before the arrival of next stimulus.
- (EAD) AP with single or multiple early after-depolarisations, i.e, if EAD amplitude is greater than 10% of action potential amplitude.
- (Alternans) APs with APD difference larger than 5 ms, i.e models that exhibit 2:1 or 2:2 responses.

Figure 4.11 depicts some examples of APs simulated for control condition (solid line) and the effect of IKr block (dashed line) in the Shannon model. Our finding shows that these AP responses are model-dependent, and not all responses were seen in every model, as shown in Table 4.2.

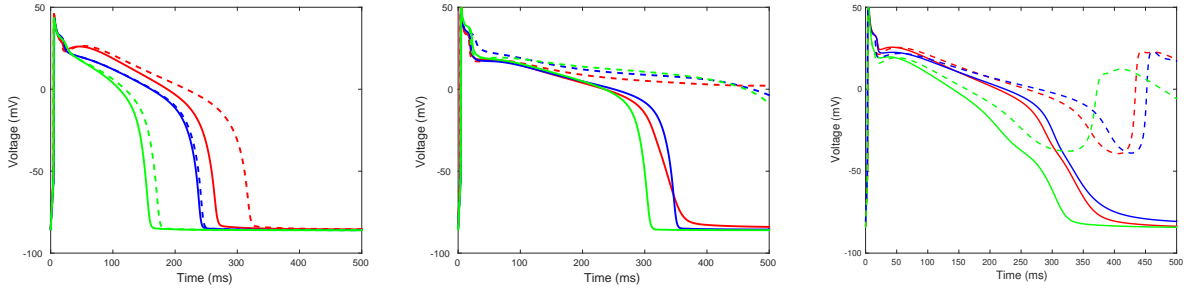


Figure 4.11: Examples of simulated AP traces obtained in several models accepted in control populations (solid line) and their responses to 30% IKr block (dashed line). **Left panel** shows examples of normal responders, **Middle panel** shows examples of hyper-responders and **Right panel** shows examples of EADs.

AP response	Experiment (%)	Shannon (%)	TenTusscher (%)	Ohara (%)
Normal response	87.4	89.2	99.4	99.93
Hyper-response	12.6	8.2	0.09	0.02
EADs	-	2.6	-	-
Alternans	-	-	0.45	-

Table 4.2: Size of sub-populations in the drug population of cell models and experiment.

4.5.4.1 Normal response

From Table 4.2, it can be seen that a majority of the cell models (approximately larger than 90%) in the respective model experienced APD prolongation when IKr was blocked. The Shannon model makes a good agreement with the experimental data. Meanwhile, the other two models show a slightly higher proportion than the observed value with more than 99% of the models in the two populations exhibited normal responses. Figure 4.12 shows the scatter plot of baseline APD₉₀ values of each accepted model at 2Hz against Δ APD₉₀ attributable to IKr block, in comparison to experimental data.

In general, the APD prolonging effect of IKr block seems to be uniform in all three models. There is also no significant correlation between the baseline APD and the amount of APD prolongation following block. The degree of Δ APD does not depend on its baseline APD. This is because APD is a function of model parameters such that a given APD value can be produced by infinitely many different sets of parameter values. These sets form a continuous contour hypersurface in the parameter space (as illustrated in supplementary Figure A.2). In the Shannon model, the distribution shows that the range of Δ APD is narrow (< 25 ms) at smaller AP, but getting more pronounced as the baseline APD increases. A similar trend can be seen in the TenTusscher and Ohara models. Ohara model has the smallest spread of APD prolongation across the model population, and no model has Δ APD between 0–30 ms. Nevertheless, the mean value of Δ APD is the largest in Ohara model, highlighting the model has the most significant response to IKr channel block. This is predictable as Ohara model has the highest level of IKr magnitude

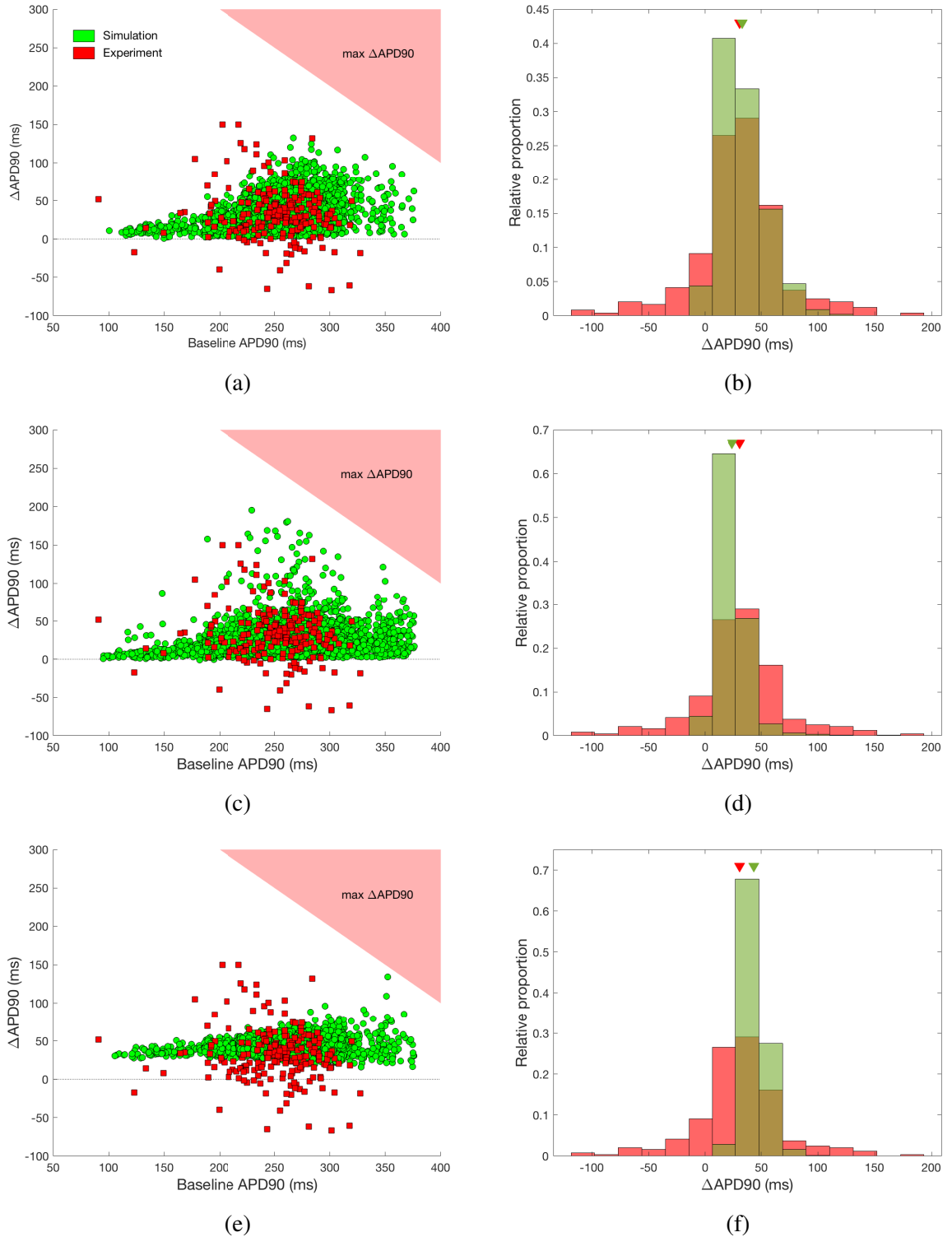


Figure 4.12: Scatter plot of net effect of IKr block on APD90 against baseline APD90 by individual cell models (paired), in comparison to experimental data (red squares). (a) is for the Shannon model, (c) is for the TenTusscher model and (e) is for the Ohara model. (b, d, f) Histograms of the distribution of ΔAPD90 across the population of models (green), compared to experimental distribution (red). Mean value of each distribution is marked as inverted triangle (\blacktriangledown). The mean and standard deviation of ΔAPD90 in each population are 33.18 ± 20.26 ms (Shannon), 24.18 ± 15.02 ms (TenTusscher), 40.29 ± 9.26 ms (Ohara) and 32.23 ± 34.46 ms (experiment). Red triangle region in (a,c,e) is the maximum ΔAPD90 allowed for the respective baseline APD90.

(Figure 4.9a) in comparison to the other two models; hence, more IKr current could be reduced.

The TenTusscher model has the smallest mean of APD prolonging effect with 76.5% out of model population have Δ APD below the experimental mean, which makes the model prediction slightly underachieving. The general spread, however, looks comparable to experimental distributions with several models that could prolong as large as 200 ms. This did not happen in the other two model populations. Statistically speaking, among the three models, the Shannon model population shows the strongest correspondence with the experimental distribution, followed by the TenTusscher model and finally the Ohara model.

In addition, notice that none of the model population exhibited AP with APD shortening when IKr channel was reduced, in comparison to experimental data. Approximately 14.1% out of cell population (5 hearts) produced APD shortening effect following application of dofetilide. This is uncommon as class III antiarrhythmic agents like dofetilide are well-known to induce APD prolonging effect and increase the effective refractory period of an action potential (Anderson and Prystowsky 1999, Jaiswal and Goldbarg 2014, Tamargo et al. 2004). The negative Δ APD was due the effect of DMSO (refer to Chapter 3.2.4). In section 4.5.6, we explore this further by adding random noise.

4.5.4.2 Hyper-response

Following IKr block, some cells experienced extreme APD prolongation, which was beyond the stimulation cycle length (500 ms). The AP failed to repolarise before the arrival of the next stimulus current. We characterise this AP as hyper-response (see Figure 4.11). Since the amount of APD prolongation of these cells cannot be determined ($APD > CL$), the minimum Δ APD is measured as follows,

$$\Delta APD_{90_{\min}} = CL \text{ (ms)} - APD_{90_{\text{baseline}}} \text{ (ms)} \quad (4.7)$$

In computational studies, we observe that only the Shannon model exhibited hyper-response across the model population, as stated in Table 4.2. The proportion of hyper-responders in the other two models is negligible. Our result using the Ohara model is consistent with a recent study by Britton et al. (2017a). In their study, they reported that the dofetilide simulations using Ohara model did not exhibit such extreme APD prolongation, although their experimental data did exhibit the behaviour. Later, we will use result obtained by the Shannon model in order to understand the underlying cause of hyper-response. In addition, the mean baseline APD90 for hyper-responders in the Shannon model population is not significantly different from the cell population (302 ± 28 ms vs 277 ± 9 ms, respectively). The mean of minimum Δ APD is 197 ± 28 ms in the population of models, compared to experimental data which is 224 ± 44 ms.

4.5.4.3 Early after-depolarizations (EADs)

As shown earlier that blocking IKr increases the APD and hence increases the effective refractory period (ERP) of the cells. However, cells with higher ERP are vulnerable to EADs occurrence. EADs are a pro-arrhythmic event and may precipitate Torsade de Pointes (TdP) and other types of arrhythmias (Yap and Camm 2003). By definition, EADs can arise when there is an abnormal depolarization (self-amplify) during phase 2 or 3 before normal repolarization is completed. In our work, an AP is considered to generate EADs if EADs amplitude (after 100 ms of AP excitation) is 10% higher than the AP amplitude. MATLAB function 'findpeaks' was used to measure the EADs amplitude. In the experiment, the noisy signal of AP trace (see Figure 3.6) could mask EADs generation if the EADs amplitude is too small. The criterion was also used in order to distinguish the AP signal between hyper-responders and EADs.

Based on this detection criterion, only the Shannon model displayed EADs in response to IKr block. No EADs was observed in the other two models and experimental data. EADs generation in response to IKr block, however, is more common when cells are stimulated at slower pacing rates. This has been reported in several clinical studies (Guo et al. 2011, Nalos et al. 2012) and computational modelling (Cooper et al. 2016, Costabal et al. 2018, O'Hara and Rudy 2012). Fast pacing rate (2Hz) used in our work should prevent EADs. In another study conducted by Lu et al. (2001), they demonstrated that there are species differences in EAD occurrence with rabbit cells constituted the most sensitive species. This is probably why the Shannon model showed a slight tendency to exhibit EADs, compared to other two human AP models. Also, we speculate that EAD generation in the Shannon model is highly linked to the level of INaCa and ICaL magnitudes in this model. Compared to the Ohara and TenTusscher models, the Shannon model possesses the largest degree of INaCa and ICaL currents (Figure 4.9a) which makes the model prone to displaying EADs.

4.5.4.4 Parameter distributions for each AP response

To study the ionic current properties in each AP response, we only consider results obtained from the Shannon model population as this is the only model that exhibited various AP responses following IKr block. Distribution of parameters for the TenTusscher and Ohara models are similar for both control population and normal responders, except for gKr as it was the only parameter changed. Analysing the parameter distributions in three sub-populations of the Shannon model show that IKr plays an important role in the prolongation of APD as depicted in Figure 4.13. In normal responders, most of the parameters have identical median values with the control population (blue distribution), except for gKr. The discrepancy is because gKr was the only channel blocked under drug condition. Indeed, more than 90% of the model population experienced a normal AP response when IKr was reduced; hence we could expect that the parameter values were not significantly distinct from the control population.

For hyper-responders, gNaK, gKr, gtos, gK1 have almost similar median values with the

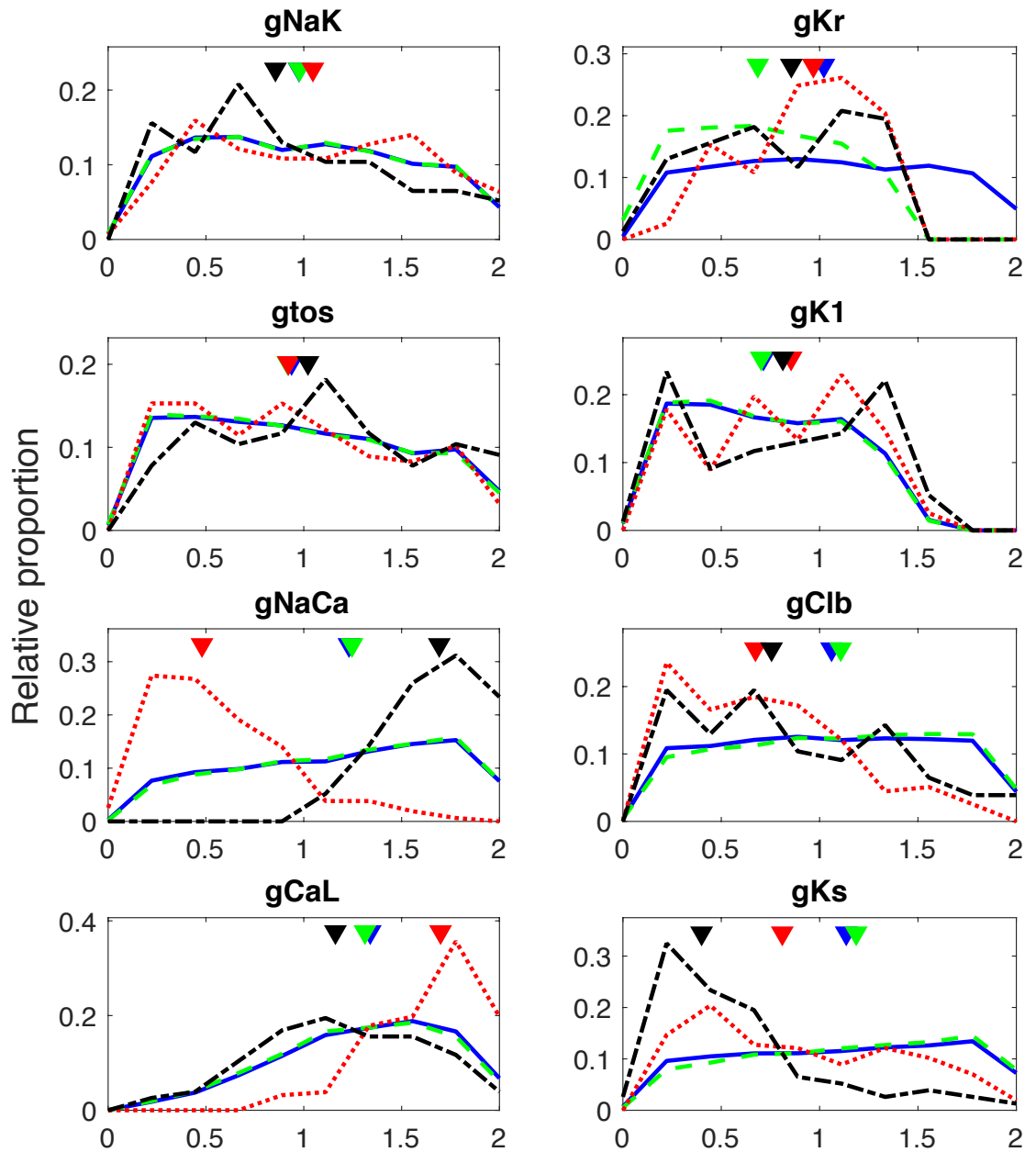


Figure 4.13: Distribution of values for the eight ionic conductances varied in the Shannon population for models within all three classified responses in comparison to control population. Blue solid line is for control population, green dashed line is for normal responders, red dotted line is for hyper-responders, and black dashed-dotted line is for EADs. Inverted triangle symbol (▼) denotes the median value of each distribution.

control population. Both median of gKs and gClb decreased by approximately 28% and 35%, in comparison to their values in the control population, respectively. Median value of gCaL in hyper-response shows a significant increase (31%) with most of the parameter values strictly covered in the top region of the sampled value. gNaCa was drastically reduced with median value approximately 0.5.

In contrast to the above, gNaCa increased dramatically in models with EADs and the allowed values of this conductance of which were within a narrow subset of the sampled range (top half of the sampled range). It is well known that Na/Ca exchange current is responsible for EADs formation (Qu et al. 2013, Weiss et al. 2010). Other conductances such as gCaL, gKr and gNaK showed a small reduction in the median values, whereas gtos was increased by about 10%.

In a recently published paper by Varshneya et al. (2018), they demonstrated that less arrhythmic behaviour was observed in models with higher IKs level. Particularly, models with low IKs are more susceptible to EADs when ICaL is elevated. Our model population with EADs strongly support the finding as most of gKs conductance covered the bottom half of the parameter range. In addition, INaK expression was also found to have a major role in generating EADs. In another study by Britton et al. (2017b), the results showed that when EADs was generated, INaK was smaller than its baseline values. This is in agreement with our finding where median of gNaK was reduced slightly (approximately 13%) in comparison with the control population.

4.5.4.5 Correlation between ion conductances of sub-populations

Figure 4.14 shows the 2D density plots of the distributions of selected pairs of ionic conductances in three sub-populations of Shannon model. These results show that normal responders span a broader range of sampled values, compared to hyper-responders and EADs. In normal responders, majority of parameters span almost the entire range (up to $\pm 100\%$ of their values from the original parameter set of the baseline model), with the exception being for gCaL. gCaL spans mostly the top half region of the sampled values.

Meanwhile, in hyper-responders and EADs classes, there is a more tightly concentrated distribution of parameter values. This contrasts with the wide spread of parameter values in normal responders. For instance, gCaL in hyper-responders are more often in the top region of the parameter space (larger than $\times 1.5$), whereas for gNaCa are more often in the bottom half of the range. In EADs, gCaL are uniformly distributed across the sampled values, whereas gNaCa covers the top region of parameter range (larger than $\times 1.1$), highlighting the significant role of INaCa to generate EADs. Our results also demonstrate that these AP behaviours could only occur when current magnitudes are within a certain value.

To measure and compare the correlation between each pair of ionic conductances in the three model subpopulations, we used the partial correlation coefficient as plotted in Figure 4.15. In general, we can see that most of the ionic pairs have a strong correlation ($PCC > 0.5$). Interestingly, PCC in both hyper-responder and EADs are more pronounced and larger than normal responder.

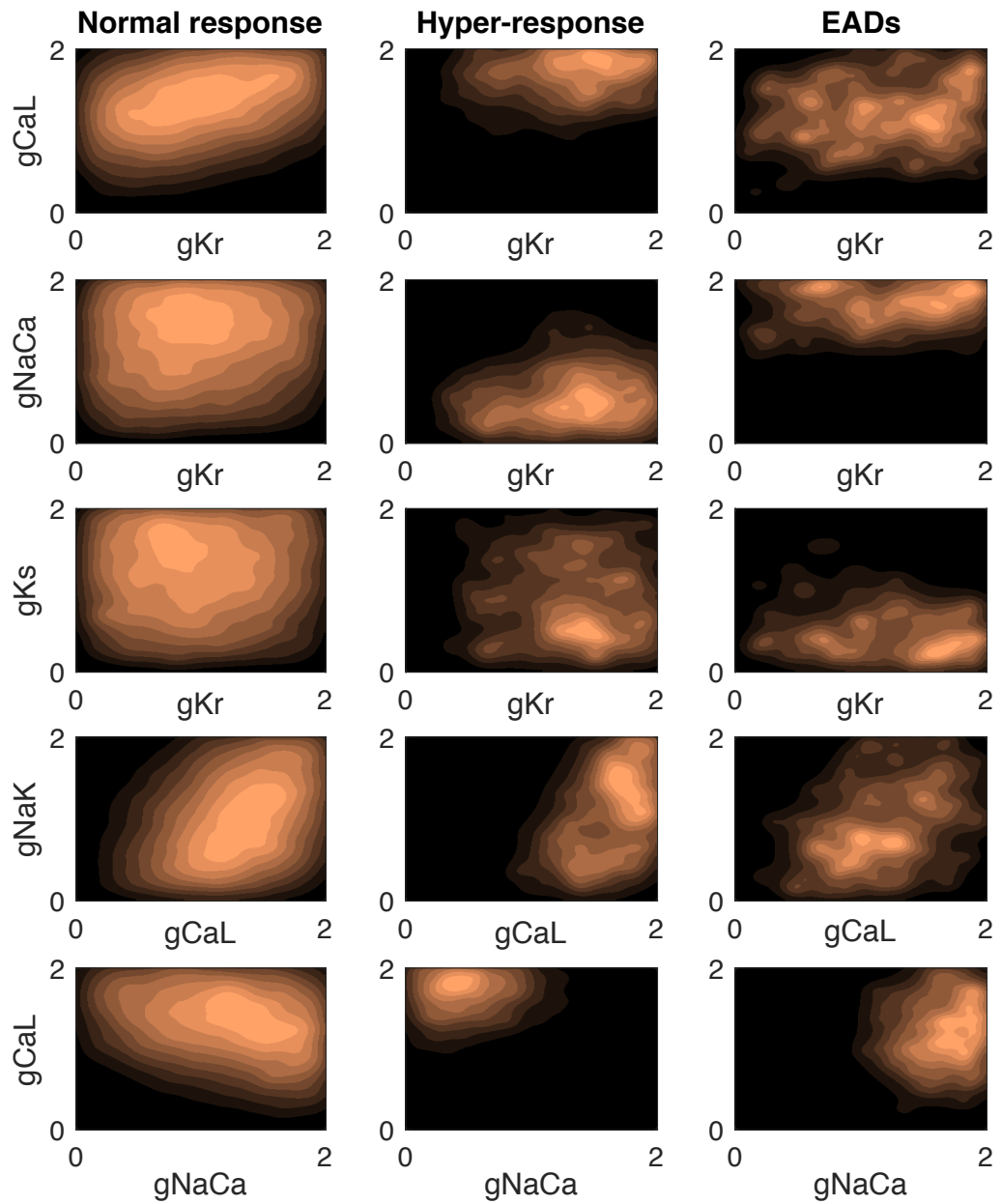


Figure 4.14: 2D density estimation plots showing the relationship between selected ion channel pairs in normal responder, hyper-responder and EADs. Brighter orange is the region with the most data points and black region is the region without the parameter values.

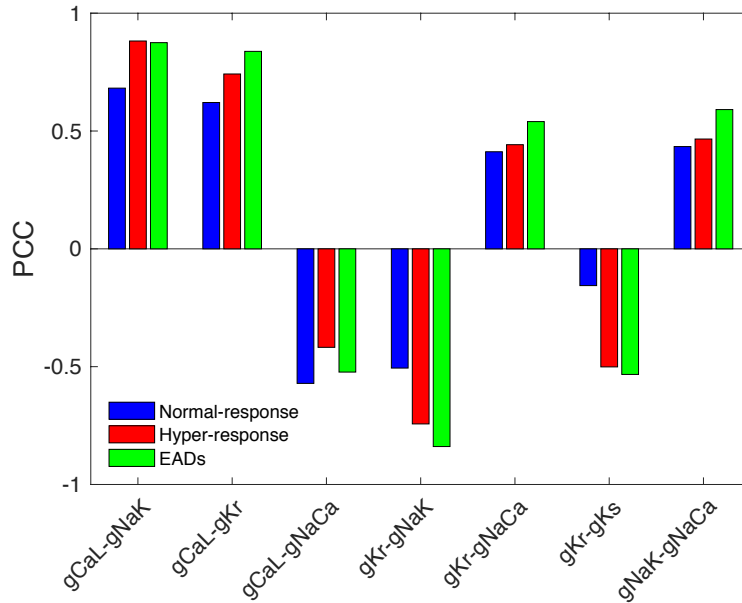


Figure 4.15: PCC of selected pairs of ionic conductances in three sub-populations of Shannon model ($P < 0.0001$; paired t-test).

The most noticeable change is shown by gKr-gKs pair, where the value increased by more than double. In humans/rabbits, the AP repolarisation duration at baseline is mostly modulated by IKr and slightly by IKs. However, following the IKr block, the role is taken by small IKs. Models with low gKs (high gKr) increase the probability of hyper-response and EADs formation. In models with EADs, PCC of gCaL-gKr has the highest value compared with the other two responses. It tells us that coexpression between these two ionic currents plays a significant role in the development of arrhythmias (EADs) in response to a drug that blocks IKr.

4.5.4.6 The ionic mechanisms of hyper-responders and EADs

In this section, we discuss the mechanisms and physiology of hyper-responders and EADs by linking these responses to dynamic changes of ionic currents. In order to do this, we first constructed two archetypal models to represent both responses in an attempt to understand the underlying causes of the behaviours. These models were built by using the median values of ion conductances across the model population (Figure 4.13). Parameter values are listed in Table 4.3.

Hyper-response Figure 4.16 depicts the action potential and selected ionic currents of the archetypal model of hyper-response. Under normal condition, the formation of AP plateau region is mainly influenced by inward current I_{CaL} . At the end of this phase, I_{CaL} slowly begins to diminish as activation of time-dependent outward potassium current IKr and IKs will dominate the other ionic currents, hence forcing the AP to repolarize. Nevertheless, during the application of IKr blocker, IKr is not properly activated, and I_{CaL} remains to dominate (Figure 4.16b). This

Parameter	Normal-response	Hyper-response	EADs
gNaK	1.0	0.95	0.84
gKr	1.0	1.38	1.20
gKs	1.21	0.9	0.56
gCaL	1.29	1.7	1.22
gNaCa	1.25	0.52	1.72
gK1	0.73	0.77	0.67
gtoS	0.91	0.9	1.15
gClb	1.11	0.72	0.73

Table 4.3: Parameter values used to construct the archetypal models. Values were extracted from the median value of each conductance in the respective models subpopulation (Figure 4.13).

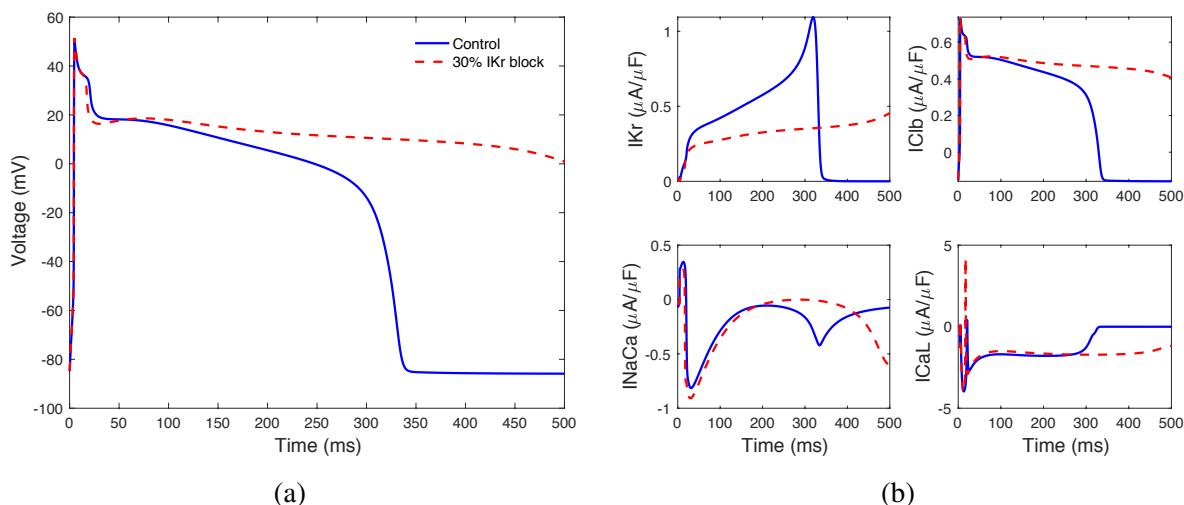


Figure 4.16: Traces of (a) action potential and the corresponding (b) ionic currents in archetypal model of hyper-response. Solid line shows the model outputs under control condition and the dashed line shows the model outputs after the IKr block.

prevents the AP from repolarizing. Moreover, the long plateau is also contributed more or less by continuous activation of outward potassium current IKr and chloride current, IClb.

EADs EADs generation normally occurs when outward currents are reduced, or inward currents are increased or both, such that the net outward current needed to repolarize the AP is compromised, leading to increase in APD (Qu et al. 2013, Weiss et al. 2010). Under these conditions, any mechanism which regeneratively increases net inward current can potentially overcome and reverse repolarization. It is known that L-type calcium current and Na/Ca exchange current are responsible for EADs formation. When IKr is blocked, predomination of ICaL over the time-dependent outward currents like IKr and IClb cause the AP repolarization to be aborted and lead the membrane potential to self-amplify (Figure 4.17a). As membrane potential depolarizes during the EAD, ICaL slowly inactivates, and time-dependent outward currents are further activated ((Figure 4.17b)). If ICaL remains to predominate, repolarization

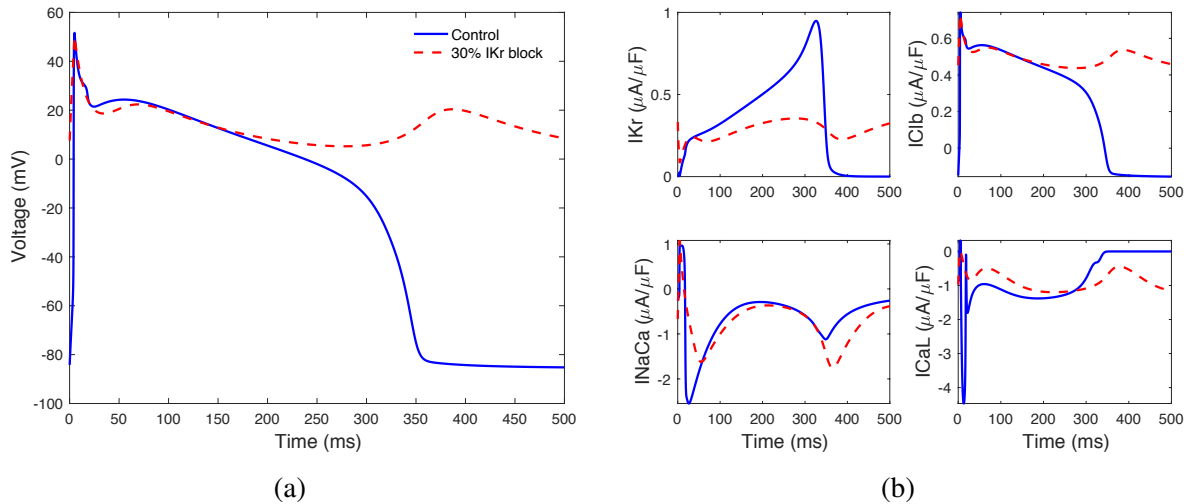


Figure 4.17: Traces of (a) action potential and the corresponding (b) ionic currents in archetypal model of EADs. Solid line shows the model outputs under control condition and the dashed line shows the model outputs after the IKr block.

can be altogether aborted, producing a ICaL -mediated AP upstroke that can result in a triggered beat, or a run of triggered beats.

The second primary current that facilitates EAD occurrence is INaCa (Luo and Rudy 1994b). Na/Ca exchanger is responsible for exchanging three sodium ions for one calcium ion from the cytoplasm, producing an inward current. If the intracellular calcium is still elevated during repolarization, INaCa gets larger, thereby resisting repolarization (Figure 4.17a). Nevertheless, INaCa cannot trigger the membrane potential to depolarize itself, unless if the intracellular calcium increases further. Since during the initial phase of EADs, ICaL increases dramatically, it would trigger additional calcium release from the sarcoplasmic reticulum. In consequence, it leads to an increase in INaCa (Figure 4.17b), increasing the probability of EADs generation.

A crucial caveat is that ICaL and INaCa are such highly interacting currents that it is generally fruitless to debate which one plays a more critical role to cause EADs. The correct viewpoint is that these two currents act synergistically to generate EADs, with their relative contributions varying under specific conditions. Thus, targeting either current alone may suffice to prevent EADs by suppressing their synergy.

4.5.4.7 IKr and ICaL conductances are the main determinant of APD prolongation

Earlier works by Sarkar and Sobie (2011) and Britton et al. (2013) showed that the expression level of IKr conductance plays a significant role on APD prolongation. In order to further support this result, we isolated a group of models that have baseline APD_{90} between 250–280 ms. Two sub-groups of small ΔAPD_{90} (< 15 ms) and large ΔAPD_{90} (> 60 ms) were then separated and the differences between ion conductances values were identified. For simplicity, we denote the first model subgroup as D_{small} and the second one as D_{large} . From Figure 4.18, we can observe

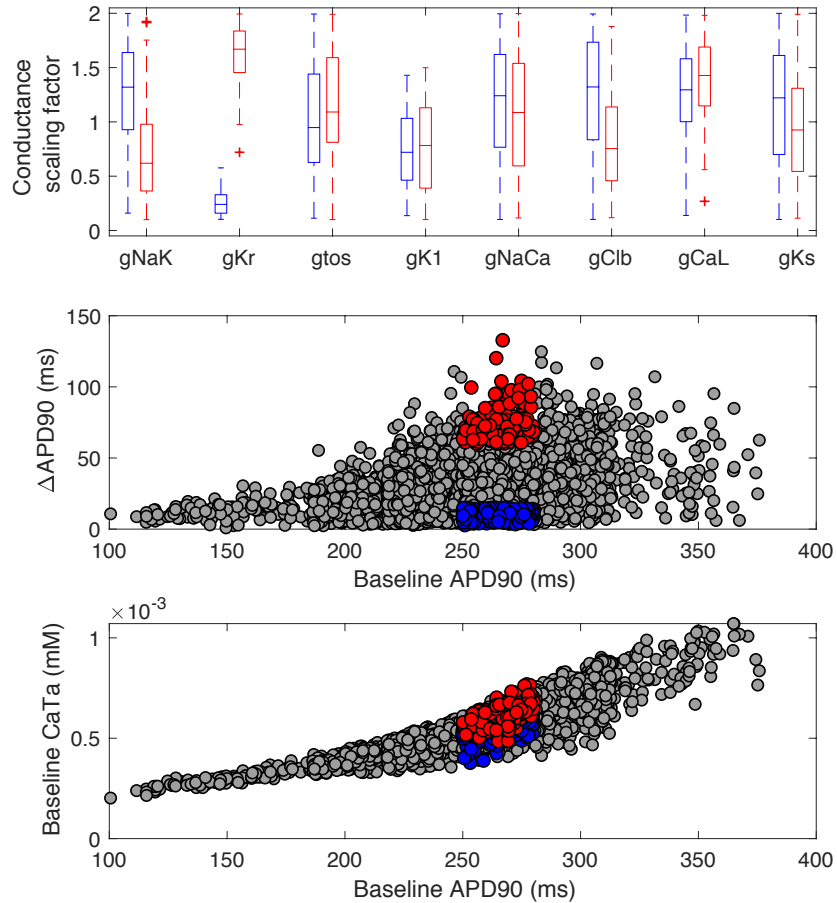


Figure 4.18: Small $\Delta APD90$ vs Large $\Delta APD90$. Top panel: Ion conductance differences in D_{large} (red) and D_{small} (blue). Both sub-groups of models have similar baseline APD90 between 250–280 ms. Middle panel: Distribution of baseline APD90 and $\Delta APD90$. Bottom panel: The corresponding calcium transient amplitude (CaTa) against baseline APD90. Data presented in this figure is for the Shannon model population only.

that models in D_{large} have larger gKr than D_{small} . Larger gKr may contribute to larger fractioning of IKr reduction, hence, lead to a larger APD prolonging effect.

Nevertheless, this is not strictly accurate because higher IKr may not necessarily result in more substantial APD prolongation. As observed in Figure 4.19, two sub-groups of models with different baseline APD90 and similar value of $\Delta APD90$ (< 20 ms) shows a different level of IKr conductance. For simplicity, we denote the first sub-group (models with APD90 between 180–210 ms) as A_{small} and the second sub-group (models with APD90 between 270–300 ms) as A_{large} . gKr in A_{small} appear to be larger than the other sub-group. Our first expectation is that models with a larger gKr would give a larger $\Delta APD90$. However, the effect is almost similar to the models with a smaller gKr, contradicting our earlier observation. This confirms that larger gKr does not always result in a more marked effect when IKr is blocked. It is possible that other

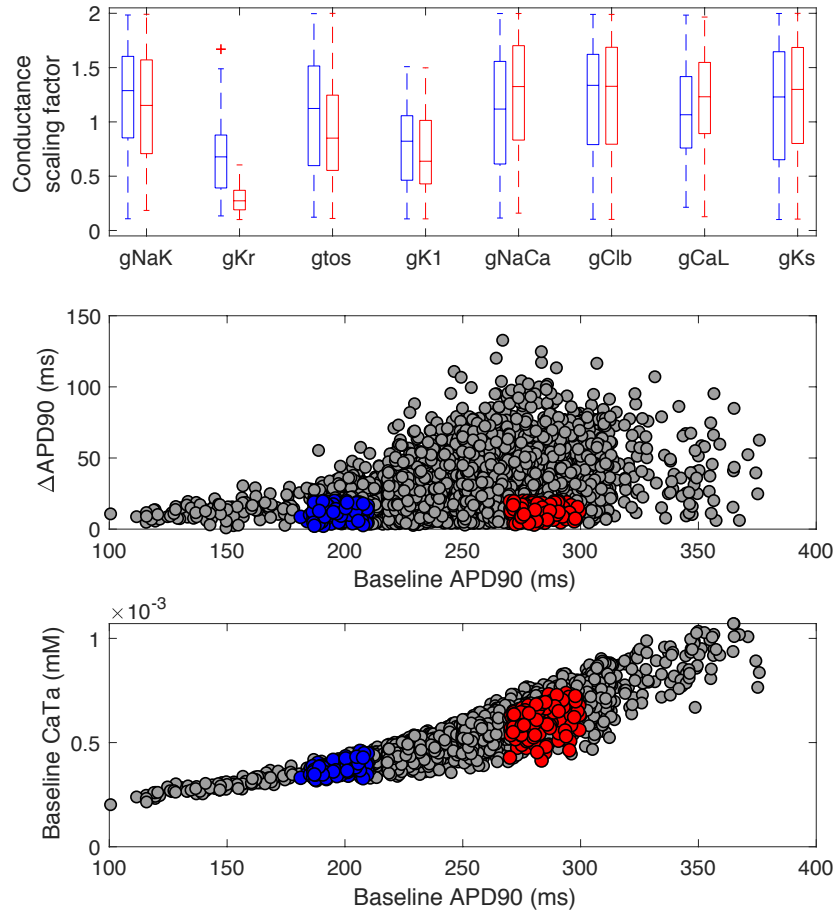


Figure 4.19: Small APD90 vs Large APD90. Top panel: Ion conductance differences in A_{large} (red) and A_{small} (blue). Both models sub-groups have Δ APD90 < 20 ms. Middle panel: Distribution of baseline APD90 and Δ APD90. Bottom panel: The corresponding Ca transient amplitude against baseline APD90.

than IKr conductance, level of calcium transient in the model may influence the APD prolonging effect.

From the bottom panel of Figure 4.18 and 4.19, we can see a strong correlation between baseline APD90 and Ca transient amplitude. Models with larger Ca transient amplitude are more likely to have a larger Δ APD90. We conclude that in order for a model to experience significant Δ APD90, both IKr conductance and Ca transient amplitude (modulated by ICaL expression) must be sufficiently large. If one of these criteria is not satisfied, the APD prolonging effect would be less significant. In extreme cases like hyper-responders, we can observe that both IKr conductance and Ca transient amplitude are larger than normal responders (see Figure 4.13 and 4.20). This offers an explanation for why no hyper-responders were observed in the model population of TenTusscher and Ohara. The TenTusscher model has sufficiently large ICaL current but small IKr current, whereas the Ohara model has the opposite characteristics (refer Figure

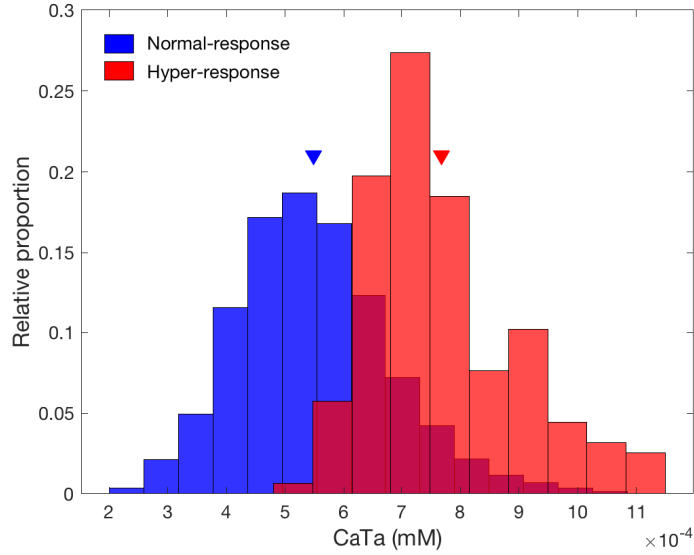


Figure 4.20: Distributions of calcium transient amplitude in normal responders (blue) and hyper-responders (red) of Shannon model population. The mean value of the normal responders distribution is $5.48 \pm 1.31 \times 10^{-4}$ mM and the mean value of the hyper-responders is $7.68 \pm 1.27 \times 10^{-4}$ mM, and the mean value locations are denoted by a triangle (\blacktriangledown).

AP biomarker	APA (mV)	RMP (mV)	APD90 (ms)
Control	134.88 ± 4.02	-85.47 ± 1.23	225.89 ± 56.10
ICaL block	132.90 ± 4.22	-85.86 ± 1.2	139.24 ± 38.96
CaT biomarker	CaTa (mM)	CaT90 (ms)	
Control	$(4.88 \pm 1.51) \times 10^{-4}$	331.93 ± 3.71	
ICaL block	$(2.53 \pm 0.62) \times 10^{-4}$	324.05 ± 5.80	

Table 4.4: Effects of L-type calcium block on AP and CaT biomarkers in the model population of Shannon. (Abbreviation : APA = AP amplitude, RMP = resting membrane potential, CaTa = CaT amplitude).

4.9a).

4.5.5 Response to L-type calcium block by nifedipine

To simulate the action of $1\mu\text{M}$ nifedipine on ventricular cells, we blocked 60% of the L-type calcium current and then observed the AP responses. Figure 4.21 shows some examples of simulated AP and calcium transient (CaT) traces before and after blocking the ICaL. APD was reduced, but there were no significant change in action potential amplitude and resting membrane potential (see also Table 4.4). Similarly, for CaT, the amplitude was reduced dramatically, but there was a small effect on calcium duration (CaT90). In all three AP models, the majority of the cell models in the population showed shortening in APD, in agreement with the experimental data and earlier clinical studies (Dangman and Hoffman 1980, Go et al. 2005).

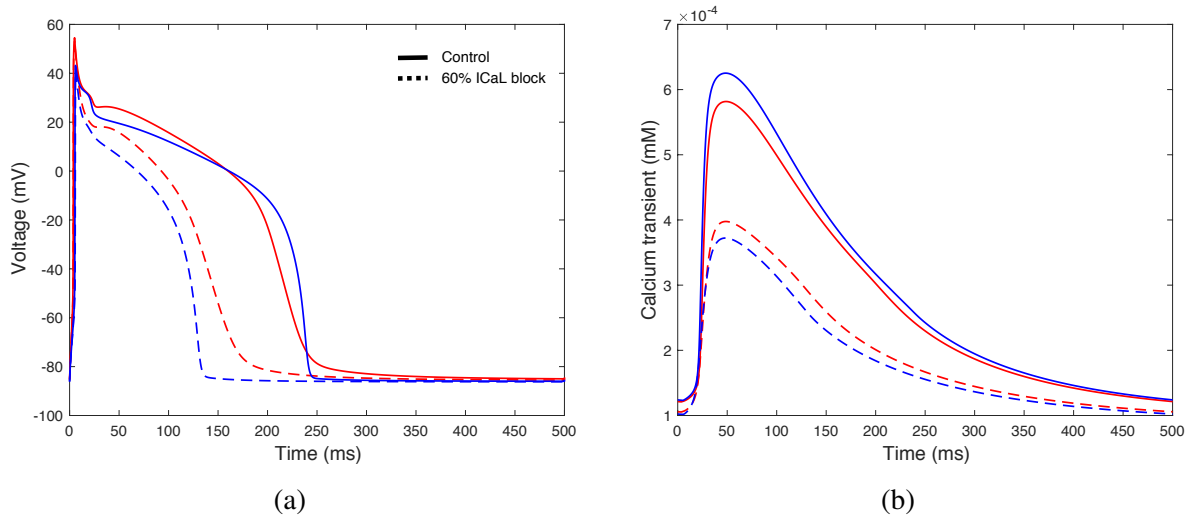


Figure 4.21: Two examples of simulated (a) AP and their corresponding (b) Ca transient traces obtained in control populations (solid line) and after 60% L-type calcium block (dashed line).

Figure 4.22 shows the distribution of degree of APD shortening against the baseline APD following ICaL block, for all three action potential models. From the figure, we can observe that the Shannon model makes a good overlap with the experimental data, in comparison to the TenTusscher and Ohara model. All models in the population experienced APD shortening when ICaL was reduced. Importantly, the model population exhibits a strong correlation between the baseline APD and Δ APD, highlighting the dependence of Δ APD on its starting AP. R^2 value is 0.53 in the Shannon model and 0.2 in the cell population. The degree of APD shortening gets large for larger baseline APD. The mean values of Δ APD between the model population of Shannon and experimental data have an excellent agreement.

On the other hand, the TenTusscher model looks to follow a similar pattern with experimental data. From Figure 4.22c, we can see that 75% out of TenTusscher model population have Δ APD from -75 to 0 ms. The drug effect is slightly underestimated compared to the mean response of the experimental data. Also, if we look closely, the model population produces a small gap at the centre of the distribution, where most of the cells concentrated at. The Ohara model, however, gives the poorest fit with the experimental distribution. The Ohara model population appear to have a uniform effect on APD, following the ICaL block (R^2 value is 0.067). The amount of APD shortening falls between -60 to 0 ms, with the mean of the distribution is shifted $\sim +65$ ms in the model distribution relative to experiments. We suspect this was due to low ICaL current magnitude (refer Figure 4.9a) in Ohara model, which prevented the models from exhibiting large Δ APD.

4.5.5.1 Larger calcium transient leads to larger drug effect

We have shown that blocking L-type calcium channels lead to APD shortening. A strong linear correlation was also displayed between baseline AP and Δ APD. We can hypothesise that models

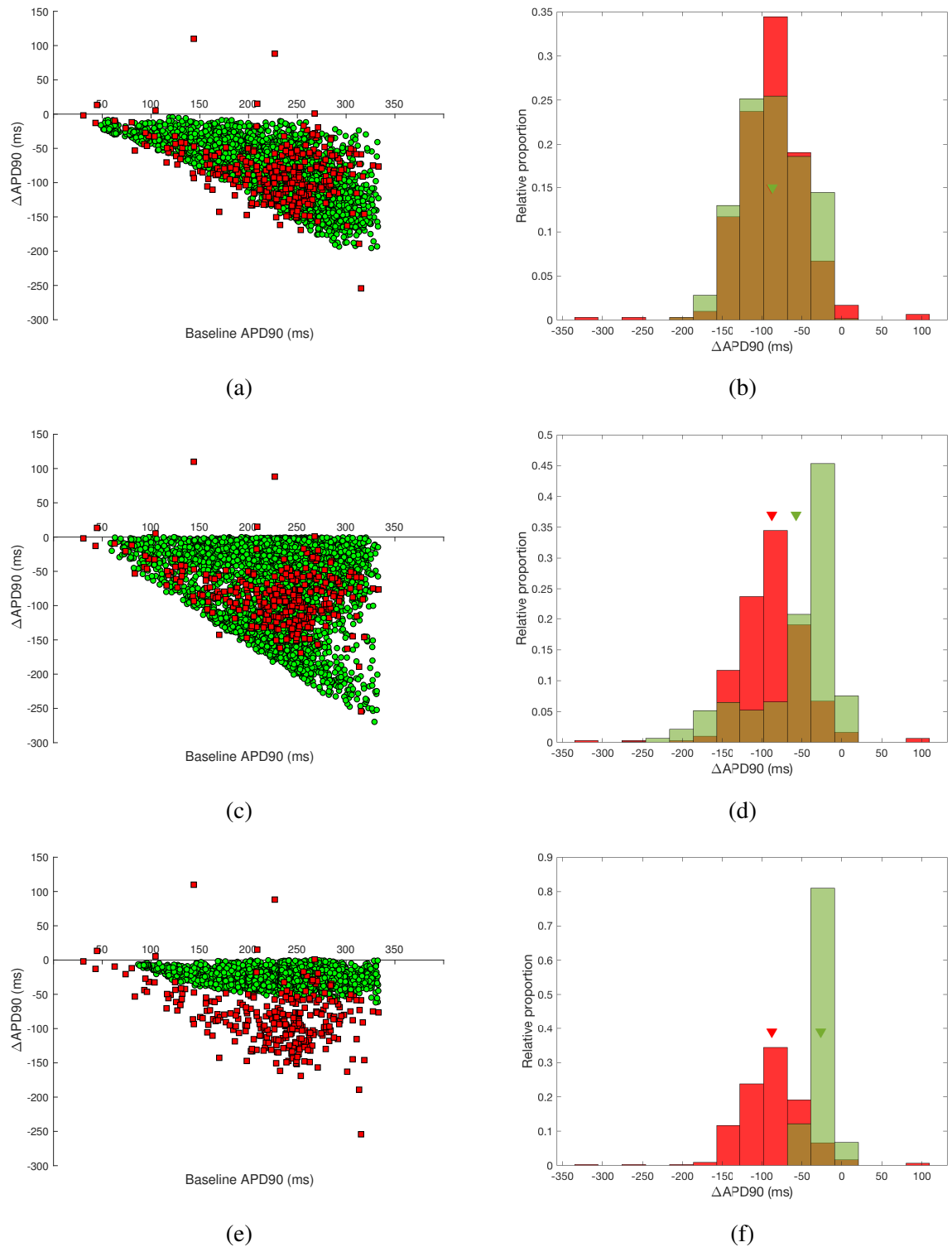


Figure 4.22: Scatter plot of net effect of 60% ICaL block on APD90 against baseline APD90 by individual cell models (paired), in comparison to experimental data (■). **(a)** is for the Shannon model, **(c)** is for the TenTusscher model and **(e)** is for the Ohara model ($P < 0.001$; paired t-test). **(b)**, **(d)**, **(f)** Histograms of the distribution of ΔAPD90 across the population of models, with mean value is marked as (▼). The mean and standard deviation of ΔAPD90 in each model are -86.7 ± 39.2 ms (Shannon), -56.8 ± 52.8 ms (TenTusscher), -21.3 ± 8.5 ms (Ohara), compared to experiment -87.3 ± 41.7 ms.

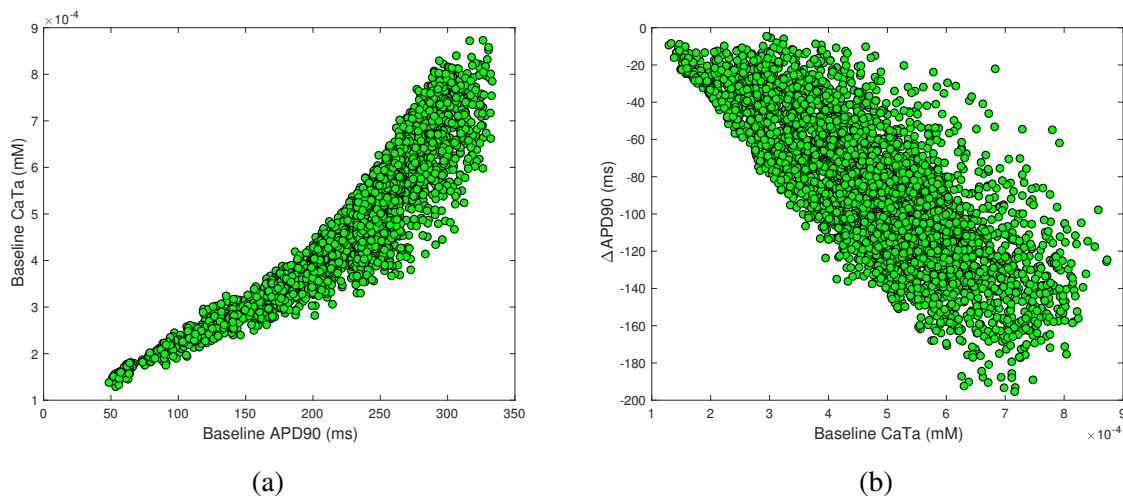


Figure 4.23: (a) Distribution of calcium transient amplitude, CaTa against baseline APD90 across the model population of Shannon. (b) Distribution of Δ APD90 against CaTa.

with small AP may have smaller calcium transients which then prohibited the AP from having a significant degree of Δ APD. To test our hypothesis, we measured the calcium transient amplitude across the model population of Shannon and compared them against voltage biomarkers. This is plotted in Figure 4.23. From the figures, we can see clearly that both baseline APD and Δ APD have a strong linear correlation with calcium transient amplitude. Models with small APD have smaller Ca transient, which then leads to a small Δ APD.

4.5.6 Adding noise to simulation data

All measurements are subjects to experimental errors and the observations we make are never precisely representative of the process we think we are observing. Mathematically speaking, this is conceptualised as,

$$a = \hat{a} \pm \varepsilon, \tag{4.8}$$

where a is the measured value, \hat{a} is the true value and ε is the experimental noise or error. The noise is a combined measure of the inherent variation in the phenomenon we are observing and the numerous factors that interfere with the measurement. In cellular biology, cells with identical genetics, even within similar tissue samples, are often observed to have different expression levels of proteins and structures. These apparently random differences could have significant biological and medical consequences.

Recordings of the transmembrane potential of rabbit ventricular myocytes in the experiment are modulated by the extrinsic noise, probably due to non-constant physical environment (temperature, pressure, etc). Also, the effect of channel blocks on APD (Figure 3.5a and 3.5a) was influenced slightly by the effect of DMSO. Mathematical models, however, are too deterministic

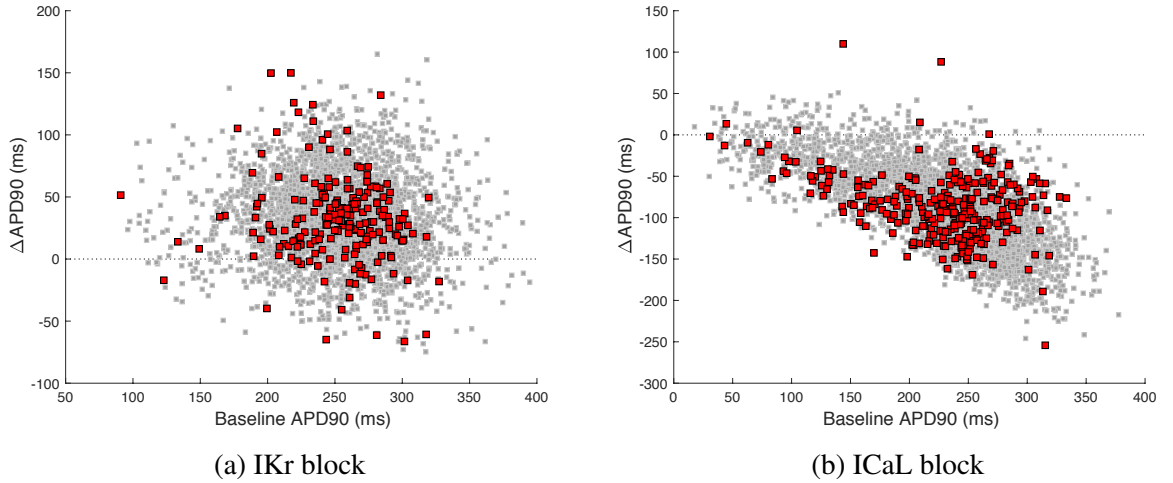


Figure 4.24: Scatter plot showing net effect of IKr and ICaL blocks on APD in the model population of Shannon after adding noise (grey), in comparison to experimental data (red).

and their outputs take no account of such noise. Hence, to replicate the noise seen in experimental measurements, we added an ‘artificial’ noise to our data using the following equation,

$$APD_{\text{exp}} \approx APD_{\text{predict}} = APD_{\text{model}} \pm \varepsilon. \quad (4.9)$$

We assumed that noise arises from an independent and identically distributed Gaussian noise ($X \sim \mathcal{N}(\mu, \sigma^2)$) with mean zero and $\sigma = 20$ ms. The value was chosen to compensate for similarly estimated errors in experimental measurements. The error was resulted due to the effect of DMSO. The DMSO is the chemical (commonly referred to as ‘vehicle’) that the drug had to be dissolved into, so that the drug could dissolve into the cells. Hence, the effect that we have seen in the measurements is due to the effect of the drug and DMSO, although DMSO mostly has a negligible effect on APD with mean value 0 ms. We only introduced the noise on the measurements of APD before and after the IKr/ICaL reduction, rather than to the entire AP trace. The ΔAPD was then measured. For this purpose, we only applied the noise on the Shannon model population.

Figure 4.24 shows the scatter net effect of IKr and ICaL blocks on APD after including the noise. For IKr block, we can see that the degree of APD prolongation has increased with a few models exhibited ΔAPD as large as 150 ms. This could not be achieved in the original model population (without the noise). Also, a sub-group of models experienced APD shortening (15.9% in the model population and 14.1% in the cell population). There is no significant correlation shown between baseline APD and APD difference. Mean value of ΔAPD in the model population remained consistent with the model population before the addition of artificial noise (33.65 ms vs 33.18 ms), but the range has increased from $\sigma = 20.26$ ms to $\sigma = 34.83$ ms. This value is comparable with ΔAPD shown in experiment (32.23 ± 34.46 ms).

For ICaL block, majority of the models experienced APD shortening, as seen in Figure 4.24b.

3.4% of the models in the population exhibited APD prolongation between 0–50 ms. The finding is in agreement with our cell populations which 2% of them experienced APD prolongation. Mean and standard deviation of Δ APD in model population and experiment are -87.3 ± 48.2 ms and -87.3 ± 41.7 ms, respectively.

4.6 Conclusion

In this study, we have investigated the underlying effects of action potential variability on the hERG and L-type calcium blocks. We compared closely experimental measurements and computational modelling of rabbit/human ventricular myocytes. Three different biophysically detailed AP models were considered in this work. They were a rabbit AP model by [Shannon et al. \(2004\)](#) and two human AP models by [Ten Tusscher et al. \(2004\)](#) and [O’Hara et al. \(2011\)](#). Population of models from randomly generated parameter sets were constructed by varying several ionic channel conductances in the respective model. The outcome of each model in predicting the effect of channel blocks was compared to each other and experimental data.

When constructing a population of models without experimental evidence for the extent of variability in parameters, the choice of level of parameter variation to sample is wide open. Our data showed that a large parameter space (0.1–2x baseline value) was required to cover the variability level shown in the experimental measurements. We initially considered smaller parameter ranges ($\pm 30\%$ and $\pm 50\%$), but obtained results that implied such variation levels were insufficient to explain the experimental data (Figure 4.5b and A.1). This suggested that a larger variation in these cell properties was needed. Moreover, an important key point in our study also demonstrated that variation in 8 ionic currents expression and the action potentials were sufficient to explain the data we have seen experimentally without the need of adding other biomarkers, for example, the biomarkers from calcium transient.

In addition, our results demonstrated that a viable AP can be generated by a wide variety of different balances of ionic currents (Figure 4.8). In an earlier work by [Banyasz et al. \(2011\)](#), they showed that there exists large variation in the magnitude of ionic currents between the guinea pig ventricular cells, with the peak of I_{CaL} and I_{Ks} exhibited coefficient of variation (std. dev/mean*100) approximately 45% and 70%, respectively. This variation is considerably large as number of cells used in the study was relatively small (5–6 cells). The finding is comparable with our own which the Shannon model population showed large variation in g_{CaL} (35%) and g_{Ks} (50%).

In most previously published work, calibration of a population of models was typically performed by making sure that all relevant models fall within the ranges of data ([Britton et al. 2013](#)). For a low and limited number of experimental samples, this approach is perfectly reasonable, with the restriction that some information inherent in the data may not be fully captured. Therefore, we have considered the data distribution as part of the calibration criterion

to improve the outcome of model population. We believe the calibration procedure used here is better and allowed us to estimate the underlying distribution of outputs represented by the data.

We understand the calibration technique we used to construct the control population is quite simplistic compared to more advanced methods such as implemented by [Lawson et al. \(2018\)](#), but it was able to match the AP biomarker distributions. Our results showed that not all models could match the experimental distribution under control condition (Figure 4.6). The baseline Shannon model exhibited shorter AP amplitude compared to the experimental recording which then lead to disagreement in APD30. Both the TenTusscher and Ohara models showed a good overlap with the experimental measurements of AP biomarkers. We then demonstrated the capacity of these model populations to predict variability in the response to drug blocking of hERG and L-type calcium channels. Among the three models, the Shannon model exhibited the most reliable correspondence with the experimental data, highlighting the importance of careful model selection in computational studies. The undesirability of relying on model output alone without recourse to experimental data was also apparent.

Our finding showed that how different models may produce different responses to IKr and ICaL blocks. For IKr block, the degree of APD prolongation was not homogenous across the model population. There was no strong correlation shown between drug effect and the baseline AP. A curious feature was the sub-group of models with extreme APD prolongation (hyper-responder), despite having the same baseline as normal responders. The reason behind this sub-population was that these models have both large IKr and ICaL expressions which could lead to bigger fractioning of IKr reduction, hence increase the degree of Δ APD. During IKr block, predomination of inward current by ICaL also prohibited the membrane potential from repolarizing, which then lead to an extreme long plateau. In addition, EADs generation was also seen in our computational model in response to IKr block. No EADs was observed in the experimental measurements. The explanation for this observation probably lies in the stimulation rate used in this study; EADs were more common when cells were stimulated at low frequency ([Guo et al. 2011](#), [Nalos et al. 2012](#)). Interestingly, we did not see hyper-response or EADs in the TenTusscher and Ohara model following IKr block. We suspected that these behaviours could only be seen in Shannon model due to high ICaL and INaCa presented in the model (Figure 4.9a). It is well known that these two ionic currents are responsible for EADs generation ([Qu et al. 2013](#), [Weiss et al. 2010](#)).

Contrasting the above, blockade of L-type calcium channels produced a baseline dependent AP shortening, and our computational models (except the Ohara model) displayed a linear correlation between baseline AP and drug effect. Models with small AP showed the smallest amount of APD shortening, compared to large AP. The cause was that these models have smaller calcium transients amplitude (Figure 4.23), which directly reduced the fractional shortening. In turn, cell models with larger calcium amplitude may exhibit wider range of Δ APD.

Part III

Analysis of a simplified model of the cardiac action potential

In the previous chapter, we used several complex models of cardiac action potential to study the AP variability and effects of ion channel blocks. This model, however, is extremely complicated due to their large parameters and variables included in the model, which may lead to parameter unidentifiability and dissimilarity in predictions (as shown in Chapter 4), even between models of similar cell type (Wilhelms et al. 2013). This makes the process of understanding the relationship between models output and model parameters more complicated, suggesting a need for a simple and robust model of cardiac action potential. In the upcoming chapters, we move from studying realistic models of action potential to studying a simpler conceptual model.

Chapter 5

The caricature Noble model

In this chapter, we provide a brief introduction to a simplified model of action potential and discuss the reason for choosing this model in our work. The model is the modified version of the caricature Noble model. We then describe the model formulations and then solve the model as initial and boundary value problem. The exact analytical solutions are derived and validated with numerical solutions. Next, we present the asymptotic solutions of the model, including both fast subsystem and slow subsystem. These asymptotic solutions will be further exploited to develop an asymptotic-numerical method in Chapter 6 and investigate the mechanism of cardiac alternans in Chapter 7. Finally, the phase portrait of the caricature Noble model and the criteria needed for the AP excitation are discussed. The material included in this chapter mostly follows results previously published in the literature for the caricature Noble model. These results are cited as appropriate within the sections below and are then applied to the modified version of the caricature Noble model.

5.1 Introduction

Caricature Noble model is a simplified model of the electrical potential of cardiac cell membranes, and the model is an accurate approximation of the classical cardiac Purkinje fibres model by Noble (1962). As mentioned in Chapter 2.5, Noble (1962) model is the first cardiac action potential model which is used as the prototype for other modern voltage-gated cardiac models. Biktashev et al. (2008) then used the model as the starting point, due to its simple functional forms, to construct the caricature Noble model by using a set of verifiable simplification steps. As a result, the caricature Noble model can be considered as a detailed ionic model because the model preserves the generic properties of cardiac excitability, such as slow repolarization, slow subthreshold response and fast accommodation (Biktashev et al. 2008). The model is also amenable to analytical works which allow an exact solution. The small parameters embedded in the model has allowed the system to be reduced asymptotically that can potentially be exploited for various purposes, for instance, derivation of action potential restitution curves and conduction

of velocity dispersion curves. Unlike most other simplified action potential models such as Fitzhugh-Nagumo model, Mitchell and Schaeffer model, Rogers and McCulloch model, Barkley model and Fenton and Karma model which fail to reproduce qualitative features of a cardiac action potential, caricature Noble model is more realistic and preserve the fundamental structures of an action potential.

The model itself has been further used to derive asymptotic expressions for the conduction velocity restitution in cardiac tissues (Simitev and Biktashev 2011), to elucidate the conditions for propagation and block of excitation in the atria (Simitev and Biktashev 2006), to understand the formation of excitation waves (Bezekci et al. 2015) and to study cellular alternans (Asgari-Targhi 2017). In line with those compelling results, we want to extend the analysis of this model by utilizing the model for various applications and analytical works.

5.2 Model formulation

The authentic caricature Noble model was formulated by Biktashev et al. (2008). The model includes three state variables, the transmembrane voltage potential $E(t)$, and the two gating variables $h(t)$ and $n(t)$ describing the inactivation of the fast inward and slow outward currents, respectively, coupled by the non-linear ordinary differential equations. The model equations are,

$$\frac{dE}{dt} = -(I_{Na} + I_K + I_{leak}) \quad (5.1a)$$

$$\frac{dh}{dt} = \frac{1}{\epsilon_1 \epsilon_2} F_h \cdot [H(E_{\dagger} - E) - h], \quad (5.1b)$$

$$\frac{dn}{dt} = F_n(E) \cdot [H(E - E_{\dagger}) - n], \quad (5.1c)$$

where $H(\cdot)$ is the Heaviside step function. $h(t)$ and $n(t)$ represent the closing and opening of the respective ion channels and ranging between 0 and 1. The caricature Noble model incorporates three different ionic currents which were formulated from Hodgkin-Huxley model. The ionic currents are sodium current, potassium current and a leak current which are formulated as follows,

$$I_{Na} = -\frac{1}{\epsilon_1 \epsilon_2} G_{Na} \cdot (E_{Na} - E) \cdot H(E - E_*) \cdot h, \quad (5.2a)$$

$$I_K = -\frac{g_2(E) \cdot n^4}{\epsilon_2}, \quad (5.2b)$$

$$I_{leak} = -\frac{G(E)}{\epsilon_2}. \quad (5.2c)$$

In the thesis (Chapter 5–7), we consider a modified version of caricature Noble model where the fourth order of variable n in equation (5.2b) is replaced by linear term in n as follows,

$$n^4 \rightarrow n. \quad (5.3)$$

The linearity is introduced in order to obtain a model with simpler analytical solutions. While the replacement of n^4 by n^1 is an arbitrary step, we will demonstrate that for appropriately selected parameter values the modified caricature Noble model behaves similarly to the original caricature Noble model. The parameter values used in the model remain similar as listed in Table 5.1. The other functions in the model are formulated as below,

$$\begin{aligned} g_2(E) &= g_{21}H(E_{\dagger} - E) + g_{22}H(E - E_{\dagger}), \\ E_2 &= (k_1/k_2 + 1)E_{\dagger} - E_1k_1/k_2, \\ E_3 &= (k_2/k_3 + 1)E_* - E_2k_2/k_3, \\ F_n(E) &= f_n [rH(E_{\dagger} - E) + H(E - E_{\dagger})], \\ G(E) &= \begin{cases} k_1(E_1 - E), & E \in (-\infty, E_{\dagger}), \\ k_2(E - E_2), & E \in [E_{\dagger}, E_*], \\ k_3(E_3 - E), & E \in [E_*, +\infty). \end{cases} \end{aligned} \quad (5.4)$$

In addition, we provide a CellML code (is available on GitHub¹) of the model which can be readily employed within various simulation tools.

5.3 Exact solutions

5.3.1 Solution of the initial value problem

It is possible to find an exact analytical solution of the modified caricature Noble model following the method of Biktashev et al. (2008) used for the original caricature Noble model. The equations (5.1b) and (5.1c) in the model are separable and fairly simple to be solved. The solutions of these two ordinary differential equations (ODEs) are then substituted into the voltage equation (5.1a) and it becomes a first order linear ODE. Consider the following initial conditions for respective variables,

$$E(0) = E_{\text{stim}} > E_*, \quad h(0) = h_0, \quad n(0) = n_0, \quad (5.5)$$

and natural continuity conditions at the ends of the three intervals separated by E_{\dagger} and E_* . The exact analytical solutions of the system (5.1) can be formulated as follows,

¹<https://github.com/hifzhudin/CaricNobleModel>

Parameters	Default
ε_1 (dimensionless)	1.0
ε_2 (dimensionless)	1.0
G_{Na} (mS/ μ F)	100/3
E_{Na} (mV)	40.0
E_{\dagger} (mV)	-80.0
E_* (mV)	-15.0
k_1 (dimensionless)	0.075
k_2 (dimensionless)	0.04
k_3 (dimensionless)	0.10
E_1 (mV)	-280/3
f_n (dimensionless)	0.0037
F_h (dimensionless)	0.5
g_{21} (mS/ μ F)	-2.0
g_{22} (mS/ μ F)	-4.0
r (dimensionless)	1.0

Table 5.1: Parameter values used in the modified caricature Noble model.

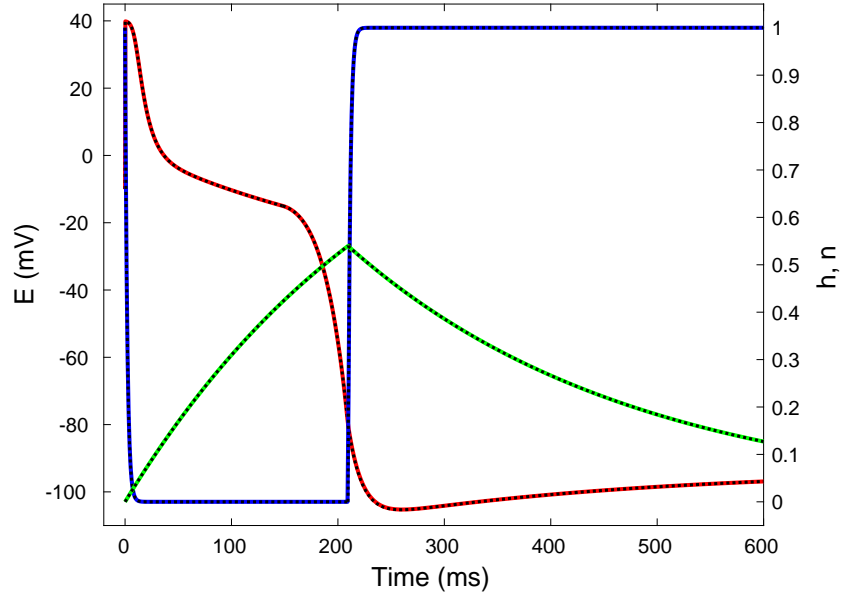


Figure 5.1: The exact analytical solutions (solid line) derived in (5.6) in comparison to numerical solutions (dotted line) for $t \in [0, 600]$. For numerical solutions, the model was solved using explicit Euler scheme with time step 0.005. The red, blue and green line correspond to variable E , h and n , respectively. The initial conditions used were $E(0) = -10$, $h(0) = 1$ and $n(0) = 0$. Parameter values used are as listed in Table 5.1.

$$n(t) = \begin{cases} n^1(t) = 1 - (1 - n_0) \exp(-f_n t), & t \in [0, t_{\dagger}] \\ n^2(t) = (1 - (1 - n_0) \exp(-f_n t_{\dagger})) \exp(f_n r(t_{\dagger} - t)), & t \in [t_{\dagger}, \infty] \end{cases} \quad (5.6a)$$

$$h(t) = \begin{cases} h^1(t) = h_0 \exp(-F_h t / (\varepsilon_1 \varepsilon_2)), & t \in [0, t_{\dagger}] \\ h^2(t) = 1 - (\exp(F_h t_{\dagger} / (\varepsilon_1 \varepsilon_2)) - h_0) \exp(-F_h t / (\varepsilon_1 \varepsilon_2)), & t \in [t_{\dagger}, \infty] \end{cases} \quad (5.6b)$$

$$E(t) = \begin{cases} E^1(t) = \exp\left[\frac{G_{Na} h_0}{F_h} \exp\left(-\frac{F_h}{\varepsilon_1 \varepsilon_2} t\right) - \frac{k_3}{\varepsilon_2} t\right] \times \left\{ E_0 \exp\left(-\frac{G_{Na} h_0}{F_h}\right) \right. \\ \quad \left. - (k_3 E_3 + g_{22}) u(\varepsilon_1 k_3, t) + g_{22} (1 - n_0) u(k_3 \varepsilon_1 - f_n \varepsilon_1 \varepsilon_2, t) \right. \\ \quad \left. - \frac{G_{Na} E_{Na} h_0}{\varepsilon_1} u(\varepsilon_1 k_3 - F_h, t) \right\}, & t \in [0, t_*] \\ E^2(t) = w(t) + [E_* - w(t_*)] \exp\left((t - t_*) \frac{k_2}{\varepsilon_2}\right), & t \in [t_*, t_{\dagger}] \\ E^3(t) = v(t) + [E_{\dagger} - v(t_{\dagger})] \exp\left(\frac{k_1}{\varepsilon_2} (t_{\dagger} - t)\right) & t \in [t_{\dagger}, \infty] \end{cases} \quad (5.6c)$$

where

$$u(\varkappa, t) = \frac{\varepsilon_1}{F_h} \left(\frac{G_{Na} h_0}{F_h}\right)^{-\varkappa/F_h} \left[\Gamma\left(-\frac{\varkappa}{F_h}, \frac{G_{Na} h_0}{F_h}\right) - \Gamma\left(-\frac{\varkappa}{F_h}, \frac{G_{Na} h_0}{F_h} \exp\left(-\frac{F_h}{\varepsilon_1 \varepsilon_2} t\right)\right) \right], \quad (5.7a)$$

$$w(\lambda) = E_2 - \frac{g_{22}}{k_2} + \frac{g_{22}(1 - n_0)}{k_2 + \varepsilon_2 f_n} \exp(-f_n \lambda), \quad (5.7b)$$

$$v(\lambda) = E_1 + \frac{g_{21}(1 - (1 - n_0) \exp(-f_n t_{\dagger}))}{k_1 - \varepsilon_2 f_n r} \exp(f_n r(t_{\dagger} - \lambda)), \quad (5.7c)$$

and $\Gamma(a, z)$ is the upper incomplete gamma function,

$$\Gamma(a, z) = \int_z^{\infty} e^{-x} x^{a-1} dx, \quad (5.8)$$

for $Re(z) > 0$ as defined in [Abramowitz and Stegun \(1965\)](#). The comparison between exact analytical and numerical solutions are shown in [Figure 5.1](#). From the Figure, we can see a good overlap between analytical and numerical solutions, indicating the accuracy of the derived analytical solutions. In comparison to the solutions of authentic caricature Noble model, the solutions derived using the modified model is shorter. In particular, a few terms in the solution of $E^1(t)$ are eliminated because of the linearity in the n variable. The solutions of h and n are remained similar.

Similar approach can also be used to obtain the solutions for different AP responses i.e. for

slow over-threshold and sub-threshold responses. The slow over-threshold response is the case when the initial value of the voltage is larger than the threshold value of the slow-system (5.16) but smaller than E_* such that $E_2 < E_{\text{stim}} < E_*$. The AP evolution described using the slow-system is without the fast upstroke as the sodium current modulated by h -gating is not activated. The latter response is when the initial value of E is smaller than the threshold value of the slow-system (5.16) i.e. $E_{\text{stim}} < E_2$. In this case, the voltage will just decays towards its global equilibrium. The analytical solutions for these two responses using the original caricature Noble model can be found in [Asgari-Targhi \(2017\)](#).

5.3.2 Solution of the boundary value problem

Next, we derive the solution of the boundary value problem (BVP) for the modified caricature Noble model. The BVP is relevant in cases when we model periodic solutions excited by a periodic stimulus train. This generates a continuous identical AP waveform when the model is excited because the initial conditions for each variable are not changed throughout the stimulation period. In this case, we set the boundary conditions as follows,

$$E(0) = E(t = B) = E_{\text{stim}} > E_*, \quad h(0) = h(t = B), \quad n(0) = n(t = B), \quad (5.9)$$

where B is the basic cycle length. Solutions of the BVP for the original caricature Noble model are given in [Asgari-Targhi \(2017\)](#). Here we follow the same procedure to derive the corresponding solutions for the modified model. By imposing the above boundary conditions (5.9), the particular

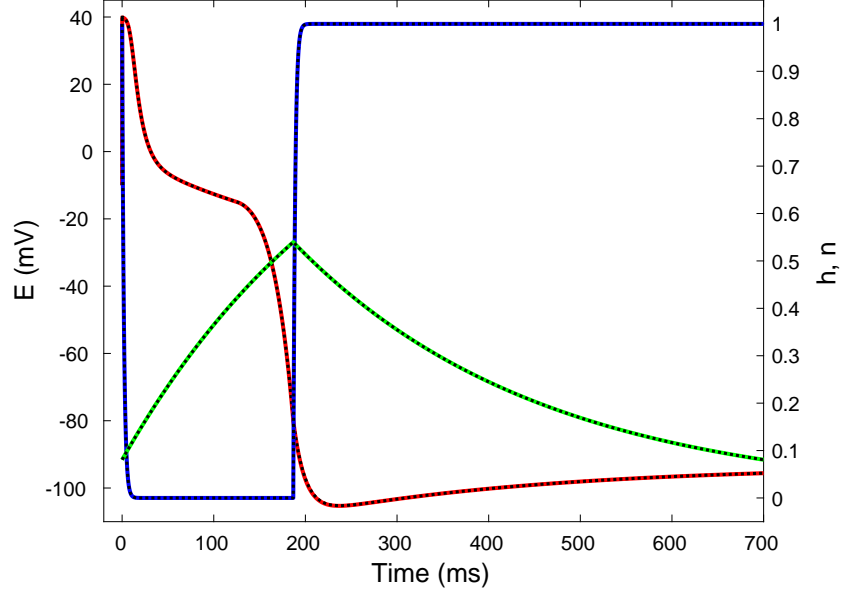


Figure 5.2: The exact analytical solutions (solid line) derived in (5.10) in comparison to numerical solutions (dotted line) for $B = 700$ ms. The red, blue and green line correspond to variable E , h and n , respectively. Parameter values used are as listed in Table 5.1

solutions are as follows,

$$n(t) = \begin{cases} \overset{1}{n}(t) = 1 - C_1 \exp(-f_n t), & t \in [0, t_{\dagger}] \\ \overset{2}{n}(t) = \left(1 - C_1 \exp(-f_n t_{\dagger})\right) \exp(f_n r(t_{\dagger} - t)), & t \in [t_{\dagger}, \infty] \end{cases} \quad (5.10a)$$

$$h(t) = \begin{cases} \overset{1}{h}(t) = D_1 \exp(-F_h t / (\varepsilon_1 \varepsilon_2)), & t \in [0, t_{\dagger}] \\ \overset{2}{h}(t) = 1 - \left(\exp(F_h t_{\dagger} / (\varepsilon_1 \varepsilon_2)) - D_1\right) \exp(-F_h t / (\varepsilon_1 \varepsilon_2)), & t \in [t_{\dagger}, \infty] \end{cases} \quad (5.10b)$$

$$E(t) = \begin{cases} \overset{1}{E}(t) = \exp\left[\frac{G_{Na} D_1}{F_h} \exp\left(-\frac{F_h}{\varepsilon_1 \varepsilon_2} t\right) - \frac{k_3}{\varepsilon_2} t\right] \times \left\{E_0 \exp\left(-\frac{G_{Na} D_1}{F_h}\right) - (k_3 E_3 + g_{22})u(\varepsilon_1 k_3, t) + g_{22} C_1 u(k_3 \varepsilon_1 - f_n \varepsilon_1 \varepsilon_2, t) - \frac{G_{Na} E_{Na} D_1}{\varepsilon_1} u(\varepsilon_1 k_3 - F_h, t)\right\}, & t \in [0, t_*] \\ \overset{2}{E}(t) = w(t) + [E_* - w(t_*)] \exp\left((t - t_*) \frac{k_2}{\varepsilon_2}\right), & t \in [t_*, t_{\dagger}] \\ \overset{3}{E}(t) = v(t) + [E_{\dagger} - v(t_{\dagger})] \exp\left(\frac{k_1}{\varepsilon_2} (t_{\dagger} - t)\right) & t \in [t_{\dagger}, \infty] \end{cases} \quad (5.10c)$$

where

$$C_1 = \left(1 - \exp(f_n r(t_{\dagger} - B))\right) / \left(1 - \exp((-f_n t_{\dagger}) - f_n r(B - t_{\dagger}))\right), \quad (5.11a)$$

$$D_1 = \left(1 - \exp\left(\frac{F_h(t_{\dagger} - B)}{\varepsilon_1 \varepsilon_2}\right)\right) / \left(1 - \exp\left(\frac{-F_h B}{\varepsilon_1 \varepsilon_2}\right)\right), \quad (5.11b)$$

$$u(\varkappa, t) \equiv \frac{\varepsilon_1}{F_h} \left(\frac{G_{Na} D_1}{F_h}\right)^{\frac{\varkappa}{F_h}} \left[\Gamma\left(-\frac{\varkappa}{F_h}, \frac{G_{Na} D_1}{F_h}\right) - \Gamma\left(-\frac{\varkappa}{F_h}, \frac{G_{Na} D_1}{F_h} \exp\left(-\frac{F_h t}{\varepsilon_1 \varepsilon_2}\right)\right) \right], \quad (5.11c)$$

$$w(\lambda) = E_2 - \frac{g_{22}}{k_2} + \frac{g_{22} C_1}{k_2 + \varepsilon_2 f_n} \exp(-f_n \lambda), \quad (5.11d)$$

$$v(\lambda) = E_1 + \frac{g_{21}(1 - C_1 \exp(-f_n t_{\dagger}))}{k_1 - \varepsilon_2 f_n r} \exp(f_n r(t_{\dagger} - \lambda)). \quad (5.11e)$$

We now have the exact solutions of the equations (5.1) as a function of B . The solutions are plotted in Figure 5.2 for $B = 700$ ms and they are compared with numerical solutions. For the numerical solutions, the modified caricature Noble model was solved using ‘dsolve’ command in Maple 18 with the numeric option for the ODE system boundary value problem. Notice that the gating variables reach its initial value after one basic cycle length. If another AP is excited, then a similar AP waveform will be produced as the initial values of the gating variables are as same as the previous one.

5.4 Asymptotic solutions

Taking the limit of $\varepsilon_1, \varepsilon_2 \rightarrow 0^+$, the modified caricature Noble model can be dissected into asymptotically reduced systems, which then provide much insight into the dynamics of the full model. The derivation of the asymptotic solutions of this model are explained in the following subsections. The method used to derive the asymptotic solutions is similar as published in [Biktashev et al. \(2008\)](#).

5.4.1 Superfast-time system

We assume that our original system has a multiple timescales and consider a ‘super-fast’ timescale T which is $T = t/(\varepsilon_1 \varepsilon_2)$. The time t is stretched into super-fast timescale T as the $\varepsilon_1 \rightarrow 0$. From the chain rule of differential equation, we have

$$\frac{d}{dt} = \frac{1}{\varepsilon_1 \varepsilon_2} \frac{d}{dT}. \quad (5.12)$$

Substitute the above expression into (5.1) and taking the limit of $\varepsilon_1 \rightarrow 0$, we obtain the essential dynamical variables of E and h ,

$$\frac{dE}{dT} = G_{Na}(E_{Na} - E)H(E - E_*)h, \quad (5.13a)$$

$$\frac{dh}{dT} = F_h(H(E_{\dagger} - E) - h). \quad (5.13b)$$

n is reduced to $dn/dT = 0$. This system describes the fast upstroke of the action potential. Solving the above system (5.13), we can derive the explicit asymptotic solutions for this stage which are,

$$E = E_{Na} - (E_{Na} - E_0) \exp\left(\frac{G_{Na}}{F_h}(e^{-F_h T} - 1)\right), \quad (5.14a)$$

$$h = \exp^{-F_h T}, \quad (5.14b)$$

where $E_0 = E_{\text{stim}}$ is the initial condition for variable E . The maximal overshoot voltage, E_{max} is obtained as the fast time T goes to infinity,

$$E_{\text{max}} = E_{\infty} = \lim_{T \rightarrow \infty} E(T) = E_{Na} - (E_{Na} - E_0) \exp\left(-\frac{G_{Na}}{F_h}\right). \quad (5.15a)$$

Since $\exp(-G_{Na}/F_h) \approx 10^{-29}$, the maximal overshoot voltage E_{max} is extremely close to E_{Na} . The $h(T) = 0$ as T tends to infinity.

5.4.2 Slow-time system

The slow-time system is obtained by directly taking the limit of $\varepsilon_1 \rightarrow 0$ in (5.1). By doing this, we have $h(t) = H(E_{\dagger} - E)$. Substituting this into equation (5.1a) will eliminate the first term and left us with a reduced system as following,

$$\frac{dE}{dt} = \frac{1}{\varepsilon_2} \left(g_2(E)n + G(E) \right), \quad (5.16a)$$

$$\frac{dn}{dt} = F_n(E) (H(E - E_{\dagger}) - n). \quad (5.16b)$$

This system describes the post-overshoot drop, plateau and recovery stages of the action potential. The slow-time system can be further asymptotically split into two systems discussed below.

5.4.2.1 Fast-slow-time subsystem

Consider the ‘fast-slow’ timescale $t \sim \varepsilon_2$, or equivalently $\tau \sim (\varepsilon_2)^{-1}$, which is $\tau = t/\varepsilon_2$. The time t is stretched into fast-slow timescale τ as the $\varepsilon_2 \rightarrow 0$. Using the chain rule of differential

equation as previous, we obtain,

$$\frac{d}{dt} = \frac{1}{\varepsilon_2} \frac{d}{d\tau}. \quad (5.17)$$

We then substitute the expression into (5.16) and take the limit of $\varepsilon_2 \rightarrow 0$ to yield,

$$\frac{dE}{d\tau} = g_2(E)n + G(E), \quad (5.18a)$$

$$\frac{dn}{d\tau} = 0. \quad (5.18b)$$

The system above describes the post-overshoot drop and the repolarisation stages of the action potential.

5.4.2.2 Slow-slow-time subsystem

The slow-slow time subsystem is obtained directly from equations (5.16) by taking the limit of $\varepsilon_2 \rightarrow 0$. The system is described below,

$$0 = g_2(E)n + G(E), \quad (5.19a)$$

$$\frac{dn}{dt} = F_n(E) (H(E - E_{\dagger}) - n). \quad (5.19b)$$

This system describes the plateau and the recovery stages of the action potential. We will further extend the results of these asymptotic structures to develop a robust asymptotic-numerical method (Chapter 7) and to understand the mechanism of cardiac alternans (Chapter 8), respectively.

5.5 Phase plane analysis

Phase plane analysis is closely related to the asymptotic analysis we discussed above. It is a graphical tool for visualising how the solutions of a given system of differential equations would behave in the long run with respect to a set of initial conditions. The phase plane can help us to provide several important pieces of information such as

- providing motion trajectories corresponding to various initial conditions,
- examining the qualitative features of the trajectories,
- checking the stability of the equilibrium points of the system.

In addition, one can also explore the behaviour of a nonlinear system from various initial conditions without the need of solving the equations analytically. However, the phase plane method is most easily applicable to the second-order system as for higher-order the graphical representation can be computationally and geometrically complex.

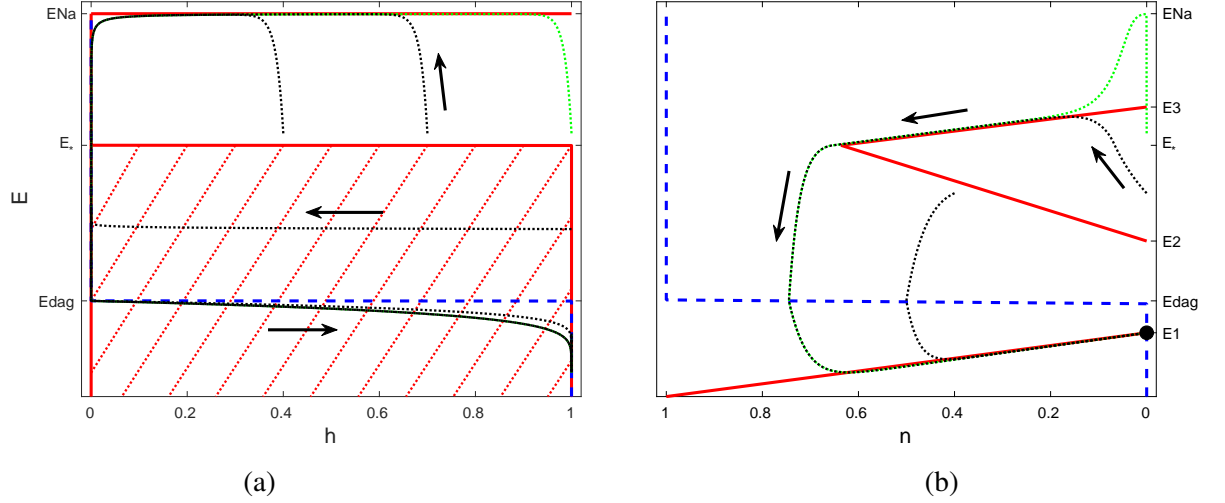


Figure 5.3: The phase portrait of the (a) fast-time subsystem and the (b) slow-time subsystem of modified caricature Noble model. Blue dashed line is the nullcline of $h(t)$ in (a) and $n(t)$ in (b). The solid red lines and the cross-hatched region in (a) and (b) are the nullclines of $E(t)$. Dotted black lines with attached arrows are the trajectories. Dotted green line is the corresponding action potential. The black dot point in (b) is the equilibrium point of the slow subsystem. Abbreviation : $E_{dag} = E_{\dagger}$.

Consider a first order vector-matrix system, $\mathbf{x}' = \mathbf{f}(\mathbf{x}(t))$, $\mathbf{x} \in \mathfrak{R}^2$, for each initial condition, $\mathbf{x}_0 = (x_0, y_0)$ there corresponds a unique solution $\mathbf{x}(t) = (x(t), y(t))$, represented a parametric curve in xy -plane. The parametric curve is called a trajectory of the system. In order to understand how the trajectories behave in a phase plane, we need to construct the nullclines. The nullcline is a set of points in the phase plane such that $d\mathbf{x}/dt = 0$. Algebraically, we find the nullcline by solving $\mathbf{f}(\mathbf{x}(t)) = 0$ and the intersections between the nullclines on a xy -plane are the equilibrium points. A point is called an equilibrium point of the system when the solutions are not changing and they stay in their initial state forever.

5.5.1 Phase plane of modified caricature Noble model

To explain the phase plane of modified caricature Noble model, we follow the analysis published in [Biktashev et al. \(2008\)](#) and [Simitev and Biktashev \(2011\)](#). We use the fast and slow-time asymptotic presented in the previous section. We first find the nullclines of the fast-time system, by setting the equations (5.13a) and (5.13b) to $dE/dT = 0$ and $dh/dt = 0$, respectively. Solving the right hand side of these equations, we have the nullclines of the fast-time subsystem as below,

$$H(E - E_*) = 0, \quad E = E_{Na}, \quad h = 0, \quad \text{and} \quad h = H(E_{\dagger} - E). \quad (5.20)$$

These nullclines are plotted in Figure 5.3a. The cross hatched regions in the figure separates the excitation threshold of the system. The excitation of the action potential depends on the

threshold value of the system, where in our model is represented by the E_* . If $E_{\text{stim}} \geq E_*$, then the super-fast subsystem is activated and generating the fast upstroke as shown in Figure 5.3a. If the E_{stim} is smaller than the threshold value, the action potential either follows the slow-time subsystem (without upstroke) or decays back to its resting membrane potential. Note that the fast-time subsystem only determines the steep upstroke, not the duration of APs.

The phase portrait of the slow subsystem (5.16) can be observed in Figure 5.3b. The nullclines of the subsystem are obtained by following similar approach as explained before and we have,

$$E = \frac{g_{22}}{k_3}n + E_3, \quad E = -\frac{g_{22}}{k_2}n + E_2, \quad E = \frac{g_{21}}{k_1}n + E_1, \quad \text{and} \quad n = H(E - E_{\dagger}). \quad (5.21)$$

The E -nullclines can be divided into two parts; the ‘systolic’ and ‘diastolic’ branch. The ‘systolic’ branches are represented by the first two nullclines between $E \in [E_2, E_3]$ and the ‘diastolic’ branch is described by the third nullcline of E when $E \in (-\infty, E_1]$. The equilibrium point of the subsystem is the solution of the intersection between E and n nullclines. From our analysis, we find that these two nullclines intersect at $(E, n) = (E_1, 0)$. This is indicated by black dot in Figure 5.3b. From the figure, the super-slow gating variable n takes the maximal value at

$$n_* = k_2(E_2 - E_*)/g_{22}, \quad (5.22)$$

which is when $E = E_*$. This consideration determines the excitability properties of the slow-time system (5.16). As shown in Figure 5.3b, if E_{stim} is larger than E_2 , the trajectory will be repelled by the lower systolic branch and attracted by the upper one, and thus making a large excursion. The trajectory moves along the diastolic branch to the equilibrium point and stops there, unless another external stimulus is applied, hence repeats the whole cycle. If E_{stim} is smaller than E_2 , the trajectory will just decay back to its equilibrium point and no AP is generated. In addition, the generation of AP also depends on n_{thr} and it can only be excited if it satisfies the following threshold,

$$n(t=0) < n_{\text{thr}} = \begin{cases} 0, & E_{\text{stim}} < E_2, \\ \frac{k_2(E_2 - E_{\text{stim}})}{g_{22}} = n_* \frac{E_2 - E_{\text{stim}}}{E_2 - E_*}, & E_{\text{stim}} \in [E_2, E_*], \\ n_*, & E_{\text{stim}} > E_*, \end{cases} \quad (5.23)$$

such that $n_{\text{thr}} \in [0, n_*)$. n_{thr} in the second equation is obtained by replacing the equation with g_{22} in (5.22).

5.6 Conclusion

In this chapter, we have introduced a simplified model of cardiac action potential, the so-called ‘modified Caricature Noble model’ following closely the methods of [Biktashev et al. \(2008\)](#)

and [Simitev and Biktashev \(2011\)](#). The original model was modified where the fourth order of variable n in equation (5.2b) was replaced by linear term in n . The entire right hand side of the voltage equation is now piecewise-linear and so easier to solve and analyse. The model has three variables and includes two essential ionic currents which are sodium and potassium currents. Due to its simplicity, the model could be solved analytically. We derived the exact analytical solutions of the model, using both the initial value problem and boundary value problem. This is practically impossible with detailed action potential model due to large parameters and variables presented in the model.

Also, we derived the asymptotic solutions of the model based on its timescale. In Chapter 7 and 8, we will use the solutions to construct an efficient numerical method and study the mechanisms of cardiac alternans, respectively. We ended the chapter by explaining the phase portrait of the fast-time subsystem and slow time subsystem of the modified caricature Noble model. The excitation threshold of an action potential was also discussed. From this chapter, we can see that the model offers several advantages, in terms of theoretical perspective and computational tractability. It can also replace other more complicated action potential models due to its simplicity. In the next chapter, we aim to propose the model as a generic model of action potential by fitting the model to several complex models.

Chapter 6

Estimation of parameters in models of single-cell cardiac action potential

6.1 Introduction

Advances in experimental techniques have driven to a proliferation of mathematical models of single-cell cardiac electrophysiology. Models exist for various types of cardiac cells, for various species as well as for cells in various stages of physiological remodelling. A number of excellent review articles have been published to summarise state of the art in the field (Clayton 2001, Fenton and Cherry 2008, Noble et al. 2012). Many of the models are available in curated electronic form (CellML 1998) along with simulation tools (Clerx et al. 2016, McFarlane and Biktasheva 2008, Mirams et al. 2013) to mention but a few. However, detailed cardiac models have a set of well-known drawbacks. The main one is uncertainty in model structure and parameter values (non-uniqueness, redundancy), which means that very few models, if any at all, can be used without adjustment on data other than the data on which their parameter values have been fitted. The limitation is due to several factors, for instance, biological variability from preparation to preparation, experiment/data-specific, non-reproducible and parameters estimated by fitting to different species. Further disadvantages of those models include computationally expensive (Clayton et al. 2011), difficult for conceptual understanding and causal inference.

It is, therefore, necessary to obtain simplified mathematical models which can aid conceptual understanding and causal inference. Some of the properties of such model are sufficiently simple mathematical form, consist a small number of parameters, can be easily fitted to reproduce a wide range of experimental data and including patient-specific data, amenable to further mathematical simplification and interpretation, and lastly, computationally inexpensive in both single-cell and tissue configurations. A number of simplified models have been proposed to address this need (Nickerson and Hunter 2010), and most have become very popular and frequently used, for example, Aliev and Panfilov (1996) and Mitchell and Schaeffer (2003). Some bear no relation to experimental data and actual cardiac electrophysiology (Barkley 1991, FitzHugh 1961, Tonnelier

2002). Others have been formulated specifically with cardiac applications in mind (Fenton and Karma 1998). These models also have drawbacks. For example, Fitzhugh-Nagumo model was lacking important cardiac properties, including a realistic APD restitution curve and failed to reproduce some qualitative features of an action potential. Meanwhile, Fenton-Karma model was used to study arrhythmia, but it could not reproduce a proper action potential waveform.

With this motivation, we use the modified caricature Noble model with the aim of finding estimates for the values of its parameters such that the model would replicate the behaviour of state-of-the-art models of ventricular and atrial excitation. The modified caricature Noble model is fitted to the following biophysically detailed models such as the authentic Noble (1962) model of Purkinje fibres, the human ventricular model of Luo and Rudy (1991) and the human atrial model of Courtemanche et al. (1998). We also fit the model to experimental measurements of healthy and failing rabbit ventricular myocytes (McIntosh et al. 2000). The action potential morphology and the action potential duration (APD) restitution curves are reproduced to capture the important characteristics of the ionic model. Fitting qualitatively different models to a common mathematical structure offers a number of advantages for their use and interpretation as well essential differences can be identified.

The parameter estimation is done using robust ‘out-of-the-box’ tools widely available within popular numerical libraries such as MATLAB, NAG, Numpy. We implement a simple parameter estimation method, the so-called ‘Nelder-Mead simplex method’ (Nelder and Mead 1965) in our fitting algorithm. In general, the study aims to demonstrate a simple out of the box parameter estimation methods and propose a simple, intuitive model with analytical solutions. We begin this chapter by introducing some mathematical tools which will be used in our work. Using the modified caricature Noble model, we carry out a simple parameter sensitivity test on every parameter in the model and observe their effects on action potential characteristics. Then, we explain the method of parameter estimation and the fitting protocols used in this work. The fitting results on various biophysically detailed action potential models and experimental AP recordings are discussed in the following section. Finally, we end the chapter with a conclusion.

6.2 Methods

6.2.1 Parameter selection and sensitivity analysis

Optimisation process is computationally expensive and time-consuming as the process depends on the number of parameters that we want to estimate in the model. Large parameter number could increase the parameter space, which would then add complexity in fitting algorithm to search the optimised values. Hence, to avoid this computational challenge, one needs to identify which parameters require optimisation. In several of earlier works, model ionic conductances were chosen as the main components due to a huge number of parameters existed in the model

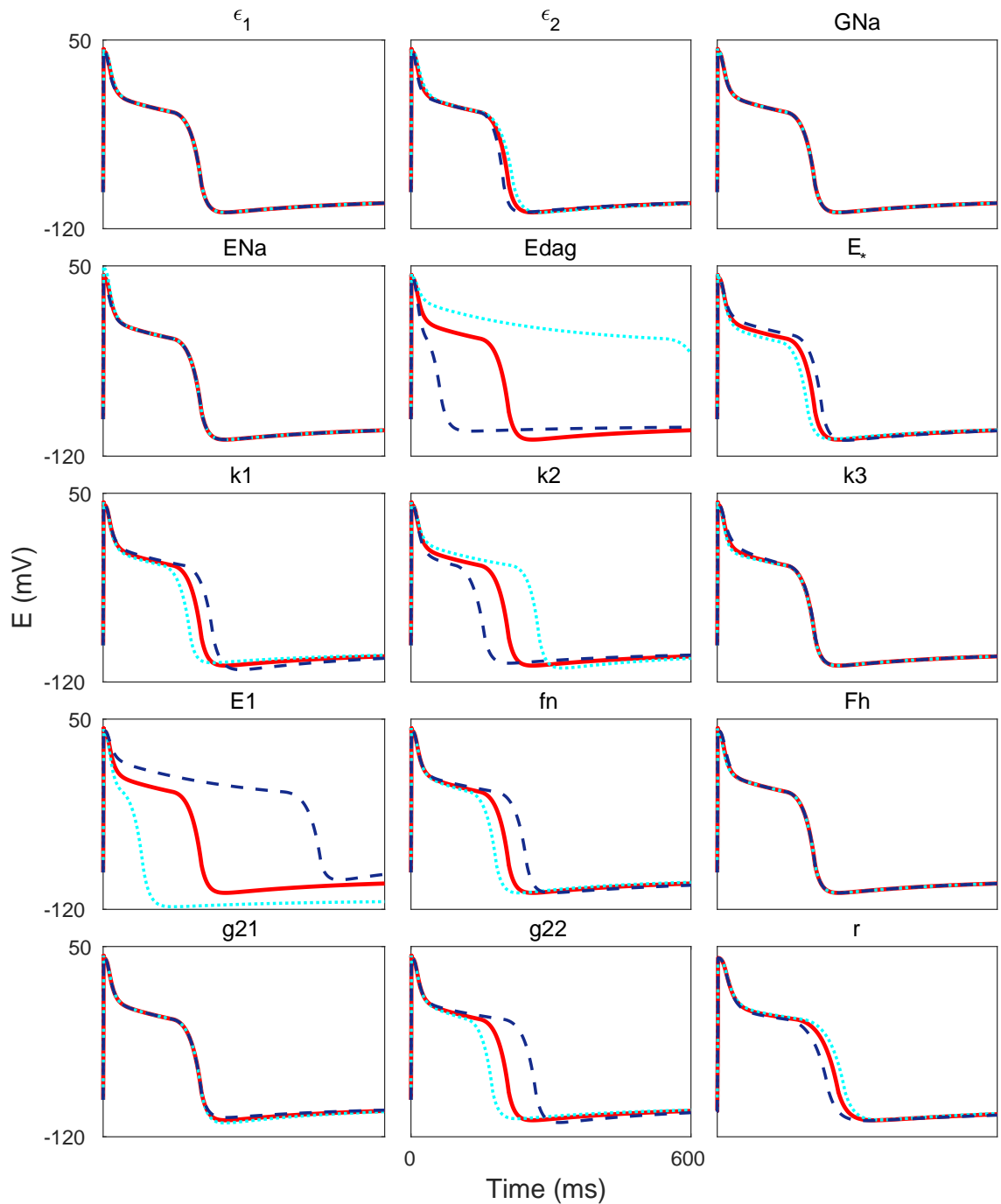


Figure 6.1: Sensitivity analysis test for every parameter in the modified caricature Noble model. Each parameter was perturbed for $\pm 20\%$ from its baseline value and the model was paced at 600 ms. The solid red line is the action potential with parameter values given in Table 6.2, the dashed blue line is the action potential with -20% perturbation and the dotted cyan line is the action potential with $+20\%$ perturbation. Abbreviation : Edag = E_{\dagger} .

(Groenendaal et al. 2015, Sarkar and Sobie 2010, Syed et al. 2005). Meanwhile, some have included all parameters in the model that define membrane current amplitudes and kinetics in their fitting algorithm (Cairns et al. 2017, Dokos and Lovell 2004, Guo et al. 2013). Technically, the choice of fitting parameters is based on the importance of the particular parameter in influencing the AP characteristics. Although this is less of a burden for a simplified model due to the small parameter number present in the model.

Hence, to understand the influence of each parameter in the modified caricature Noble model to AP morphology, we performed a simple parameter sensitivity test on every parameter in the model. Each parameter was perturbed for $\pm 20\%$, and any changes to action potential were recorded. This is depicted in Figure 6.1. From the Figure, it shows that some parameters are very sensitive to perturbation, and some have a small effect on the action potential morphology. We summarise the parameter sensitivity analysis and the effect of parameter changes in Table 6.1. From the table, we can see that particular parameter influences the specific region of AP feature. For example, the maximal voltage is controlled by E_{Na} and the resting membrane potential is influenced by E_1 only. Some of them even influence more than a single property of the action potential. For instance, E_* , E_{\dagger} , g_{22} and f_n control the action potential repolarisation, but E_* and E_{\dagger} also contribute to the AP plateau.

To understand the effect of parameter perturbation on action potential morphology, we discuss and relate the change in parameter values with the phase portrait of the model (Figure 5.3). We only discuss for several parameters. First and foremost, we begin with the E_{Na} that modulates the AP amplitude. In the system, increasing the value of E_{Na} could shift the E-nullcline (5.20) up (as shown by the top red line in Figure 5.3a), hence, increase the duration of the AP to reach maximum excitation. E_{\dagger} controls the transition point between inactivation and activation of super-fast h variable (refer to the blue dashed line in Figure 5.3a). When the value is decreased, the transition point is also delayed. In consequence, the voltage stays on the E-nullcline (the left red line in Figure 5.3a) a little bit longer before the transition begins, thus, prolonged the APD. E_1 is the equilibrium point of the system, which directly controls the resting membrane potential of caricature Noble model. Changing the value will alter the steady-state of the model. Other parameters like g_{22} , k_2 and k_3 control the intersection point of two E-nullclines (two upper solid red lines in Figure 5.3b) as these parameters directly govern the equations of E-nullcline (5.21). This intersection point is the point where AP begins to shift from plateau to repolarisation state. Altering any of the values will shift the intersection point to another point, which then affects the action potential duration. In addition, ε_1 and G_{Na} control the steepness of the front which is already very steep so not much effect is seen visually. ε_2 controls the steepness of the front and the back of the AP in the secondary slow-fast subsystem. While this effect is dominated by much faster sodium current in the front, it is visible in the APD variation in the back.

AP features	Parameters
Upstroke	E_{Na}
Post-drop repolarisation	k_3
Plateau	$E_*, E_{\dagger}, E_1, k_2, k_3$
Repolarisation/APD	$\epsilon_2, f_n, g_{22}, k_1, k_2, E_1, E_*, E_{\dagger}, r$
Resting membrane potential	E_1

Table 6.1: Summary of parameter effects on the important AP features of modified caricature Noble model.

6.2.2 Method of parameter estimation

One of the primary challenges of complex computational models is the large number of free parameters that must be determined. How best to fit these parameters to the targeted data has been the subject of numerous investigations (Dokos and Lovell 2004, Guo et al. 2013). To date, there have been various parameter estimation methods applied for cardiac action potential models including maximum-likelihood estimation (Milescu et al. 2005), principal-axis fitting (Vandenberg and Bezanilla 1991), genetic algorithms (Kaur et al. 2014, Syed et al. 2005, Tomek et al. 2019), and the widely used empirical ‘hand-tuning’ of free parameters (Baranauskas and Martina 2006, Mickus et al. 1999), whereby parameters were tweaked incrementally to achieve a qualitatively acceptable fit to the data, as defined by the modellers. The empirical adjustment technique depends primarily on operator intuition, developed through analysis and interpretation of many data sets. It is subjective, functionally slow, and does not satisfy the increasingly stringent requirements for robustness and reproducibility.

In contrast to hand fitting, automatic parameter optimisation procedures can survey a much larger parameter space, determine quantitatively best fits to multiple voltage-clamp datasets simultaneously, are reproducible, relatively easy to implement, and if given the right constraints on the optimisation criteria can achieve a physiologically relevant parameter set. For both automatic and ‘manual’ optimisation, it is not always possible to definitively identify a unique global minimum; multiple local minima may be identified that correspond to a parameter set that ‘fits’ the data with sufficiently meaningful precision. The parameter estimation method that has been applied in our work is based on a standard MATLAB routine for unconstrained multivariable function. The toolbox is an implementation of bounded Nelder-Mead simplex method of Lagarias et al. (1998) that minimises the real-valued function $f(x)$ where $x \in \mathbb{R}$, without the need of looking the derivative (Nelder and Mead 1965). In our optimisation process, we implemented the modified MATLAB function ‘fminsearchbnd’. The MATLAB code can be downloaded from the provided link¹. Our preliminary finding using other parameter estimation methods such as genetic algorithm and Bayesian optimization produced a large fitting error when the AP was fitted, in comparison to the Nelder-Mead simplex method. We could not find the reason of this

¹<https://uk.mathworks.com/matlabcentral/fileexchange/8277-fminsearchbnd-fminsearchcon>

discrepancy and this is a direction for further research.

The parameter estimation method implemented in this work is straightforward and relatively robust, despite its several limitations. One of them is that it does not guarantee convergence to a global minimum. The routine might stop at a particular local minimum which is far from the optimised parameter values. If this happens, the initial guess needs to be changed. Latin hypercube sampling method (as discussed in Chapter 4) can be used to generate many random parameter combinations of initial guess and cover the specified region space uniformly. Furthermore, we also find that this method has an acceptable runtime, even though it has been reported earlier by [Moreno et al. \(2016\)](#) that this method is computationally expensive. In our work, a single fitting of AP waveform (refer to the middle panel in Figure 6.2) in the Luo-Rudy model took approximately 40-50 minutes. This simulation was carried out for six parameters, and convergence tolerance set up to 10^{-4} . From our experience, we find that the robustness and computational cost of optimisation method may vary as it mainly depends on many factors like the number of parameters used, the closeness of the initial guess with respect to a local minimum, size of convergence tolerance, the complexity of the model and fitting protocols. Nevertheless, the runtime is not our priority here, as the main objective is to fit the AP morphology. If that is the case, one needs to consider the implementation of a more robust optimisation method, see ([Cairns et al. 2017](#), [Kirkpatrick et al. 1983](#), [Rios and Sahinidis 2013](#), [Syed et al. 2005](#)).

In conclusion, the toolbox and method applied here are reasonably simple and easy to understand, and it is sufficiently accurate for other purposes. We also provide the MATLAB codes of our fitting work in the appendix for the benefit of others.

6.2.3 Fitting protocols

6.2.3.1 Data used

To avoid a highly computational cost, a single AP fitting at particular pacing cycle length was considered ([Dokos and Lovell 2004](#), [Guo et al. 2013](#), [Syed et al. 2005](#)). We fitted our model to both experimental and model-generated data by considering the voltage output only. For model-generated data, the AP was paced for 11 beats at basic cycle length 1500 ms to produce the most stable AP waveform. The last AP then was extracted for fitting purpose. The voltage transient was discretised in as a set of ordered pairs $\{(t_i, V_i)\}$ where $i = 1 \dots M$. The trace was also simulated with equally time points of 0.1 ms to ensure there was enough coverage in the region where the signals exhibited high variance. All model codes were downloaded from the CellML model repository, and the model equations were solved using the MATLAB function `ode15s` with relative and absolute tolerances at 10^{-6} , respectively.

For experimental data, we used the voltage data of rabbit ventricular myocytes from [McIntosh et al. \(2000\)](#) for both healthy and heart failure conditions. The data was extracted from the

published manuscript using the WebPlotDigitizer software². To increase the resolution of the voltage data, we interpolated the data (using MATLAB function *interp1*) by adding more points over the entire AP duration with time step 0.05 ms.

6.2.3.2 Fitness function

In order to produce the optimal fitting result, we considered multiple fitness functions (Cairns et al. 2017, Guo et al. 2013), giving priority to minimisation of the curve error and also the action potential duration. In the optimisation routine, our main objective was to minimise the following total error function,

$$E_{\text{total}} = E_{\text{AP}} + E_{\text{APD90}}. \quad (6.1)$$

In particular, the functions error are defined as below,

$$E_{\text{AP}} = \frac{1}{M} \sum_{i=1}^M \frac{|V_i^{\text{sim}} - V_i^{\text{target}}|}{|V_i^{\text{target}}|}, \quad (6.2)$$

and

$$E_{\text{APD90}} = \frac{|\text{APD}_{90}^{\text{sim}} - \text{APD}_{90}^{\text{target}}|}{|\text{APD}_{90}^{\text{target}}|} \quad (6.3)$$

where V_i^{sim} and V_i^{target} are the voltage values of our model and the target data respectively. $\text{APD}_{90}^{\text{sim}}$ and $\text{APD}_{90}^{\text{target}}$ are the APD_{90} of respective models. The second error function allows the fitting algorithm to prioritise the APD_{90} when optimising the AP morphology.

6.2.3.3 Restitution curves

APD restitution curve plays an important role in describing the dynamics of an action potential when the pacing rate is varied. In this work, we only consider the dynamic pacing method. The protocol is started by pacing the myocyte at a steady-state pacing rate for 11 beats until the AP is adequately equilibrated, then the action potential duration, APD_{90} of the last action potential is measured. APD_{90} is measured approximately at 90% of the AP repolarisation. Next, the pacing rate is shortened, and the procedure is repeated. However, since the aim of the study was only fitting the AP shape at normal condition, the alternans behaviour was not considered. The APD restitution curve is constructed by plotting the APD_{90} values against basic cycle lengths (BCL).

6.2.3.4 Simulation workflow

The simulation starts by optimising the AP morphology of the model with some values of initial guess. The potential parameters to be estimated were chosen from the sensitivity analysis in the previous section. Once the fitting routine was finished, we directly used the new estimated

²<https://automeris.io/WebPlotDigitizer/>

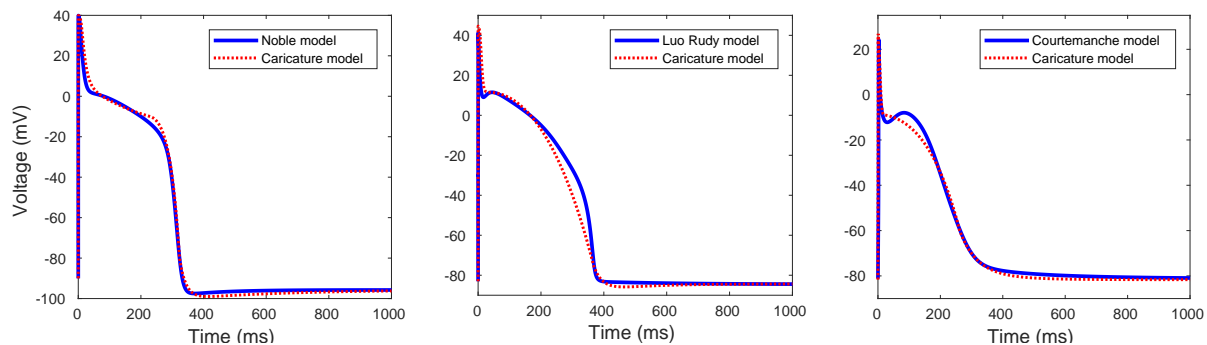


Figure 6.2: The AP morphologies of the respective models after fitting process. Each model was paced at basic cycle length of 1500 ms.

parameters to generate the APD restitution curves as described above. The relative mean error of the APD restitution curves between the caricature and targeted models was then measured using the following formula,

$$E_{\text{APDcurve}} = \frac{1}{W} \sum_{i=1}^W \frac{|\text{APD90}_i^{\text{sim}} - \text{APD90}_i^{\text{target}}|}{|\text{APD90}_i^{\text{target}}|}, \quad (6.4)$$

where the $\text{APD90}_i^{\text{sim}}$ and $\text{APD90}_i^{\text{target}}$ are the APD90 of the respective models at a particular BCL. BCL_i was increased from $\text{BCL}_1 = 400$ to $\text{BCL}_W = 2000$ ms with an increment of 100 ms. If the E_{APDcurve} was still large, the initial guess was changed and the entire process was repeated until we found the most acceptable fitting results.

6.3 Fitting to action potential models

In this section, we show the results of the parameter estimation method that we have carried out on several cardiac AP models. The models selected are ranging from various parts of the heart which are Purkinje model by Noble (1962), atrial model by Courtemanche et al. (1998) and ventricular model by Luo and Rudy (1991). We demonstrate that our modified caricature Noble model is generic enough to reproduce the AP characteristics of various models.

6.3.1 Fitting to a single action potential

A single pacing period of 1500 ms was considered to fit the AP morphology using the fitting protocols as described before. The new estimated parameter values obtained after parameter estimation process are listed in Table 6.2. This is an optimisation problem in high-dimensional parameter space, with presumably many local minima. Therefore, it is difficult to ascertain if a given solution of the minimisation procedure is the best possible one. The results of the fitting are shown in Figure 6.2. As one can see, the modified caricature Noble model is able to capture

all the AP morphologies of various ionic models with reasonable error values. The mean relative errors of AP morphology for the respective fitting results are listed in Table 6.3.

From the table and right panel of Figure 6.2, it shows that the fitting of modified caricature Noble model to the Courtemanche model has the biggest discrepancy. The discrepancies can be seen at the post overshoot drop and plateau regions. Our model fails to capture the deep notch produced in the Courtemanche model. This suggests that either the fitting algorithm does not settle into the part of parameter space that would reproduce the deep notch or that model formulation itself is not flexible enough to match the feature. We suspect that it is the latter, as the model lacks specific ionic currents that could create the notch phase which is produced by the activation of transient outward K^+ and Na^+/Ca^{2+} exchanger currents (Santana et al. 2010). Penaranda et al. (2012) has shown that incorporating the fast transient outward current can reproduce the characteristic notch in phase 1 of the AP. Meanwhile, for the Luo-Rudy model, the modified caricature Noble model is not able to accurately fit the AP at repolarisation stage. The membrane potential in our model drops faster and quicker than the Luo-Rudy model. However, from the Figure and computed relative error, one can still conclude that the AP of our model qualitatively gives an excellent agreement to the respective model.

6.3.2 Fitting to a restitution curve

Using the new estimated parameter values, we then generated the APD restitution curves of modified caricature Noble model by following the dynamic pacing protocol. We compare the results of the curves with the respective models, as shown in Figure 6.3. From the Figure, one can see a good agreement between our model and the target models. This result demonstrates that our modified caricature Noble model can preserve most of the important characteristics of AP waveforms at various basic cycle lengths, ranging from 400 to 2000 ms. We did not decrease the basic cycle length further as this might cause the model to exhibit alternans behaviour which is beyond the scope of this study. For alternans problem, different approach of parameter estimation method is needed as demonstrated in Cairns et al. (2017). In Chapter 8, we will reapply the optimisation procedure designed in this chapter to study cardiac alternans.

6.3.3 Insights into models and the influence of parameters

Our experience in finding parameterisations to match various data sets have led us to new ways of understanding the modified caricature Noble model and its parameters. Table 6.2 summarises the new parameter sets needed to reproduce the AP characteristics of each targeted model. In this section, we discuss briefly, the effect of the change of some of the key parameters to the AP characteristics of various cardiac ionic models.

To begin with, we first look at the fast and stiff region of the action potential, which is the upstroke or depolarisation. The depolarisation stage normally occurs due to the higher

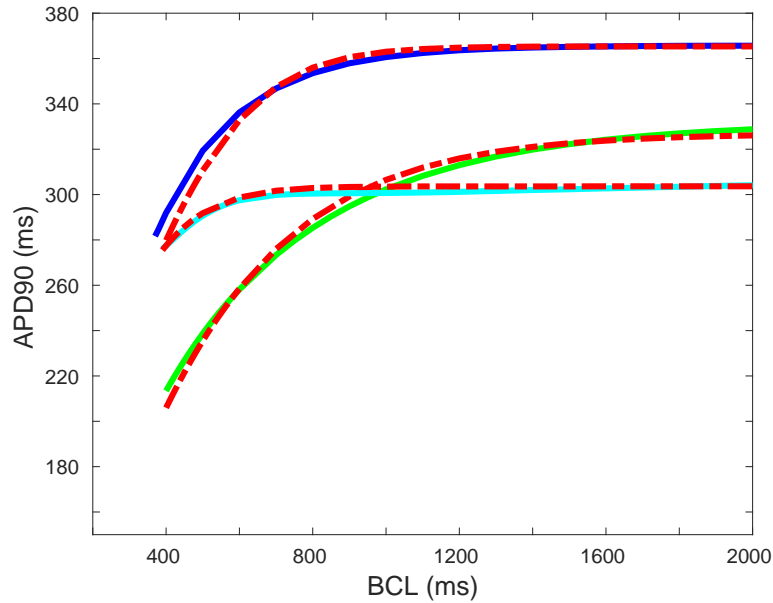


Figure 6.3: The restitution curves of modified caricature Noble model (dashed line) in comparison to the target AP models. Blue line is the APD curve of Luo-Rudy model, the cyan line is the APD curve of Courtemanche model and the green line is the APD curve of Noble model. BCL is shortened from 2000 ms until 400 ms.

concentration of sodium ions outside of the cell membrane rush into the cell through its particular channels, which latter increase the inward sodium current. The membrane potential then rises extremely within a short period. The higher the sodium inward current, the larger the membrane potential would rise. However, the peak value of this membrane potential differs in different region of the cardiac. For instance, in ventricular, the value is about 40–45 mV (Hund and Rudy 2004, Luo and Rudy 1991, Mahajan et al. 2008), while the value is slightly lower in atrial which is approximately 24–40 mV (Wilhelms et al. 2013). In the modified caricature Noble model, the peak of the fast inward current is mainly controlled by parameter E_{Na} . The higher the AP amplitude, the higher the value of E_{Na} . From Table 6.2, it is shown that the E_{Na} is the highest in the Luo-Rudy model, and the smallest is in the Courtemanche model.

After the upstroke, the post-overshoot drop begins to take over momentarily. During this stage, the sodium ion gates start to close immediately and the potassium ion channels open, hence allowing potassium ions to travel out of the cell. The gradient of the dropping voltage in each model is not similar. The Noble model has the least steep gradient, followed by the Luo-Rudy and Courtemanche model. In the modified caricature Noble model, k_3 determines how steep the dropping value of the voltage. Decreasing this parameter value will decrease the gradient of the dropping voltage and also reduce the plateau region. The Noble model seems to have the lowest value of k_3 since it is the least steep among the other models. However, for the other two models, we are not able to make any remark since k_3 also controls the plateau of the action potential. The difference in the plateau region has undoubtedly affected the estimated value.

Parameters	Default	Noble	Luo-Rudy	Courtemanche
G_{Na}	100/3	100/3	100/3	100/3
E_{Na}	40.0	40.0	45.0	24.3
E_{\dagger}	-80.0	-80.0	-75.0	-60.0
E_*	-15.0	-10.0	11.5	-9.0
k_1	0.075	0.04932	0.03602	0.01702
k_2	0.04	0.03033	0.00443	0.007173
k_3	0.10	0.08007	0.33946	0.99977
E_1	-93.333	-95.667	-84.333	-81.667
f_n	0.0037	0.004471	0.003781	0.00353
F_h	0.5	0.5	0.5	0.5
g_{21}	-1.0	-0.28325	-0.14359	-0.02303
g_{22}	-9.0	-2.15744	-0.36512	-0.25370
r	1.0	0.7	1.8	2.8

Table 6.2: Comparison of the default value of the parameters in [Biktashev et al. \(2008\)](#) with the value used in our modified caricature Noble model after parameter fitting.

Model	Noble	Luo-Rudy	Courtemanche	Exp. (Healthy)	Exp. (Heart failure)
AP morphology	0.2629	0.4194	0.5774	0.231	0.1213

Table 6.3: The mean relative error of AP morphology between the modified caricature Noble model and targeted models/data.

The membrane potential of Noble and Courtemanche model at plateau region is approximately -10 mV and -9 mV, respectively. The Luo-Rudy model has the largest voltage value, which is about 11 mV. In our model, E_* is one of the parameters that modulate the voltage value at the plateau region. The estimated value is consistent for each model, where E_* in the Luo-Rudy model is the biggest since it has the biggest value of voltage during the plateau phase. The Noble model obtains the smallest E_* .

The next phase is the action potential duration. The APD of each model is not similar. From [Figure 6.3](#), it is clear that this value is varied in each model where the Luo-Rudy shows the largest APD (~ 365 ms), then followed by the Noble model (~ 310 ms) and lastly the Courtemanche model (~ 285 ms). As shown in the sensitivity test, there are many parameters that explicitly and implicitly control the action potential duration, for example, E_* , k_2 , f_n , g_{22} and so on. It is possible to obtain similar APD value for different parameter combinations. Hence, a direct comparison between parameters in every model is difficult due to multiplicative roles of these parameters.

The resting membrane potential (RMP) is the final stage of an action potential, where the ionic balances inside the cell are restored for the next excitation. Our fitting results show different RMP for each model, which the Noble model has the lowest value (-95 mV). RMP value in the Luo-Rudy and Courtemanche model is roughly -84 mV and -81 mV, respectively. In the modified caricature Noble model, the resting membrane potential is mainly influenced by parameter E_1 .

This reduced the computational cost of our fitting process as we could manually adjust the value without the need of including the parameter in our fitting algorithm. Our fitting results show an excellent agreement between the estimated value and the RMP of each model, as listed in Table 6.2.

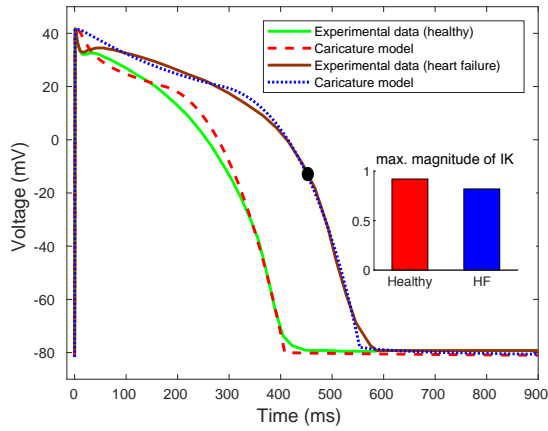
Briefly, we have provided some interpretations of the main parameters in our modified caricature Noble model when fitted to various biophysically detailed action potential models. However, full and direct comparisons for every parameter are difficult due to the complexity of the parameter space. We hope that this analysis gives us some understanding and meaningful insight into how the parameters in our model work.

6.3.4 Model performance

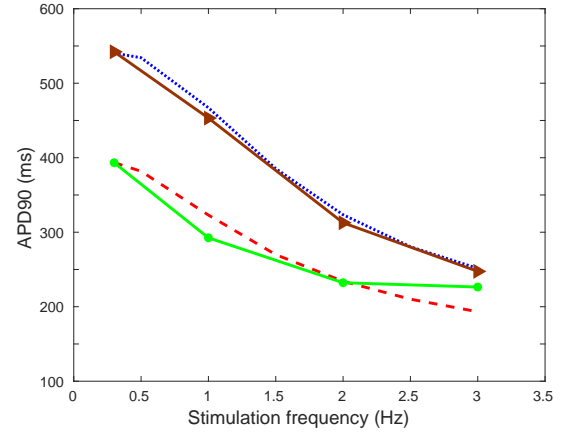
We analyse the efficiency of our model in comparison to the targeted model by calculating the execution time of all the models. To do so, we measured the time taken of each model to generate 1000 action potentials at a fixed basic cycle length of 1000 ms. Each model was solved using the MATLAB function `ode15s`. Our finding shows that the modified caricature Noble model took approximately about 180s to run the simulation. The Luo Rudy and Courtemanche model required about 1246s and 1634s, respectively. From this result, we acknowledge that the modified caricature Noble model is six times faster than the Luo-Rudy model and nine times faster than the Courtemanche model. In complex tissue simulation, this could potentially reduce the computational workload and runtime.

6.4 Fitting to experimental data

Prolongation of the action potential duration is a well-known feature of human ventricular myocardium from patients with severe heart failure and have been recorded in many clinical studies (Hegyi et al. 2018, Kaab et al. 1996, Li et al. 2004, McIntosh et al. 2000). Several factors likely contribute to such APD prolongation, for instance, decrease in potassium currents (Akar and Rosenbaum 2003, Beuckelmann et al. 1993, Tsuji et al. 2000) and increase in late sodium currents (Valdivia et al. 2005). Hence, we use the modified caricature Noble model as the toolbox to understand the ionic mechanism of AP differences in healthy and failing cardiac cells. To do this, we fitted the model to experimental data of AP waveforms in McIntosh et al. (2000). In the paper, they examined the changes of action potential and intracellular calcium transient characteristics in isolated cardiac myocytes from sub-epicardial, mid-myocardial, and sub-endocardial regions of the left ventricle of rabbits with heart failure. Their main finding showed that in the heart failure group, APD90 and calcium transient duration (CaD50) were prolonged in both sub-epicardial and mid-myocardial cells. These changes were significant at lower stimulus frequencies but the relative effect diminished at higher frequencies (3 Hz). For



(a) Action potential waveforms.



(b) The APD restitution curves.

Figure 6.4: (a) Action potential waveforms of both modified caricature Noble model and experimental data at stimulation frequency of 0.3 Hz. The solid lines are the action potential from the single cardiac myocytes isolated from the left ventricle of healthy and heart failure rabbit hearts (●). The dashed and dotted line are the corresponding action potentials of modified caricature Noble model. Small inset figure is the maximal magnitude of time-dependent potassium current of the respective models. (b) The relationship between stimulus frequency and APD90. The green and brown lines are the the restitution curve for healthy and heart failure cell, respectively. The dashed and dotted lines are the corresponding restitution curves of modified caricature Noble model.

Parameters	Healthy	Heart failure
G_{Na}	100/3	100/3
E_{Na}	41.5	41.5
E_{\dagger}	-80.0	-78.0
E_*	20.0	20.0
k_1	0.0231	0.0173
k_2	0.0057	0.0068
k_3	0.0471	0.031
E_1	-245/3	-245/3
f_n	0.0043	0.0040
F_h	0.5	0.5
g_{21}	0.0409	0.0405
g_{22}	-1.097	-0.9461
r	0.4	0.6

Table 6.4: The parameters values of modified caricature Noble model after fitting to the experimental data of healthy and failing myocytes at 0.3 Hz pacing rate.

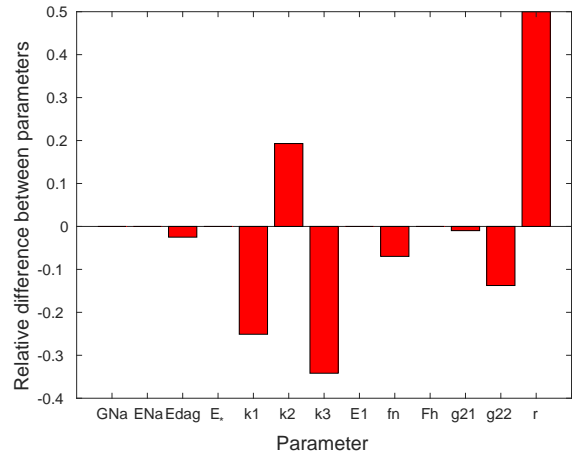


Figure 6.5: Relative difference between the set of parameters in healthy and HF groups.

our purpose, we only fitted our model to the AP morphology of mid myocardium cells (Mcells) in both healthy and failing myocytes.

6.4.1 Fitting to a single action potential

Similar to previous results, a single AP fitting was considered using the fitting protocols as explained before. The modified caricature Noble model was fitted to isolated cardiac ventricular cells at a pacing rate of 0.3 Hz (3333 ms) for both healthy and heart failure (HF) states. Figure 6.4a shows the AP morphologies after the fitting process. As observed in the Figure, the discrepancy largely occurs in the plateau phase. The modified caricature Noble model exhibits extended plateau before the voltage begins to drop. We also measured the mean relative error of the respective curves as listed in Table 6.3 and the error is relatively small. Table 6.4 shows the estimated parameter values of our model after fitting to experimental data. In Figure 6.5, it also shows that the most affected parameters in the model with HF are those related to potassium and leak currents. The parameters are k_1 , k_2 , k_3 , r and g_{22} . These parameters need to be adjusted in order to compensate the large APD exhibited in the HF group. Other parameters like E_{Na} and E_1 are similar in both states since the APs have identical action potential amplitude and resting membrane potential.

As mentioned earlier, various factors are likely to contribute to the APD prolongation in failing myocardium. To date, numerous investigations have highlighted the importance of potassium current downregulation in HF myocytes (Akar and Rosenbaum 2003, Beuckelmann et al. 1993, Tsuji et al. 2000). Our fitting results show that in failing myocyte, the maximal magnitude of time-dependent potassium current is roughly 10% smaller than the healthy myocyte, as depicted in Figure 6.4a, hence causing the APD prolongation.

6.4.2 Fitting to a restitution curve

Following the dynamic pacing protocol, we constructed the APD restitution curve using the new estimated parameter values and we plotted the result in Figure 6.4b. For a given stimulation frequency, failing myocytes exhibited larger APD90 than the healthy myocytes. At high stimulation frequency, APD90 for both groups shows a less substantial difference. Our modified caricature Noble model manages to reproduce accurate APD restitution curve for the HF myocyte, compared to healthy myocyte. For healthy myocyte, the discrepancy occurs at several stimulation frequencies, and it gets pronounced at stimulation frequency larger than 2 Hz, where the modified caricature Noble model produced smaller APD90 than the experimental data of healthy myocytes. The relative error between the two curves, however, is relatively minimal and acceptable, as measured in Table 6.3.

6.5 Conclusion

In this chapter, we have demonstrated a simple parameter fitting protocol and presented the modified caricature Noble model as a generic model of cardiac electrical activity. Using the

Nelder-Mead simplex method, the model exhibited extensive flexibility by reproducing the action potential waveforms of several detailed cardiac electrophysiology models and experimental measurements of healthy and failing rabbit myocytes. The fitted AP morphology showed some discrepancies at a particular region of AP phase. For example, when fitting to the Courtemanche model, the AP deep notch in phase 1 was not accurately captured by our model. A probable reason is that the modified caricature Noble model lacks of ionic currents that can reproduce the specific AP feature, which in this case is transient outward potassium currents, *I_{to}*. Apart from fitting the AP morphologies, we also successfully managed to fit the APD restitution curves of the respective models and data, hence encapsulating the model's AP dynamics at different basic cycle lengths. Future work needs to include fitting the CV restitution properties of the modified caricature Noble model to the targeted models in order to examine the AP propagation in a spatially extended tissue simulation.

Unlike some other simplified action potential models, the parameters and variables in the modified caricature Noble model could have the physiological meaning as the model was derived from a genuine cell model (Biktashev et al. 2008, Noble 1962). Therefore, our results could be translated into physiology. For instance, when fitting to healthy and failing rabbit cardiomyocytes, we found that the maximal magnitude of time-dependent potassium current in the healthy model was a bit larger than the heart failure model. This finding is in agreement with some earlier experimental studies (Akar and Rosenbaum 2003, Beuckelmann et al. 1993, Tsuji et al. 2000). The parameter estimation framework demonstrated in this chapter will be further used in Chapter 8 to study the mechanisms of cardiac alternans. Finally, parameter fitting of modified caricature Noble model demonstrated in this chapter has shown that the model could potentially replace other more complicated models for various analytical approaches, such as, looking for the mechanisms of cardiac alternans and developing an efficient numerical method.

Also, the ability to connect a model representation of the Purkinje system with the complex structure of the ventricles opened new opportunities to understand arrhythmogenesis, and specifically, the contribution of Purkinje to the initiation and maintenance of reentry (Trayanova and Winslow 2011). Berenfeld and Jalife (1998) made the very first attempt to incorporate the Purkinje system in a whole-heart model. The 2-variable Fitzhugh-Nagumo model of cellular kinetics was assigned to each system with different parameter sets. Other recent studies employed two different AP models to couple the two systems (Purkinje and ventricular) and developed a 3D tissue model (Aslanidi et al. 2009b, Vigmond and Clements 2007). As part of our motivation, future work should aim to utilise our finding in this chapter to be used for whole-heart modelling.

Chapter 7

Efficient numerical method for the solution of the modified caricature Noble model

7.1 Introduction

The nature of cardiac electrical activity requires very fine spatio-temporal resolutions and a long period of simulation, which may render the process to be computationally expensive. Typically, organ level simulations commonly involve millions of grid points and the solution of the reaction-diffusion system has to be solved over thousands of time steps. Such enormous computational demands can only be overcome with the aid of advanced numerical methods and parallel computing approaches. Nevertheless, this is still time-consuming and the execution process may take hours and days. For instance, a simulation of 1 min cardiac activity in a tissue model with 4.3 million cells, using a rabbit ventricular model by [Mahajan et al. \(2008\)](#) took more than 4.5 days ([Plank et al. 2009](#)). There have been numerous attempts to solve the cardiac electrophysiology problem numerically, but yet it still remains an open question that demands a powerful method and efficient algorithm.

In essence, the finite difference (FD) method has been widely used by a large number of groups to solve the electrophysiology model (see, e.g. [Barkley \(1991\)](#), [Ji and Fenton \(2016\)](#), [Moghaderi and Dehghan \(2017\)](#), [Murillo and Cai \(2004\)](#)). Compared to other available numerical methods, FD method is the most common method used to solve this system due to its simplicity, easy implementation and quite straightforward. However, the drawback of this method is that it is difficult to describe smooth surfaces such as the surface of the heart without steps that might cause some challenges to implementing boundary conditions ([Clayton et al. 2011](#)). For complex modelling of action potential propagation in cardiac tissue geometry, finite element (FE) method might be more suitable to be applied because the method allows us to have non-uniform size and shape of small subdomains. The method is considerably robust and more efficient, especially for simulations with anatomically complex geometry ([Goktepe and Kuhl 2009](#), [Hurtado et al. 2016](#), [Vigmond et al. 2002](#)). Nevertheless, FE method requires one to give additional effort into both

formulation and running the software, in comparison to FD method.

In addition, explicit, semi-implicit (also known as IMEX) and fully implicit methods have been comprehensively implemented for solving the time and space dependence equations in the cardiac electrophysiology model. The choice of the time-stepping scheme for the system plays a vital role in their stability, accuracy, computational cost and as well as memory use. Typically, the explicit time-stepping scheme is the most famous one (see, e.g. [Dowle et al. \(1997\)](#), [Hanslien et al. \(2005\)](#), [Ji and Fenton \(2016\)](#)) due to its easy implementation. However, the explicit scheme is always limited to a stability constraint in which the time step must be sufficiently small to ensure the stability of the solution; otherwise, the action potential model cannot be solved. Therefore, many extensive efforts to encounter the issue have moved to the application of a fully implicit method which is more stable for large time step ([Ji and Fenton 2016](#), [Murillo and Cai 2004](#)). The implicit scheme also takes much less computational time compared to the explicit method but require the solution of a nonlinear system of equations which demanding extra computation. A good alternative between the two methods is the semi-implicit scheme. This method allows us to rewrite the differential operator into two parts where the nonlinear term is solved explicitly and the linear term is evaluated implicitly. Moreover, this method has a stronger stability condition compared to the explicit method but weaker than the implicit scheme ([Ethier and Bourgault 2008](#)).

In general, numerous attempts have been made in order to develop robust and efficient numerical schemes for solving the cardiac electrophysiology model from a single cell to the complex geometry of whole heart simulation. Worth to mention here is like operator splitting method ([Qu and Garfinkel 1999](#), [Strang 1968](#)), parallel implementation ([Epanchintsev et al. 2016](#), [Migliore et al. 2015](#)), using lookup tables ([Cooper et al. 2015](#)) and adaptive numerical scheme ([Campos et al. 2011](#), [Moghaderi and Dehghan 2017](#)). These are among the common strategies used to speed up the calculation time. Despite all these approaches, solving a biophysically detailed ionic model is still too expensive, even with the aid of powerful computing facility. In conclusion, it is a subjective matter to say which method is the most effective as they all have limit and advantage over each other.

With this motivation, in this chapter, we use the asymptotic structure of modified caricature Noble model as described earlier in Chapter 5 to develop an efficient asymptotic-numerical method. In particular, we implement the heterogeneous multiscale method on this model by using its fast and slow time subsystems. The method was initially proposed by [Weinan and Engquist \(2003\)](#) and the idea was extended for solving a cardiac AP model. Prior to our knowledge, no research in cardiac electrophysiology has applied this approach on an action potential which becomes our primary motivation to explore the limitation of the method. The approach is then compared with other numerical solvers to investigate its stability and efficiency.

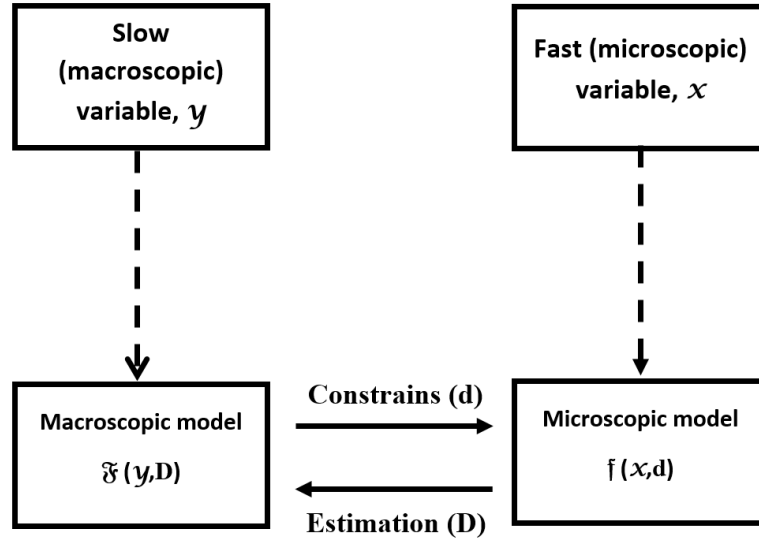


Figure 7.1: The general framework of HMM model.

7.2 Heterogeneous multiscale method

Weinan and Engquist (2003) introduced the heterogeneous multiscale model (HMM) as a general methodology for the efficient numerical computation of multiscale problems. It provides a framework for designing new methods for a large number of multiscale problems. The method is widely used for solving a system with very different dynamics and time scale as many phenomena in nature happen in multiple active scales like the combustion (Weinan et al. 2011), fluid dynamics (Ren and Weinan 2005), cancer modelling (Deisboeck et al. 2011) and many others.

The framework starts with a predetermined form of the macroscopic model, $\mathfrak{F}(y, D)$ where y is the macroscopic variable and D is the missing component of the incomplete macroscopic model. The component D can be measured using the microscopic model when the estimate data is needed. On the other hand, we can define the microscopic model by $\mathfrak{f}(x, d)$ such that $d = d(y)$. d is the constrain value provided by the macroscopic model to the microscopic model. Once the microscopic model is solved, the missing part of the macroscopic model can be estimated. The interaction between the macroscopic and microscopic model is illustrated as in Figure 7.1. In order to outline the procedures of HMM framework, let us start with a simple fast-slow system of the form,

$$\begin{aligned} \frac{dx}{dt} &= \frac{1}{\varepsilon}(-x + h(y)) \\ \frac{dy}{dt} &= g(x, y) \end{aligned} \quad (7.1)$$

x is the microscopic (fast) variable and y is the macroscopic (slow) variable. One can find the attracting critical manifold and the associated slow-flow of such system by taking the limit of ε

goes to zero to obtain

$$C_0 = \{(x, y) \in \mathfrak{R}^2 | x = h(y)\}. \quad (7.2)$$

The macroscopic model is then defined as,

$$\frac{dy}{dt} = g(h(y), y) =: G(y) \quad (7.3)$$

and the microscopic model can be found by rescaling the normal time scale using the approximation $\tau = t/\varepsilon$. Then, we have

$$\frac{dx}{d\tau} = -x + h(y). \quad (7.4)$$

For simplicity, the steps of HMM model can be summarised as follows,

1. We begin the procedure from an initial point, y_n provided by the macroscopic model. The given point is used to reinitialise the microscopic model

$$x_{n,0} = y_n \quad (7.5)$$

where n represents the macroscopic time step.

2. Then, we perform a finite number of microtime steps by using the microsolver denoted as $S_{\delta\tau}$,

$$x_{n,k+1} = S_{\delta\tau}(x_{n,k}, y_n) \quad (7.6)$$

where $k = 0, 1, \dots, K-1$ and $\delta\tau > 0$. The value of K is chosen to be sufficiently large enough, so that $x_{n,K}$ would reach a stationary point or value.

3. Finally, the macroscopic model is solved for the next macrotime step using the macrosolver, $S_{\Delta t}$,

$$y_{n+1} = S_{\Delta t}(x_{n,K}, y_n). \quad (7.7)$$

4. Go to step 2.

Each time step of macroscopic model equals to several time steps of microscopic model. The interaction between the macroscopic and microscopic time scales is depicted in Figure 7.2.

7.3 Implementation of heterogeneous multiscale method on modified caricature Noble model

We implement the heterogeneous multiscale method (HMM) on the modified caricature Noble model by considering the super-fast time system (5.13) and the slow time system (5.16) as the microscopic and macroscopic solver, respectively. The procedures are similar as outlined

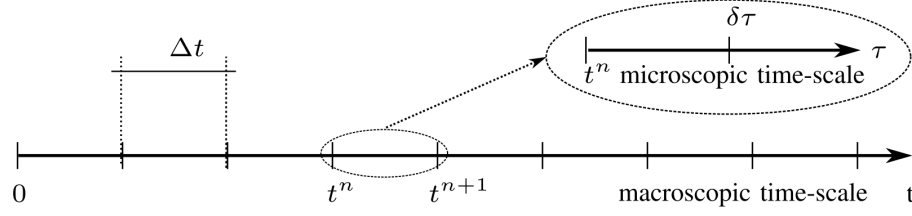


Figure 7.2: Representation of the macroscopic and microscopic time scales in HMM.

previously. For simplicity, we choose the forward Euler scheme to be the macro and micro solver of the two reduced systems. The algorithms for microscopic system are as follows,

$$\begin{aligned} E_{i,k+1} &= E_{i,k} + \delta\tau [G_{Na}(E_{Na} - E_{i,k})H(E_{i,k} - E_*)h_{i,k}], \\ h_{i,k+1} &= h_{i,k} + \delta\tau [F_h(H(E_{\dagger} - E_{i,k}) - h_{i,k})], \end{aligned} \quad (7.8)$$

where $k = 1 \dots K - 1$ and $\delta\tau > 0$ is the microtime step. K must be sufficiently large such that E reaches the maximum voltage, E_{Na} . If K is too small, E will not be able to reach its stationary point which then will affect the trajectory of the macroscopic solver. This is because the initial condition for the macroscopic solver is obtained from the microscopic solver. The algorithms for macroscopic solver are

$$\begin{aligned} E_{i+1,K} &= E_{i,K} + \Delta t \frac{1}{\varepsilon_2} (\tilde{g}_2(E_{i,K})n_{i,K} + \tilde{G}(E_{i,K})), \\ n_{i+1,K} &= n_{i,K} + \Delta t [F_n(E_{i,K})(H(E_{i,K} - E_{\dagger}) - n_{i,K})]. \end{aligned} \quad (7.9)$$

Implementing the above algorithms, then we obtain the results as depicted in Figure 7.3. The initial condition used to excite the action potential was $E(0) = -10$, $h(0) = 1$, and $n(0) = 0$. The results show a very good agreement with exact analytical solution, except a negligible discrepancy in the post over-shoot drop region. The discrepancy in the post overshoot-drop is because the region is solved using the slow subsystem where the value of $\varepsilon_1 \approx 0$, meanwhile, in the full system the value of $\varepsilon_1 = 1$. However, the important AP biomarkers, for example, action potential duration, maximum voltage, amplitude, resting membrane potential are still well preserved.

For further investigation on the stability and efficiency of this solver, we compare the result with several other finite difference methods. The numerical methods are the explicit Euler, implicit Euler, 4th order Runge-Kutta, 2nd order Adam Bashforth and [Rush and Larsen \(1978\)](#) method. These solvers are very well-known and commonly used to solve the action potential model. The algorithms for each solvers are as follows,

- Explicit Euler method

Explicit Euler method is a first order method and it is the most basic explicit method for

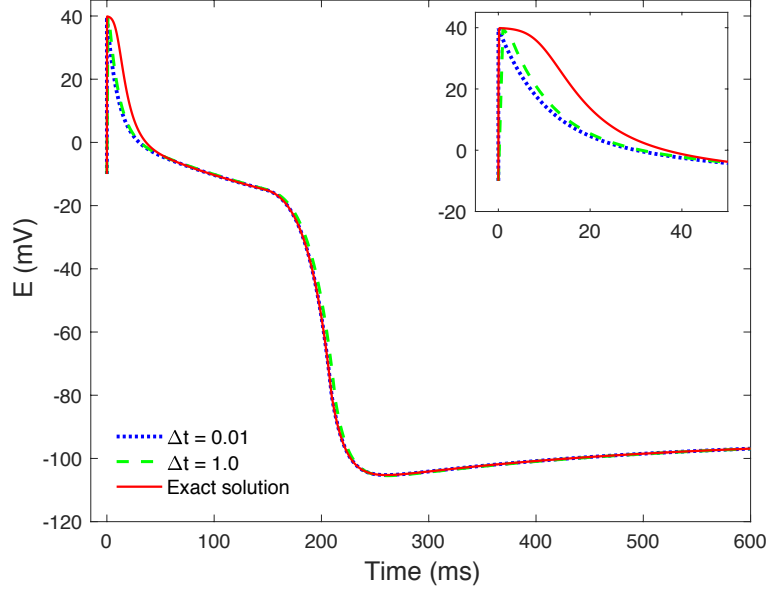


Figure 7.3: The solution of E solved using HMM in comparison to the exact solution (solid red line). Dotted blue and dashed green line are for $\Delta t = 0.01$ and 1.0 , respectively. The global mean error for both solutions are 0.35 and 0.6 . The small inset figure is the solution of E for $t \in [0, 50]$.

numerical integration of ordinary differential equations. The solver is defined below,

$$y_{i+1} = y_i + \Delta t \mathbf{F}(y_i, t_i), \quad (7.10)$$

where $y = E, h, n$ and \mathbf{F} is the local kinetics of each variables as defined in eqs. (5.1), (5.3) and (5.4). For all the numerical solvers, h and n were solved first, then the results were substituted in the E equation.

- Implicit Euler method

The scheme for this implicit method (or backward Euler method) is,

$$y_{i+1} = y_i + \Delta t \mathbf{F}(y_{i+1}, t_{i+1}). \quad (7.11)$$

Due to linearity of \mathbf{F} , the algorithms can be split into three respective intervals. They are,

If $E \in [E_*, \infty)$,

$$E_{i+1} = \frac{E_i + \frac{\Delta t}{\varepsilon_2} \left(\frac{G_{Na} E_{Na} h_{i+1}}{\varepsilon_1} + g_{22} n_{i+1} + k_3 E_3 \right)}{1 + \frac{\Delta t}{\varepsilon_2} \left(\frac{G_{Na} h_{i+1}}{\varepsilon_1} + k_3 \right)}, \quad (7.12)$$

$$h_{i+1} = \frac{h_i}{1 + \Delta t \frac{F_h}{\varepsilon_1 \varepsilon_2}},$$

$$n_{i+1} = \frac{n_i + \Delta t f_n}{1 + \Delta t f_n}.$$

If $E \in [E_+, E_*)$,

$$\begin{aligned} E_{i+1} &= \frac{E_i + \frac{\Delta t}{\varepsilon_2}(g_{22}n_{i+1} - k_2E_2)}{1 - \frac{\Delta t}{\varepsilon_2}k_2}, \\ h_{i+1} &= \frac{h_i}{1 + \Delta t \frac{F_h}{\varepsilon_1 \varepsilon_2}}, \\ n_{i+1} &= \frac{n_i + \Delta t f_n}{1 + \Delta t f_n}. \end{aligned} \quad (7.13)$$

If $E \in [-\infty, E_+)$,

$$\begin{aligned} E_{i+1} &= \frac{E_i + \frac{\Delta t}{\varepsilon_2}(g_{21}n_{i+1} + k_1E_1)}{1 + \frac{\Delta t}{\varepsilon_2}k_1}, \\ h_{i+1} &= \frac{h_i + \Delta t \frac{F_h}{\varepsilon_1 \varepsilon_2}}{1 + \Delta t \frac{F_h}{\varepsilon_1 \varepsilon_2}}, \\ n_{i+1} &= \frac{n_i}{1 + \Delta t f_n r}. \end{aligned} \quad (7.14)$$

- 4th order Runge-Kutta (RK4) method

Runge-Kutta is a higher order method compared to Euler method, which requires the method to take some intermediate steps before taking a second step. The scheme is described below,

$$\begin{aligned} y_{i+1} &= y_i + \frac{1}{6}(k_1 + 2k_2 + 2k_3 + k_4), \\ k_1 &= \Delta t \mathbf{F}(y_i, t_i), \\ k_2 &= \Delta t \mathbf{F}(y_i + \frac{k_1}{2}, t_i + \frac{\Delta t}{2}), \\ k_3 &= \Delta t \mathbf{F}(y_i + \frac{k_2}{2}, t_i + \frac{\Delta t}{2}), \\ k_4 &= \Delta t \mathbf{F}(y_i + k_3, t_i + \Delta t). \end{aligned} \quad (7.15)$$

- 2nd order Adam-Bashforth (AB) method

Adam-Bashforth method is a linear multistep method. The method uses the information from several previous points and derivative values in order to solve for the next time step. The algorithm is as follows,

$$y_{i+2} = y_{i+1} + \frac{3}{2}\Delta t \mathbf{F}(y_{i+1}, t_{i+1}) - \frac{1}{2}\Delta t \mathbf{F}(y_i, t_i). \quad (7.16)$$

- Rush-Larsen (RL) method

The gating variables h and n in (5.1) can be reformulated as

$$\frac{dz}{dt} = \frac{z_\infty - z}{\tau_z}, \quad \text{where, } z_\infty = \frac{\alpha_z}{\alpha_z + \beta_z}, \quad \tau_z = \frac{1}{\alpha_z + \beta_z}, \quad (7.17)$$

	HMM	Explicit Euler	Implicit Euler
max Δt	2.0	0.06	3.0
	Rush-Larsen	Runge-Kutta	Adam-Bashforth
max Δt	0.06	0.13	0.05

Table 7.1: Approximation of maximum time step allowed for each numerical solver to accurately solve the modified caricature Noble model. The solution diverges if the value of the time step is larger than the listed value.

and $\alpha_z = \alpha_z(E)$ and $\beta_z = \beta_z(E)$ for $z = h, n$. For this model, α_z and β_z are defined as below,

$$\begin{aligned}\alpha_h &= H(E_{\dagger} - E) \frac{F_h}{\varepsilon_1 \varepsilon_2}, & \beta_h &= \frac{F_h}{\varepsilon_1 \varepsilon_2} (1 - H(E_{\dagger} - E)), \\ \alpha_n &= H(E - E_{\dagger}) F_n(E), & \beta_n &= F_n(E) (1 - H(E - E_{\dagger})).\end{aligned}\tag{7.18}$$

The RL method assumes that the transmembrane voltage E is constant over each time step and allowing (7.17) to be treated as linear ODE with an exact solution given by,

$$z_{i+1} = z_{\infty} + (z_i - z_{\infty}) \exp(-\Delta t / \tau_z).\tag{7.19}$$

For other non-gating variables, one can solve using any available numerical method. For simplicity and the sake of comparison, we use explicit Euler method for solving E .

These solvers are used to solve the modified caricature Noble model by varying the time step from the smallest possible value until the method no longer converges where the action potential is no longer produced.

7.4 The efficiency of the method

We then compare the results from all these solvers with HMM in order to investigate the stability limit and execution time. For the stability limit, we solved the modified caricature Noble model using various time steps for every solver. The AP global mean error between numerical and exact solutions was measured by using the following equation,

$$\varepsilon = \frac{1}{M} \sum_{i=1}^M |E_i^{\text{num}} - E_i^{\text{exact}}|\tag{7.20}$$

where E_i^{num} and E_i^{exact} are the computed voltage, E with numerical solver and exact solution (5.6), respectively. To measure the execution time of each solver, we calculated the time needed for the particular solver to solve for 100 action potentials at a basic cycle length of 1000 ms. Each simulation was executed using MATLAB v2017b with a 64-bit Intel processor. The results for both global mean error and CPU time are shown in Figure 7.4. As what we expected, the

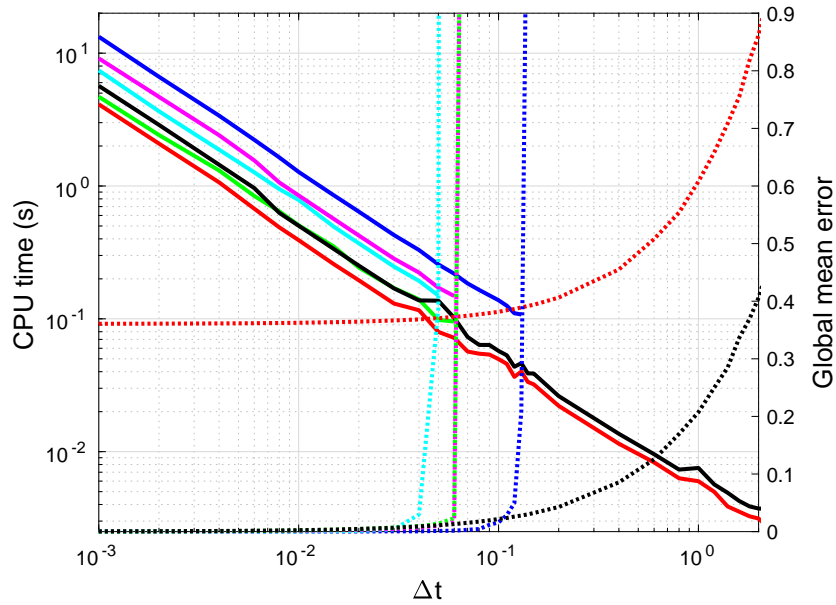


Figure 7.4: The CPU time and global mean error for various numerical methods used to solve the modified caricature Noble model. The solid lines and dotted lines are the CPU time and global mean error for every used methods, respectively. The CPU time for Rush-Larsen method is overlapped by the CPU time of Euler method. Red is for HMM, blue is for Runge-Kutta, green is for explicit Euler, black is for implicit Euler, cyan is for Adam-Bashforth and magenta is for Rush-Larsen method.

CPU time decreases as the size of the time-step increases. This is because the solver needs to take fewer time steps to solve the model when the time step is increased. From the Figure, we can also observe that HMM has the fastest computational time compared to other numerical solvers. Explicit Euler and implicit Euler methods are slightly slower than HMM and these two methods seem to be comparable between each other, but it is only valid for very small time-step (Δt approximately less than 0.06). The explicit Euler method breaks after the solver reaches the maximum time step. Runge-Kutta is the slowest solver because the solver needs to solve large algorithms at every time step. Adam-Bashforth and Rush-Larsen exhibit comparable CPU time.

Other than faster computational time, the stability and the accuracy of the method are also important. The primary goal is to construct a numerical scheme that not only has a faster execution time but can also preserve the accuracy of the solutions. In comparison to other numerical methods, HMM and the implicit Euler method are the most stable, although HMM accumulates larger global mean error than all other methods (Figure 7.4). The large value exhibited in HMM is mainly due to the difference in the post-overshoot drop, as shown in Figure 7.3. Nevertheless, from our viewpoint, the error level here is still acceptable since the important action potential biomarkers are still well preserved. In addition, the implicit Euler maintains a small global mean error, despite increasing in time step. Also, from Table 7.1, we can see that the implicit Euler method has the biggest time step before the method breaks. From our

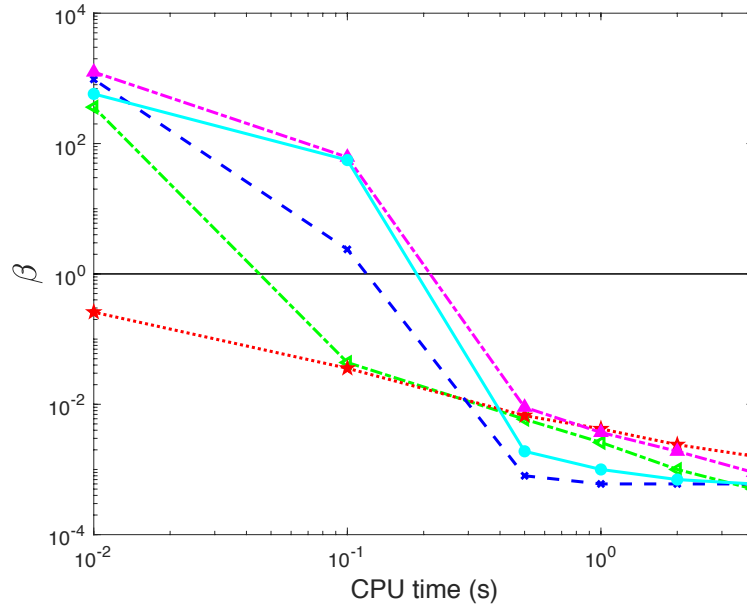


Figure 7.5: The log-log plot of method efficiency, β . The black solid line at $\beta = 1$ indicates the efficiency of HMM in comparison to other numerical methods. The green line is for the explicit Euler method, the blue line is for the implicit Euler method, the cyan line is for AB method, the blue line is for RK4 method and the magenta line is for the RL method.

study, we find that the second most stable method is shown by HMM, followed by Runge-Kutta method and the least stable method is Adam-Bashforth method. Explicit Euler, Rush-Larsen and Adam-Bashforth methods have almost similar stability limit and are the least stable.

The efficiency of each numerical method is evaluated based on its ability to solve the model with less computational time but at the same time preserves the accuracy of the solution. To quantify the efficiency of every solver, we use the following equation,

$$\text{Method efficiency, } \beta = \frac{\varepsilon \text{ of method X for CPU time } \alpha}{\varepsilon \text{ of HMM for CPU time } \alpha}. \quad (7.21)$$

The global mean error of a particular method is compared with HMM at similar CPU time. At a given CPU time, if HMM has lower global mean error than the other solver, then it shows that HMM has a better resolution and accuracy level. Thus, suggesting that HMM is more efficient than the other solver. In particular, if the value of β is greater than 1, then it indicates that HMM is more efficient than the compared method. The result for the method efficiency between HMM and other numerical methods is shown in Figure 7.5. From the Figure, we can observe that at CPU time larger than 0.5 seconds (time step below than ~ 0.04), the HMM is less efficient than the other schemes. This is because HMM produces a considerably large global mean error, although this method has faster computational time than most of the other schemes. As the time step gets larger (CPU time reduces), the HMM becomes more efficient than the other solvers, with the exception being for the implicit Euler method. At large time step, the other methods

reach their stability limit and eventually they diverge, making HMM more efficient. The implicit Euler scheme remains with the most excellent accuracy, despite increasing in time step.

In conclusion, from our analysis, we show that the implicit Euler scheme is the most efficient numerical solver for this model. The next most efficient method is HMM, then followed by the explicit Euler method and Runge-Kutta. The Rush-Larsen and Adam Bashforth method have almost equal efficiency level. Note that although the implicit Euler method seems the best, it is only possible to apply the method on this model because the model is linear and so equation (5.1) can be solved to give (7.12), (7.13) and (7.14). For a general nonlinear AP model, the equation that describes the process of action potential excitation cannot be inverted and so the implicit Euler is not easily implemented. But the HMM can be applied and it has similar efficiency. Also, the choice of a numerical method to be used to solve the model may depend on the goal of the particular work. If the accuracy of the solution is the only priority, then all of the above methods are suitable to be implemented, regardless of their computational speed.

7.5 Error analysis for heterogeneous multiscale method

This error analysis for heterogeneous multiscale method was discussed in Kuehn (2015). In order to illustrate the error analysis, we consider a simple system of ODEs as defined in (7.1). For simplicity, we apply the forward Euler method on our both HMM microsolver and macrosolver. For HMM macrosolver we have,

$$y^{n+1} = y^n + \Delta t \tilde{g}(y^n) \quad (7.22)$$

such that $\tilde{g}(y^n) = g(x^{n,k}, y^n)$. Meanwhile, for HMM microsolver, we have

$$x^{n,k+1} = x^{n,k} + \Delta \tau (x^{n,k} - h(y^n)) \quad (7.23)$$

where $\Delta \tau = \Delta t / \varepsilon$ and $k = 0, 1, \dots, M$. k must be sufficiently large so that $x^{n,M}$ will approach N (stationary value). Next, we consider the global error between the HMM macrosolver and the true slow flow (exact solution) defined as follows,

$$E^n = y^n - Y(t^n) \quad (7.24)$$

where $t^n = n\Delta t$. From the definition of global error, we have,

$$\begin{aligned}
\frac{E^{n+1} - E^n}{\Delta t} &= \frac{y^{n+1} - Y^{n+1} - y^n + Y^n}{\Delta t}, \\
&= \frac{y^n + \Delta t \tilde{g}(y^n) - y^n - [Y^{n+1} - Y^n]}{\Delta t}, \\
&= \frac{\Delta t \tilde{g}(y^n) - [Y^{n+1} - Y^n] + \Delta t G(Y^n) - \Delta t G(Y^n)}{\Delta t}, \\
&= \tilde{g}(y^n) - G(Y^n) - \left[\frac{Y^{n+1} - Y^n}{\Delta t} + G(Y^n) \right], \\
&= \tilde{g}(y^n) - G(Y^n) - G(y^n) + G(y^n) - T^n,
\end{aligned} \tag{7.25}$$

such that T^n is the local truncation error. We then rearrange the equation and take the norms, to get

$$|E^{n+1}| = |E^n + \Delta t (G(y^n) - G(Y^n))| + |\Delta t (\tilde{g}(y^n) - G(y^n))| - \Delta t |T^n|. \tag{7.26}$$

Note that by Lipschitz condition, we have,

$$|G(y^n) - G(Y^n)| \leq L_G |y^n - Y^n| = L_G |E^n|, \tag{7.27}$$

where L_G is the Lipschitz constant and plucking the above equation into (7.26), yields

$$|E^{n+1}| \leq (1 + \Delta t L_G) |E^n| + \Delta t |T^n| + \Delta t |\tilde{g}(y^n) - G(y^n)|. \tag{7.28}$$

for $n = 0, 1, \dots, N-1$. If we look at closely, the first two terms on the right hand side appear in the common global error analysis for the forward Euler method on the macroscale. The last term contains the error on the microscale. Taking the inequality, we can show by induction such that

$$\begin{aligned}
|E^n| &\leq \left[\max_{0 \leq n \leq N-1} |T^n| + \max_{0 \leq n \leq N-1} |\tilde{g}(y^n) - G(y^n)| \right] ((1 + \Delta t L_G)^n - 1), \\
&= [E_{\text{mac},N} + E_{\text{mic},N}] ((1 + \Delta t L_G)^n - 1), \\
&\leq [E_{\text{mac},N} + E_{\text{mic},N}] (\exp(L_G n \Delta t) - 1),
\end{aligned} \tag{7.29}$$

for $n = 0, 1, \dots, N$. This inequality shows that the error analysis techniques for the macroscale solver for HMM is not similar to the standard methods because of the extra error term in the microsolver approximation. Next, we want to estimate the error for microscale solver, $E_{\text{mic},N}$. In particular, we want to estimate $|\tilde{g}(y^n) - G(y^n)|$. Using the definition of Lipschitz condition, we have,

$$\begin{aligned}
|\tilde{g}(y^n) - G(y^n)| &= |g(x^{n,M}, y^n) - g(h(y^n), y^n)|, \\
&\leq L_g |x^{n,M} - h(y^n)|,
\end{aligned} \tag{7.30}$$

such that L_g is the Lipschitz constant. We hold this for the moment and let us define

$$e^{n,k} = x^{n,k} - h(y^n), \quad (7.31)$$

where $e^{n,k}$ is the error between HMM microsolver and the true slow flow. From the HMM microsolver, we have,

$$\begin{aligned} e^{n,k} &= [x^{n,k+1} + \Delta\tau(x^{n,k} - h(y^n))] - h(y^n), \\ &= [x^{n,k+1} - h(y^n)] + \Delta\tau(x^{n,k} - h(y^n)), \\ &= e^{n,k+1} + \Delta\tau e^{n,k}. \end{aligned} \quad (7.32)$$

Rearrange the equation, we get,

$$e^{n,k+1} = e^{n,k}(1 - \Delta\tau), \quad (7.33)$$

for $k = 0, 1, \dots, M$. Iterating the equation leads to

$$e^{n,M} = e^{n,0}(1 - \Delta\tau)^M. \quad (7.34)$$

Using the result of the last argument in (7.30) and (7.31) yield

$$\begin{aligned} L_g|x^{n,M} - h(y^n)| &= L_g|e^{n,M}|, \\ &= L_g|e^{n,0}(1 - \Delta\tau)^M|. \end{aligned} \quad (7.35)$$

Therefore, from (7.30), we end with

$$|\tilde{g}(y^n) - G(y^n)| \leq L_g|e^{n,0}(1 - \Delta\tau)^M|. \quad (7.36)$$

We can now define the error for HMM microsolver in (7.29). From the last inequality, we have

$$\begin{aligned} E_{\text{mic},N} &= \max_{0 \leq n \leq N-1} |\tilde{g}(y^n) - G(y^n)|, \\ &\leq \max_{0 \leq n \leq N-1} L_g|e^{n,0}(1 - \Delta\tau)^M|, \\ &= \kappa_1|1 - \Delta\tau|^M, \end{aligned} \quad (7.37)$$

where $\kappa_1 = \max_{0 \leq n \leq N-1} L_g|e^{n,0}| = L_g \max_{0 \leq n \leq N-1} |x^{n,0} - h(y^n)|$. Substituting the last argument into (7.29), the global error for HMM with Euler micro and macrosolvers is defined as following,

$$|E^n| \leq [\kappa_0\Delta t + \kappa_1|1 - \Delta\tau|^M](\exp(L_G n\Delta t) - 1). \quad (7.38)$$

The error $|E^n|$ has one term for the macrosolver and it can be made small by choosing $0 < \Delta t \ll 1$. Meanwhile, we can also minimize the macrosolver error by using $\Delta \tau < 1$ and making M sufficiently large. The decoupling approach in this method makes it possible to choose two different step sizes, which then stabilizes the method.

7.6 Drawbacks of the heterogeneous multiscale method

In this section, we briefly discuss the limitation of HMM. First and foremost, the application of HMM method is not straightforward and can only work if the model can be dissected into microscopic and macroscopic systems. For a biophysically detailed model of cardiac electrophysiology, this might be extremely challenging and difficult due to a large number of state variables present in the model. An ideal approach is to consider the reduction version of such a model using a robust asymptotic reduction method (Biktasheva et al. 2006). Also, the implementation of this method requires us to know the “speed” of each variable in the model, i.e., to identify which variables have a fast, intermediate and slow timescale, before the model can be split up to fast and slow-time systems. In order to distinguish the variables according to their speed, a speed analysis (see Suckley (2004)) needs to be carried out beforehand.

The HMM can be applied to tissue simulation by including it as a component within an operator splitting method (Qu and Garfinkel 1999, Strang 1968). This is a direction for further research.

7.7 Conclusion

In this chapter, we have introduced an efficient asymptotic-numerical method for solving the modified caricature Noble model by using the asymptotic structures of the model. We showed that the method has better stability and more robust in comparison to other numerical solvers (explicit Euler, Runge-Kutta, Adam Bashforth, Rush-Larsen method), with the exception being for implicit Euler method. The method also has the fastest execution time with an acceptable global mean error. The large error was mainly due to discrepancy at the post-overshoot drop (Figure 7.3). The method, however, still preserved the important action potential biomarkers. Note that although the implicit Euler method exhibited the best efficiency, the method, however, is only possible to apply on this model because the model is linear. For a more detailed AP model, the method cannot be easily implemented as the equation that describes the process of action potential excitation is nonlinear. At each time step, the solver needs to solve the algebraic equation and this process increases the computational load. But the HMM can be applied on the those models and it has comparable efficiency. In addition, the HMM also has several drawbacks which require further investigation.

In the next chapter, we further extend the analysis and application of caricature Noble model

to investigate the mechanisms of cardiac alternans. The slow-slow time system of the model will be used again to derive the analytical formula of APD restitution curve and then to identify the region of parameter values where alternans will appear.

Chapter 8

Mechanisms of cardiac alternans

8.1 Introduction

Cardiac alternans is a condition wherein the heartbeat cyclically varies between weak and strong despite a constant heart rate. It was described many years ago in experimental conditions and clinically, in particular, in patients with heart disease like atrial fibrillation. It is a severe condition which may lead to death. Hence, understanding the mechanisms and causes of cardiac alternans is very important, especially for controlling, treating and terminating the onset of alternans.

Numerical simulation and experimental studies have made significant contributions to understand the mechanisms of cardiac alternans (Bayer et al. 2016, Edwards and Blatter 2014, Fox et al. 2002, Karma 1994, Ten Tusscher et al. 2007). To date, restitution properties of cardiac cells have been utilised to explain the alternans behaviour, where it describes a functional relationship between the duration of a cardiac action potential and the length of its previous diastolic interval. However, the experimental protocols for measuring restitution encounter a number of difficulties, including that of distinguishing the ultimate periodic regime from transient behaviour because of the presence of cardiac memory (Gilmour et al. 1997, Tolkacheva et al. 2003).

Standard experimental protocols like dynamic restitution pacing method require the cell to be periodically stimulated at a fixed interval of basic cycle length until it settles into a stable periodic response. Several periodic responses have been recorded in experiments (Hall et al. 1999, Visweswaran et al. 2013). For instance, every successful stimulus may excite an action potential with an identical shape (1:1 response). However, under certain conditions, only every second stimulus may excite an action potential and produce a 2:1 response. Under different conditions, the action potential duration may alternate between long and short (alternans 2:2 response). It is commonly assumed that the 1:1 response represents the healthy function of the cardiac cell; meanwhile, the other two responses are viewed as “instabilities” of the normal response which may potentially lead to cardiac arrhythmias (Cherry et al. 2012, Karma 1994). Hence, the action potential duration (APD) restitution maps can be used to study such instabilities. On the other hand, cardiac alternans can still occur due to other ion mechanisms, for example, fluctuation

calcium handling dynamics which is caused by calcium currents (Tomek et al. 2018, Tse et al. 2016). However, in this study, we will only focus on the AP-driven alternans as the model does not include the calcium current.

With this motivation, here in this chapter, we want to derive an explicit discrete restitution map for caricature Noble model and study their equilibrium branches and bifurcations. We then explore the regions in the parameter space of caricature Noble model where normal 1:1 response and alternans 2:2 occur. The parameter space is validated with some numerical simulations (see section 8.4). We also develop a framework formulated in terms of boundary value problems for studying cardiac restitution. This framework can be used to derive analytically or compute numerically different branches of the action potential duration restitution map from the full excitable models. Our method is validated by comparing the asymptotic restitution map with the boundary value problem formulated restitution curves. Note that this is a continuation of the work by Asgari-Targhi (2017). Due to this, we use the original caricature Noble model (with n^4) as formulated in (5.1) and (5.2). The exact analytical and asymptotic solutions of this model were derived in Appendix A.2. In this chapter, we improve and make minor corrections to earlier works by Asgari-Targhi (2017); in particular, we

- validate and confirm the proofs of some lemmas and propositions.
- construct new figures of APD restitution curves using both IVP and BVP and compare them with asymptotic restitution curve.
- fit the model to a canine ventricular model and validate the region in the parameter space where normal 1:1 response and alternans occur.

8.2 APD restitution map from the slow-slow-time system

Action potential sequence is excited by the periodic pacing condition. The success of the excitation of the next AP depends on the previous diastolic interval (DI), which is the rest period between repolarisation and the next excitation. The relation between APD and DI was first described by using a graphical method, relating them to APD restitution map (Nolasco and Dahlen 1968). The APD restitution map relates the durations of subsequent APs and is usually written in the following variants,

$$\begin{aligned} \text{APD}_{k+1} &= \varphi(\text{APD}_k) \\ &= \varphi(B - \text{DI}_k) \end{aligned} \tag{8.1}$$

where B is the basic cycle length and it is kept constant for every stimulation. In this section, our aim is to derive a simple APD restitution map using the slow-slow time system in caricature

Noble model. The simplest APD restitution map of (5.1) and (5.2) is obtained in the limits $\varepsilon_1, \varepsilon_2 \rightarrow 0^+$ as follows.

Lemma 8.2.1. *For an AP sequence generated using slow-slow time system (A.15),*

$$APD_k = a(n_{k-1}), \quad a(x) \equiv f_n^{-1} \log((1-x)/(1-n_*)), \quad (8.2a)$$

$$D_k = d(n_k), \quad d(x) \equiv (rf_n)^{-1} \log(n_*/x), \quad (8.2b)$$

$$n_k \equiv n(kB), \quad k \in \mathbb{N}.$$

such that $n_k = n(kB)$ represents the value of gating variable n at the beginning of the $(k+1)$ -st AP for $k \in \mathbb{N}$. n_* is the maximal value of super-slow gating variable n and the value is defined as in (5.22) but with the power of $1/4$.

Proof. The result can be obtained by integrating the equation (A.15b) along the systolic branch as following,

$$\begin{aligned} APD_k &= \int_{(k-1)B}^{(k-1)B+APD_k} dt = \frac{1}{f_n} \int_{n(k-1)B}^{n_*} \frac{dn}{f_n(1-n)} \\ &= -\frac{1}{f_n} \log(1-n) \Big|_{n(k-1)B}^{n_*} = \frac{1}{f_n} \log\left(\frac{1-n_{k-1}}{1-n_*}\right), \\ D_k &= \int_{(k-1)B+APD_k}^{kB} dt = -\frac{1}{rf_n} \int_{n_*}^{n(kB)} \frac{dn}{n} \\ &= -\frac{1}{rf_n} \log(n) \Big|_{n_*}^{n(kB)} = \frac{1}{rf_n} \log\left(\frac{n_*}{n_k}\right). \end{aligned} \quad (8.3)$$

□

Proposition 1. *An APD restitution map relating APD_{k+1} to APD_k is given by*

$$\begin{aligned} APD_{k+1} &= \Phi(APD_k), \\ \Phi(APD) &= F(\tilde{\mathbf{a}}, A) = F(\mathbf{a}, B-A) = \frac{1}{f_n} \log\left(\frac{1-n_* \exp(-rf_n(B-APD))}{1-n_*}\right), \end{aligned} \quad (8.4)$$

where $\tilde{\mathbf{a}} = [\mathbf{a}, B]^T = [r, f_n, n_*, B]^T$ is a vector of parameters.

Proof. From Lemma (8.2.1), we have

$$D_k = \frac{1}{rf_n} \log\left(\frac{n_*}{n_k}\right) \quad (8.5)$$

and we know that $D_k = B - APD_k$. Substituting this into the above equation yields,

$$B - APD_k = \frac{1}{rf_n} \log\left(\frac{n_*}{n_k}\right) \quad (8.6)$$

and from some algebraic rearrangements, we can express n_k in terms of other parameters

$$n_k = n_* \exp(-rf_n(B - \text{APD}_k)). \quad (8.7)$$

The result is obtained by plucking n_k in expression (8.2a) written for APD_{k-1} and it gives us,

$$\text{APD}_{k+1} = \frac{1}{f_n} \log \left(\frac{1 - n_* \exp(-rf_n(B - \text{APD}_k))}{1 - n_*} \right). \quad (8.8)$$

□

Lemma (8.2.1) describes the parametric representation of the action potential duration restitution map and Proposition (8.4) expresses an equivalent explicit representation. Next, we can begin to find the fixed points of Φ and Φ^2 which corresponds to 1:1 and 2:2 responses, respectively.

Proposition 2. *The equation $\overline{\text{APD}} = \Phi(\overline{\text{APD}})$ has a unique solution branch given in parametric form by*

$$\overline{\text{APD}} = a(\bar{n}), \quad \overline{D} = d(\bar{n}), \quad (8.9)$$

with a parameter $\bar{n} \in [0, n_{thr}]$ which $n_{thr} \in [0, n_*)$.

Proof. To find the fixed point of Φ , we can either directly solve the transcendental equation $\overline{\text{APD}} = \Phi(\overline{\text{APD}})$ or use the parametric representation of Lemma (8.2.1). For simplicity, we choose the later method as solving the transcendental equation might be analytically impossible. In a 1:1 response, we have $\text{APD}_k = \text{APD}_{k+1}$ and $D_k = D_{k+1}$. From Lemma (8.2.1), these are equivalent to $a(n_{k-1}) = a(n_k)$ and $d(n_k) = d(n_{k+1})$, respectively. By the bijectivity of the logarithmic function, we have the following solutions $n_{k-1} = n_k \equiv \bar{n}$ and $n_k = n_{k+1} \equiv \bar{n}$, respectively. From here, we deduce that in a 1:1 response, the action potentials begin from similar values of the n gate, \bar{n} , hence expressions (8.9) hold. The parameter \bar{n} is a gating variable and must be in between 0 and 1. In addition, AP cannot be excited below the n_{thr} , hence, $\bar{n} \in [0, n_{thr}]$. □

Proposition 3. *The equation $\overline{\overline{\text{APD}}} = \Phi \circ \Phi(\overline{\overline{\text{APD}}})$ has three solution branches: the first one is identical to (8.9), and the other two are given in parametric form by*

$$\overline{\overline{\text{APD}}}_{\text{even}} = a(\alpha n_b), \quad \overline{\overline{D}}_{\text{even}} = d(n_b), \quad (8.10a)$$

$$\overline{\overline{\text{APD}}}_{\text{odd}} = a(n_b), \quad \overline{\overline{D}}_{\text{odd}} = d(\alpha n_b), \quad (8.10b)$$

$$n_b = \left(\alpha^{1/r} - 1 \right) / \left(\alpha^{(r+1)/r} - 1 \right), \quad (8.10c)$$

with a parameter $\alpha \in (0, \infty)$.

Proof. We use the equivalent parametric representation of Lemma (8.2.1) to find the fixed points of Φ^2 , rather than solving the transcendental equation $\overline{\overline{\text{APD}}} = \Phi \circ \Phi(\overline{\overline{\text{APD}}})$ directly. For 2:2

AP responses, we have these relations; $\text{APD}_k = \text{APD}_{k+2}$ and $\text{APD}_{k+1} = \text{APD}_{k+3}$ as well as $D_k = D_{k+2}$ and $D_{k+1} = D_{k+3}$. By implementing equations (8.2), we obtain $n_k = n_{k+2} \equiv n_a$ and $n_{k+1} = n_{k+3} \equiv n_b$. Since the BCL, B is constant, we have,

$$B = \text{APD}_k + D_k = \text{APD}_{k+1} + D_{k+1} \Leftrightarrow a(n_a) + d(n_b) = a(n_b) + d(n_a). \quad (8.11)$$

From expressions (8.2), then we get

$$\begin{aligned} \frac{1}{f_n} \log \left(\frac{1-n_a}{1-n_*} \right) + \frac{1}{rf_n} \log \left(\frac{n_*}{n_b} \right) &= \frac{1}{f_n} \log \left(\frac{1-n_b}{1-n_*} \right) + \frac{1}{rf_n} \log \left(\frac{n_*}{n_a} \right) \\ \log \left[\left(\frac{1-n_a}{1-n_*} \right) \left(\frac{n_*}{n_b} \right)^{1/r} \right] &= \log \left[\left(\frac{1-n_b}{1-n_*} \right) \left(\frac{n_*}{n_a} \right)^{1/r} \right] \\ (1-n_a)^r \left(\frac{n_*}{n_b} \right) &= (1-n_b)^r \left(\frac{n_*}{n_a} \right) \\ \left(\frac{1-n_a}{1-n_b} \right)^r &= \frac{n_b}{n_a}. \end{aligned} \quad (8.12)$$

Next, we set $n_a = \alpha n_b$ where α is the ratio between n_a and n_b . Replacing n_a with this expression to obtain

$$\begin{aligned} \left(\frac{1-\alpha n_b}{1-n_b} \right)^r &= \frac{n_b}{\alpha n_b} \\ \frac{1-\alpha n_b}{1-n_b} &= \frac{1}{\alpha^{1/r}} \\ 1-\alpha n_b &= \frac{1}{\alpha^{1/r}} (1-n_b) \\ -\alpha n_b + \frac{1}{\alpha^{1/r}} n_b &= \frac{1}{\alpha^{1/r}} - 1 \\ n_b \left(\frac{1}{\alpha^{1/r}} - \alpha \right) &= \frac{1}{\alpha^{1/r}} - 1 \\ n_b &= \frac{\alpha^{1/r} - 1}{\alpha^{1+1/r} - 1} \end{aligned} \quad (8.13)$$

Notice that (8.11) is invariant regardless of switching n_a and n_b , hence we set $n_a \geq n_b$. Since both n_a and n_b are always nonnegative, we then have $n_a/n_b = \alpha \in [1, \infty)$. \square

Proposition 4. *The equilibrium (8.9) of the APD restitution map (8.4) loses stability in a flip (period-doubling) bifurcation at*

$$n_{\text{bif}} = 1/(1+r) \quad (8.14a)$$

or in terms of the BCL, alternatively at

$$B_{\text{bif}} = \frac{1}{f_n} \log \left(\frac{r n_*^{1/r} (1+r)^{(1-r)/r}}{(1-n_*)} \right). \quad (8.14b)$$

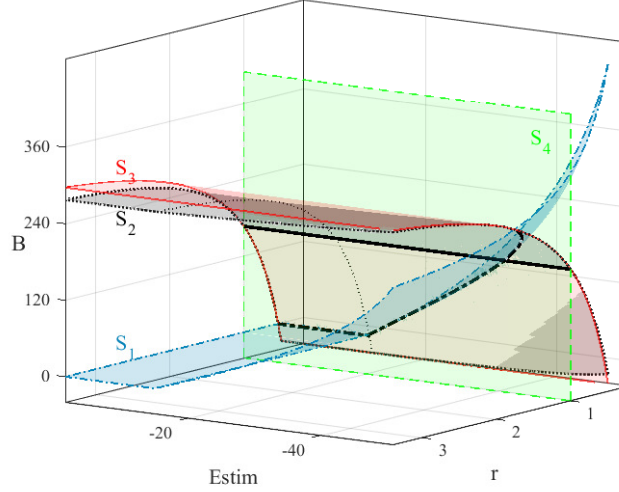


Figure 8.1: Bifurcation set in the Estim-r-B parameter space. The blue surface S1 is defined by (8.19) and indicates the threshold for existence of the 1:1 response. The transparent black surface S2 given by (8.20a) is the threshold for existence of the 2:2 response. The red surface S3 is defined by (8.14b) and illustrates the region where 2:2 response bifurcates from the 1:1 response. The green surface S4 with equation $r = 1$ separates region of alternans ($r > 1$) from healthy response ($r < 1$).

Proof. The result can be obtained by differentiating (8.4) with respect to APD,

$$\begin{aligned} \left. \frac{\partial F}{\partial \text{APD}} \right|_{\overline{\text{APD}}} &= \left. \frac{\partial}{\partial \text{APD}} \left[\frac{1}{f_n} \log \left(\frac{1 - n_* \exp(-rf_n(B - \text{APD}))}{1 - n_*} \right) \right] \right|_{\overline{\text{APD}}} \\ &= - \frac{n_* r \exp(-rf_n(B - \overline{\text{APD}}))}{1 - n_* \exp(-rf_n(B - \overline{\text{APD}}))} \end{aligned} \quad (8.15)$$

and then by setting $\left. \frac{\partial F}{\partial \text{APD}} \right|_{\overline{\text{APD}}} = -1$ (a condition where a fixed point is unstable and period doubling bifurcation occurs), we have

$$\begin{aligned} - \frac{n_* r \exp(-rf_n(B - \overline{\text{APD}}))}{1 - n_* \exp(-rf_n(B - \overline{\text{APD}}))} &= -1, \\ n_* \exp(-rf_n(B - \overline{\text{APD}}))(r + 1) &= 1, \\ n_* \exp(-rf_n \overline{\text{D}}) &= \frac{1}{r + 1}. \end{aligned} \quad (8.16)$$

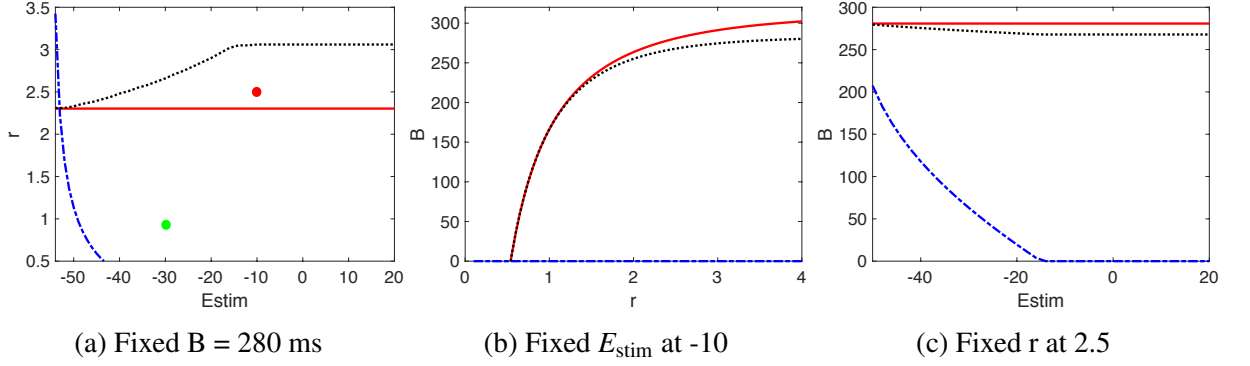


Figure 8.2: Cross-sections of the bifurcation set in Figure 8.1 at particular parameter values. The red and green dots in (a) are the parameter sets that we choose to construct the restitution curves in Figures 8.4a and 8.5a, respectively. The region between black line and red line is where the alternans occur.

Using equation (8.2b), the equation yields

$$\begin{aligned}
 n_* \exp(-r f_n d(\bar{n})) &= \frac{1}{r+1}, \\
 n_* \exp(-\log(n_*/\bar{n})) &= \frac{1}{r+1}, \\
 \bar{n} &= \frac{1}{r+1}.
 \end{aligned} \tag{8.17}$$

Evaluating (8.9) at $\bar{n} = 1/(r+1)$, we then get

$$\begin{aligned}
 \text{APD}_{\text{bif}} = a(n_{\text{bif}}) &= \frac{1}{f_n} \log\left(\frac{1/(1+r) - 1}{n_* - 1}\right) \\
 B_{\text{bif}} = a(n_{\text{bif}}) + d(n_{\text{bif}}) &= \frac{1}{f_n} \log\left(\frac{r n_*^{1/r} (1+r)^{(1-r)/r}}{1 - n_*}\right).
 \end{aligned} \tag{8.18}$$

□

Proposition 5. *The threshold value of BCL for excitation of a 1:1 response is*

$$\begin{aligned}
 \overline{\text{APD}}_{\text{thr}} = a(n_{\text{thr}}) &= f_n^{-1} \log\left(\frac{1 - n_{\text{thr}}}{1 - n_*}\right), \\
 \overline{D}_{\text{thr}} = d(n_{\text{thr}}) &= (r f_n)^{-1} \log(n_*/n_{\text{thr}}), \\
 \overline{B}_{\text{thr}} &= \overline{\text{APD}}_{\text{thr}} + \overline{D}_{\text{thr}}.
 \end{aligned} \tag{8.19}$$

Proof. Recall that the k -th AP can only be excited by a super-threshold stimulus $E_{\text{stim}} > E_2$ for which $n_{k-1} < n_{\text{thr}}$ where n_{thr} is given by (5.23). The result then follows by evaluation of (8.2.1) at $n = n_{\text{thr}}$. □

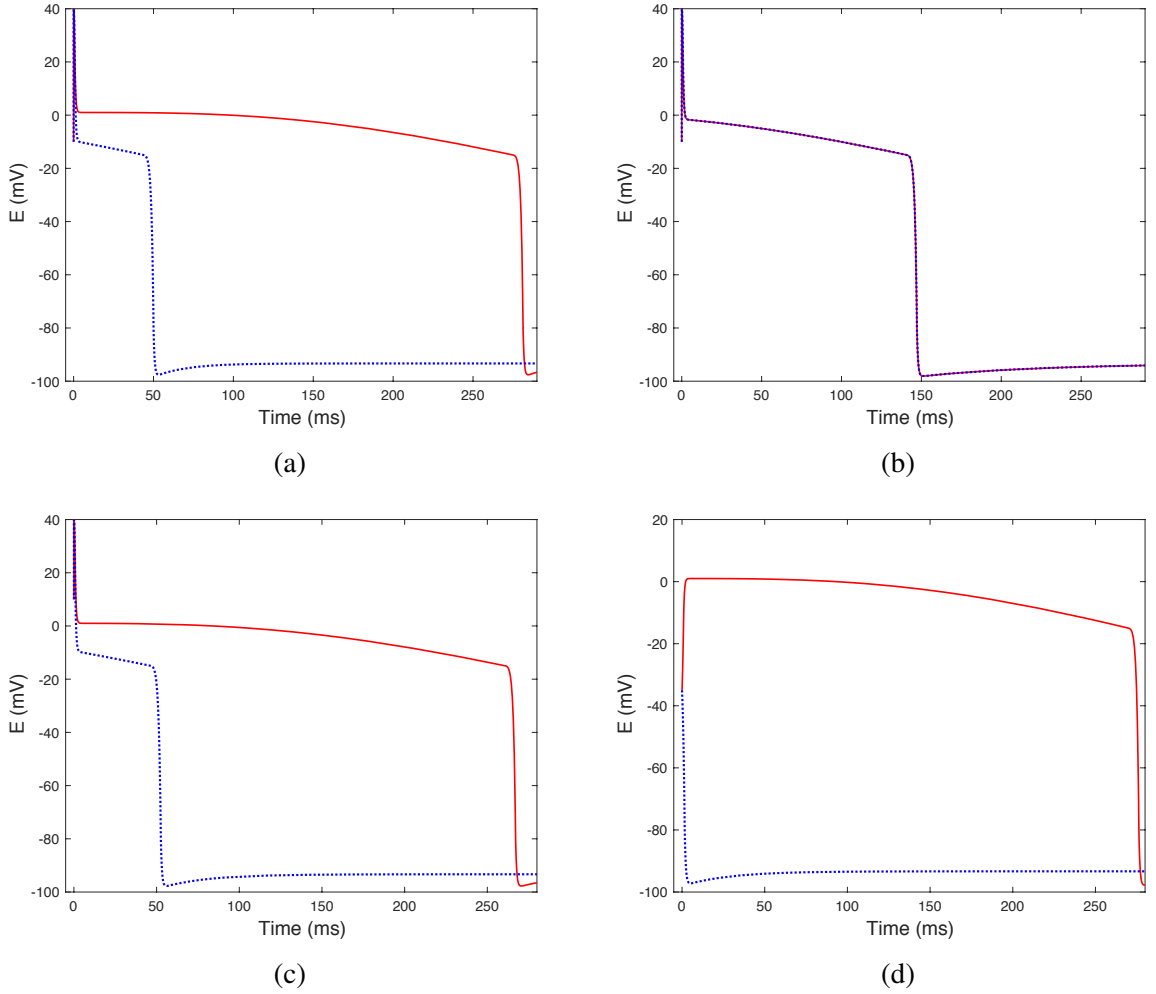


Figure 8.3: (**Top row**) Examples of AP trace generated using full system of caricature Noble model in the case of (a) $r = 3.5$ and (b) $r = 0.9$. $\varepsilon_2 = 0.05$, $E_{\text{stim}} = -10$ and $B = 290$ ms are fixed in both cases. (**Bottom row**) Examples of AP trace in the case of (c) $E_{\text{stim}} = 10$ mV and (d) $E_{\text{stim}} = -35$ mV. $\varepsilon_2 = 0.05$, $r = 2.5$ and $B = 280$ ms are fixed in both cases. Solid line and dashed line in each panel represent the action potential at 19-th and 20-th beat, respectively.

Proposition 6. *The threshold value of BCL for excitation of a 2:2 response is*

$$\bar{B}_{\text{thr}} = a(n_{\text{thr}}) + d(n_{\text{thr}}\alpha(n_{\text{thr}})) = a(n_{\text{thr}}\alpha(n_{\text{thr}})) + d(n_{\text{thr}}), \quad (8.20a)$$

where $\alpha(n_{\text{thr}})$ is the solution of the transcendental equation

$$n_{\text{thr}} = \left(\alpha^{1/r} - 1 \right) / \left(\alpha^{(r+1)/r} - 1 \right). \quad (8.20b)$$

Figure 8.1 shows the bifurcation set in the E_{stim} - r - B parameter space which is plotted using (8.19), (8.20a) and (8.14b). From the figure, we can see the region where alternans has appeared. In particular, the alternans mostly occur when $r > 1$ and the response disappear when $r < 1$. We plot examples of AP trace to demonstrate the parameter case in Figures 8.3a and 8.3a. The

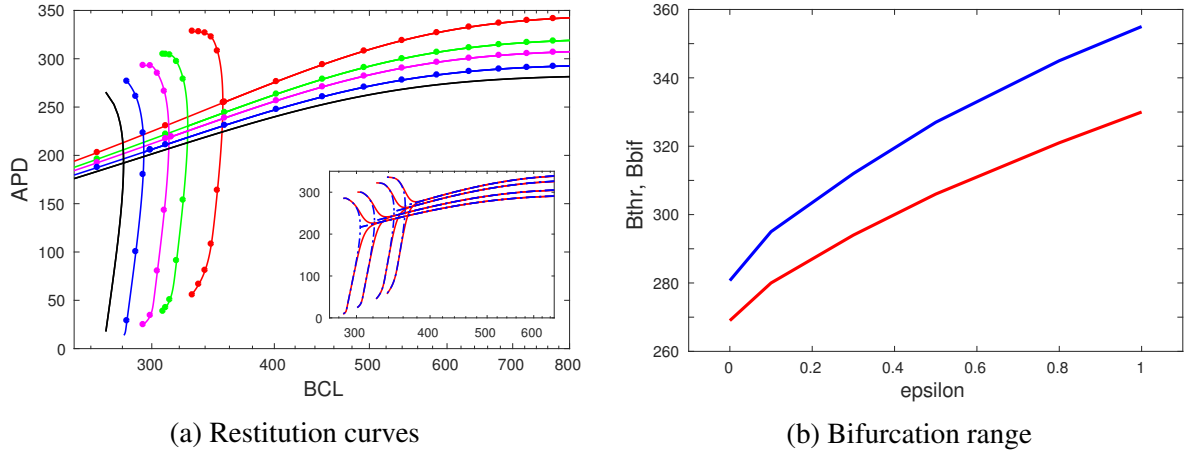


Figure 8.4: (a) The 1:1 and 2:2 restitution curves using analytical (solid line) and numerical BVP (circle dot). The red, green, magenta and blue curves correspond to $\epsilon_2 = 1, 0.5, 0.3, 0.1$, respectively. The black curve is the restitution curve of asymptotic solution corresponding to $\epsilon_2 = 0$. The inset figure shows the comparison of restitution curves between our approach (blue line) and dynamic pacing method (red line). r and E_{stim} are fixed at 2.5 and -10, respectively. (b) The region between two curves is where stable alternans occur. The blue and red curves are the data points for B_{bif} and $\overline{B}_{\text{thr}}$, respectively.

existence of the 2:2 alternans occurs in a very tight region, and it also depends on the value of E_{stim} . When a sufficiently strong E_{stim} is applied, the period of existence of 2:2 alternans becomes more prominent, as observed in Figure 8.2a. Given a similar condition of r and B , the model could exhibit 2:1 response when we paced the model using a weaker stimulus strength. Examples of AP trace for these two conditions can be seen in Figures 8.3c and 8.3d. A likely explanation for this behaviour is that the excitation threshold (5.23) gets affected by the value of E_{stim} . Although 2:1 response is not within the scope of our study, it is good to point out that strength of the stimulus is also responsible for 2:2 response and can only be achieved at the specific condition.

8.3 Constructing the APD restitution curves

APD restitution curve is used to exhibit the dynamical behaviour of action potentials when stimulating at various pacing rates. It can be characterised into two different types which are the normal 1:1 restitution curve and the alternans 2:2 restitution curves. The latter happens due to rapid heart rate and then trigger the APs to alternate between long and short waveforms, which is a common behaviour during arrhythmia. In this section, we want to construct the 1:1 and 2:2 restitution curves of caricature Noble model using the analytical formula in (8.9) and (8.10). We then compare the results with the APD restitution curves generated using the analytical solutions of boundary value problem.

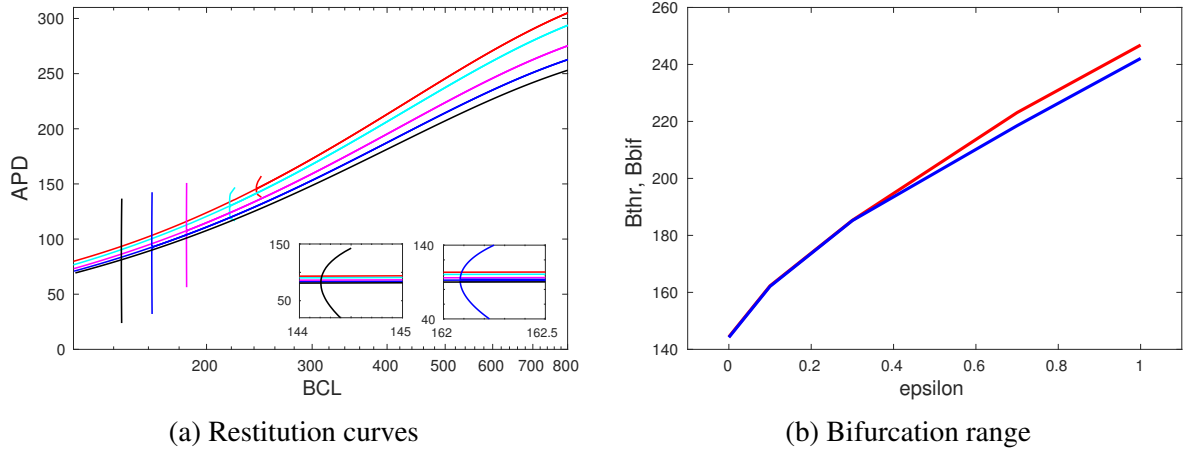


Figure 8.5: (a) The 1:1 and 2:2 restitution curves in the case of (unstable) alternans. The red, cyan, magenta and blue curves correspond to $\epsilon_2 = 1.0, 0.7, 0.3, 0.1$, respectively. The black curve is the restitution curve of asymptotic solution corresponding to $\epsilon_2 = 0$. r and E_{stim} are fixed at 0.9 and -30, respectively. (b) The region between two curves is where unstable alternans occur. The blue and red curves are the data points for B_{bif} and $\overline{B_{thr}}$, respectively.

8.3.1 1:1 restitution curves

To construct the 1:1 restitution curve, we pose the periodic boundary conditions as below,

$$\begin{aligned}
 E(0) &= E(t = B) = E_0 > E_*, \\
 h(0) &= h(t = B), \quad n(0) = n(t = B).
 \end{aligned}
 \tag{8.21}$$

and impose them to the solutions of initial value problem in (A.5a), (A.5b) and (A.5c). We firstly chose the value of n_0 which was varied between 0 and n_{thr} and then solved for t_{\dagger} such that (A.5a) satisfied $\overset{1}{n}(t = t_{\dagger}) = \overset{2}{n}(t = t_{\dagger})$. When constructing the restitution curve, t_{\dagger} was used as the cut-off value for APD90. After obtaining the t_{\dagger} , we then numerically solved for B such that $\overset{2}{n}(t = B) = n_0$ was satisfied. The equation was solved using Maple18 software with fsolve command. The processes were repeated for different value of n_0 within the specified interval. Value of t_{\dagger} and its corresponding B were used to construct the restitution curve. Similar result can be obtained using the formula in equations (A.8a), (A.8b) and (A.8c) because they are already satisfied the boundary conditions. For the numerical solutions, the caricature Noble model was solved using ‘dsolve’ command in Maple18 with the numeric option for the ODE system boundary value problem. The results were then compared with the analytical solutions.

8.3.2 Alternans (2:2) restitution curves

To construct the alternans 2:2 restitution curve, the following periodic boundary conditions must be satisfied,

$$\begin{aligned} E_{\text{even}}(0) &= E_{\text{odd}}(t = B) = E_0 > E_*, \\ h_{\text{even}}(0) &= h_{\text{odd}}(t = B), \quad h_{\text{odd}}(0) = h_{\text{even}}(t = B), \\ n_{\text{even}}(0) &= n_{\text{odd}}(t = B), \quad n_{\text{odd}}(0) = n_{\text{even}}(t = B). \end{aligned} \quad (8.22)$$

From these conditions and analytical solutions in (A.5a) and (A.5b), we then have,

$$\begin{aligned} n_{\text{even}}^1(0) &= n_{\text{odd}}^2(B), \quad n_{\text{even}}^2(B) = n_{\text{odd}}^1(0), \\ h_{\text{even}}^1(0) &= h_{\text{odd}}^2(B), \quad h_{\text{even}}^2(B) = h_{\text{odd}}^1(0), \end{aligned} \quad (8.23)$$

These equations were solved simultaneously using the solutions of the initial value problem in (A.5a), (A.5b) and (A.5c)). The processes are as similar explained previously.

Figure 8.4a shows the 1:1 and alternans (2:2) restitution curves constructed using both analytical and numerical BVP approaches for r greater than one (stable alternans) and for different values of ε_2 . From the figure, we can see that the analytical solutions make a good overlap with the numerical solutions. We then compared the outcome with the restitution curve from asymptotic solutions (8.9) and (8.10). In order to do that, the value of ε_2 in the analytical solutions of IVP and BVP need to be reduced as small as possible. This is because the explicit analytical formula (8.9) was derived using slow-slow-time subsystem where $\varepsilon_{1,2}$ goes to 0, whereas the analytical solutions of IVP and BVP were formulated in the case of $\varepsilon_{1,2} = 1$. From the Figure 8.4a, we can see that as the value of ε_2 gets closer to 0, the restitution curve begins to deviate closer (from red curve to blue curve) to the asymptotic solutions. Note that only ε_2 was reduced as ε_1 does not have a significant effect on the AP repolarisation.

Similarly, Figure 8.5a shows the 1:1 and alternans (2:2) restitution curves of analytical BVP methods in the case of r less than 1 (unstable alternans). The results were compared with the restitution curve (solid black line) from the asymptotic solutions (8.9) and (8.10). For $r > 1$, the bifurcation is supercritical as shown in Figure 8.4a, whereas the bifurcation is subcritical when $r < 1$ (Figure 8.5a). Figure 8.4b and 8.5b depict the interval where the stable and unstable alternans occur for various ε_2 , respectively. In the case of unstable alternans, the interval is very tight and only gets more pronounced when ε_2 is large enough.

In addition, we also compared our methodology with standard protocol in constructing the restitution curve, which follow the dynamic pacing protocol as discussed in 6.2.3.3. From the inset Figure in 8.4a, both methods show a good correspondence, with the exception that bifurcation point (where 2:2 alternans begin to occur) is slightly delayed in our method.

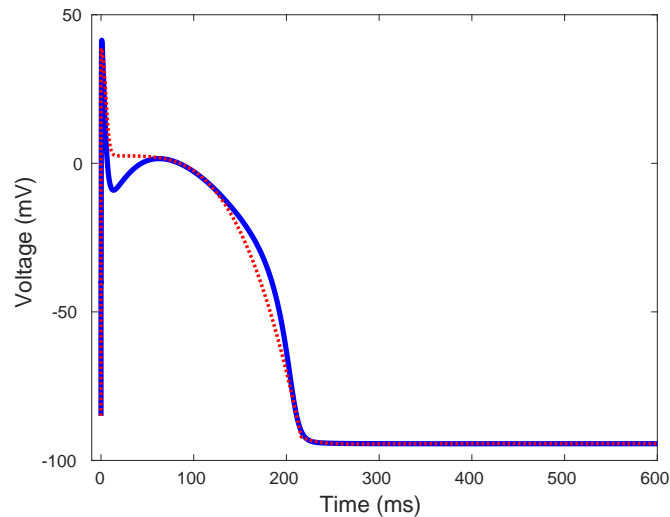


Figure 8.6: The action potential morphology of caricature Noble model (dotted line) after the fitting process in comparison with CVM (solid line) for $t \in [0, 600]$ ms. The parameter values used to plot the caricature Noble model are as listed in the left column of Table 8.1

8.4 Numerical simulation: Fitting to a ventricular model

From the parameter space plotted in Figure 8.1, it has been shown that alternans appear when r is greater than unity and disappear when r is less than that. To validate this theoretical result, we fitted the caricature Noble model to a canine ventricular model (CVM) by Fox et al. (2002) and demonstrated that alternans could be triggered when a particular parameter value is satisfied. As reported in Fox et al. (2002), the alternans behaviours in CVM could be annihilated by adjusting the peak magnitude of calcium or potassium currents in the model. For example, their result showed that increasing maximal conductance of IK_r by 62% did eliminate the alternans to the normal response. The finding motivates us to choose CVM as our baseline model in order to simulate the onset of alternans in caricature Noble model.

8.4.1 Action potential waveform

Following the similar parameter estimation method and fitting protocols as discussed in Chapter 6, we fitted our caricature Noble model to CVM model and the AP morphology is shown in Figure 8.6. Our model failed to reproduce the AP deep notch during phase 1 but rather produced a flat plateau. A probable reason is due to lack of ionic current in our model that produces the specific AP feature, where in this case is transient outward potassium current, Ito (Santana et al. 2010). Moreover, it is known that models with the same restitution properties, but different AP morphologies may give different onsets for alternans (Cherry and Fenton 2004, Penaranda et al. 2012). The other AP biomarkers like amplitude, resting potential and APD showed a good correspondence with CVM. The new estimated parameter values are listed in Table 8.1. Notice

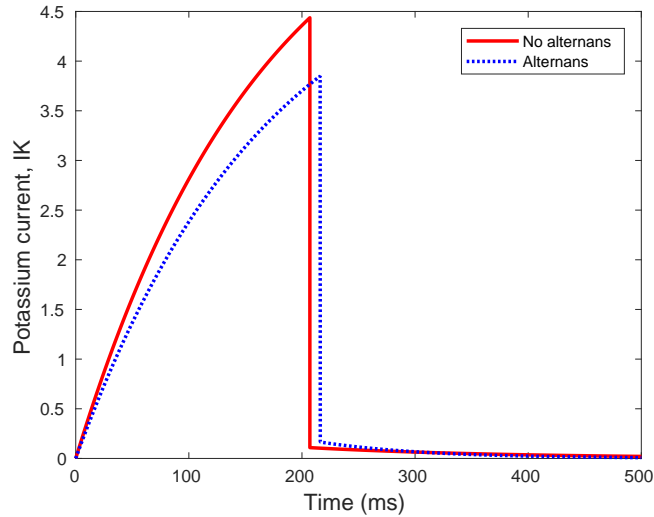


Figure 8.7: The profile of potassium currents in the models of alternans and no alternans of caricature Noble model.

Parameters	Model 1 (Alternans)	Model 2 (No Alternans)
G_{Na}	100/3	100/3
E_{Na}	40.65	40.65
E_{\dagger}	-92.0	-92.0
E_{*}	1.5	-4.0
k_1	0.02987	0.001687
k_2	0.001	0.00097
k_3	1.803977	1.707082
E_1	-94.33	-94.33
f_n	0.00592	0.00598
F_h	0.6	0.6
g_{21}	-0.22905	-0.15338
g_{22}	-5.333726	-6.249433
r	1.8	0.95

Table 8.1: Comparison of the parameter sets in the case of alternans and no alternans after fitting the caricature Noble model to CVM.

that there are two sets of parameter in the table. The first parameter set on the left is the result of fitting our caricature Noble model to the original CVM. This is the condition where alternans appear. The second parameter set comes from the fitting result of modified CVM. In the modified CVM, the IKr was increased in order to suppress the alternans behaviour. IKr has a positive correlation with APD; hence, increasing the IKr magnitude would decrease the APD. Since the AP morphology has changed due to alteration in IKr, we fitted the caricature Noble model to CVM again, giving us a new set of parameter values as listed in the second column of Table 8.1. This model is used to represent the no alternans case.

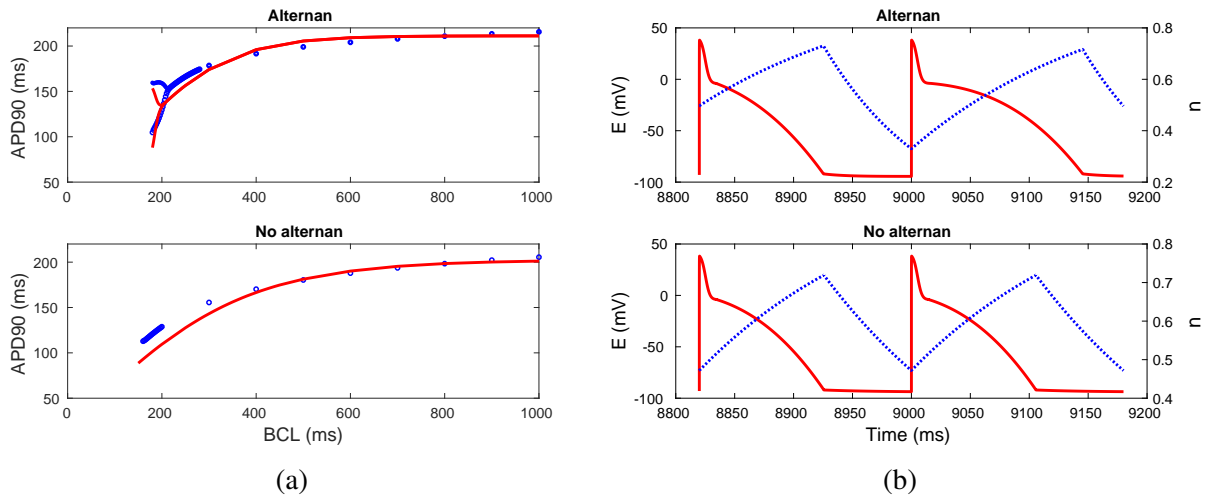


Figure 8.8: (a) The APD restitution curves of caricature Noble model (solid line) and CVM (open circle) in the case of alternans (top panel) and no alternans (bottom panel) using dynamic pacing method. The BCL is shortened from 1000 ms to 150 ms and then APD90 is recorded for each cycle length. (b) The corresponding traces of E (solid line) and n (dotted line) at BCL = 180 ms.

From the Table 8.1, we can observe that most of the parameters are almost similar, with the exception being for k_1 , E_* and r . These parameters have the most significant difference. However, from our theoretical work in the previous section, we find that k_1 and E_* do not directly contribute to the alternans. The values were the result of our parameter fitting. Since the caricature Noble model was fitted to two different AP waveforms (alternans and no alternans case), the parameter values were expected to be different. Interestingly, r possess value greater than 1 in the case of alternans, whereas smaller than 1 in the case of no alternans. The finding is consistent with the bifurcation set in Figure 8.1, highlighting the role of r in inducing the alternans. In caricature Noble model, r plays an important role in determining the excitation of next action potential as it controls the speed of n -gating variable during the diastolic phase. When r is less than 1, $F_n(E)$ decreases, hence slows down the evolution of n -gating variable. In consequence, the n -gating variable returns slowly to its resting value, which then allows more K^+ ions to leave the cell. This would increase the IK current (as depicted in Figure 8.7), which then cause the APD shortening. In consequence, the AP has a longer diastolic phase (during rapid BCL) and eventually suppresses the alternans.

However, when r is larger, the speed of n -gating variable at diastolic phase becomes even faster and has caused n to have faster return, which will eventually influence the initial condition of n for next AP. This is even more prominent during shorter BCL as the AP has short diastolic phase. As a result, this leads to alternans, as shown in Figure 8.8b. Our result regarding the IK current is consistent with the finding reported by Fox et al. (2002), where in the model of alternans, the IK current is smaller compared to another model (Figure 8.7).

8.4.2 APD restitution curve

Using the estimated parameter values in Table 8.1, we then constructed the APD restitution curves of caricature Noble model by following the dynamic pacing method described in section 6.2.3.3. The APD of the last two action potentials was measured at 90% of repolarization for each basic cycle length. Figure 8.8a shows the APD restitution curves of both alternans and no alternans cases. In the top panel of Figure 8.8a, we can see that the alternans in caricature Noble model and CVM start to appear approximately at 216 ms and 218 ms, respectively. However, in the bottom panel of Figure 8.8a alternans does not appear.

8.5 Conclusion

In this chapter, we have studied the mechanisms of cardiac alternans using a simplified action potential model. Following the work by Mitchell and Schaeffer (2003), an explicit formula for the restitution curve has been derived from the slow-slow-time system of caricature Noble model; thus the response of the model can be described by an iterated map. The stability of the map and bifurcations of equilibria of the map have been studied to determine the regions and parameter space where normal response and alternans occur. From our finding, we found that the parameter r in the slow gating variable n is responsible for the alternans occurrence. We showed that the bifurcation map loses its stability at $r = 1$ and exhibits the 2:2 response when $r > 1$. We also validated this theoretical result using numerical simulation. Particularly, we fitted the caricature Noble model to a canine ventricular model by Fox et al. (2002) and showed that the 2:2 alternans could be produced when r is greater than unity and vice versa. The other finding that arose from this study is that the potassium current has a significant role in alternans formation. We observed that in the case of high IK current, the alternans could be suppressed, in agreement with earlier work done by Fox et al. (2002). This is because IK plays an important role in the AP repolarization, and increasing the IK magnitude would shorten the APD. In consequence, this increases the diastolic phase of an AP and cells have more time to recover before the arrival of the next stimulus, hence, annihilate the alternans. On the other hand, cardiac alternans can occur due to other ion mechanisms, for example, fluctuation calcium handling dynamics which is caused by calcium currents (Tse et al. 2016). This model, however, did not include calcium current in the first place which limits our ability to study the role of calcium currents in alternans occurrence.

Part IV

Conclusion and supporting materials

Chapter 9

Conclusion

We end this thesis by providing a summary of the results presented in the previous chapters. We also outline the key contributions made to the existing literature. Possible future works are also described.

9.1 Summary and discussion

Sudden cardiac is a serious global issue and coronary heart disease is the commonest precipitating factor causing 80k deaths/year ([Townsend et al. 2014](#)). Hence, with the aid of experimental and clinical studies, computational models of action potential propagation are potentially powerful tools for investigating normal and abnormal myocardial behaviour. This thesis continues the progress by paving another path to understand and answer some of the related problems in cardiac modelling. In particular, the thesis looked to focus on the analysis and application of models of single-cell cardiac electrical excitation. To summarise the thesis, we recall that the main goals of this work are,

1. to determine the distributions of ion channel conductance values that capture the electrophysiological heterogeneity measured in large populations of rabbit ventricular cardiomyocytes and assess the effect this heterogeneity has on drug action,
2. to develop parameter estimation method and introduce the ‘modified’ caricature model as a generic action potential model by fitting the model to several biophysically detailed action potential models, as well as experimental measurements,
3. to develop an efficient numerical method for solution of the action potential model equations,
4. to study the mechanism of cardiac alternans and derive an explicit equation of APD restitution curve.

Chapter 2 In this chapter, we provided the essential background in cardiac electrophysiology and generation of an action potential. A review on the development of cardiac electrophysiology model was provided, beginning with the pioneer action potential model by [Hodgkin and Huxley \(1952\)](#). Our focus was on some of the ground-breaking models that lead to further development in computational modelling of cardiac cellular electrophysiology. We then pointed out several important applications of action potential models in investigating the mechanisms of arrhythmia and their usage in the pharmaceutical industry as a tool to develop new cardiac drugs. Finally, we ended this chapter by reviewing some of the experimental techniques ever used to measure the signal of action potentials in cardiac cells. Limitations and advantages of such experimental methods were discussed.

Chapter 3 In this chapter, we discussed the experimental measurements of rabbit ventricular cells provided by our collaborators (lead by Prof. Godfrey Smith). The chapter was begun by explaining the experimental techniques used to record the signal of APs, under both control and drug blocks. The heterogeneity of APs between the region of basal and apical of epicardium was discussed, where both regions showed a comparable level of heterogeneity. We analysed the data and extracted the calibration ranges for some AP biomarkers. These experimental ranges were used further to construct the model population in Chapter 4. Besides, in this chapter, the effect of two drugs that blocking hERG and L-type calcium channels on a population of rabbit ventricular cells were also studied. Each AP of the cells exhibited a different degree of responses, where hERG block resulted in APD prolongation and hyper-response. Meanwhile, L-type calcium block caused APD shortening. The mechanisms of these responses, however, were not fully understood due to limitation in the information of ionic currents.

Chapter 4 In this chapter, our task was to achieve Goal 1. We have investigated the underlying effects of action potential variability on hERG and L-type calcium blocks. Three AP models of rabbit/human ventricular myocytes were used to study the problem, and the individual results were compared with the experimental measurements. The models were rabbit AP model by [Shannon et al. \(2004\)](#) and two human AP models by [Ten Tusscher et al. \(2004\)](#) and [O'Hara et al. \(2011\)](#). An ensemble of 10,000–30,000 variants of each model with different value of ionic conductances was randomly generated using Latin hypercube sampling method in order to capture cell-to-cell variability. Each model variant was numerically solved by stimulation a train of 1000 action potentials at pacing rate 2Hz. Only viable APs that passed our quality control criteria were kept for further analysis. The model populations were calibrated using our experimental ranges and distributions. We then demonstrated the ability of these models populations to predict variability in response to drug blocking of hERG and L-type calcium channels. Among the three models, the Shannon model exhibited the best correspondence with our experimental data, highlighting the importance of careful model selection and appropriate

use for computational studies. The finding also demonstrated that it has become difficult for us to rely on model output alone without recourse to experimental data.

Blockade of hERG channels exhibited APD prolongation to the majority of the cell models in the population. No correlation was observed between the baseline APD and amount of APD prolongation. The highly variable spread of Δ APD in each model highlighted the differences of ionic currents properties in the respective models. For instance, the Ohara model possessed the most substantial IKr expression, which then resulted in tremendous APD-prolonging effect. In addition, following IKr block, some cells models experienced extreme APD prolongation beyond the basic cycle length (500 ms). We characterised the response as ‘hyper-response’. A possible cause is due to higher I_{CaL} expression present in these models, which then resulted in more prolonged AP plateau. Another curious feature was the generation of EADs in Shannon model. Interestingly, EADs formation was not seen in the other two models and our experimental data. The response was an unusual behaviour since EADs was more common in slower stimulation frequency (Cooper et al. 2016, Costabal et al. 2018, Guo et al. 2011, Nalos et al. 2012). Compared to the other two models, Shannon model was found to have the largest I_{CaL} and I_{NaCa}, and we suspected these two ionic currents were responsible for EADs occurrence.

In addition, we have also studied the effect of I_{CaL} block by nifedipine. In contrast to the first drug, I_{CaL} blocker did not significantly alter the resting membrane potential, the amplitude of action potential of rabbit ventricular myocytes but has caused the shortening to the duration of an action potential. Similar finding was reported in Amlie et al. (1979), Dangman and Hoffman (1980) and Go et al. (2005). The Δ APD was shown to have a negative linear correlation with the baseline APD. Models with small AP showed a smaller degree of APD shortening, compared to models with larger AP which tend to experienced larger Δ APD. A concrete answer to this was that in models of large AP had larger I_{CaL} expression and larger calcium transient amplitude, which then contributed to more dynamic responses. Finally, our finding in this chapter has highlighted two important aspects 1) Model selection is very important in computational modelling as each model could have a different capability in predicting the AP responses towards channel blocks, 2) AP variability within cells has significant impact to channel blocks and should not be disregarded.

Chapter 5 In this chapter, we provided a brief introduction to a simplified model of action potential, the so-called ‘caricature Noble model’ and discussed the advantages of this model compared to other simplified models. In the thesis (Chapter 5–7), we considered a modified version of caricature Noble model where the fourth order of variable n in equation (5.2b) was replaced by linear term in n . We then described the model formulations and then solved the model as initial and boundary value problem. The exact analytical solutions were derived and validated with numerical solutions. Next, we presented the asymptotic solutions of the model, including both fast subsystem and slow subsystem. These asymptotic solutions were used to develop an asymptotic-numerical method in Chapter 7 and investigated the mechanism of cardiac

alternans in Chapter 8. Furthermore, the phase portrait of the modified caricature Noble model and the criteria needed for the AP excitation were also explained.

Chapter 6 We then used the modified caricature Noble model in order to address Goal 2. In particular, we demonstrated a simple parameter estimation method, the so-called, ‘Nelder-Mead simplex method’ to fit the model to various biophysically detailed models of action potential and experimental measurements of healthy and failing rabbit cardio-myocytes. The fitting protocols and parameter sensitivity analysis were also discussed. Using the optimisation methodologies, the modified caricature Noble model was shown to have the capability to reproduce the action potential morphologies of various cell types of the targeted models, with some discrepancies at a particular part of AP phase. In addition, we also managed to fit the restitution curves of the respective models and experimental data, hence capturing the model’s AP dynamics at different pacing cycle lengths. Compared to some other simplified action potential models, the parameters and variables in this model could have the physiological meaning as it was derived from a genuine cell model (Noble 1962). Hence, our results could be translated into physiology. For example, when fitting to experimental measurements of APs of healthy and failing myocytes, we found that the maximal magnitude of time-dependent potassium current in the healthy model is a bit larger than the heart failure model. The finding was in agreement with earlier studies in Beuckelmann et al. (1993), Tsuji et al. (2000) and Akar and Rosenbaum (2003).

Chapter 7 In this chapter, our task was to achieve Goal 3 by developing an efficient numerical method for the modified caricature Noble model. The numerical method was a combination of asymptotic solutions of the model and the implementation of the heterogeneous multiscale method by Weinan and Engquist (2003). The numerical results were validated with the analytical solutions of the modified caricature Noble model. To test the stability and robustness of this approach, we compared the method with other conventional numerical methods such as the explicit Euler method, fourth-order Runge-Kutta method and Rush-Larsen method. From our analysis, we concluded that this asymptotic-numerical method was significantly efficient than most of the other numerical solvers, in terms of accuracy and execution time. However, due to some circumstances, the application of this method requires knowledge of the asymptotic structure of the AP model solved. For the time being, we only managed to apply this method on a single cell model and further work is needed in order to implement the method to tissue simulations. Further investigations need to be done in the future to test its implementation on more realistic action potential models.

Chapter 8 The asymptotic structures of caricature model were further used in this chapter by studying the mechanism of cardiac alternans (Goal 4). This work was a continuation work by Asgari-Targhi (2017) and we revised some of her results. Importantly, from this study, we were able to identify parameters and variables that were responsible for alternans occurrence. In

particular, we showed that the time scale at which the slow gating variable evolves is responsible for inducing alternans. This is because this variable explicitly controls the duration of an action potential. The duration will be affected if the slow variable fails to return to its initial value before the arrival of the next external stimulus, hence trigger the alternans. This result is in agreement with the work done by [Mitchell and Schaeffer \(2003\)](#). Moreover, we also studied the effect of the superfast variable on the region of alternans. Our finding showed that including the superfast variable in the system would influence the bifurcation point of the restitution curve. Also, we have shown that the variable responsible for alternans occurrence is the slow activation of outward IK current. Using the optimization technique, we have demonstrated that caricature Noble model with small IK current would promote the alternans behaviour in the model and vice versa. The connection between potassium current and induction of alternans was shown in an earlier study by [Fox et al. \(2002\)](#), and the finding was consistent with our own.

9.2 Future directions

Action potential variability In this study, we only included the density of ion channels as the primary source of AP variation. However, this is not entirely true as the AP variability could also happen due to difference in the kinetic rate of gating channels. In the future, co-regulation between kinetic and density of ion channels in influencing the AP variability should be investigated further. The dynamic changes of these protein expressions may alter the balance of ionic currents that flow across the cellular membrane, which would give rise to AP variation. Furthermore, varying conductance or kinetic of gating channels alone would have a different biological interpretation as altering channel kinetics could be related to genetic mutations.

In this work, our focus was only on the variability of action potentials and their impacts on channel block. Other than AP, calcium transients also exhibit variation due to fluctuation in calcium currents. Future work should aim to incorporate the calcium transients measurements, which can be used to investigate the cell's contractility in response to pharmacological intervention. Finally, other possible work that we aim to explore is to examine the responsiveness of APD variability to cell-to-cell electrical coupling. This can be done by forming a population of cell models into sufficiently large ventricular region. For our future motivation, we include some of our preliminary results of this work in the Appendix. In a study by [Zaniboni et al. \(2000\)](#), they showed that coupling suppressed the AP variability and induced an asymmetric response in which APD90 shortening of intrinsically long action potentials was more pronounced than APD90 prolongation of short action potentials and this suppression was crucial in preventing EADs formation when IKr was blocked. Although this is not thoroughly investigated yet, our results showed that cell-to-cell variability was reduced in the tissue sample.

In a series of studies by [Sarkar and Sobie \(2010; 2011\)](#), [Sobie \(2009\)](#), the authors have used multivariable regression analysis to examine the AP variability and gain insight into the factors

that are responsible for variability in the response to proarrhythmic drugs. There, regression analysis was performed to determine how much each model parameter attenuated or exacerbated the AP prolongation caused by the IKr-blocking drug. However, their results were not supported by any experimental data. Hence, using our results in Chapter 4 with the combination of our large AP and calcium measurements of left ventricular myocytes, we aim to use similar approach and determine the relating changes in parameters when drugs are applied.

Feature of caricature Noble model From our results presented in chapter 6, 7 and 8, we found that the caricature Noble model has several advantages and could be used for various purposes in cardiac electrophysiology. In particular, we have shown that this model has the capability to reproduce the action potential morphologies and restitution curves of various cell types. The asymptotic solution of the model also offered several uses. In the thesis, we applied the solutions to develop a robust numerical algorithm for faster simulation and to study the mechanisms of alternans. These demonstrated the wide application of this model to various cardiac-related problems.

However, the model feature could still be enhanced in some respective manner. In chapter 8, we have shown that the vital role of potassium current in inducing or suppressing the cardiac alternans. In literature, the alternans occurrence could be due to other ion mechanisms, for example, fluctuation in calcium handling dynamics, which is caused by calcium currents (Tse et al. 2016). Future work should aim to incorporate calcium current into the model, and this could allow us to investigate the role of the calcium current in the mechanisms of cardiac alternans. Such modification, however, should also aim to preserve the analytical solutions of the model. Besides, the incorporation of calcium current in the caricature Noble model will also allow us to couple the model with a mechanical model. The model then can be further used to study the cell's contractility.

In the simulation of electrocardiograms (ECG) for a whole heart with various cell types, earlier researches have shown that coupling two systems like Purkinje-ventricular system required the use of two different AP models (Aslanidi et al. 2009b, Vigmond and Clements 2007) or using a similar model with a different set of parameter values (Berenfeld and Jalife 1998). An obvious reason is that typical cell model is usually built for specific cell type such as ventricular or atrial cell model; hence this model cannot be used for different cell type due to difference in action potential morphologies and duration. Interestingly, caricature Noble model could be explored to meet the purpose due to the model's flexibility in reproducing various APs from different cell types. In the future, we aim to utilise the model for whole heart simulation by coupling the system of several heart regions. The simplicity of this model may also allow us to have less demanding computational workload.

Appendix A

Codes and supplementary materials

A.1 Variability in action potential

This section provides the extended material from Chapter 4.

A.1.1 Parameter range

The range of parameter used to construct the model population depends on the hypothesis of a particular study and how good the model population to represent the experimental data. Wider parameter ranges allow for more extreme parameter values which then result in more extreme model outputs. In our work, we varied all parameters for $\pm 100\%$ in order to allow for significance spread of AP biomarkers. Earlier, we used $\pm 30\%$ and $\pm 50\%$ parameter variations, but the model's outputs were underachieving and did not accurately capture our experimental measurements (see Figure 4.5b). Also, parameter ranges have some significant influences on the outcome of models to channel block. Figure A.1 shows the net effect of drug block on APD90 for two parameter variations. We can see that when $\pm 30\%$ parameter variation was considered, the spread of ΔAPD90 is confined. There was no model with ΔAPD90 smaller than 20 ms for models with baseline between 230–300 ms. A broader drug effect is shown by the other parameter variation but the distribution does not yet accurately capture the experimental distribution.

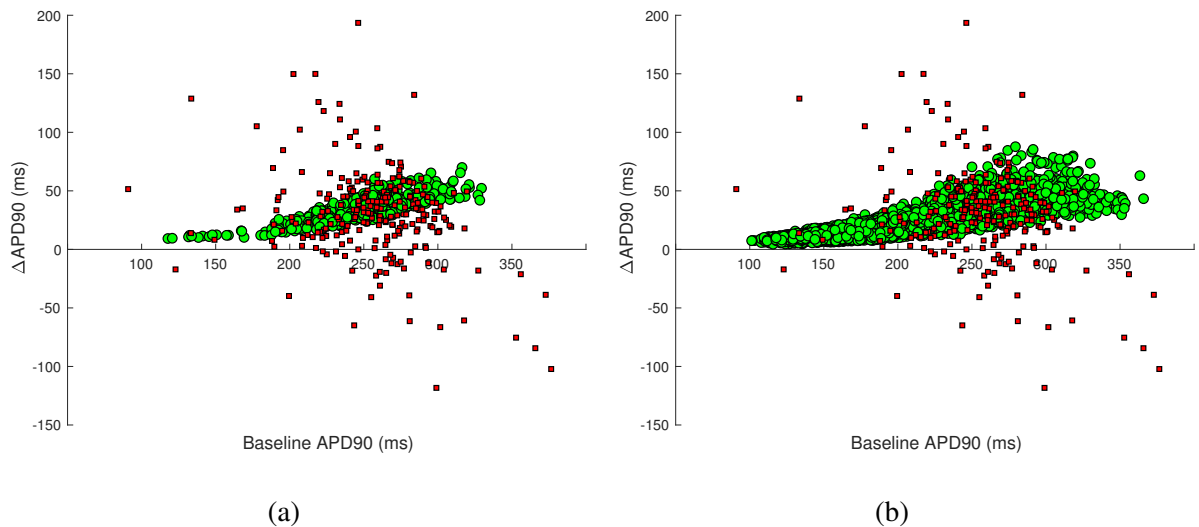


Figure A.1: Scatter plot of drug effect on APD for (a) $\pm 30\%$ and (b) $\pm 50\%$ parameter variations. Mean of ΔAPD90 in (a) and (b) is 33.6 ± 11.2 ms and 21.7 ± 12.9 ms, respectively.

A.1.2 Contour plot of APD90

APD is a function of model parameters such that a given APD value can be generated from infinitely many different parameter combinations. Figure A.2 shows the contour plot of APD90 produced by randomly varying 8 ionic conductances in the Shannon model. As shown in the figure, various different parameter sets can generate an identical APD90. These sets form a continuous contour hypersurface in the parameter space.

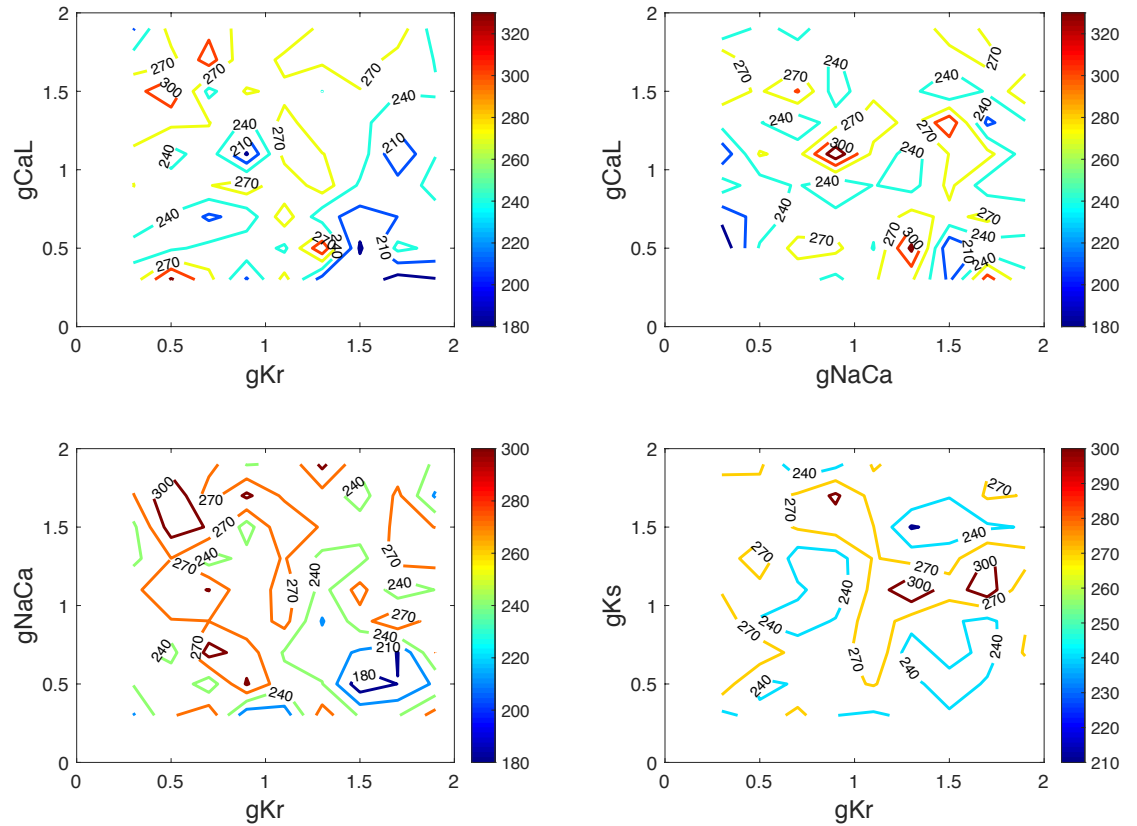


Figure A.2: Contour plot of APD90 as a function of parameter space.

A.1.3 AP morphologies in models and experiment

Figure A.3 shows the action potential morphologies in the Shannon, TenTusscher and Ohara models, in comparison to AP observed in experimental measurements from rabbit ventricular myocyte.

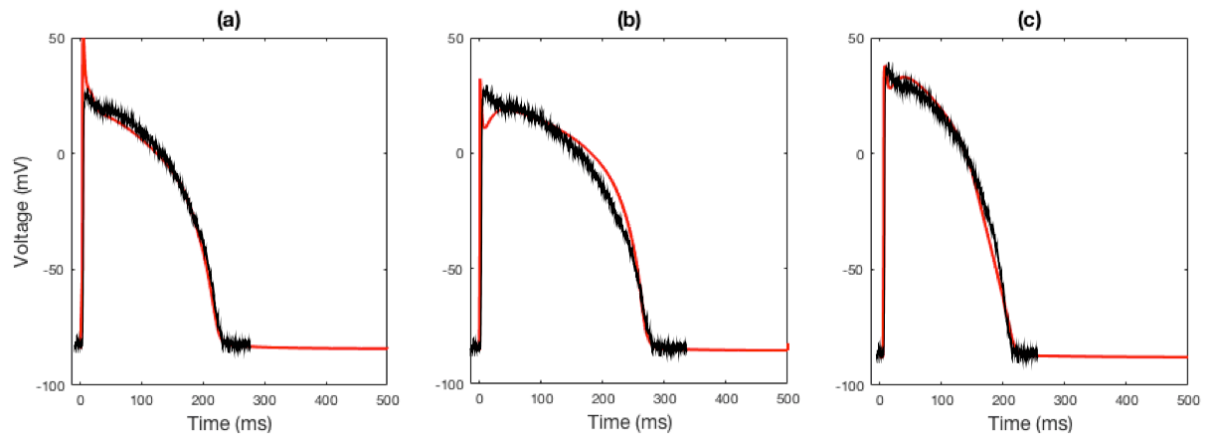


Figure A.3: Typical action potential morphologies of (a) Shannon model, (b) TenTusscher model and (c) Ohara model, in comparison to APs observed in experimental recordings from rabbit ventricular myocyte (black line).

A.1.4 Archetypal models

As discussed in section 4.5.4.6, we constructed three archetypal models as a representation of each AP response seen following IKr block. Each archetypal model was built using the median values of each conductance in the respective model subpopulation (Figure 4.13). The parameter values for each archetypal model are listed in Table 4.3. Figure A.4 shows the voltage and ionic currents in the archetypal model of normal response before and after IKr block.

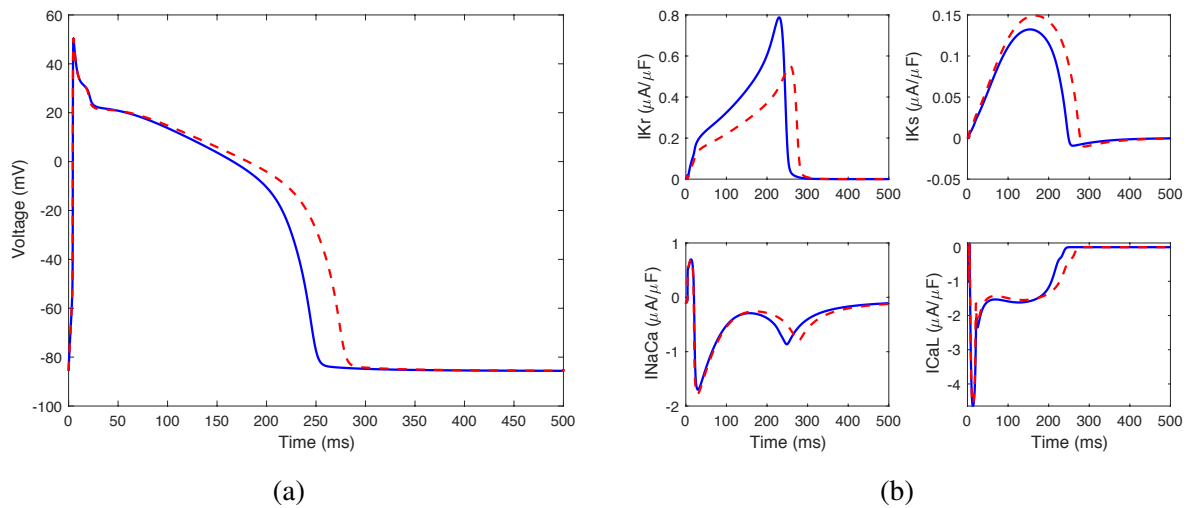


Figure A.4: The traces of (a) action potential and the corresponding (b) ionic currents in archetypal model of normal-response. Solid line is the model's outputs under control condition and the dashed line is the model's outputs after the IKr block.

A.1.5 Tissue sample with cell heterogeneity

In this section, we want to discuss how the reduction of electrophysiological heterogeneity can be achieved when individual cells are coupled to form sufficiently large ventricular regions. A likely hypothesis that we wish to investigate is that expression networks exist between key groups of ion channels/exchangers that act to stabilise regional electric signatures in the face of large intrinsic variation, essentially protecting the heart from sub-populations of myocytes that would provoke arrhythmias in healthy hearts at bradycardiac or tachycardiac conditions. To test such hypotheses and to identify key correlations and co-expression networks, we propose to develop a mathematical model whereby our experimentally-calibrated large size ensemble of numerical cells with randomly distributed parameter values are coupled to each other by Newton cooling terms corresponding to low-resistance gap junctions. Note that finding discussed in this section is preliminary and potentially require further investigations.

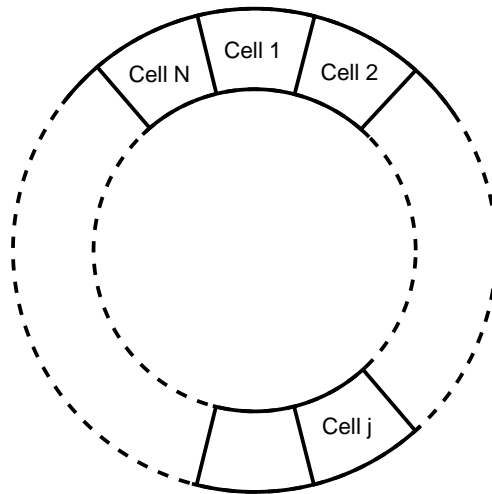


Figure A.5: Illustration of our cells arrangement in tissue sample. N heterogenous cells are alligned in a shape of ring and each cell is connected by the gap junctions.

A.1.5.1 Cell synchronisation

The theoretical fibre is composed of N Shannon cell models. Eight ionic currents are varied randomly using Latin Hypercube sampling method to form a population of cells with different ionic properties. The cells are aligned in a ring-shaped which every cell are connected to their nearest neighbour cells (Figure A.5). The membrane potential of each cell is connected by Newton cooling terms described below,

for $j = 1, 2, \dots, k$:

$$\frac{dV_j}{dt} = -\sum I_{\text{ion}} + \mu \left(\sum_{i=1}^k (V_{j+i} + V_s) - 2kV_j \right),$$

for $j = k+1, k+2, \dots, N-k$:

$$\frac{dV_j}{dt} = -\sum I_{\text{ion}} + \mu \left(\sum_{i=1}^k (V_{j+i} + V_{j-i}) - 2kV_j \right), \quad (\text{A.1})$$

for $j = N-k+1, N-k+2, \dots, N$:

$$\frac{dV_j}{dt} = -\sum I_{\text{ion}} + \mu \left(\sum_{i=1}^k (V_{j-i} + V_r) - 2kV_j \right),$$

where

$$s = \begin{cases} \alpha = \text{mod}(N + j - i, N), & \text{if } 1 \leq \alpha \leq N - 1 \\ N & \text{else} \end{cases} \quad (\text{A.2})$$

and

$$r = \begin{cases} \alpha = \text{mod}(j + i, N), & \text{if } 1 \leq \alpha \leq N - 1 \\ N & \text{else.} \end{cases} \quad (\text{A.3})$$

N is the number of cells and j is the position of the cells in the tissue ring. $m = 2k$ is the number of interaction of a cell to its neighbour cells and $\text{max}(k) = \lceil (N/2 - 1) \rceil$. $\text{max}(k)$ is introduced such that each cell in the tissue model does not have more than two interactions between similar neighbour cell. In fact, under physiological conditions, a typical left ventricular myocyte in an adult working myocardium is electrically coupled to an average of about 9-13 adjacent cells (Saffitz et al. 1994). In our work, we considered $k = 6$ (for $N \geq 30$) which every cell was connected to 12 neighbour cells. μ is the gap-junction strength and homogenous throughout the tissue sample. We applied the explicit Euler method to numerically integrate the system with time step 0.007 ms and equations (A.1) was solved simultaneously for every time step. The parameter values for each cell model were randomly taken from the experimentally-calibrated control population constructed in chapter 4. These cell models were coupled together to form a sufficiently large ventricular tissue with distinct action potential properties. Figure A.6a shows a subpopulation of action potentials before the models were coupled to each other. We can see that large AP variability, mainly in the repolarisation, is shown in the individual model. The resting membrane potential and action potential amplitude are almost identical.

Electrotonic coupling between cells is established through the formation of gap junctions between cells and the gap junctions play a pivotal role in the velocity and the safety of action potential propagation in cardiac tissue. We next examined the responsiveness of APD variability to cell-to-cell electrical coupling. Figure A.6b shows the coupling effect on cell variability. As expected, the temporal variability of action potentials in ventricular myocardium is reduced. Our result is consistent with some earlier works by Walmsley et al. (2015) and Zaniboni et al.

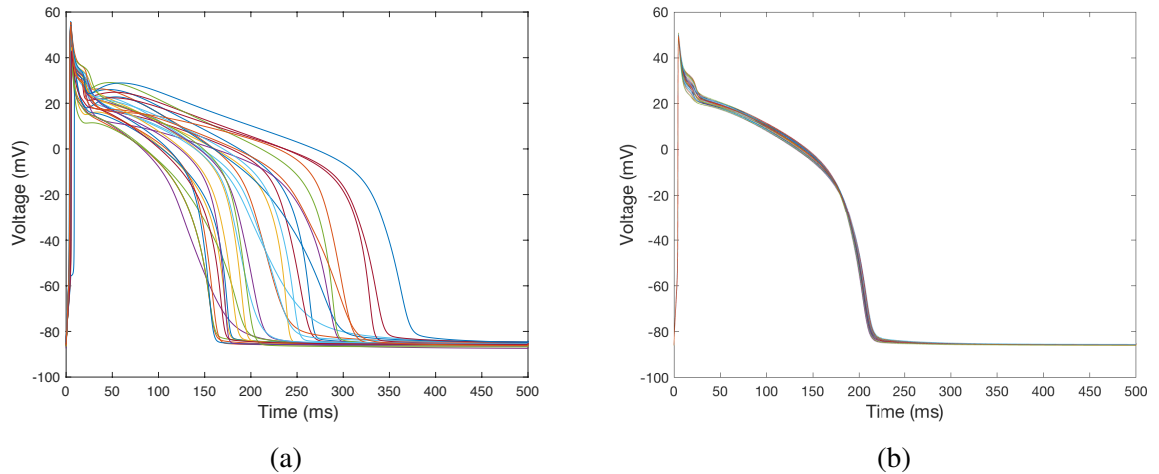


Figure A.6: Simulated temporal variability in 30 Shannon cell models (a) before the coupling ($\mu = 0$) and (b) after the coupling ($\mu = 0.5$).

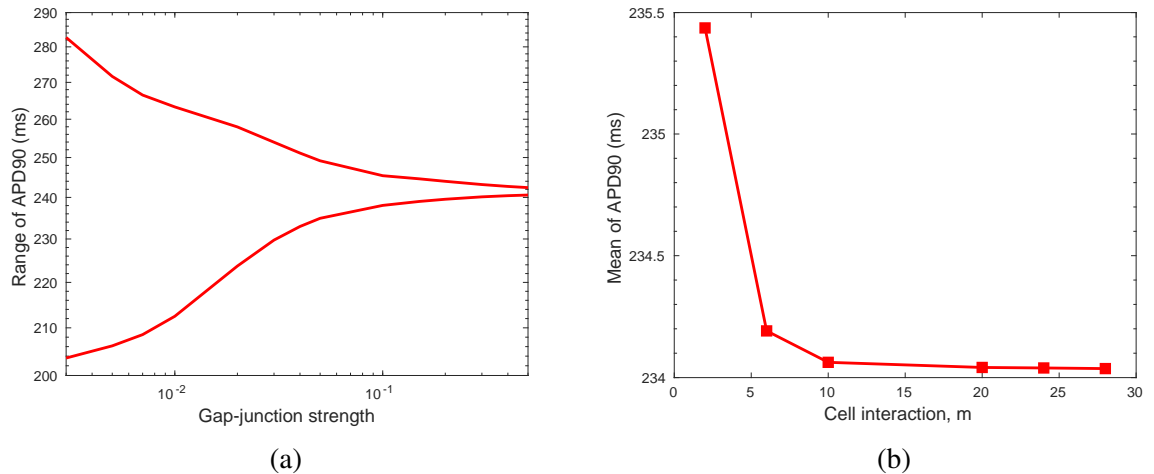


Figure A.7: Effect of (a) gap-junction strength and number of cell interaction on cell coupling.

(2000). Interestingly, our finding also shows that mean APD90 value in 30 cell models before the coupling (227.04 ms) is larger than the mean APD90 following cell coupling (209.01 ms). This demonstrates that there are important interactions occur between the cell models; rather than just simply averaging of the signals.

Also, we investigate whether the gap-junction strength has any influences on the repolarisation of these action potentials. We also want to find what is the minimum value of μ , so that the tissue model is well coupled. In order to do that, the value of μ was varied from 0.01 (the weakest coupling) to 0.5 (the strongest coupling) and the range of APD90 was measured. From Figure A.7a, we can see that the range of APD90 decreases as μ increases and the tissue model is well connected at the strongest μ . As mentioned earlier, each cardiac cell in tissue is connected to roughly 11 adjacent cells (Saffitz et al. 1994). Using our tissue model, we investigate how the number of cell interactions may contribute to the mean average of repolarisation of the cells in

the model. Figure **A.7b** shows that tissue behaviour is not affected by the number of each cell interacts with its neighbour cells.

A.2 Caricature Noble model

This section is extended material from Chapter 8. In particular, we provide the exact analytical solutions and asymptotic solutions of original caricature Noble model presented in that chapter.

A.2.1 Exact analytical solutions

A.2.1.1 Solution of the initial value problem

In this case, we set the state conditions as following,

$$E(0) = E_{\text{stim}} > E_*, \quad h(0) = h_0, \quad n(0) = n_0, \quad (\text{A.4})$$

$$n(t) = \begin{cases} \overset{1}{n}(t) = 1 - (1 - n_0) \exp(-f_n t), & t \in [0, t_{\dagger}] \\ \overset{2}{n}(t) = (1 - (1 - n_0) \exp(-f_n t_{\dagger})) \exp(f_n r(t_{\dagger} - t)), & t \in [t_{\dagger}, \infty] \end{cases} \quad (\text{A.5a})$$

$$h(t) = \begin{cases} \overset{1}{h}(t) = h_0 \exp(-F_h t / (\varepsilon_1 \varepsilon_2)), & t \in [0, t_{\dagger}] \\ \overset{2}{h}(t) = 1 - (\exp(F_h t_{\dagger} / (\varepsilon_1 \varepsilon_2)) - h_0) \exp(-F_h t / (\varepsilon_1 \varepsilon_2)), & t \in [t_{\dagger}, \infty] \end{cases} \quad (\text{A.5b})$$

$$E(t) = \begin{cases} \overset{1}{E}(t) = \exp\left(\frac{G_{Na} h_0}{F_h} \exp\left(-\frac{F_h t}{\varepsilon_1 \varepsilon_2}\right) - \frac{k_3 t}{\varepsilon_2}\right) \times \\ \left[E_0 \exp\left(-\frac{G_{Na} h_0}{F_h}\right) - k_3 E_3 u(-k_3 \varepsilon_1, t) \right. \\ \left. - g_{22} \sum_{l=0}^4 \binom{4}{l} (n_0 - 1)^l u(-k_3 \varepsilon_1 + \varepsilon_1 \varepsilon_2 l f_n, t) \right. \\ \left. - \frac{G_{Na} h_0 E_{Na}}{\varepsilon_1} u(-k_3 \varepsilon_1 + F_h, t) \right], & t \in [0, t_*] \\ \overset{2}{E}(t) = (E_* - w(t_*)) \exp\left(\frac{k_2}{\varepsilon_2} (t - t_*)\right) + w(t), & t \in [t_*, t_{\dagger}] \\ \overset{3}{E}(t) = (E_{\dagger} - m(t_{\dagger})) \exp\left(\frac{k_1}{\varepsilon_2} (t_{\dagger} - t)\right) + m(t), & t \in [t_{\dagger}, \infty] \end{cases} \quad (\text{A.5c})$$

where

$$u(\varkappa, t) \equiv \frac{\varepsilon_1}{F_h} \left(\frac{F_h}{G_{Na}h_0} \right)^{\frac{\varkappa}{F_h}} \left[\Gamma \left(\frac{\varkappa}{F_h}, \frac{G_{Na}h_0}{F_h} \right) - \Gamma \left(\frac{\varkappa}{F_h}, \frac{G_{Na}h_0}{F_h} \exp \left(-\frac{F_h t}{\varepsilon_1 \varepsilon_2} \right) \right) \right], \quad (\text{A.6a})$$

$$w(t) \equiv E_2 + g_{22} \sum_{l=0}^4 (n_0 - 1)^l \binom{4}{l} \frac{\exp(-l f_n t)}{-k_2 - l \varepsilon_2 f_n}, \quad (\text{A.6b})$$

$$m(t) \equiv E_1 + \frac{g_{21}}{k_1 - 4 \varepsilon_2 f_n r} \sum_{l=0}^4 (n_0 - 1)^l \binom{4}{l} \exp((4 f_n r - l f_n) t_{\dagger}) \exp(-4 f_n r t), \quad (\text{A.6c})$$

for $\text{Re}(z) > 0$ as defined in [Abramowitz and Stegun \(1965\)](#).

A.2.1.2 Solution of the boundary value problem

In this case, we set the state conditions as following,

$$E(0) = E(t = B) = E_{\text{stim}} > E_*, \quad h(0) = h(t = B), \quad n(0) = n(t = B), \quad (\text{A.7})$$

where B is the basic cycle length. By imposing the above boundary conditions (A.7), the general solutions are as follows:

$$n(t) = \begin{cases} \overset{1}{n}(t) = 1 - C_1 \exp(-f_n t), & t \in [0, t_{\dagger}] \\ \overset{2}{n}(t) = \left(1 - C_1 \exp(-f_n t_{\dagger}) \right) \exp(f_n r (t_{\dagger} - t)), & t \in [t_{\dagger}, \infty] \end{cases} \quad (\text{A.8a})$$

$$h(t) = \begin{cases} \overset{1}{h}(t) = D_1 \exp(-F_h t / (\varepsilon_1 \varepsilon_2)), & t \in [0, t_{\dagger}] \\ \overset{2}{h}(t) = 1 - \left(\exp(F_h t_{\dagger} / (\varepsilon_1 \varepsilon_2)) - D_1 \right) \exp(-F_h t / (\varepsilon_1 \varepsilon_2)), & t \in [t_{\dagger}, \infty] \end{cases} \quad (\text{A.8b})$$

$$E(t) = \begin{cases} \overset{1}{E}(t) = \exp \left(\frac{G_{Na} D_1}{F_h} \exp \left(-\frac{F_h t}{\varepsilon_1 \varepsilon_2} \right) - \frac{k_3 t}{\varepsilon_2} \right) \times \\ \left[E_0 \exp \left(-\frac{G_{Na} D_1}{F_h} \right) - k_3 E_3 u(-k_3 \varepsilon_1, t) \right. \\ \left. - g_{22} \sum_{l=0}^4 \binom{4}{l} (-C_1)^l u(-k_3 \varepsilon_1 + \varepsilon_1 \varepsilon_2 l f_n, t) \right. \\ \left. - \frac{G_{Na} D_1 E_{Na}}{\varepsilon_1} U(-k_3 \varepsilon_1 + F_h, t) \right], & t \in [0, t_*] \\ \overset{2}{E}(t) = (E_* - w(t_*)) \exp \left(\frac{k_2}{\varepsilon_2} (t - t_*) \right) + w(t), & t \in [t_*, t_{\dagger}] \\ \overset{3}{E}(t) = (E_{\dagger} - m(t_{\dagger})) \exp \left(\frac{k_1}{\varepsilon_2} (t_{\dagger} - t) \right) + m(t), & t \in [t_{\dagger}, \infty] \end{cases} \quad (\text{A.8c})$$

where

$$C_1 = \left(1 - \exp(f_n r(t_{\dagger} - B))\right) / \left(1 - \exp((-f_n t_{\dagger}) - f_n r(B - t_{\dagger}))\right) \quad (\text{A.9a})$$

$$D_1 = \left(1 - \exp\left(\frac{F_h(t_{\dagger} - B)}{\varepsilon_1 \varepsilon_2}\right)\right) / \left(1 - \exp\left(\frac{-F_h B}{\varepsilon_1 \varepsilon_2}\right)\right) \quad (\text{A.9b})$$

$$u(\varkappa, t) \equiv \frac{\varepsilon_1}{F_h} \left(\frac{F_h}{G_{Na} D_1}\right)^{\frac{\varkappa}{F_h}} \left[\Gamma\left(\frac{\varkappa}{F_h}, \frac{G_{Na} D_1}{F_h}\right) - \Gamma\left(\frac{\varkappa}{F_h}, \frac{G_{Na} D_1}{F_h} \exp\left(-\frac{F_h t}{\varepsilon_1 \varepsilon_2}\right)\right) \right], \quad (\text{A.9c})$$

$$w(t) \equiv E_2 + g_{22} \sum_{l=0}^4 (-C_1)^l \binom{4}{l} \frac{\exp(-l f_n t)}{-k_2 - l \varepsilon_2 f_n}, \quad (\text{A.9d})$$

$$m(t) \equiv E_1 + \frac{g_{21}}{k_1 - 4\varepsilon_2 f_n r} \sum_{l=0}^4 (-C_1)^l \binom{4}{l} \exp((4f_n r - l f_n) t_{\dagger}) \exp(-4f_n r t), \quad (\text{A.9e})$$

We now have the exact solutions of the equations (5.1) as a function of B .

A.2.2 Asymptotic decomposition

We include results of [Biktashev et al. \(2008\)](#) on the asymptotic decomposition of the caricature Noble model. Taking the limit of $\varepsilon_1, \varepsilon_2 \rightarrow 0^+$, the model can be dissected into asymptotically reduced systems, which then provide much insight into the dynamics of the full model. The derivation of the asymptotics solutions of this model are explained in the following subsections.

A.2.2.1 Superfast-time system

We assume that our original system has a multiple timescales and consider a "super-fast" timescale T which is $T = t/(\varepsilon_1 \varepsilon_2)$. The time t is stretched into super-fast timescale T as the $\varepsilon_1 \rightarrow 0$. From the chain rule of differential equation, we have

$$\frac{d}{dt} = \frac{1}{\varepsilon_1 \varepsilon_2} \frac{d}{dT}. \quad (\text{A.10})$$

Substitute the above expression into (5.1) and taking the limit of $\varepsilon_1 \rightarrow 0$, we obtain the essential dynamical variables of E and h ,

$$\frac{dE}{dT} = G_{Na} (E_{Na} - E) H(E - E_*) h, \quad (\text{A.11a})$$

$$\frac{dh}{dT} = F_h (H(E_{\dagger} - E) - h). \quad (\text{A.11b})$$

This system describes the fast upstroke of the action potential. Solving the above system (A.11), we can derive the explicit asymptotic solutions for this stage which are,

$$E = E_{Na} - (E_{Na} - E_0) \exp\left(\frac{G_{Na}}{F_h}(e^{-F_h T} - 1)\right), \quad (\text{A.12a})$$

$$h = \exp^{-F_h T}. \quad (\text{A.12b})$$

The maximal overshoot voltage, E_{\max} is obtained as the fast time T goes to infinity,

$$E_{\max} = E_{\infty} = \lim_{T \rightarrow \infty} E(T) = E_{Na} - (E_{Na} - E_0) \exp\left(-\frac{G_{Na}}{F_h}\right) \quad (\text{A.13a})$$

Since $\exp(-G_{Na}/F_h) \approx 10^{-29}$, the maximal overshoot voltage E_{\max} is extremely close to E_{Na} . The $h(T) = 0$ as T tends to infinity.

A.2.2.2 Slow-time system

The slow-time system is obtained by directly taking the limit of $\varepsilon_1 \rightarrow 0$ in (5.1). By doing this, we have $h(t) = H(E_{\dagger} - E)$. Plucking this into equation (5.1a) will eliminate the first term and left us with a reduced system as following,

$$\frac{dE}{dt} = \frac{1}{\varepsilon_2} \left(g_2(E)n^4 + G(E) \right) \quad (\text{A.14a})$$

$$\frac{dn}{dt} = F_n(E) \left(H(E - E_{\dagger}) - n \right). \quad (\text{A.14b})$$

This system describes the post-overshoot drop, plateau and recovery stages of the action potential.

A.2.2.3 Slow-slow-time system

The slow-slow time subsystem is obtained directly from equations (5.1) by taking the limit of $\varepsilon_1 \rightarrow 0$ and $\varepsilon_2 \rightarrow 0$ simultaneously. The system is described below,

$$0 = g_2(E)n^4 + G(E), \quad (\text{A.15a})$$

$$\frac{dn}{dt} = F_n(E) \left(H(E - E_{\dagger}) - n \right). \quad (\text{A.15b})$$

This system describes the plateau and the recovery stages of the action potential.

A.3 MATLAB codes for parameter fitting

In this section, we provide several codes used for the optimization problem in Chapter 5 and 7.

A.3.1 Code 1

This is the main code used to run the entire simulation and fitting algorithms.

```
1 clear all;
2
3 tStart = tic;
4
5 %% choose the pacing rate
6 BCL = 1500;
7
8 paramEstimation(BCL);
9
10 tEnd = toc(tStart);
11 fprintf('Elapsed times is %d mins and %.0f secs\n', ...
12 floor(tEnd/60), rem(tEnd,60));
```

A.3.2 Code 2

This code was used to carry out the parameter estimation method. Note that the 'fminsearchbnd3' was downloaded from <https://github.com/faiq/findingsolo/blob/master/fminsearchbnd3.m>. This is a modified MATLAB code for MATLAB function 'fminsearch' where the parameter searching is only considered within the specified interval.

```
1 function paramEstimation(BCL)
2
3 clearvars -global
4 global VOI_EXACT STATES_EXACT P_NEW APD_EXACT rValue PacingRate
5
6 PacingRate = BCL;
7 rValue = r;
8
9 %% AP data of the targeted model
10 [VOI_EXACT, STATES_EXACT] = LuoRudy(PacingRate);
11
12 %% Measure the APD90 of the targeted model
13 VOI_TEMP = 0:0.05:PacingRate;
14 STATES_INTERP =interp1(VOI_EXACT, STATES_EXACT(:,1), VOI_TEMP, 'pchip');
15 R = STATES_INTERP;
16
17 for j = length(VOI_TEMP):-1:1
18     % we set the APD90 occurs at voltage = -70mV
19     if (R(j) >= -70.0)
20         Repol2 = VOI_TEMP(j);
21         break;
22     end
```

```

23 end
24
25 APD_EXACT = Repol2;
26
27 %% specify the initial guess of each parameter
28 P(1) = g22;
29 P(2) = k1;
30 P(3) = k2;
31 P(4) = k3;
32 P(5) = g21;
33 P(6) = fn;
34
35 % specify the boundary limit of each parameter
36 inf_limit(1) = g22_0;    sup_limit(1) = g22_1;
37 inf_limit(2) = k1_0;    sup_limit(2) = k1_1;
38 inf_limit(3) = k2_0;    sup_limit(3) = k2_1;
39 inf_limit(4) = k3_0;    sup_limit(4) = k3_1;
40 inf_limit(5) = g21_0;    sup_limit(5) = g21_1;
41 inf_limit(6) = fn_0;    sup_limit(6) = fn_1;
42
43 %% minimize AP morphology
44 options = optimset('PlotFcns',@optimplotfval, ...
45     'LargeScale','off','Display','iter', ...
46     'MaxFunEvals',50000,'TolX',1e-3, ...
47     'TolFun',1e-3,'TolCon',1e-3,'DiffMaxChange',0.5,...
48     'DiffMinChange',1e-4,'MaxIter',5000);
49
50 [Pmin] = fminsearchbnd3(@Objfun_AP,P,inf_limit,sup_limit,options);
51 Pfinal = Pmin;
52
53 %% print out the value of new estimated parameter
54 format short;
55 disp('Estimated parameter:');
56 disp(Pfinal)
57
58 %% generate APD restitution curves using dynamic pacing method
59 [Output] = APDrestitutioncurve(Pfinal);
60
61 %% store the data in a .dat file
62 fileID = fopen(sprintf('Caric_paramEstimate_PCL_%d.dat', PacingRate) , 'w');
63 fprintf(fileID,'%9f \r\n', Pfinal);
64 fclose(fileID);
65
66 end

```

A.3.3 Code 3

This code was used to optimize the objective function.

```
1 function Error = Objfun_AP(Parameter)
2
3 global VOI_EXACT STATES_EXACT APD_EXACT PacingRate rValue
4
5 %% Run the caricature model using the estimated parameters
6 [VOI_SOL, STATES_SOL] = Caric_Noble_model(Parameter,PacingRate);
7
8 %% find predicted values x(tdata)
9 STATES_PRED = interp1(VOI_SOL, STATES_SOL(:,1), VOI_EXACT, 'pchip');
10
11 %% plot the fitting result for every iteration
12 k = length(VOI_EXACT);
13
14 figure(1)
15 % plot AP of targeted data
16 plot(VOI_EXACT(), STATES_EXACT(:,1), 'b', 'LineWidth', 3);
17 hold on
18 % plot AP of caricature model
19 plot(VOI_SOL, STATES_SOL(:,1), 'r', 'LineWidth', 3);
20 hold off
21 drawnow
22
23 %% Measure the APD of caricature model
24 APD_caric = MeasureAPD(VOI_SOL, STATES_SOL);
25
26 %% compute the (global) mean relative error for the AP morphology
27 Error = 0;
28 for i = 1:length(VOI_EXACT)
29     Error = Error + abs((STATES_PRED(i) - ...
30     STATES_EXACT(i))./STATES_EXACT(i));
31 end
32
33 %% Measure the APD difference between Caricature model and the targeted
    model
34 APDdiffer = abs(APD_caric - APD_EXACT);
35
36 %% Combine both error
37 Error = Error + APDdiffer;
38
39
40 end
```

Bibliography

- Abramowitz, M. and Stegun, I. A., editors (1965). Handbook of mathematical functions: with formulas, graphs, and mathematical tables. *Dover*, New York.
- Akar, F. G. and Rosenbaum, D. S. (2003). Transmural electrophysiological heterogeneities underlying arrhythmogenesis in heart failure. *Circulation Research*, 93(7):638–645.
- Aliev, R. R. and Panfilov, A. V. (1996). A simple two-variable model of cardiac excitation. *Chaos, Solitons and Fractals*, 7(3):293 – 301.
- Amlie, J. P., Refsum, H., and Landmark, K. (1979). The effect of nifedipine on the monophasic action potential and refractoriness of the right ventricle of the dog heart in situ after β -adrenergic receptor blockade. *Acta Pharmacologica et Toxicologica*, 44(3):185–190.
- Anderson, J. L. and Prystowsky, E. N. (1999). Sotalol: An important new antiarrhythmic. *American Heart Journal*, 137(3):388 – 409.
- Anonymous (1997). FDA announces plan to halt marketing of terfenadine. *American Journal of Health-System Pharmacy*, 54(4):342–342.
- Antzelevitch, C. and Fish, J. (2001). Electrical heterogeneity within the ventricular wall. *Basic Research in Cardiology*, 96(6):517–527.
- Antzelevitch, C., Sicouri, S., Litovsky, S. H., Lukas, A., Krishnan, S. C., Di Diego, J. M., Gintant, G. A., and Liu, D. W. (1991). Heterogeneity within the ventricular wall. electrophysiology and pharmacology of epicardial, endocardial, and m cells. *Circulation Research*, 69(6):1427–1449.
- Armoundas, A. A., Tomaselli, G. F., and Esperer, H. D. (2002). Pathophysiological basis and clinical application of t-wave alternans. *Journal of the American College of Cardiology*, 40(2):207 – 217.
- Asgari-Targhi, A. (2017). Action potential duration alternans in mathematical models of excitable cells. PhD thesis, University of Glasgow.
- Aslanidi, O. V., Boyett, M. R., Dobrzynski, H., Li, J., and Zhang, H. (2009a). Mechanisms of transition from normal to reentrant electrical activity in a model of rabbit atrial tissue: Interaction of tissue heterogeneity and anisotropy. *Biophysical Journal*, 96(3):798–817.

- Aslanidi, O. V., Stewart, P., Boyett, M. R., and Zhang, H. (2009b). Optimal velocity and safety of discontinuous conduction through the heterogeneous purkinje-ventricular junction. *Biophysical Journal*, 97(1):20 – 39.
- Attin, M. and Clusin, W. T. (2009). Basic concepts of optical mapping techniques in cardiac electrophysiology. *Biological Research For Nursing*, 11(2):195–207.
- Balakrishnan, M., Chakravarthy, V. S., and Guhathakurta, S. (2015). Simulation of cardiac arrhythmias using a 2D heterogeneous whole heart model. *Frontiers in Physiology*, 6:374.
- Ballouz, S., Mangala, M. M., Perry, M. D., Heitmann, S., Gillis, J. A., Hill, A. P., and Vandenberg, J. I. (2019). Co-expression of calcium channels and delayed rectifier potassium channels protects the heart from proarrhythmic events. *bioRxiv*.
- Banville, I., Chattipakorn, N., and Gray, R. A. (2004). Restitution dynamics during pacing and arrhythmias in isolated pig hearts. *Journal of Cardiovascular Electrophysiology*, 15(4):455–463.
- Banyasz, T., Fulop, L., Magyar, J., Szentandrassy, N., Varro, A., and Nanasi, P. P. (2003). Endocardial versus epicardial differences in L-type calcium current in canine ventricular myocytes studied by action potential voltage clamp. *Cardiovascular Research*, 58(1):66–75.
- Banyasz, T., Horvath, B., Jian, Z., Izu, L. T., and Chen-Izu, Y. (2011). Sequential dissection of multiple ionic currents in single cardiac myocytes under action potential-clamp. *Journal of Molecular and Cellular Cardiology*, 50(3):578 – 581.
- Baranauskas, G. and Martina, M. (2006). Sodium currents activate without a Hodgkin and Huxley-type delay in central mammalian neurons. *Journal of Neuroscience*, 26(2):671–684.
- Barkley, D. (1991). A model for fast computer simulation of waves in excitable media. *Physica D: Nonlinear Phenomena*, 49(1):61 – 70.
- Bartos, D. C., Grandi, E., and Ripplinger, C. M. (2015). Ion channels in the heart. *American Cancer Society*.
- Bayer, J. D., Lalani, G. G., Vigmond, E. J., Narayan, S. M., and Trayanova, N. A. (2016). Mechanisms linking electrical alternans and clinical ventricular arrhythmia in human heart failure. *Heart Rhythm*, 13(9):1922 – 1931. Atrial Fibrillation.
- Beeler, G. W. and Reuter, H. (1977). Reconstruction of the action potential of ventricular myocardial fibres. 268:177–210.
- Berenfeld, O. and Jalife, J. (1998). Purkinje-muscle reentry as a mechanism of polymorphic ventricular arrhythmias in a 3-dimensional model of the ventricles. *Circulation Research*, 82(10):1063–1077.

- Bers, D. M. (1993). Excitation-contraction coupling and cardiac contractile force. Springer Netherlands.
- Bers, D. M. (2002). Cardiac Na/Ca exchange function in rabbit, mouse and man: What's the difference? *Journal of Molecular and Cellular Cardiology*, 34(4):369 – 373.
- Bers, D. M. (2008). Calcium cycling and signaling in cardiac myocytes. *Annual Review of Physiology*, 70(1):23–49.
- Beuckelmann, D. J., Nabauer, M., and Erdmann, E. (1993). Alterations of K⁺ currents in isolated human ventricular myocytes from patients with terminal heart failure. *Circulation Research*, 73(2):379–385.
- Bezekci, B., Idris, I., Simitsev, R. D., and Biktashev, V. N. (2015). Semianalytical approach to criteria for ignition of excitation waves. *Physical Review E*, 92(4).
- Biktashev, V. N., Suckley, R. S., Elkin, Y. E., and Simitsev, R. D. (2008). Asymptotic analysis and analytical solutions of a model of cardiac excitation. *Bulletin of Mathematical Biology*, 70(2):517–554.
- Biktasheva, I. V., Simitsev, R. D., Suckley, R. S., and Biktashev, V. N. (2006). Asymptotic properties of mathematical models of excitability. *Philosophical Trans. of the Royal Soc. A*, 364(1842):1283–1298.
- Binstock, L. and Goldman, L. (1971). Rectification in instantaneous potassium current? voltage relations in myxocolla giant axons. *The Journal of Physiology*, 217(3):517–531.
- Bishop, M. J., Gavaghan, D. J., Trayanova, N. A., and Rodriguez, B. (2007). Photon scattering effects in optical mapping of propagation and arrhythmogenesis in the heart. *Journal of Electrocardiology*, 40(6, Supplement 1):S75 – S80.
- Brennan, T., Fink, M., and Rodriguez, B. (2009). Multiscale modelling of drug-induced effects on cardiac electrophysiological activity. *European Journal of Pharmaceutical Sciences*, 36(1):62 – 77.
- Britton, O. J., Abi-Gerges, N., Page, G., Ghetti, A., Miller, P. E., and Rodriguez, B. (2017a). Quantitative comparison of effects of dofetilide, sotalol, quinidine, and verapamil between human ex vivo trabeculae and in silico ventricular models incorporating inter-individual action potential variability. *Frontiers in Physiology*, 8:597.
- Britton, O. J., Bueno-Orovio, A., Van Ammel, K., Lu, H. R., Towart, R., Gallacher, D. J., and Rodriguez, B. (2013). Experimentally calibrated population of models predicts and explains intersubject variability in cardiac cellular electrophysiology. *Proceedings of the National Academy of Sciences*, 110(23):E2098–E2105.

- Britton, O. J., Bueno-Orovio, A., Virag, L., Varro, A., and Rodriguez, B. (2014). Effect of inter-subject variability in determining response to IKr block in human ventricular myocytes. In *Computing in Cardiology 2014*, pages 869–872.
- Britton, O. J., Bueno-Orovio, A., Virag, L., Varro, A., and Rodriguez, B. (2017b). The electrogenic Na⁺/K⁺ pump is a key determinant of repolarization abnormality susceptibility in human ventricular cardiomyocytes: A population-based simulation study. *Frontiers in Physiology*, 8:278.
- Brunner, M., Peng, X., Liu, G. X., Ren, X.-Q., Ziv, O., Choi, B.-R., Mathur, R., Hajjiri, M., Odening, K. E., Steinberg, E., Folco, E. J., Pringa, E., Centracchio, J., Macharzina, R. R., Donahay, T., Schofield, L., Rana, N., Kirk, M., Mitchell, G. F., Poppas, A., Zehender, M., and Koren, G. (2008). Mechanisms of cardiac arrhythmias and sudden death in transgenic rabbits with long qt syndrome. *The Journal of Clinical Investigation*, 118(6):2246–2259.
- Bueno-Orovio, A., Cherry, E. M., and H., F. F. (2008). Minimal model for human ventricular action potentials in tissue. *Journal of Theoretical Biology*, 253(3):544 – 560.
- Bueno-Orovio, A., Sanchez, C., Pueyo, E., and Rodriguez, B. (2014). Na/K pump regulation of cardiac repolarization: insights from a systems biology approach. *European Journal of Physiology*, 466(2):183–193.
- Burton, F. L. and Cobbe, S. M. (2001). Dispersion of ventricular repolarization and refractory period. *Cardiovascular Research*, 50(1):10–23.
- Cairns, D. I., Fenton, F. H., and Cherry, E. M. (2017). Efficient parameterization of cardiac action potential models using a genetic algorithm. *Chaos: An Interdisciplinary Journal of Nonlinear Science*, 27(9):093922.
- Campos, R. S., Lobosco, M., and dos Santos, R. W. (2011). Adaptive time step for cardiac myocyte models. *Procedia Computer Science*, 4:1092 – 1100.
- Castaneda, M. P., Walsh, C. A., Woroniecki, R. P., Del Rio, M., and Flynn, J. T. (2005). Ventricular arrhythmia following short-acting nifedipine administration. *Pediatric Nephrology*, 20(7):1000–1002.
- CellML (1998). The CellML project – CellML. *Access date: 2017-11-29*.
- Cherry, E. M. and Fenton, F. H. (2004). Suppression of alternans and conduction blocks despite steep apd restitution: electrotonic, memory, and conduction velocity restitution effects. *American Journal of Physiology-Heart and Circulatory Physiology*, 286(6):H2332–H2341.
- Cherry, E. M. and Fenton, F. H. (2008). Visualization of spiral and scroll waves in simulated and experimental cardiac tissue. *New Journal of Physics*, 10(12):125016.

- Cherry, E. M., Fenton, F. H., and Gilmour, R. F. (2012). Mechanisms of ventricular arrhythmias: a dynamical systems-based perspective. *American Journal of Physiology-Heart and Circulatory Physiology*, 302(12):H2451–H2463.
- Clay, J. (2009). Determining K⁺ channel activation curves from K⁺ channel currents often requires the Goldman-Hodgkin-Katz equation. *Frontiers in Cellular Neuroscience*, 3:20.
- Clay, J. R. (1991). A paradox concerning ion permeation of the delayed rectifier potassium ion channel in squid giant axons. *The Journal of Physiology*, 444(1):499–511.
- Clayton, R. H. (2001). Computational models of normal and abnormal action potential propagation in cardiac tissue: linking experimental and clinical cardiology. *Physiol Meas.*, 22(3):R15–R34.
- Clayton, R. H., Bernus, O., Cherry, E. M., Dierckx, H., Fenton, F. H., Mirabella, L., Panfilov, A. V., Sachse, F. B., Seemann, G., and Zhang, H. (2011). Models of cardiac tissue electrophysiology: Progress, challenges and open questions. *Progress in Biophysics and Molecular Biology*, 104(1):22 – 48.
- Clerx, M., Collins, P., Lange, E., and Volders, P. G. A. (2016). Myokit: A simple interface to cardiac cellular electrophysiology. *Progress in Biophysics and Molecular Biology*, 120(1):100 – 114.
- Cohen, L. B., Keynes, R. D., and Hille, B. (1968). Light scattering and birefringence changes during nerve activity. *Nature*, 218(5140):438–441.
- Cohen, L. B. and Salzberg, B. M. (1978). Optical measurement of membrane potential, pages 35–88. Springer Berlin Heidelberg, Berlin, Heidelberg.
- Cooper, J., Scharm, M., and Mirams, G. R. (2016). The cardiac electrophysiology web lab. *Biophysical Journal*, 110(2):292 – 300.
- Cooper, J., Spiteri, R. J., and Mirams, G. R. (2015). Cellular cardiac electrophysiology modeling with chaste and cellml. *Frontiers in Physiology*, 5:511.
- Corrado, C. and Niederer, S. A. (2016). A two-variable model robust to pacemaker behaviour for the dynamics of the cardiac action potential. *Mathematical Biosciences*, 281:46 – 54.
- Costabal, F. S., Yao, J., and Kuhl, E. (2018). Predicting the cardiac toxicity of drugs using a novel multiscale exposure-response simulator. *Computer Methods in Biomechanics and Biomedical Engineering*, 21(3):232–246.
- Courtemanche, M., Ramirez, R. J., and Nattel, S. (1998). Ionic mechanisms underlying human atrial action potential properties: insights from a mathematical model. *American Journal of Physiology-Heart and Circulatory Physiology*, 275(1):H301–H321.

- Crumb, W. J., Vicente, J., Johannesen, L., and Strauss, D. G. (2016). An evaluation of 30 clinical drugs against the comprehensive in vitro proarrhythmia assay (CiPA) proposed ion channel panel. *Journal of Pharmacological and Toxicological Methods*, 81:251 – 262. Focused Issue on Safety Pharmacology.
- Dan, G.-A., Martinez-Rubio, A., Agewall, S., Boriani, G., Borggrefe, M., Gaita, F., van Gelder, I., Gorenek, B., Kaski, J. C., Kjeldsen, K., Lip, G. Y. H., Merkely, B., Okumura, K., Piccini, J. P., Potpara, T., Poulsen, B. K., Saba, M., Savelieva, I., Tamargo, J. L., Wolpert, C., and Group, E. S. D. (2018). Antiarrhythmic drugs-clinical use and clinical decision making: a consensus document from the European Heart Rhythm Association (EHRA) and European Society of Cardiology (ESC) Working Group on Cardiovascular Pharmacology, endorsed by the Heart Rhythm Society (HRS), Asia-Pacific Heart Rhythm Society (APHRS) and International Society of Cardiovascular Pharmacotherapy (ISCP). *EP Europace*, 20(5):731–732an.
- Dangman, K. H. and Hoffman, B. F. (1980). Effects of nifedipine on electrical activity of cardiac cells. *The American Journal of Cardiology*, 46(6):1059 – 1067.
- Deisboeck, T. S., Wang, Z., Macklin, P., and Cristini, V. (2011). Multiscale cancer modeling. *Annual Review of Biomedical Engineering*, 13(1):127–155.
- Demir, S. S., Clark, J. W., Murphey, C. R., and Giles, W. R. (1994). A mathematical model of a rabbit sinoatrial node cell. *American Journal of Physiology-Cell Physiology*, 266(3):C832–C852.
- Dhamoon, A. S. and Jalife, J. (2005). The inward rectifier current (IK1) controls cardiac excitability and is involved in arrhythmogenesis. *Heart Rhythm*, 2(3):316 – 324.
- Di Diego, J. M., Sun, Z. Q., and Antzelevitch, C. (1996). Ito and action potential notch are smaller in left vs. right canine ventricular epicardium. *American Journal of Physiology-Heart and Circulatory Physiology*, 271(2):H548–H561.
- Di Francesco, D. and Noble, D. (1985). A model of cardiac electrical activity incorporating ionic pumps and concentration changes. *Philosophical Transactions of the Royal Society of London. B, Biological Sciences*, 307(1133):353–398.
- Doke, S. K. and Dhawale, S. C. (2015). Alternatives to animal testing: A review. *Saudi Pharmaceutical Journal*, 23(3):223 – 229.
- Dokos, S. and Lovell, N. H. (2004). Parameter estimation in cardiac ionic models. *Progress in Biophysics and Molecular Biology*, 85(2-3):407–431.
- Dowle, M., Martin Mantel, R., and Barkley, D. (1997). Fast simulations of waves in three-dimensional excitable media. *International Journal of Bifurcation and Chaos*, 07(11):2529–2545.

- Draper, M. H. and Weidmann, S. (1951). Cardiac resting and action potentials recorded with an intracellular electrode. *The Journal of Physiology*, 115(1):74–94.
- Duan, D. (2009). Phenomics of cardiac chloride channels: the systematic study of chloride channel function in the heart. *The Journal of Physiology*, 587(10):2163–2177.
- Edwards, A. G. and Louch, W. E. (2017). Species-dependent mechanisms of cardiac arrhythmia: A cellular focus. *Clinical Medicine Insights: Cardiology*, 11:1179546816686061.
- Edwards, J. N. and Blatter, L. A. (2014). Cardiac alternans and intracellular calcium cycling. *Clinical and Experimental Pharmacology and Physiology*, 41(7):524–532.
- Epanchintsev, T., Pravdin, S., Sozykin, A., and Zverev, V. (2016). Parallel simulation of scroll wave dynamics in the human heart using the fenics framework. *Procedia Computer Science*, 101:68 – 75.
- Ethier, M. and Bourgault, Y. (2008). Semi-implicit time-discretization schemes for the bidomain model. *SIAM J. Numerical Analysis*, 46:2443–2468.
- Fearnley, C. J., Roderick, H. L., and Bootman, M. D. (2011). Calcium signaling in cardiac myocytes. *Cold Spring Harbor Perspectives in Biology*, 3(11).
- Fendyur, A. and Spira, M. (2012). Toward on-chip, in-cell recordings from cultured cardiomyocytes by arrays of gold mushroom-shaped microelectrodes. *Frontiers in Neuroengineering*, 5:21.
- Fenton, F. and Karma, A. (1998). Vortex dynamics in three-dimensional continuous myocardium with fiber rotation: Filament instability and fibrillation. *Chaos: An Interdisciplinary Journal of Nonlinear Science*, 8(1):20–47.
- Fenton, F. H. and Cherry, E. M. (2008). Models of cardiac cell. *Scholarpedia*, 3(8):1868. revision #91508.
- Festing, S. and Wilkinson, R. (2007). The ethics of animal research. *EMBO reports*, 8(6):526–530.
- FitzHugh, R. (1961). Impulses and physiological states in theoretical models of nerve membrane. *Biophysical Journal*, 1:445–456.
- Fox, J. J., McHarg, J. L., and Gilmour, R. F. (2002). Ionic mechanism of electrical alternans. *American Journal of Physiology-Heart and Circulatory Physiology*, 282(2):H516–H530. PMID: 11788399.
- Frankenhaeuser, B. (1962). Potassium permeability in myelinated nerve fibres of xenopus laevis. *The Journal of Physiology*, 160(1):54–61.

- Franzone, P. C., Pavarino, L. F., and Scacchi, S. (2014). *Mathematical cardiac electrophysiology*. Springer International Publishing.
- Gadsby, D. C. (1980). Activation of electrogenic Na⁺/K⁺ exchange by extracellular K⁺ in canine cardiac Purkinje fibers. *Proceedings of the National Academy of Sciences*, 77(7):4035–4039.
- Garfinkel, A., Kim, Y. H., Voroshilovsky, O., Qu, Z., Kil, J. R., Lee, M. H., Karagueuzian, H. S., Weiss, J. N., and Chen, P. S. (2000). Preventing ventricular fibrillation by flattening cardiac restitution. *Proceedings of the National Academy of Sciences*, 97(11):6061–6066.
- Gemmell, P. (2014). Ionic basis for variability in repolarisation and its implications in pathological response. PhD thesis, University of Oxford.
- Gemmell, P., Burrage, K., Rodriguez, B., and Quinn, T. A. (2014). Population of computational rabbit-specific ventricular action potential models for investigating sources of variability in cellular repolarisation. *PLOS ONE*, 9(2):1–13.
- Gemmell, P., Burrage, K., Rodriguez, B., and Quinn, T. A. (2016). Rabbit-specific computational modelling of ventricular cell electrophysiology: Using populations of models to explore variability in the response to ischemia. *Progress in Biophysics and Molecular Biology*, 121(2):169 – 184.
- Gilmour, R. F., Otani, N. F., and Watanabe, M. A. (1997). Memory and complex dynamics in cardiac purkinje fibers. *American Journal of Physiology-Heart and Circulatory Physiology*, 272(4):H1826–H1832.
- Go, A., Srivastava, S., Collis, L., Coetzee, W. A., and Artman, M. (2005). Negative inotropic effect of nifedipine in the immature rabbit heart is due to shortening of the action potential. *Pediatric research*, 57(3):399–403.
- Goktepe, S. and Kuhl, E. (2009). Computational modeling of cardiac electrophysiology: A novel finite element approach. *International Journal for Numerical Methods in Engineering*, 79(2):156–178.
- Goldhaber, J. I., Xie, L. H., Duong, T., Motter, C., Khuu, K., and Weiss, J. N. (2005). Action potential duration restitution and alternans in rabbit ventricular myocytes. *Circulation Research*, 96(4):459–466.
- Goldman, D. E. (1943). Potential, impedance, and rectification in membranes. *Journal of General Physiology*, 27(1):37–60.
- Grandi, E., Pandit, S. V., Voigt, N., Workman, A. J., Dobrev, D., Jalife, J., and Bers, D. M. (2011). Human atrial action potential and calcium model. *Circulation Research*, 109(9):1055–1066.

- Groenendaal, W., Ortega, F. A., Kherlopian, A. R., Zygmunt, A. C., Krogh-Madsen, T., and Christini, D. J. (2015). Cell-specific cardiac electrophysiology models. *PLOS Computational Biology*, 11(4):1–22.
- Guevara, M., Ward, G., Shrier, A., and Glass, L. (1984). Electrical alternans and period doubling bifurcations. *IEEE Comp Cardiol*, (562):167–170.
- Guo, D., Liu, Q., Liu, T., Elliott, G., Gingras, M., Kowey, P. R., and Yan, G. (2011). Electrophysiological properties of hbi-3000: A new antiarrhythmic agent with multiple-channel blocking properties in human ventricular myocytes. *Journal of Cardiovascular Pharmacology*, 57(1):79–85.
- Guo, T., Al Abed, A., Lovell, N. H., and Dokos, S. (2013). Optimisation of a generic ionic model of cardiac myocyte electrical activity. *Computational and Mathematical Methods in Medicine*, 2013:1–20.
- Hall, G. M., Bahar, S., and Gauthier, D. J. (1999). Prevalence of rate-dependent behaviors in cardiac muscle. *Phys. Rev. Lett.*, 82:2995–2998.
- Hamby, D. M. (1994). A review of techniques for parameter sensitivity analysis of environmental models. *Environmental Monitoring and Assessment*, 32(2):135–154.
- Hanslien, M., Karlsen, K. H., and Tveito, A. (2005). A maximum principle for an explicit finite difference scheme approximating the hodgkin-huxley model. *BIT Numerical Mathematics*, 45(4):725–741.
- Hegyi, B., Bossuyt, J., Ginsburg, K. S., Mendoza, L. M., Talken, L., Ferrier, W. T., Pogwizd, S. M., Izu, L. T., Chen-Izu, Y., and Bers, D. M. (2018). Altered repolarization reserve in failing rabbit ventricular myocytes. *Circulation: Arrhythmia and Electrophysiology*, 11(2):e005852.
- Heijman, J., Zaza, A., Johnson, D. M., Rudy, Y., Peeters, R. L. M., Volders, P. G. A., and Westra, R. L. (2013). Determinants of beat-to-beat variability of repolarization duration in the canine ventricular myocyte: A computational analysis. *PLOS Computational Biology*, 9(8):1–14.
- Henney, J. E. (2000). Withdrawal of troglitazone and cisapride. *JAMA*, 283(17):2228–2228.
- Herron, T. J., Lee, P., and Jalife, J. (2012). Optical imaging of voltage and calcium in cardiac cells and tissues. *Circulation Research*, 110(4):609–623.
- Hill, A. V. (1910). The possible effects of the aggregation of the molecules of haemoglobin on its dissociation curves. *The Journal of Physiology*, 40:i–vii.
- Hodgkin, A. L. and Huxley, A. F. (1952). A quantitative description of membrane current and its application to conduction and excitation in nerve. *J. Physiology*, 117:500–544.

- Hodgkin, A. L. and Katz, B. (1949). The effect of sodium ions on the electrical activity of the giant axon of the squid. *The Journal of Physiology*, 108(1):37–77.
- Hoffman, B. F. and Cranefield, P. F. (1964). The physiological basis of cardiac arrhythmias. *The American Journal of Medicine*, 37(5):670 – 684.
- Hund, T. J. and Rudy, Y. (2004). Rate dependence and regulation of action potential and calcium transient in a canine cardiac ventricular cell model. *Circulation*, 110(20):3168–3174.
- Hurtado, D. E., Castro, S., and Gizzi, A. (2016). Computational modeling of non-linear diffusion in cardiac electrophysiology: A novel porous-medium approach. *Computer Methods in Applied Mechanics and Engineering*, 300:70 – 83.
- Jaiswal, A. and Goldberg, S. (2014). Dofetilide induced torsade de pointes: Mechanism, risk factors and management strategies. *Indian Heart Journal*, 66(6):640 – 648.
- Janse, M. J., Opthof, T., and Kleber, A. G. (1998). Animal models of cardiac arrhythmias1. *Cardiovascular Research*, 39(1):165–177.
- Jeyaraj, D., Haldar, S. M., Wan, X., McCauley, M. D., Ripperger, J. A., Hu, K., Lu, Y., Eapen, B. L., Sharma, N., Ficker, E., Cutler, M. J., Gulick, J., Sanbe, A., Robbins, J., Demolombe, S., Kondratov, R. V., Shea, S. A., Albrecht, U., Wehrens, X. H. T., Rosenbaum, D. S., and Jain, M. K. (2012). Circadian rhythms govern cardiac repolarization and arrhythmogenesis. *Nature*, 483(7387):96–99.
- Ji, Y. C. and Fenton, F. H. (2016). Numerical solutions of reaction-diffusion equations: Application to neural and cardiac models. *American Journal of Physics*, 84(8):626–638.
- Kaab, S., Nuss, H. B., Chiamvimonvat, N., O'Rourke, B., Pak, P. H., Kass, D. A., Marban, E., and Tomaselli, G. F. (1996). Ionic mechanism of action potential prolongation in ventricular myocytes from dogs with pacing-induced heart failure. *Circulation Research*, 78(2):262–273.
- Kaese, S., Frommeyer, G., Verheule, S., van Loon, G., Gehrman, J., Breithardt, G., and Eckardt, L. (2013). The ecg in cardiovascular-relevant animal models of electrophysiology. *Herzschrittmachertherapie + Elektrophysiologie*, 24(2):1435–1544.
- Kaestner, L. (2013). Calcium signalling in cardiac myocytes, pages 24–25. Springer Berlin Heidelberg, Berlin, Heidelberg.
- Kamino, K., Hirota, A., and Fujii, S. (1981). Localization of pacemaking activity in early embryonic heart monitored using voltage-sensitive dye. *Nature*, 290(5807):595–597.
- Kang, C., Brennan, J., Kuzmiak-Glancy, S., Garrott, K., Kay, M., and Efimov, I. (2016). Technical advances in studying cardiac electrophysiology – role of rabbit models. *Progress in Biophysics and Molecular Biology*, 121(2):97 – 109.

- Karma, A. (1994). Electrical alternans and spiral wave breakup in cardiac tissue. *Chaos*, 4:461–472.
- Kaur, J., Nygren, A., and Vigmond, E. J. (2014). Fitting membrane resistance along with action potential shape in cardiac myocytes improves convergence: Application of a multi-objective parallel genetic algorithm. *PLOS ONE*, 9(9):1–10.
- Keener, J. P. and Sneyd, J. (1991). *Mathematical physiology*. Springer, Berlin.
- Keldermann, R. H., ten Tusscher, K. H. W. J., Nash, M. P., Hren, R., Taggart, P., and Panfilov, A. V. (2008). Effect of heterogeneous APD restitution on VF organization in a model of the human ventricles. *American Journal of Physiology-Heart and Circulatory Physiology*, 294(2):H764–H774.
- Kimura, S., Bassett, A. L., Kohya, T., Kozlovskis, P. L., and Myerburg, R. J. (1986). Simultaneous recording of action potentials from endocardium and epicardium during ischemia in the isolated cat ventricle: relation of temporal electrophysiologic heterogeneities to arrhythmias. *Circulation*, 74(2):401–409.
- Kirkpatrick, S., Gelatt, C. D., and Vecchi, M. P. (1983). Optimization by simulated annealing. *Science*, 220(4598):671–680.
- Kirsch, G. E., Trepakova, E. S., Brimecombe, J. C., Sidach, S. S., Erickson, H. D., Kochan, M. C., Shyjka, L. M., Lacerda, A. E., and Brown, A. M. (2004). Variability in the measurement of hERG potassium channel inhibition: Effects of temperature and stimulus pattern. *Journal of Pharmacological and Toxicological Methods*, 50(2):93 – 101.
- Kneller, J., Kalifa, J., Zou, R., Zaitsev, A. V., Warren, M., Berenfeld, O., Vigmond, E. J., Leon, L. J., Nattel, S., and Jalife, J. (2005). Mechanisms of atrial fibrillation termination by pure sodium channel blockade in an ionically-realistic mathematical model. *Circulation Research*, 96(5):e35–e47.
- Knight, A. (2013). Animals in research: do the costs outweigh the benefits? <https://theconversation.com/animals-in-research-do-the-costs-outweigh-the-benefits-16390>.
- Kogan, B. Y., Karplus, W. J., Billett, B. S., Pang, A. T., Karagueuzian, H. S., and Khan, S. S. (1991). The simplified FitzHugh-Nagumo model with action potential duration restitution: Effects on 2D wave propagation. *Physica D: Nonlinear Phenomena*, 50(3):327 – 340.
- Kohl, P., Bollensdorff, C., and Garny, A. (2006). Effects of mechanosensitive ion channels on ventricular electrophysiology: experimental and theoretical models. *Experimental Physiology*, 91(2):307–321.

- Kohl, P., Noble, D., Hunter, P. J., Noble, D., and Rudy, Y. (2001). Models of cardiac ventricular action potentials: iterative interaction between experiment and simulation. *Philosophical Transactions of the Royal Society of London. Series A: Mathematical, Physical and Engineering Sciences*, 359(1783):1127–1142.
- Koivumaki, J. T., Korhonen, T., and Tavi, P. (2011). Impact of sarcoplasmic reticulum calcium release on calcium dynamics and action potential morphology in human atrial myocytes: A computational study. *PLOS Computational Biology*, 7(1):1–14.
- Kuehn, C. (2015). Numerical methods. Springer International Publishing.
- Lachaud, Q. (2019). Development of a medium high throughput electrophysiology method to study cellular heterogeneity in the rabbit heart. PhD thesis, University of Glasgow.
- Lagarias, J. C., Reeds, J. A., Wright, M. H., and Wright, P. E. (1998). Convergence properties of the Nelder–Mead simplex method in low dimensions. *SIAM Journal on Optimization*, 9(1):112–147.
- Lang, C., Koren, G., and Odening, K. (2016). Transgenic rabbit models to investigate the cardiac ion channel disease long qt syndrome. *Progress in Biophysics and Molecular Biology*, 121(2):142 – 156.
- Lawson, B. A. J., Drovandi, C. C., Cusimano, N., Burrage, P., Rodriguez, B., and Burrage, K. (2018). Unlocking data sets by calibrating populations of models to data density: A study in atrial electrophysiology. *Science Advances*, 4(1).
- Lelovas, P. P., Kostomitsopoulos, N. G., and Xanthos, T. T. (2014). A comparative anatomic and physiologic overview of the porcine heart. *Journal of the American Association for Laboratory Animal Science : JAALAS*, 53(5):432–438.
- Li, G. R., Lau, C. P., Leung, T. K., and Nattel, S. (2004). Ionic current abnormalities associated with prolonged action potentials in cardiomyocytes from diseased human right ventricles. *Heart Rhythm*, 1(4):460–468.
- Litovsky, S. H. and Antzelevitch, C. (1988). Transient outward current prominent in canine ventricular epicardium but not endocardium. *Circulation Research*, 62(1):116–126.
- Liu, D. W., Gintant, G. A., and Antzelevitch, C. (1993). Ionic bases for electrophysiological distinctions among epicardial, midmyocardial, and endocardial myocytes from the free wall of the canine left ventricle. *Circulation Research*, 72(3):671–687.
- Lopez-Lopez, J. R., Shacklock, P. S., Balke, C. W., and Wier, W. G. (1994). Local, stochastic release of Ca²⁺ in voltage-clamped rat heart cells: visualization with confocal microscopy. *The Journal of Physiology*, 480(1):21–29.

- Lou, Q., Li, W., and Efimov, I. R. (2011). Multiparametric optical mapping of the langendorff-perfused rabbit heart. *J. Vis. Exp.*, (55):e3160.
- Lovell, N. H., Cloherty, S. L., Celler, B. G., and Dokos, S. (2004). A gradient model of cardiac pacemaker myocytes. *Progress in Biophysics and Molecular Biology*, 85(2):301 – 323. Modelling Cellular and Tissue Function.
- Lu, H. R., Marien, R., Saels, A., and De Clerck, F. (2001). Species plays an important role in drug-induced prolongation of action potential duration and early afterdepolarizations in isolated purkinje fibers. *Journal of Cardiovascular Electrophysiology*, 12(1):93–102.
- Luo, C. H. and Rudy, Y. (1991). A model of the ventricular cardiac action potential. depolarization, repolarization, and their interaction. *Circulation Research*, 68(6):1501–1526.
- Luo, C. H. and Rudy, Y. (1994a). A dynamic model of the cardiac ventricular action potential. I. Simulations of ionic currents and concentration changes. *Circulation Research*, 74(6):1071–1096.
- Luo, C. H. and Rudy, Y. (1994b). A dynamic model of the cardiac ventricular action potential. II. Afterdepolarizations, triggered activity, and potentiation. *Circulation Research*, 74(6):1097–1113.
- Mahajan, A., Shiferaw, Y., Sato, D., Baher, A., Olcese, R., H., X. L., Yang, M. J., Chen, P. S., Restrepo, J. G., Karma, A., Garfinkel, A., Qu, Z., and Weiss, J. N. (2008). A rabbit ventricular action potential model replicating cardiac dynamics at rapid heart rates. *Biophysical Journal*, 94(2):392–410.
- Maleckar, M. M., Greenstein, J. L., Trayanova, N. A., and Giles, W. R. (2008). Mathematical simulations of ligand-gated and cell-type specific effects on the action potential of human atrium. *Progress in Biophysics and Molecular Biology*, 98(2):161–170.
- McAllister, R. E., Noble, D., and Tsien, R. W. (1975). Reconstruction of the electrical activity of cardiac Purkinje fibres. *The Journal of Physiology*, 251(1):1–59.
- McFarlane, R. and Biktasheva, I. V. (2008). Beatbox - a computer simulation environment for computational biology of the heart. *BCS International Academic Conference "Visions of Computer Science"*.
- McIntosh, M. A., Cobbe, S. M., and Smith, G. L. (2000). Heterogeneous changes in action potential and intracellular Ca²⁺ in left ventricular myocyte sub-types from rabbits with heart failure. *Cardiovascular Research*, 45(2):397–409.

- McKay, M. D., Beckman, R. J., and Conover, W. J. (1979). A comparison of three methods for selecting values of input variables in the analysis of output from a computer code. *Technometrics*, 21(2):239.
- Mickus, T., Jung, H., and Spruston, N. (1999). Properties of slow, cumulative sodium channel inactivation in rat hippocampal CA1 pyramidal neurons. *Biophysical Journal*, 76(2):846–860.
- Migliore, M., Xia, Y., Wang, K., and Zhang, H. (2015). Parallel optimization of 3d cardiac electrophysiological model using gpu. *Computational and Mathematical Methods in Medicine*, 2015.
- Milescu, L. S., Akk, G., and Sachs, F. (2005). Maximum likelihood estimation of ion channel kinetics from macroscopic currents. *Biophysical Journal*, 88(4):2494–2515.
- Mirams, G. R., Arthurs, C. J., Bernabeu, M. O., Bordas, R., Cooper, J., Corrias, A., Davit, Y., Dunn, S.-J., Fletcher, A. G., Harvey, D. G., Marsh, M. E., Osborne, J. M., Pathmanathan, P., Pitt-Francis, J., Southern, J., Zenzemi, N., and Gavaghan, D. J. (2013). Chaste: An open source C++ library for computational physiology and biology. *PLOS Computational Biology*, 9(3):1–8.
- Mitchell, C. and Schaeffer, D. G. (2003). A two-current model for the dynamics of cardiac membrane. *Bulletin of Mathematical Biology*, 65(3):767–793.
- Moghaderi, H. and Dehghan, M. (2017). Mixed two-grid finite difference methods for solving one-dimensional and two-dimensional Fitzhugh-Nagumo equations. *Mathematical Methods in the Applied Sciences*, 40(4):1170–1200.
- Moreno, J. D., Lewis, T. J., and Clancy, C. E. (2016). Parameterization for in-silico modeling of ion channel interactions with drugs. *PLOS ONE*, 11(3):1–22.
- Moreno, J. D., Zhu, Z. I., Yang, P.-C., Bankston, J. R., Jeng, M.-T., Kang, C., Wang, L., Bayer, J. D., Christini, D. J., Trayanova, N. A., Ripplinger, C. M., Kass, R. S., and Clancy, C. E. (2011). A computational model to predict the effects of class I anti-arrhythmic drugs on ventricular rhythms. *Science Translational Medicine*, 3(98):98ra83–98ra83.
- Murillo, M. and Cai, X. C. (2004). A fully implicit parallel algorithm for simulating the non-linear electrical activity of the heart. *Numerical Linear Algebra with Applications*, 11(2-3):261–277.
- Muszkiewicz, A., Britton, O. J., Gemmell, P., Passini, E., Sanchez, C., Zhou, X., Carusi, A., Quinn, T. A., Burrage, K., Bueno-Orovio, A., and Rodriguez, B. (2016). Variability in cardiac electrophysiology: Using experimentally-calibrated populations of models to move beyond the single virtual physiological human paradigm. *Progress in Biophysics and Molecular Biology*, 120(1):115 – 127.

- Nalos, L., Varkevisser, R., Jonsson, M. K. B., Houtman, M. J. C., Beekman, J. D., van der Nagel, R., Thomsen, M. B., Duker, G., Sartipy, P., de Boer, T. P., Peschar, M., Rook, M. B., van Veen, T. A. B., van der Heyden, M. A. G., and Vos, M. A. (2012). Comparison of the IKr blockers moxifloxacin, dofetilide and E-4031 in five screening models of pro-arrhythmia reveals lack of specificity of isolated cardiomyocytes. *British Journal of Pharmacology*, 165(2):467–478.
- Nash, M. P., Bradley, C. P., Sutton, P. M., Clayton, R. H., Kallis, P., Hayward, M. P., Paterson, D. J., and Taggart, P. (2006). Whole heart action potential duration restitution properties in cardiac patients: a combined clinical and modelling study. *Experimental Physiology*, 91(2):339–354.
- Neher, E. and Sakmann, B. (1976). Single-channel currents recorded from membrane of denervated frog muscle fibres. *Nature*, (260):799–802.
- Nelder, J. A. and Mead, R. (1965). A simplex method for function minimization. *The Computer Journal*, 7(4):308–313.
- Nerbonne, J. M. and Kass, R. S. (2005). Molecular physiology of cardiac repolarization. *Physiological Reviews*, 85(4):1205–1253.
- Ni, H., Morotti, S., and Grandi, E. (2018). A heart for diversity: Simulating variability in cardiac arrhythmia research. *Frontiers in Physiology*, 9:958.
- Nickerson, D. P. and Hunter, P. J. (2010). Cardiac cellular electrophysiological modeling. *Springer US*, Boston, MA.
- Niederer, S. A., Fink, M., Noble, D., and Smith, N. P. (2009). A meta-analysis of cardiac electrophysiology computational models. *Experimental Physiology*, 94(5):486–495.
- Noble, D. (1962). A modification of the Hodgkin-Huxley equations applicable to Purkinje fibre action and pace-maker potentials. *J. Physiology*, 160:317–352.
- Noble, D. (2011). Successes and failures in modeling heart cell electrophysiology. *Heart Rhythm*, 8(11):1798 – 1803.
- Noble, D., Garny, A., and Noble, P. J. (2012). How the Hodgkin-Huxley equations inspired the Cardiac Physiome Project. *The Journal of Physiology*, 590(11):2613–2628.
- Noble, D. and Tsien, R. W. (1968). The kinetics and rectifier properties of the slow potassium current in cardiac purkinje fibres. *The Journal of Physiology*, 195(1):185–214.
- Noble, D. and Tsien, R. W. (1969a). Outward membrane currents activated in the plateau range of potentials in cardiac purkinje fibres. *The Journal of Physiology*, 200(1):205–231.

- Noble, D. and Tsien, R. W. (1969b). Reconstruction of the repolarization process in cardiac purkinje fibres based on voltage clamp measurements of membrane current. *The Journal of Physiology*, 200(1):233–254.
- Nolasco, J. B. and Dahlen, R. W. (1968). A graphic method for the study of alternation in cardiac action potentials. *Journal of Applied Physiology*, 25(2):191–196.
- Nygren, A., Fiset, C., Firek, L., Clark, J. W., Lindblad, D. S., Clark, R. B., and Giles, W. R. (1998). Mathematical model of an adult human atrial cell. *Circulation Research*, 82(1):63–81.
- Odening, K. E., Baczko, I., and Brunner, M. (2020). Animals in cardiovascular research: important role of rabbit models in cardiac electrophysiology. *European Heart Journal*, 41(21):2036–2036.
- Ogura, T., Shuba, L. M., and McDonald, T. F. (1995). Action potentials, ionic currents and cell water in guinea pig ventricular preparations exposed to dimethyl sulfoxide. *Journal of Pharmacology and Experimental Therapeutics*, 273(3):1273–1286.
- O’Hara, T. and Rudy, Y. (2012). Quantitative comparison of cardiac ventricular myocyte electrophysiology and response to drugs in human and nonhuman species. *American Journal of Physiology-Heart and Circulatory Physiology*, 302(5):H1023–H1030.
- O’Hara, T., Virag, L., Varra, A., and Rudy, Y. (2011). Simulation of the undiseased human cardiac ventricular action potential: Model formulation and experimental validation. *PLOS Computational Biology*, 7(5):1–29.
- Pandit, S. V. and Jalife, J. (2013). Rotors and the dynamics of cardiac fibrillation. *Circulation Research*, 112(5):849–862.
- Panfilov, A. V. (2006). Is heart size a factor in ventricular fibrillation? Or how close are rabbit and human hearts? *Heart Rhythm*, 3(7):862–864.
- Passini, E., Britton, O. J., Lu, H. R., Rohrbacher, J., Hermans, A. N., Gallacher, D. J., Greig, R. J. H., Bueno-Orovio, A., and Rodriguez, B. (2017). Human in silico drug trials demonstrate higher accuracy than animal models in predicting clinical pro-arrhythmic cardiotoxicity. *Frontiers in Physiology*, 8:668.
- Passini, E., Mincholé, A., Coppini, R., Cerbai, E., Rodriguez, B., Severi, S., and Bueno-Orovio, A. (2016). Mechanisms of pro-arrhythmic abnormalities in ventricular repolarisation and anti-arrhythmic therapies in human hypertrophic cardiomyopathy. *Journal of Molecular and Cellular Cardiology*, 96:72 – 81. Special Issue: Computational Modelling of the Heart.
- Pathmanathan, P. and Gray, R. A. (2018). Validation and trustworthiness of multiscale models of cardiac electrophysiology. *Frontiers in Physiology*, 9:106.

- Peachey, T. C., Diamond, N. T., Abramson, D. A., Sudholt, W., Michailova, A., and Amirriazi, S. (2008). Fractional factorial design for parameter sweep experiments using Nimrod/E. *Scientific Programming*, 16:217–230.
- Penaranda, A., Cantalapiedra, I. R., Bragard, J., and Echebarria, B. (2012). Cardiac dynamics: a simplified model for action potential propagation. *Theoretical Biology and Medical Modelling*, 9(1):50.
- Plank, G., Burton, R. A. B., Hales, P., Bishop, M., Mansoori, T., Bernabeu, M. O., Garny, A., Prassl, A. J., Bollensdorff, C., Mason, F., Mahmood, F., Rodriguez, B., Grau, V., Schneider, J. E., Gavaghan, D., and Kohl, P. (2009). Generation of histo-anatomically representative models of the individual heart: tools and application. *Philosophical Transactions of the Royal Society A: Mathematical, Physical and Engineering Sciences*, 367(1896):2257–2292.
- Potse, M. (2012). Mathematical modeling and simulation of ventricular activation sequences: Implications for cardiac resynchronization therapy. *Journal of Cardiovascular Translational Research*, 5(2):146–158.
- Priebe, L. and Beuckelmann, D. J. (1998). Simulation study of cellular electric properties in heart failure. *Circulation Research*, 82(11):1206–1223.
- Prinz, A., Bucher, D., and Marder, E. (2004). Similar network activity from disparate circuit parameters. *Nat. Neurosci.*, 7(12):1345–1352.
- Pueyo, E., Malik, M., and Laguna, P. (2008). A dynamic model to characterize beat-to-beat adaptation of repolarization to heart rate changes. *Biomedical Signal Processing and Control*, 3(1):29 – 43.
- Puglisi, J. L. and Bers, D. M. (2001). LabHEART: an interactive computer model of rabbit ventricular myocyte ion channels and Ca transport. *American Journal of Physiology-Cell Physiology*, 281(6):C2049–C2060.
- Qu, Z. and Garfinkel, A. (1999). An advanced algorithm for solving partial differential equation in cardiac conduction. *IEEE Transactions on Biomedical Engineering*, 46(9):1166–1168.
- Qu, Z. and Weiss, J. N. (2005). Effects of Na⁺ and K⁺ channel blockade on vulnerability to and termination of fibrillation in simulated normal cardiac tissue. *American Journal of Physiology-Heart and Circulatory Physiology*, 289(4):H1692–H1701.
- Qu, Z., Xie, L.-H., Olcese, R., Karagueuzian, H. S., Chen, P.-S., Garfinkel, A., and Weiss, J. N. (2013). Early afterdepolarizations in cardiac myocytes: beyond reduced repolarization reserve. *Cardiovascular Research*, 99(1):6–15.

- Rahm, A.-K., Lugenbiel, P., Schweizer, P. A., Katus, H. A., and Thomas, D. (2018). Role of ion channels in heart failure and channelopathies. *Biophysical Reviews*, 10(4):1097–1106.
- Rees, C. M., Yang, J.-H., Santolini, M., Lusic, A. J., Weiss, J. N., and Karma, A. (2018). The Ca^{2+} transient as a feedback sensor controlling cardiomyocyte ionic conductances in mouse populations. *eLife*, 7:e36717.
- Ren, W. and Weinan, E. (2005). Heterogeneous multiscale method for the modeling of complex fluids and micro-fluidics. *Journal of Computational Physics*, 204(1):1 – 26.
- Reuter, H. (1967). The dependence of slow inward current in purkinje fibres on the extracellular calcium-concentration. *The Journal of Physiology*, 192(2):479–492.
- Reuter, H. and Seitz, N. (1968). The dependence of calcium efflux from cardiac muscle on temperature and external ion composition. *The Journal of Physiology*, 195(2):451–470.
- Rios, L. M. and Sahinidis, N. V. (2013). Derivative-free optimization: a review of algorithms and comparison of software implementations. *Journal of Global Optimization*, 56(3):1247–1293.
- Rogers, J. M. and McCulloch, A. D. (1994). A collocation-galerkin finite element model of cardiac action potential propagation. *IEEE Transactions on Biomedical Engineering*, 41(8):743–757.
- Romero, L., Pueyo, E., Fink, M., and Rodriguez, B. (2009). Impact of ionic current variability on human ventricular cellular electrophysiology. *American Journal of Physiology-Heart and Circulatory Physiology*, 297(4):H1436–H1445.
- Roy, T., Bourgault, Y., and Pierre, C. (2017). Analysis of time-stepping methods for the monodomain model.
- Rush, S. and Larsen, H. (1978). A practical algorithm for solving dynamic membrane equations. *IEEE Transactions on Biomedical Engineering*, BME-25(4):389–392.
- Saffitz, J. E., Kanter, H. L., Green, K. G., Tolley, T., and Beyer, E. C. (1994). Tissue-specific determinants of anisotropic conduction velocity in canine atrial and ventricular myocardium. *Circulation research*, 74 6:1065–70.
- Sakmann, B. and Neher, E. (1984). Patch clamp techniques for studying ionic channels in excitable membranes. *Annual Review of Physiology*, 46(1):455–472.
- Sampson, K. J., Iyer, V., Marks, A. R., and Kass, R. S. (2010). A computational model of Purkinje fibre single cell electrophysiology: implications for the long QT syndrome. *The Journal of Physiology*, 588(14):2643–2655.

- Sanchez, C., Bueno-Orovio, A., Wettwer, E., Loose, S., Simon, J., Ravens, U., Pueyo, E., and Rodriguez, B. (2014). Inter-subject variability in human atrial action potential in sinus rhythm versus chronic atrial fibrillation. *PLOS ONE*, 9(8):1–14.
- Santana, L. F., Cheng, E. P., and Lederer, W. J. (2010). How does the shape of the cardiac action potential control calcium signaling and contraction in the heart? *Journal of Molecular and Cellular Cardiology*, 49(6):901 – 903.
- Sarkar, A. X. and Sobie, E. A. (2010). Regression analysis for constraining free parameters in electrophysiological models of cardiac cells. *PLOS Computational Biology*, 6(9):1–11.
- Sarkar, A. X. and Sobie, E. A. (2011). Quantification of repolarization reserve to understand interpatient variability in the response to proarrhythmic drugs: A computational analysis. *Heart Rhythm*, 8(11):1749 – 1755.
- Shah, R. R. (2007). Withdrawal of terodiline: A tale of two toxicities. *John Wiley & Sons, Ltd.*
- Sham, J. S., Hatem, S. N., and Morad, M. (1995). Species differences in the activity of the $\text{Na}^+/\text{Ca}^{2+}$ exchanger in mammalian cardiac myocytes. *The Journal of Physiology*, 488(3):623–631.
- Shannon, T. R., Wang, F., Puglisi, J., Weber, C., and Bers, D. M. (2004). A mathematical treatment of integrated Ca dynamics within the ventricular myocyte. *Biophysical Journal*, 87(5):3351–3371.
- Sigg, D. (2010). Cardiac electrophysiology methods and models. Springer New York.
- Simitev, R. D. and Biktashev, V. (2011). Asymptotics of conduction velocity restitution in models of electrical excitation in the heart. *Bulletin of Mathematical Biology*, 73(1):72–115.
- Simitev, R. D. and Biktashev, V. N. (2006). Conditions for propagation and block of excitation in an asymptotic model of atrial tissue. *Biophys. J.*, 90(7):2258–2269.
- Snowden, T. J., van der Graaf, P. H., and Tindall, M. J. (2017). Methods of model reduction for large-scale biological systems: A survey of current methods and trends. *Bulletin of Mathematical Biology*, 79(7):1449–1486.
- Sobie, E. A. (2009). Parameter sensitivity analysis in electrophysiological models using multi-variable regression. *Biophysical Journal*, 96(4):1264 – 1274.
- Sovilj, S., Magjarevic, R., Lovell, N. H., and Dokos, S. (2013). A simplified 3D model of whole heart electrical activity and 12-lead ECG generation. *Computational and Mathematical Methods in Medicine*, 2013:10.

- Spiteri, R. J. and Dean, R. C. (2010). Stiffness analysis of cardiac electrophysiological models. *Annals of Biomedical Engineering*, 38(12):3592–3604.
- Strang, G. (1968). On the construction and comparison of difference schemes. *SIAM Journal on Numerical Analysis*, 5(3):506–517.
- Su, Z., Li, F., Spitzer, K. W., Yao, A., Ritter, M., and Barry, W. H. (2003). Comparison of sarcoplasmic reticulum Ca²⁺-ATPase function in human, dog, rabbit, and mouse ventricular myocytes. *Journal of Molecular and Cellular Cardiology*, 35(7):761–767.
- Suckley, R. (2004). The asymptotic structure of excitable systems of equations. PhD thesis, University of Liverpool.
- Sundnes, J., Lines, G. T., Cai, X., Nielsen, B. F., Mardal, K., and Tveito, A. (2006). Mathematical models, pages 21–56. Springer Berlin Heidelberg, Berlin, Heidelberg.
- Syed, Z., Vigmond, E., Nattel, S., and Leon, L. J. (2005). Atrial cell action potential parameter fitting using genetic algorithms. *Medical & Biological Engineering & Computing*, 43(5):561–571.
- Tagliatela, M. and Stefani, E. (1993). Gating currents of the cloned delayed-rectifier K⁺ channel DRK1. *Proceedings of the National Academy of Sciences*, 90(10):4758–4762.
- Tamargo, J., Caballero, R., Gomez, R., Valenzuela, C., and Delpon, E. (2004). Pharmacology of cardiac potassium channels. *Cardiovascular Research*, 62(1):9–33.
- Ten Tusscher, K. H. W. J., Bernus, O., Hren, R., and Panfilov, A. V. (2006). Comparison of electrophysiological models for human ventricular cells and tissues. *Progress in Biophysics and Molecular Biology*, 90(1):326 – 345.
- Ten Tusscher, K. H. W. J., Hren, R., and Panfilov, A. V. (2007). Organization of ventricular fibrillation in the human heart. *Circulation Research*, 100(12):e87–e101.
- Ten Tusscher, K. H. W. J., Noble, D., Noble, P. J., and Panfilov, A. V. (2004). A model for human ventricular tissue. *American Journal of Physiology-Heart and Circulatory Physiology*, 286(4):H1573–H1589.
- Thompson, J. M. T., Kohl, P., Noble, D., Winslow, R. L., and Hunter, P. J. (2000). Computational modelling of biological systems: tools and visions. *Philosophical Transactions of the Royal Society of London. Series A: Mathematical, Physical and Engineering Sciences*, 358(1766):579–610.
- Tirziu, D., Giordano, F. J., and Simons, M. (2010). Cell communications in the heart. *Circulation*, 122(9):928–937.

- Tolkacheva, E. G., Schaeffer, D. G., Gauthier, D. J., and Krassowska, W. (2003). Condition for alternans and stability of the 1:1 response pattern in a “memory” model of paced cardiac dynamics. *Phys. Rev. E*, 67:031904.
- Tolkacheva, E. G., Schaeffer, D. G., Gauthier, D. J., and Mitchell, C. C. (2002). Analysis of the Fenton-Karma model through an approximation by a one-dimensional map. *Chaos: An Interdisciplinary Journal of Nonlinear Science*, 12(4):1034–1042.
- Tomek, J., Bueno-Orovio, A., Passini, E., Zhou, X., Mincholé, A., Britton, O., Bartolucci, C., Severi, S., Shrier, A., Virag, L., Varro, A., and Rodriguez, B. (2019). Development, calibration, and validation of a novel human ventricular myocyte model in health, disease, and drug block. *eLife*, 8:e48890.
- Tomek, J., Bueno-Orovio, A., and Rodriguez, B. (2020). Tor-ord-dyncl: an update of the tor-ord model of human ventricular cardiomyocyte with dynamic intracellular chloride. *bioRxiv*.
- Tomek, J., Tomkova, M., Zhou, X., Bub, G., and Rodriguez, B. (2018). Modulation of cardiac alternans by altered sarcoplasmic reticulum calcium release: A simulation study. *Frontiers in Physiology*, 9:1306.
- Tonnelier, A. (2002). The McKean’s caricature of the Fitzhugh-Nagumo model I. The space-clamped system. *SIAM Journal on Applied Mathematics*, 63(2):459–484.
- Towbin, J. A. and Bowles, N. E. (2001). Molecular genetics of left ventricular dysfunction. *Current Molecular Medicine*, 1(1):81–90.
- Townsend, N., Williams, J., Bhatnagar, P., Wickramasinghe, K., and Rayner, M. (2014). Cardiovascular disease statistics. *British Heart Foundation: London*.
- Trayanova, N. A. (2014). Mathematical approaches to understanding and imaging atrial fibrillation. *Circulation Research*, 114(9):1516–1531.
- Trayanova, N. A. and Boyle, P. M. (2014). Advances in modeling ventricular arrhythmias: from mechanisms to the clinic. *WIREs Systems Biology and Medicine*, 6(2):209–224.
- Trayanova, N. A. and Chang, K. C. (2016). How computer simulations of the human heart can improve anti-arrhythmia therapy. *The Journal of Physiology*, 594(9):2483–2502.
- Trayanova, N. A. and Winslow, R. (2011). Whole-heart modeling. *Circulation Research*, 108(1):113–128.
- Trovato, C., Passini, E., Nagy, N., Varro, A., Abi-Gerges, N., Severi, S., and Rodriguez, B. (2020). Human purkinje in silico model enables mechanistic investigations into automaticity and pro-arrhythmic abnormalities. *Journal of Molecular and Cellular Cardiology*, 142:24–38.

- Tse, G., Wong, S. T., Tse, V., Lee, Y. T., Lin, H. Y., and Yeo, J. M. (2016). Cardiac dynamics: Alternans and arrhythmogenesis. *Journal of Arrhythmia*, 32(5):411 – 417.
- Tsuji, Y., Opthof, T., Kamiya, K., Yasui, K., Liu, W., Lu, Z., and Kodama, I. (2000). Pacing-induced heart failure causes a reduction of delayed rectifier potassium currents along with decreases in calcium and transient outward currents in rabbit ventricle. *Cardiovascular Research*, 48(2):300–309.
- Tsujimae, K., Murakami, S., and Kurachi, Y. (2008). In silico study on the effects of IK_{Kr} block kinetics on prolongation of human action potential after atrial fibrillation-induced electrical remodeling. *American Journal of Physiology-Heart and Circulatory Physiology*, 294(2):H793–H800.
- Valdivia, C. R., Chu, W. W., Pu, J., Foell, J. D., Haworth, R. A., Wolff, M. R., Kamp, T. J., and Makielski, J. C. (2005). Increased late sodium current in myocytes from a canine heart failure model and from failing human heart. *Journal of Molecular and Cellular Cardiology*, 38(3):475–483.
- Vandenberg, C. A. and Bezanilla, F. A. (1991). Sodium channel gating model based on single channel, macroscopic ionic, and gating currents in the squid giant axon. *Biophys J.*, 60(6):1511—1533.
- Varshneya, M., Devenyi, R. A., and Sobie, E. A. (2018). Slow delayed rectifier current protects ventricular myocytes from arrhythmic dynamics across multiple species. *Circulation: Arrhythmia and Electrophysiology*, 11(10):e006558.
- Victorri, B., Vinet, A., Roberge, F. A., and Drouhard, J. P. (1985). Numerical integration in the reconstruction of cardiac action potentials using Hodgkin-Huxley-type models. *Computers and Biomedical Research*, 18(1):10 – 23.
- Vigmond, E. J., Aguel, F., and Trayanova, N. A. (2002). Computational techniques for solving the bidomain equations in three dimensions. *IEEE Transactions on Biomedical Engineering*, 49(11):1260–1269.
- Vigmond, E. J. and Clements, C. (2007). Construction of a computer model to investigate sawtooth effects in the purkinje system. *IEEE Transactions on Biomedical Engineering*, 54(3):389–399.
- Visweswaran, R., McIntyre, S. D., Ramkrishnan, K., Zhao, X., and Tolkacheva, E. G. (2013). Spatiotemporal evolution and prediction of [Ca²⁺]_i and APD alternans in isolated rabbit hearts. *Journal of Cardiovascular Electrophysiology*, 24(11):1287–1295.

- Voigt, N., Heijman, J., Wang, Q., Chiang, D. Y., Li, N., Karck, M., Wehrens, X. H., Nattel, S., and Dobrev, D. (2014). Cellular and molecular mechanisms of atrial arrhythmogenesis in patients with paroxysmal atrial fibrillation. *Circulation*, 129(2):145–156.
- Walmsley, J., Mirams, G. R., Pitt-Francis, J., Rodriguez, B., and Burrage, K. (2015). Application of stochastic phenomenological modelling to cell-to-cell and beat-to-beat electrophysiological variability in cardiac tissue. *Journal of Theoretical Biology*, 365:325 – 336.
- Wei, D. (2005). Whole Heart Modeling and Computer Simulation, pages 81–117. Springer US, Boston, MA.
- Weinan, E. and Engquist, B. (2003). The heterogenous multiscale methods. *Commun. Math. Sci.*, 1(1):87–132.
- Weinan, E., Engquist, B., and Sun, Y. (2011). The heterogeneous multiscale methods with application to combustion. *Springer Netherlands*.
- Weiss, J. N., Garfinkel, A., Karagueuzian, H. S., Chen, P. S., and Qu, Z. (2010). Early afterdepolarizations and cardiac arrhythmias. *Heart Rhythm*, 7(12):1891 – 1899.
- Weissenburger, J., Nesterenko, V., and Antzelevitch, C. (2000). Transmural heterogeneity of ventricular repolarization under baseline and long qt conditions in the canine heart in vivo: Torsades de pointes develops with halothane but not pentobarbital anesthesia. *Journal of Cardiovascular Electrophysiology*, 11(3):290–304.
- West, T. C. (1955). Ultramicroelectrode recording from the cardiac pacemaker. *Journal of Pharmacology and Experimental Therapeutics*, 115(3):283–290.
- Wilhelms, M., Hettmann, H., Maleckar, M., Koivumaki, J., Dossel, O., and Seemann, G. (2013). Benchmarking electrophysiological models of human atrial myocytes. *Frontiers in Physiology*, 3:487.
- Wuskell, J. P., Boudreau, D., Wei, M., Jin, L., Engl, R., Chebolu, R., Bullen, A., Hoffacker, K. D., Kerimo, J., Cohen, L. B., Zochowski, M. R., and Loew, L. M. (2006). Synthesis, spectra, delivery and potentiometric responses of new styryl dyes with extended spectral ranges. *Journal of Neuroscience Methods*, 151(2):200 – 215.
- Yamashita, T., Sekiguchi, A., Iwasaki, Y., Sagara, K., Inuma, H., Hatano, S., Fu, L., and Watanabe, H. (2003). Circadian variation of cardiac K⁺ channel gene expression. *Circulation*, 107(14):1917–1922.
- Yao, J. A., Du, X., Lu, D., Baker, R. L., Daharsh, E., and Atterson, P. (2005). Estimation of potency of hERG channel blockers: Impact of voltage protocol and temperature. *Journal of Pharmacological and Toxicological Methods*, 52(1):146 – 153.

- Yap, Y. G. and Camm, A. J. (2003). Drug induced qt prolongation and torsades de pointes. *Heart (British Cardiac Society)*, 89(11):1363–1372.
- Zaniboni, M., Pollard, A. E., Yang, L., and Spitzer, K. W. (2000). Beat-to-beat repolarization variability in ventricular myocytes and its suppression by electrical coupling. *American Journal of Physiology-Heart and Circulatory Physiology*, 278(3):H677–H687.
- Zhang, H., Garratt, C. J., Zhu, J., and Holden, A. V. (2005). Role of up-regulation of IK1 in action potential shortening associated with atrial fibrillation in humans. *Cardiovascular Research*, 66(3):493–502.
- Zhu, R., Millrod, M. A., Zambidis, E. T., and Tung, L. (2016). Variability of action potentials within and among cardiac cell clusters derived from human embryonic stem cells. *Scientific Reports*, 6(1):2045–2322.